Charles University in Prague

Faculty of Mathematics and Physics

DOCTORAL THESIS

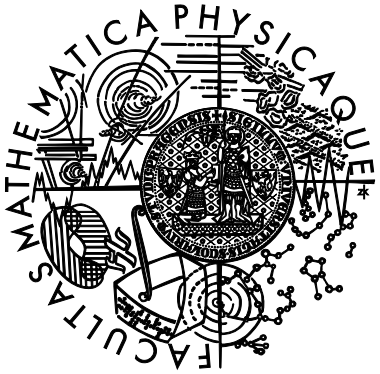

Mgr. Karel Jelínek

Dynamics of the bow shock and magnetopause

Department of Surface and Plasma Science

Thesis supervisor: Prof. RNDr. Zdeněk Němeček, DrSc.

Study Branch: f-2

Prague 2012

I declare that I carried out this doctoral thesis independently, and only with the cited sources, literature and other professional sources.

I understand that my work relates to the rights and obligations under the Act No. 121/2000 Coll., the Copyright Act, as amended, in particular the fact that the Charles University in Prague has the right to conclude a license agreement on the use of this work as a school work pursuant to Section 60 paragraph 1 of the Copyright Act.

In Prague, May 14, 2012 Mgr. Karel Jelínek .....

Acknowledgements

In the first place, I would like warmly thank to my supervisor Prof. Zdeněk Němeček and no less to Prof. Jana Šafránková. Their guidance, ideas, supports and help followed my whole master and doctoral study and their tireless efforts lead eventually to this thesis.

I want to thank Doc. Ondřej Santolik and Doc. Lubomír Přech whose programming tools I utilize for data processing. Next, I would like to acknowledge all staff and my colleagues of the department of Surface and Plasma Science for numerous interesting discussion (including V.D. Vítek).

Especial thanks go to my family, my parents, to my wife and eventually to my little son who were so patient during thesis writing.

Název práce: *Dynamika okolozemní rázové vlny a magnetopauzy*

Autor: *Karel Jelínek*

Katedra: *Katedra fyziky povrchů a plazmatu*

Vedoucí disertační práce: *Prof. RNDr. Zdeněk Němeček, DrSc.*
Katedra fyziky povrchů a plazmatu

e-mailová adresa: *zdenek.nemecek@mff.cuni.cz*

Abstrakt: *Meziplanetární prostor je unikátní laboratoří, která nám pomáhá odhalovat (i) chování plazmatu za různých podmínek, (ii) vznik nestabilit a (iii) interakci plazmatu s překážkami, například s magnetosférou Země. Předložená disertační práce se zabývá výzkumem vnější magnetosféry Země založeným na dálkovém průzkumu plejádou vědeckých družic, např. IMP-8, INTERBALL-1, MAGION-4, Geotail, Cluster-II a Themis.*

Sluneční vítr, který je monitorován družicemi WIND a ACE v Lagrangeově bodě L1, působí svým dynamickým tlakem na zemské magnetické pole, které vytváří protitlak. Hranici, kde se tlakové působení vyrovnává, nazýváme magnetopauza. Díky nadzvukové rychlosti slunečního větru dochází před magnetopauzou ke vzniku rázové vlny a oblast mezi těmito hranicemi, kde již plazma obtéká překážku, nazýváme přechodová oblast.

Výsledkem práce je prohloubení znalostí o závislosti tvaru a polohy rázové vlny a magnetopauzy na (1) orientaci meziplanetárního magnetického pole, (2) orientaci magnetického dipólu Země, (3) upřesnění závislosti na dynamickém tlaku slunečního větru a (4) určení rychlosti pohybu rázové vlny. Mimořádným výsledkem je unikátní automatická metoda pro rozpoznání magnetosférických oblastí, která vedla k vytvoření nového empirického modelu poloh rázové vlny a magnetopauzy.

Klíčová slova: *zemská magnetosféra, rázová vlna, magnetopauza, přechodová oblast, empirický model*

Title: *Dynamics of the bow shock and magnetopause*

Author: *Karel Jelínek*

Department: *Department of Surface and Plasma Science*

Supervisor: *Prof. RNDr. Zdeněk Němeček, DrSc.*
Department of Surface and Plasma Science

e-mail address: *zdenek.nemecek@mff.cuni.cz*

Abstract: *The interplanetary space is a unique laboratory which allows us to discover (i) a behavior of the plasma under different conditions, (ii) origin of its instabilities, and (iii) its interaction with obstacles such as the Earth's magnetosphere. The present thesis analyzes the outer Earth's magnetosphere. The results are based on the in situ sensing by a variety of the spacecraft (e.g., IMP-8, INTERBALL-1, MAGION-4, Geotail, Cluster-II and Themis).*

The solar wind curently monitored by the WIND and ACE spacecraft near the Lagrange point L1 affects by its dynamic pressure the Earth's magnetic field which acts as a counter-pressure and the boundary where these pressures are balanced is the magnetopause. Due to supersonic solar wind speed, the bow shock forms in front of the magnetopause and a region in between, where plasma flows around an obstacle is named the magnetosheath.

The thesis contributes to a deaper understanding of the dependence of magnetopause and bow shock shapes and positions, especially, (1) on the orientation of the interplanetary magnetic field, (2) on the orientation of the Earth's magnetic dipole, (3) a correction of the dependence on the solar wind dynamic pressure and (4) a determination of the speed of the bow shock motion. The most important result is unique authomatic method for recognition of different magnetosheric regions, which led to development of the new empirical magnetopause and bow shock models.

Keywords: *Earth's magnetosphere, bow shock, magnetopause, magnetosheath, empirical model*

Contents

Chapter 1

Introduction

Space physics is much younger branch of physics than, for example, astrophysics because we cannot easily explore cosmic environment without the spacecraft. Until the 20th century, space plasma has been observed only indirectly as a solar corona during eclipse, in form of auroral lightening, and by the magnetic field measurement on the Earth's surface during magnetic storm and substorm, or as a orientation of tail of comets. The main progress of exploration started after a first launch of satellites with scientific payloads, e.g., LUNA 1 and EXPLORER. In these times, theoretical concepts were confronted with real data and scientists started realizing how the processes in our near-space are complex.

The Earth's magnetosphere emerges as a consequence of interaction between the magnetic field of the Earth and the solar wind. Latter is the radial flow of charged particles from the solar corona. The solar wind drags within plasma the magnetic field which is "frozen-in". The solar wind is highly conductive and therefore it cannot penetrate thought the Earth's magnetic field, thus it flows around it. Thus, the Earth's magnetic field is closed inside a cavity around the solar wind plasma. In other words, the magnetic field is an obstacle for the incoming solar wind and its shape is a consequence of equilibrium between the solar wind dynamic pressure on one side and the magnetic field pressure of the Earth on the other side. The boundary where the pressure equilibrium takes place is called "the magnetopause".

A mean solar wind velocity is about 400 km/s and typical MHD waves travel with 60 km/s; it means that the solar wind moves supersonically and therefore, in front of the magnetopause, a shock waves arises that we call "the bow shock".

In present thesis, we deal with the dynamic changes of magnetospheric boundaries, particularly with the bow shock and magnetopause. Magnetospheric structures will be described in more details in the next chapter.

Chapter 2

The solar wind and the Earth's magnetosphere

In this chapter, we briefly introduce an origin of the solar wind (SW), its typical parameters and mechanism of its interaction with the Earth's magnetosphere (MS).

2.1 The solar wind plasma

The solar wind is almost fully ionized plasma with ion composition dominated by hydrogen H^+ ($\approx 96\%$) and helium He^{++} ($\approx 4\%$); the density of other elements fall down rapidly with its nuclear number and the density of electrons fulfils quasi-neutrality of the solar wind plasma.

In contrary to emitted infrared and visible light by the Sun's surface which an integral value of energy flux is very stable ($\delta \approx 0.1\%$), all parameters of the solar wind plasma highly fluctuate. In Fig 2.1 a)-d), 2D-distributions of several plasma parameters measured by the ACE spacecraft in the solar wind from Jun 2001 to Jun 2011 are plotted. In the figure, it is not clearly seen that distributions consist of two populations, however, there is present so called "slow" and "fast" solar wind populations. The slow solar wind is observed more frequently and has a broader distribution of the magnetic field and particle density and its origin is in solar corona what corresponds to its composition. The fast solar wind has a broader thermal energy distribution and reaches a lower density and magnetic field and its composition matches solar photosphere because it originates in coronal holes (Fig. 2.2). Mean values of the solar wind parameters at the distance of 1 AU are summarized in Table 2.1.

Although the solar wind is collisionless – it interacts through the Coulomb force only – the plasma with a higher velocity cannot penetrate to the slower plasma because of presence of the magnetic field. Such interaction allows a compression

parameter	value
proton density	$6.6\,\mathrm{cm}^{-3}$
electron density	$7.1\,\mathrm{cm}^{-3}$
He_{++} density	$0.25\,\mathrm{cm}^{-3}$
solar wind velocity	$450\,\mathrm{km\,s}^{-1}$
proton temperature	$1.2 \times 10^5\,\mathrm{K}$
electron temperature	$1.4 \times 10^5\,\mathrm{K}$
magnitude of the magnetic field	$7 \times 10^{-9}\,\mathrm{T}$

Table 2.1: Mean values of observed solar wind parameters in the Earth's vicinity.

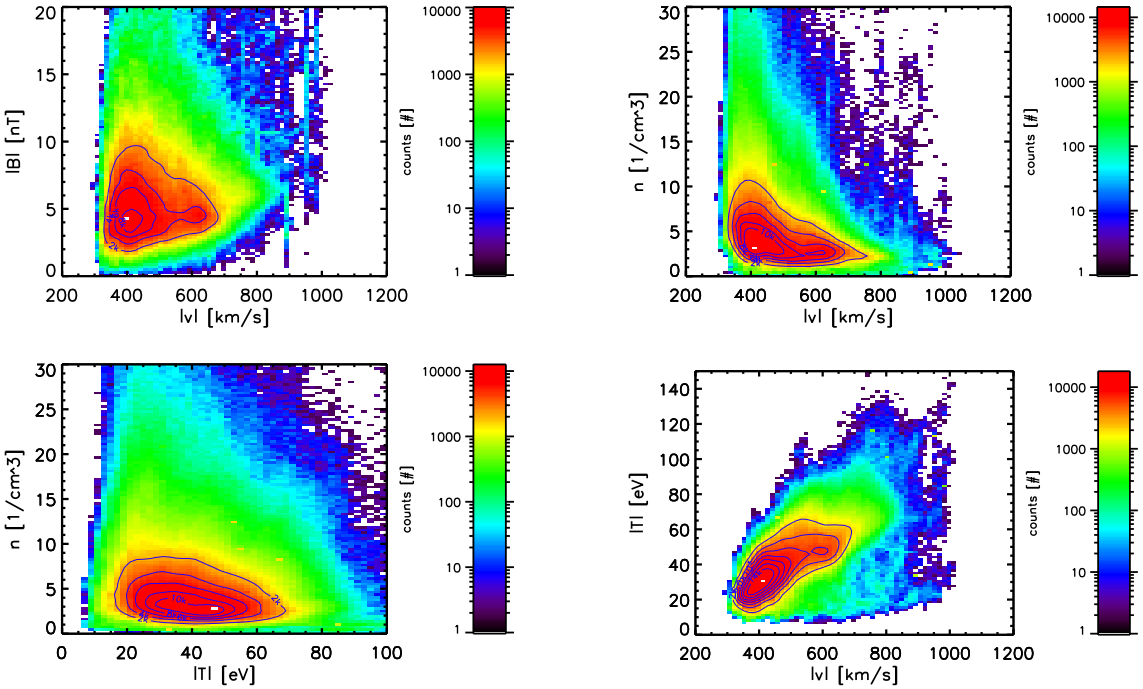

Figure 2.1: 2D histograms of solar wind observations by the ACE spacecraft for four key parameters. Here, it is not possible to distinguish between slow and fast solar winds, however, in the 4D histogram of n,v,T and B (plasma density, velocity, temperature and the magnetic field) it does.

and rarefaction which are illustrated in Figure 2.3.

The plasma flow is neither always radial, the direction of the solar wind velocity fluctuates from its mean radial direction, nor uniformly distributed to all directions. The slow solar wind during solar minimum is spread in latitudes about 30-35 degrees from the solar equator, on the other hand, during solar maximum, it was also recorded near Sun's poles.

The slow and fast solar winds are not only sources of the plasma, there are other events during those the Sun emits burst of plasma, they are a coronal mass ejection (CME). CMEs are associated with the solar flares which result as a release of the accumulated magnetic energy at the Sun.

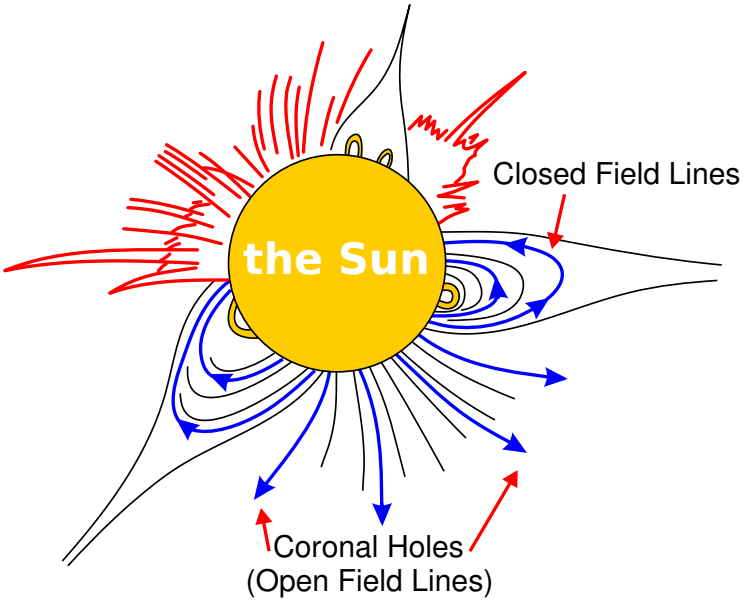

Figure 2.2: Sketch of possible magnetic field structures in the solar corona (Kivelson and Russell [1995]).

2.2 Magnetic field of the Sun and IMF

Another important feature of the solar wind is its *frozen-in magnetic field* which we call the interplanetary magnetic field (IMF). When the solar wind escapes from the solar corona it drags within the solar magnetic field and thus its strength and direction in a given point of the interplanetary space are determined by the processes at the origin as well as by the turbulent motion of the solar wind.

The magnetic field of the Sun is created by the so called magnetohydrodynamic dynamo. A thermodynamic convection of the magnetized plasma in the Sun's convection region generates an additional magnetic field. Because of differential rotation of the Sun, the equatorial period is 25 days but at poles 35 days, the plasma rotates faster at equator and wind-up magnetic field lines. When the magnetic field is wound-up enough – the gradient of magnetic field between neighbouring latitudes is strong to start magnetic reconnection – it can unwind and create magnetic loop outward the Sun surface and that can be optically observed.

The Sun magnetic field has quite complicated spatial distribution and temporal evolution. Almost radial magnetic field connected with the heliosphere is dominant on poles. The solar wind propagates along these open field lines with larger mean speed and we call this state the fast solar wind. In lower latitudes ($\pm 30°$) near the Sun's surface, the magnetic field lines are connected between the North and the South hemisphere and create closed loops. These loops are pulled out by the solar wind flow, they become highly elongated but a part of the solar wind energy is lost and thus this region is occupied by the slow solar wind. The plane which divides

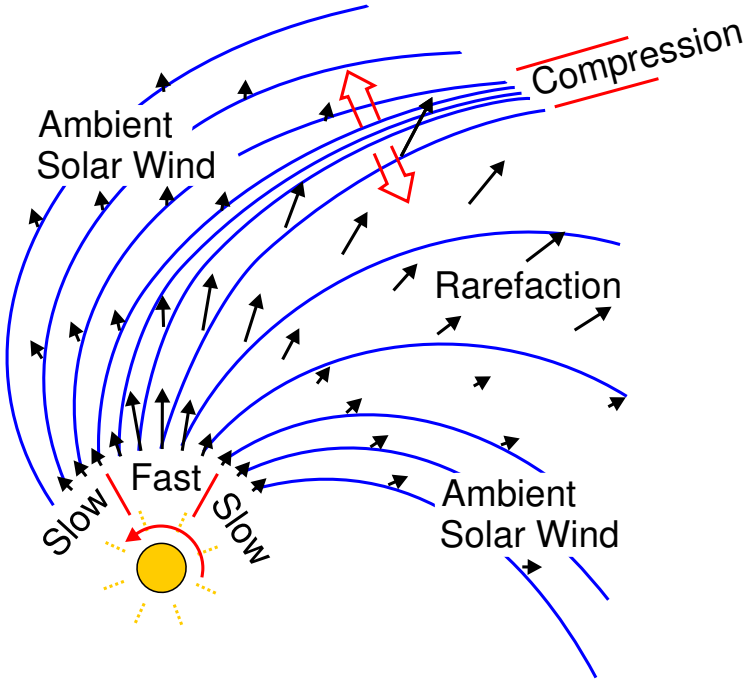

Figure 2.3: The slow–fast solar wind interaction which can develop to the interplanetary shock.

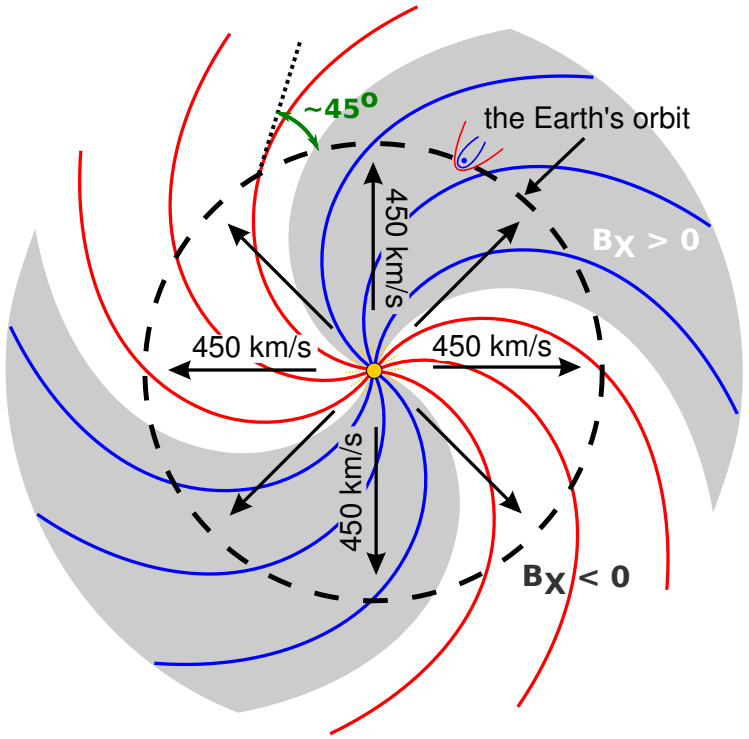

Figure 2.4: The IMF orientation in the equatorial plane along the Parker spiral (adapted from Kivelson and Russell [1995]).

oppositely oriented magnetic field orientations is called neutral sheet and its shape depends on the phase of the solar cycle. During solar minimum, there are most probable two or four intersection of neutral sheet with the ecliptic plane. This is documented in Fig. 2.4. Within solar maximum, the shape of the neutral sheet is more complicated and the equator could cross islands with different orientations, this leads to higher variability of the interplanetary magnetic field. Because the solar wind expands almost radially and the Sun rotates resulting magnetic field lines has a spiral shape – we call it a Parker spiral. At the distance of 1 AU (astronomical unit), the mean direction of IMF with respect to the Sun–Earth line is 45^o.

2.3 The Earth's magnetosphere

The Earth's magnetosphere is formed as a consequence of interaction of the solar wind with the Earth's magnetic field. The first comprehensive concept was made by Sydney Chapman and his student Vincenzo Ferraro [Chapman and Ferraro, 1930]. Now, after many years of remote measurements by spacecraft, physicists developed the model of Earth's magnetosphere; its simplified scheme with a different regions is depicted in Figure 2.5.

The magnetosphere is usually divided into inner and outer magnetosphere and the boundary between them we call magnetopause (MP). Boundary between Earth's magnetosphere and the solar wind is the bow shock (BS). The solar wind is considered undisturbed in front of the bow shock, but this is not exactly true because of presence of a "foreshock". The foreshock originates at the bow shock and is formed by reflected and accelerated solar wind particles moving along IMF towards the undisturbed solar wind. Some amount of a plasma from the magnetosheath – a thick layer between the bow shock and magnetopause – can penetrate through the so called magnetospheric cusps into regions over Earth's magnetic poles and further to the inner magnetosphere.

As it can be seen from the figure, the inner magnetosphere is further structured but the present thesis deals with the outer magnetosphere and thus we will not discuss this structure.

2.4 The solar wind-magnetopause interaction

The magnetopause is a layer/region determined by the pressure balance between the total pressure on the magnetosheath side and the magnetic pressure on the magnetospheric side. A strong dependence of the magnetopause shape and location on the solar wind dynamic pressure was established and also the dependence on

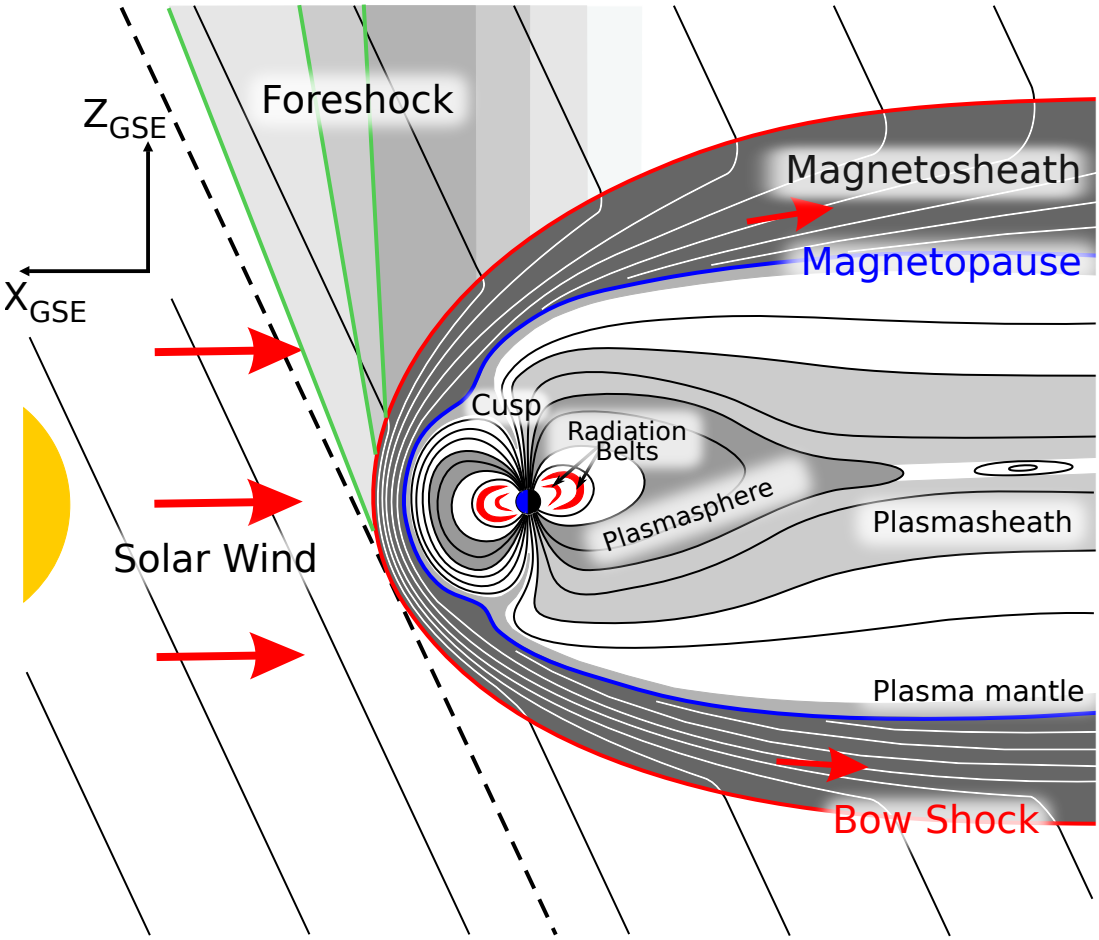

Figure 2.5: Schematic picture of regions playing an important role in interaction of the solar wind with the Earth's magnetosphere.

the strength and IMF orientation has been noted by Aubry et al. [1970]. In early published papers [Fairfield, 1971; Formisano et al., 1973, 1979; Sibeck et al., 1991; Roelof and Sibeck, 1993; Petrinec and Russell, 1996; Shue et al., 1997, 1998; Boardsen et al., 2000] it was found that the upstream dynamic pressure strongly influences the Earth's magnetopause position. In some of these models, a stand-off position, R is scaled with the solar wind dynamic pressure, p as $R \approx \sqrt[6]{p}$ that is based on an assumption of the dipole Earth magnetic field. On the other hand, the pressure scaling factor was included as a free fitting parameter to other models. The authors found it to be larger than 6 (e.g., 6.16 in Boardsen et al. [2000] or 6.6 in Shue et al. [1997, 1998]). By contrast, the recent paper of Lin et al. [2010] proposed the lower scaling factor of 4.8. The factor of 5.2 follows from an analysis of the global MHD model made by Lu et al. [2011].

Furthermore, it was found that the second parameter driving the position and shape of the magnetopause is the B_Z component of the interplanetary magnetic field (IMF) because many features of magnetospheric dynamics are controlled by

the interaction between the interplanetary and terrestrial magnetic fields. Dungey [1961] suggested that the mechanism responsible for this interaction is magnetic field reconnection taking place at the magnetopause, where the two fields meet. The general properties of this interaction are a change in the topology of the reconnecting fields and magnetic energy conversion into thermal and bulk energies of the plasma and it drives the large scale magnetospheric convection (mirrored in the ionospheric convection) with the electric field it creates [Dungey, 1953; Sweet, 1958; Parker, 1963; Petschek, 1964; Yeh and Axford, 1970]. The fast reconnection model was created by Petschek [1964] and its basic idea is that (partly) antiparallel magnetic field lines can, when meeting, merge together and produce two topologically totally different field lines. Schematics of magnetic reconnection are shown in Fig. 2.6. Two cases of IMF orientations important for our thesis are depicted in Fig. 2.7. For the southward IMF orientation (Fig. 2.7, right), the strongest gradient of the magnetic field lies along the Sun-Earth line (subsolar region), the Earth magnetic field is eroded by reconnection and the magnetosphere is compressed. During intervals of northward IMF (Fig. 2.7, left), reconnection takes place on the flanks of the magnetopause.

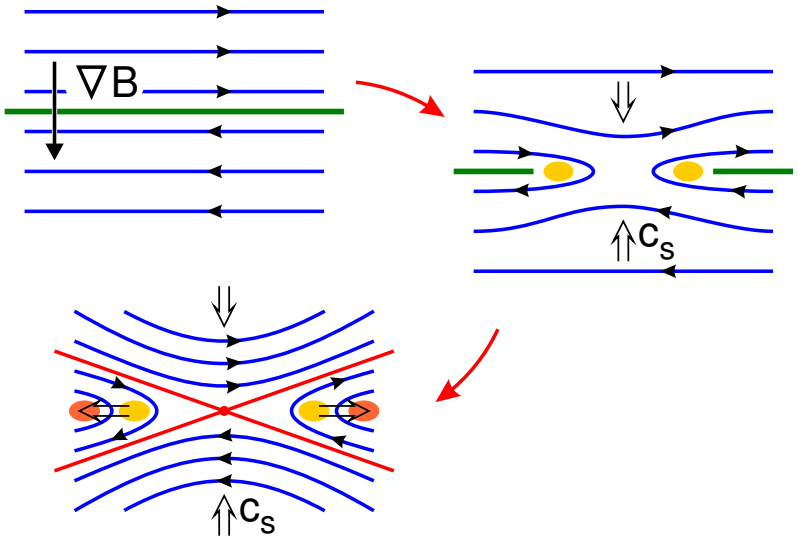

Figure 2.6: Magnetic field reconnection schematics. High magnetic field gradient $\nabla\vec{B}$ causes an instability which converts magnetic energy into kinetic and thermal. The reconnection rate, c_s also depends on plasma β on both sides and it is limited by the thermal velocity (Phan et al. [2010]).

Thus, it is supposed that mainly the IMF B_Z can affect the magnetopause position. This effect is a subject of the papers by Sibeck et al. [1991]; Roelof and Sibeck [1993]; Petrinec and Russell [1996]; Shue et al. [1997, 1998] and many others and its influence is included into the models. On the other hand, Verigin et al. [2009] argued that no dependence of the subsolar magnetopause position on the IMF B_Z component has been revealed in a large set of the Interball data.

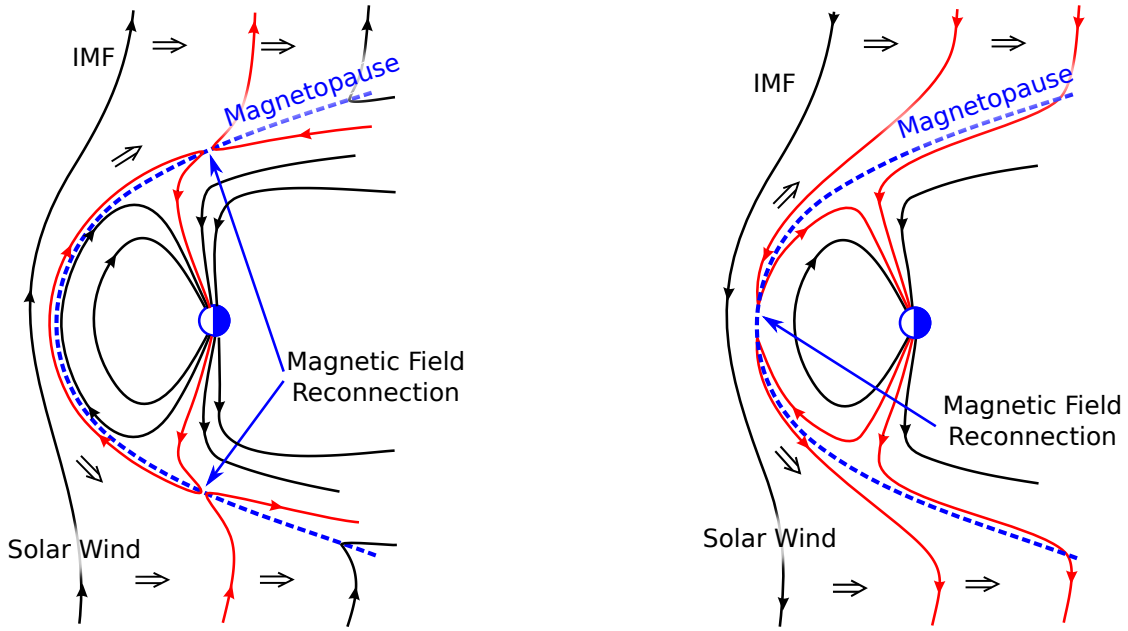

Figure 2.7: Magnetic field reconnection at the magnetopause for strictly northward (left panel) and southward (right) orientations of the IMF.

On the other hand, Fairfield et al. [1990] indicated that a radial IMF orientation may be an alternative dominant factor which can cause the magnetopause expansion in the subsolar region. They supposed that foreshock pressure fluctuations convect through the subsolar bow shock into the magnetosheath and influence the subsolar magnetopause location. The position of the foreshock in front of the bow shock is controlled by the θ_{Bn} angle. This angle is defined as the angle between the IMF and local normal to the bow shock as it is demonstrated in Fig. 2.8. In the subsolar region, this angle coincides with the angle between the IMF vector and the Earth-Sun line. In the case of a radial IMF, the foreshock is located upstream of a whole dayside bow shock. Under this condition, Merka et al. [2003b] reported larger amplitude of magnetopause oscillations.

Boardsen et al. [2000] developed an empirical model of the shape of the near-Earth high-latitude magnetopause that is parameterized by the solar wind dynamic pressure, IMF B_Z component and dipole tilt angle (it is the angle between the Z_{GSM} axis and Earth's magnetic dipole). The authors argued that the dipole tilt angle and solar wind pressure are the most significant factors influencing the shape of the high-latitude magnetopause and that the IMF B_Z dependence can be found only if the pressure and tilt angle effects are removed by a proper scaling. Similar results were reported by Tsyganenko [1998] and by Eastman et al. [2000]. Safrankova et al. [2005] have analyzed high-latitude magnetopause crossings and suggested a simple correction of the Petrinec and Russell [1996] model that reflects the magnetopause indentation in the cusp region. This indentation was later explicitly included into

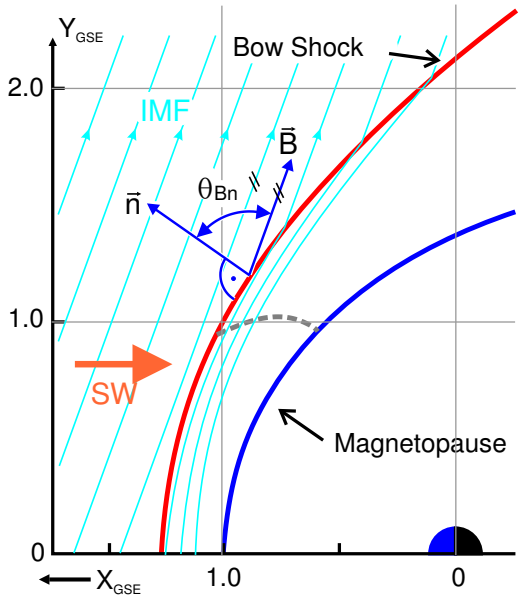

Figure 2.8: Definition of the Θ_{Bn} angle: the angle between the IMF orientation and local normal to the bow shock surface.

the Lin et al. [2010] model. This situation is schematically demonstrated in Fig. 2.9. In the left part, 3D sketch of the high-latitude magnetopause surface is shown, whereas several cross-sections are depicted in the right part. On the other hand, the presence of this indentation was questioned in several papers [Zhou and Russell, 1997; Lavraud et al., 2004].

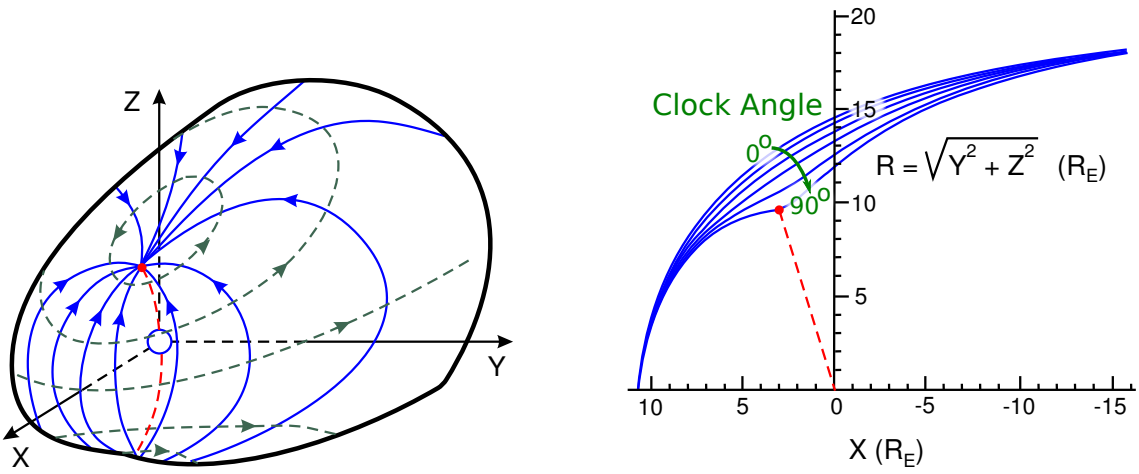

Figure 2.9: (left panel) A shape of the magnetopause. Full blue lines correspond to Earth's magnetic field lines and dashed green lines to direction of currents on the magnetopause surface. (right plot) Magnetopause intersection. The top blue curve represents the magnetopause intersection in the XY plane, other curves are intersections with increasing clock angle up to 90° which is in the XZ plane.

The solar wind plasma flow is supersonic, therefore the bow shock rises ahead of the magnetopause. The Earth's bow shock is the most studied collisionless shock

[see, e.g., Burgess, 1995]. The shape, position, and motion of the Earth's bow shock have been a subject of experimental and theoretical research for the last four decades. In course of these years, many bow shock models (predominantly empirical) have been developed (e.g., Merka et al. [2003a] for a survey). In these models, the bow shock has been approximated using ellipsoidal, paraboloidal or hyperboloidal surfaces with varying standoff distances under assumption that both position and shape can be expressed as a function of upstream plasma parameters (usually by the dynamic pressure of the incoming solar wind and by upstream Mach numbers).

The most known model of the bow shock was published by Fairfield [1971]. This model is based only on observations made near the ecliptic plane and thus the model is two-dimensional second-order fit to bow shock positions. It assumes axial symmetry along the solar wind flow direction and does not include any corrections to compensate effects of the solar wind dynamic pressure except an aberration due to the orbital motion of Earth. Formisano et al. [1971] found that the bow shock location can be predicted with a higher accuracy when the upstream magnetosonic Mach number is taken into account. Slavin and Holzer [1981] examined Mach number effects on the shock position and compared results with the gasdynamic theory. This topic was treated by many authors in the past, especially in connection with studies focused on unusual positions of the bow shock crossings (e.g., Fairfield and Feldman [1975]; Farris et al. [1991]; Cairns et al. [1995].

Formisano [1979] developed a bow shock model parametrized by both upstream dynamic pressure and magnetosonic Mach number. Further, Nemecek and Safrankova [1991] used the Formisano approach and suggested a new model including explicitly the solar wind dynamic pressure, magnetosonic Mach number and interplanetary magnetic field strength. Peredo et al. [1995] developed a three-dimensional empirical model predicting the statistical bow shock position and shape for arbitrary values of the solar wind pressure, IMF, and Alfvén Mach number. They investigated the influence of variations in the sonic (M_S), Alfvenic (M_A), and magnetosonic (M_{MS}) Mach numbers as well as the orientation of IMF. The authors removed the effects associated with Earth's orbital motion by rotating the crossings into aberrated GSE coordinates. Changes due to solar wind dynamic pressure variations have been taken into consideration by normalizing the observed crossings to the average value of 3.1 nPa and variations due to different IMF orientations were taken into account by rotating all crossings into geocentric interplanetary medium coordinates [Bieber and Stone, 1979], where the B_Z component of the IMF vanishes.

Other point of view was presented in the paper of Farris and Russell [1994] where the authors investigated analytical hydrodynamic and MHD formulas across the bow shock and along the boundary of an obstacle to the solar wind flow. They found

that the bow shock position can be better described by downstream Mach number and upstream plasma parameters. The main difference of this approach from those used in previous estimations is that the bow shock moves toward infinity for very low upstream Mach numbers, which is what the authors expected physically (e.g., Russell and Zhang, 1992). On the other hand, the suggested correction of the bow shock position is negligible for the Mach numbers which are frequently observed. Moreover, the authors suggest to use the radius of curvature of the magnetopause for the determination of the magnetosheath thickness rather than a distance of the subsolar point from the Earth center. We would like to note that the application of this suggestion would lead to a more stable bow shock position because the distance of the subsolar magnetopause from the Earth decreases, whereas the radius of curvature and, consequently, the magnetosheath thickness increases when IMF B_Z becomes more negative.

A similar approach to the prediction of the bow shock location was used by many other authors (e.g., Russell and Zhang, 1992; Grabbe, 1997). Cairns and Grabbe [1994] developed an MHD theory for the bow shock stand-off distance and the thickness of the magnetosheath. The global three-dimensional MHD simulations of Cairns and Lyon [1995] further improved the theory and obtained the expression for both parameters. The magnetosheath thickness strongly depended on the Alfvenic and sonic Mach numbers and on the angle between the solar wind velocity and direction of IMF. Their bow shock predictions agreed with gasdynamic predictions in the high M_A limit [Spreiter et al., 1966].

Using aerodynamics, Seiff and Whiting [1962] empirically showed that the stand-off distance of the bow shock normalized by the radius of the obstacle (magnetopause) is nearly linearly proportional to the inverse density ratio across the bow shock. Spreiter et al. [1966] applied this knowledge to gasdynamic flow around a magnetosphere and showed that the density ratio is related to the compressibility of the medium and the asymptotic free-stream Mach number, M, thus the relationship between these quantities is as follows:

$$\Delta_{MSH} = D\frac{(\gamma-1)M_A^2+2}{(\gamma+1)(M_A^2-1)}$$

where γ is the polytropic index. This expression was later included into the bow shock model by Formisano et al. [1973]. The coefficient of 1.1 is supposed to be valid for explanation of the bow shock position in front of a blunt obstacle [Seiff and Whiting, 1962]. However, Spreiter et al. [1966] did not change the shape of the obstacle to test whether this value is valid for other blunt obstacles.

Furthermore, an influence of other parameters on locations of both boundaries was examined in different papers; for example, a rotation of the direction of the

magnetic field across the magnetosheath [Pudovkin et al., 1982], both IMF polar and azimuthal angles, and the angle between the IMF and the bow shock normal [Laakso et al., 1998; Safrankova et al., 2003], IMF B_Y component [Sibeck et al., 2000], or Alfvénic fluctuations dominating the solar wind [Tsubouchi et al., 2000]. Moreover, larger displacements of boundaries as a result of their interaction with different solar wind discontinuities (e.g., HFAs (hot flow anomaly), strong interplanetary shocks, pressure pulses) were widely discussed by many authors [Sibeck et al., 1999; Farrugia et al., 2008; Zhang et al., 2009; Jacobsen et al., 2009].

The magnetosheath, a region bounded at its outer edge by the bow shock and by the magnetopause at its inner edge, plays an important role in these processes because it is the environment through which energy and momentum are transported from the solar wind towards the magnetopause. In the MHD description, the magnetosheath reconfigures the upstream solar wind flow and its frozen-in magnetic field to the state specified by the magnetopause boundary conditions. However, it is a simplification because this approach does not account for kinetic processes operating on small-scale lengths which also contribute to the plasma behavior. Estimates of the global plasma properties in the magnetosheath are predominantly based on the results of the gasdynamic model predictions of Spreiter et al. [1966] and Spreiter and Stahara [1980]. Their model assumes that bulk flow properties of the solar wind past a planetary obstacle can be described by the continuum equations of hydrodynamics for a single-component gas. A simplified non-self-consistent prescription for the magnetic field, which is frozen kinematically to the flow, means that magnetic forces are omitted from the momentum equation.

In the model, the solar wind flows along the Sun-Earth line, strikes the subsolar magnetopause and then is diverted radially from this point. The model further predicts that velocity decreases from the bow shock to the magnetopause, whereas the density and temperature increase in the vicinity of the stagnation streamline. Farther from the subsolar region, the density and the velocity decrease but the temperature increases through radial profiles from the bow shock to the dayside magnetopause. Along the flanks of the near-Earth magnetotail, minimum velocities and maximum temperatures occur in the middle magnetosheath. The plasma flowing radially away from the stagnation streamline accelerates up to the solar wind speed and becomes increasingly like the solar wind toward the flanks, where the bow shock is weaker. Two examples of the Spreiter et al. [1966] results are shown in Figs. 2.10 and 2.11. These predictions were generally confirmed by experimental studies but the gasdynamic approach cannot elucidate the problems of fluctuations of parameters because it allows only a single wave mode.

From the above survey, it follows that the models still do not sufficiently describe

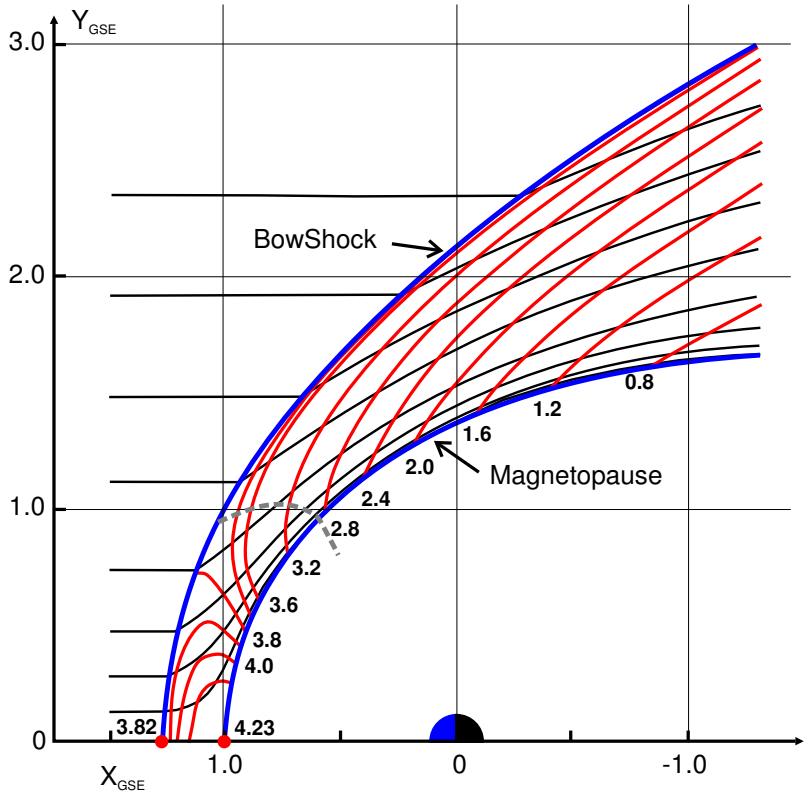

Figure 2.10: Output of the Spreiter et al. [1966] model. Black curves represent flow lines and iso-lines of constant compression ratio are shown by red. The value of this ratio is also depicted.

observed bow shock and magnetopause locations, especially for unusual conditions in the solar wind. The existing theories can apply to a magnetosphere immersed in a uniform, steady state solar wind plasma/field environment, which, of course, is an idealized and simplified picture of the highly variable reality. Therefore when comparing the observations to current theories or models one expects a scatter of the bow shock/magnetopause locations from the model predictions. In general, in order to compare model predictions with observations, large numbers of observed bow shock crossings are required. However, during periods of prolonged steady solar wind conditions, individual crossings can be readily compared to the various model predictions.

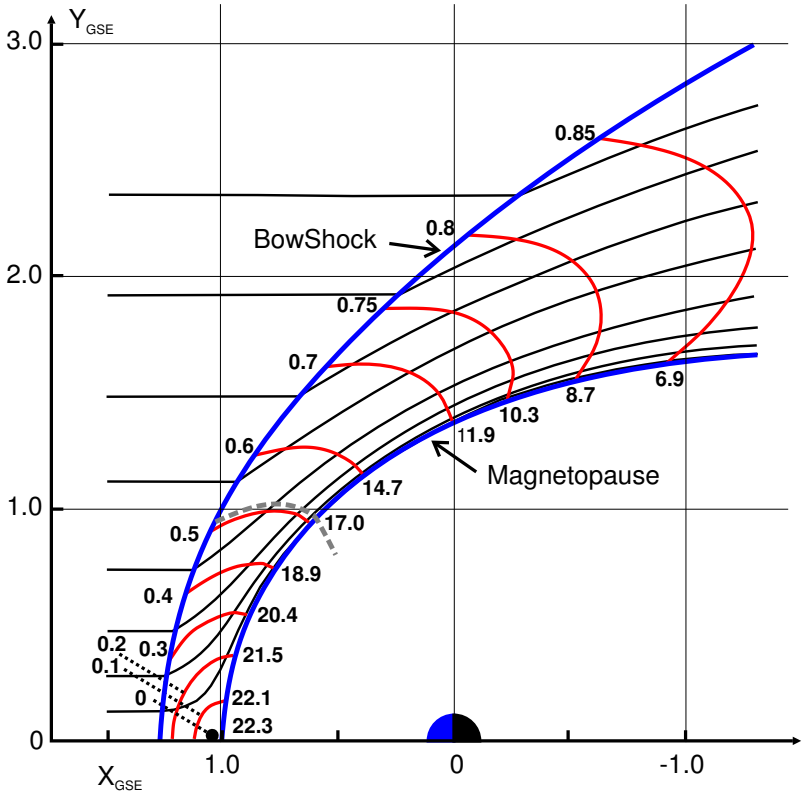

Figure 2.11: A similar figure to 2.10 with iso-lines of constant velocity ratio that are identical with isotherms in this model. The values of the velocity ratio are in the left side and temperature ratios in the right side of the magnetosheath.

Chapter 3

The aims of the thesis

The prediction of locations of both outer magnetosphere boundaries - the bow shock and magnetopause - is a proof of our understanding of the processes governing the solar wind - magnetosphere interaction. However, the models describing these boundaries as a function of upstream parameters are based on a statistical processing of crossings observed by a single spacecraft. Such crossings locate the bow shock/magnetopause in motion, i.e., in a non–equilibrium state and this fact can be a source of significant errors. Moreover, many other processes can influence locally their particular positions (e.g., reconnection, unusual orientation of the IMF, etc.). For these reasons, the main task of this thesis was a study of the bow shock and/or magnetopause dynamics. The investigation is based on multipoint spacecraft measurements in the case studies as well as on statistical data processing. We can precise our general task into several directions:

(1) Two-point observations of the bow shock speed;

(2) Simultaneous observations of the bow shock and magnetopause motions;

(3) An influence of the tilt angle change on the bow shock position;

(4) Findings of the sources of uncertainties between the model prediction and measured bow shock and/or magnetopause locations;

(5) An influence of a radial orientation of the interplanetary magnetic field on location/deformation of the magnetopause;

(6) All these particular studies aimed as a tool for development of a new model of the bow shock and magnetopause locations.

Chapter 4

Data used and their processing

In the thesis, two-point cases as well as statistical studies are presented. For this reason, we discuss data sources and briefly summarize the description and properties of used instruments placed on different spacecraft in Appendix B. The case studies used closely separated Magion-4/Interball-1 satellite pair or five probes of the Themis mission. On the other hand, for statistical studies, particular data sets were used:

(1) To correction of the empirical model of Nemecek and Safrankova [1991], the set consisting of $\sim$ 5400 bow shock crossings from Interball-1, Magion-4, IMP 8, Geotail, and Cluster spacecraft (details in [Jerab et al., 2005]) was accumulated. For these crossings, Wind upstream solar wind parameters were used. The set included both outbound and inbound crossings, many of them being multiple.

(2) To discussion of the dependence of a bow shock location on the tilt angle ([Jelinek et al., 2008b]), the same set of bow shocks was used;

(3) To study of the bow shock velocity and its small-scale motion, the subset including only the Interball-1 and Magion-4 crossings of these boundaries was applied;

(4) To develop the new model of both boundaries and its verification and to find of a dependence of the magnetopause location on the radial IMF, we prepared: (i) two sets of Themis magnetopause ($\sim$ 5.400) and bow shock ($\sim$ 6.700) crossings, and (ii) used the continuous measurements of the plasma parameters and magnetic field by five Themis probes at 2007-2009.

(5) Furthermore, particular and statistical studies were complemented with data from the solar wind monitors, namely from Wind and ACE.

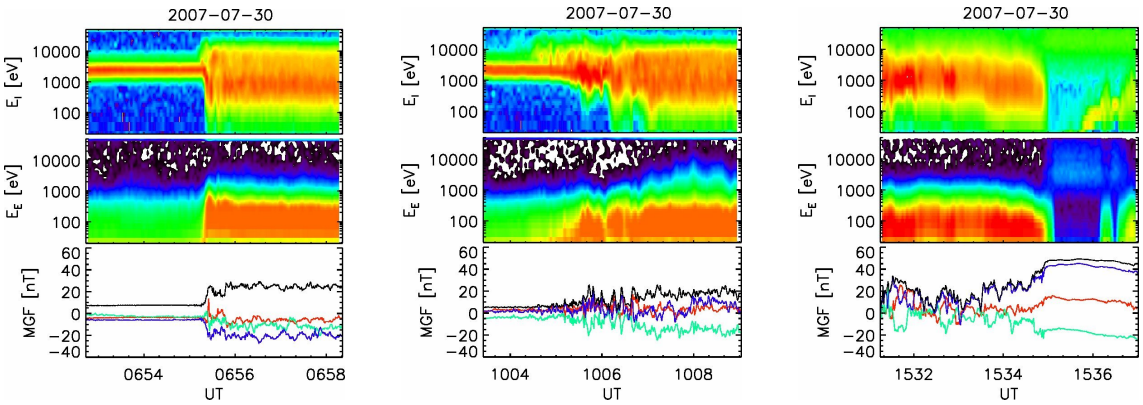

Figure 4.1: Examples of data plots used to identification of quasi-perpendicular (left) and quasi-parallel (middle) bow shocks and magnetopause (right). For all cases, the top panel represents the ion energy distribution, the middle panel is the electron energy distribution, and the bottom panel shows the magnetic field.

In this section, we present two topics: (i) the creation of the Themis database of magnetopause and bow shock crossings, respectively, and (ii) data processing to developing new models of the magnetopause and bow shock locations.

4.1 Themis database preparation

All five THEMIS probes were launched on February 17, 2007 into very similar elliptical and near-equatorial orbits [Angelopoulos, 2008]. Our analysis uses magnetopause and bow shock crossings identified by a visual inspection of the plots containing plasma moments, ion, and electron spectra [McFadden et al., 2008], and magnetic field data [Auster et al., 2008] with the best available time resolution. Examples of an identification of quasiperpendicular and quasiparallel bow shock and magnetopause crossings from data plots are shown in Fig. 4.1. The inspected periods were June–August and November 2007 and May–August 2008; altogether we collected 6660 bow shock and 5.330 magnetopause crossings for which the upstream data from Wind and ACE were available. Many of these crossings were multiple.

The locations of all crossings are shown in Figure 4.2. We note here that the analyzed data were collected during a solar minimum (2007 and 2008) and thus the solar wind dynamic pressure was often well below its average value with the most probable value ∼1 nPa. In combination with a low Themis apogee in the first stage (Fig. 4.2 left) of the Themis mission (in 2007), it represents a bias for bow shock observations. Figure 4.2 right shows distributions of magnetopause and bow shock crossings through the second stage of the THEMIS mission (2008) when the apogee reached 20 R_E.

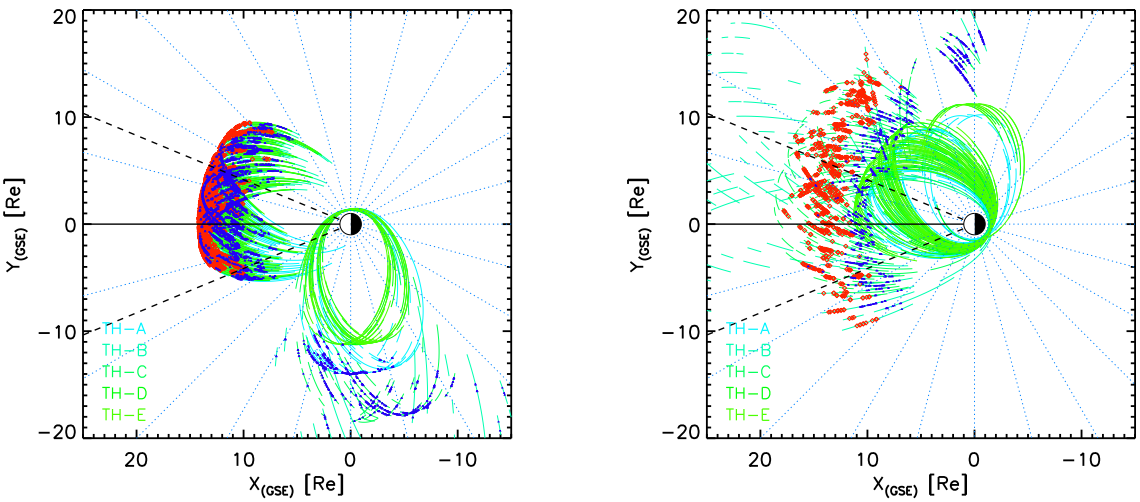

Figure 4.2: Positions of bow shock and magnetopause crossings observed by all THEMIS spacecraft during the years of 2007 (left) and 2008 (right).

4.2 Elimination of the orbital bias

To avoid a misinterpretation of our data, we developed a method which allows us to combine crossings from the 2007 and 2008 years and to suppress bias caused by orbital limitations. We used the procedure of Jelinek et al. [2009] that weights the number of crossings by a time that the spacecraft spent in a particular bin. Since it is generally accepted that the main parameter controlling the magnetopause (and therefore the bow shock) position is the upstream dynamic pressure, we created so called p_{dyn}–R histograms of crossings and a similar histogram of all observations.

The principle of a creation of such histograms is documented in Fig. 4.3. Using one–minute averages of p_{dyn} from ACE and a radial distance of the Themis spacecraft, R, we collected the 2D table of numbers of observations with given R and p_{dyn} coordinates (top panel); a similar table combined numbers of crossings (bottom panel). In Fig. 4.4, the color scale shows the number of observations of bow shock (left) and magnetopause (right) crossings in bins of 0.1 nPa width and 0.1 R_E height. Since a majority of crossings was recorded in 2007, one can clearly see a cut-off caused by the Themis apogee, thus this cut-off requires an application of an appropriate data normalization prior to a further analysis. The normalization is based on assumptions that all parts of Themis orbits above 8 R_E were inspected and all crossings of boundaries were identified, and that we used only those crossings for which the solar wind data were available. Using solar wind observations from the Wind, we construct normalization p_{dyn}–R table from all inspected Themis data. This table is shown in Fig. 4.5 in the same format as in the previous figure. The color scale shows how many minutes the spacecraft spent in a particular bin. The ratio of the number of crossings identified in a particular bin (Fig. 4.4) and the

number of minutes that the spacecraft spent in the same bin (Fig. 4.5) provide a probability of appearance of the boundary crossings in each bin.

The result of this procedure is plotted in two panels of Fig. 4.6. It can be seen that the bias is almost suppressed (bias cannot be completely suppressed by the presented method because of the bins without any THEMIS data) and it is possible to find mean positions of both boundaries which are shown as the solid lines.

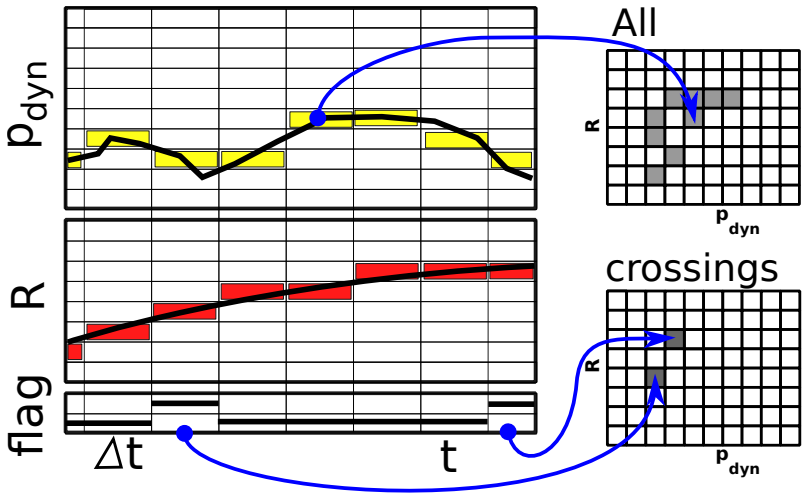

Figure 4.3: A sketch of the R–p_{dyn} histogram creation.

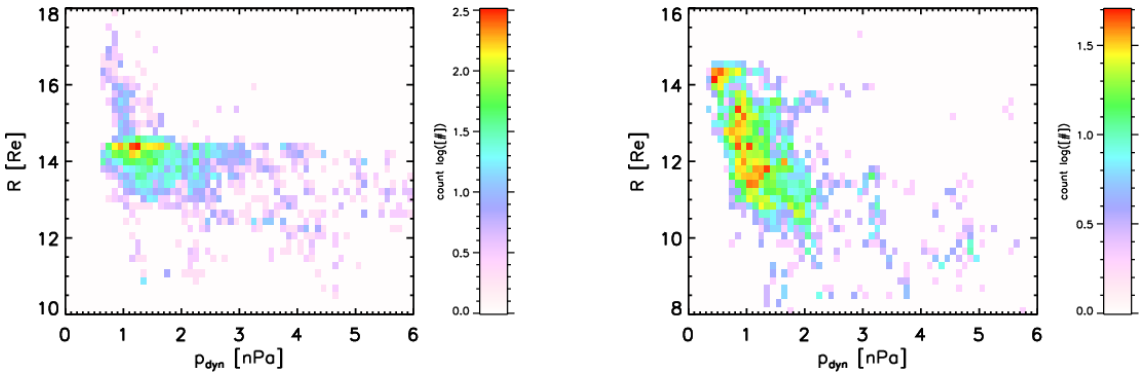

Figure 4.4: Distributions of BS (left) and MP (right) crossings in the p_{dyn}–R histogram. Note that in all histograms, a pure white color represents no crossing in one–minute interval or no measured data within given intervals.

4.3 Automatic identification of boundaries from plasma and magnetic field measurements

For our method, we take advantage of orbits of five THEMIS spacecraft that move through all investigated regions: the solar wind (SW), the magnetosheath (MSH),

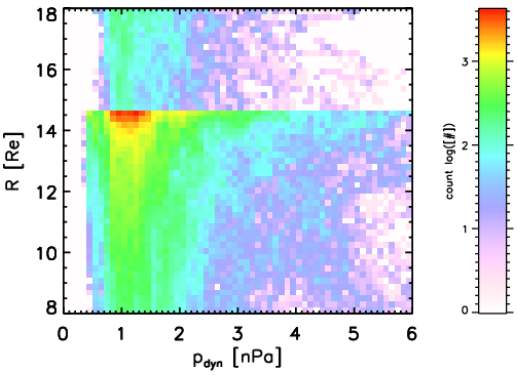

Figure 4.5: Distribution of one–minute intervals in which the Themis spacecraft were located in a particular distance from the Earth, and the magnetosphere was influenced by a particular dynamic pressure. Only local times from 1030 to 1330 UT are combined. The value of $R = 14.6$ demonstrates a orbital limit of the 2007 data set.

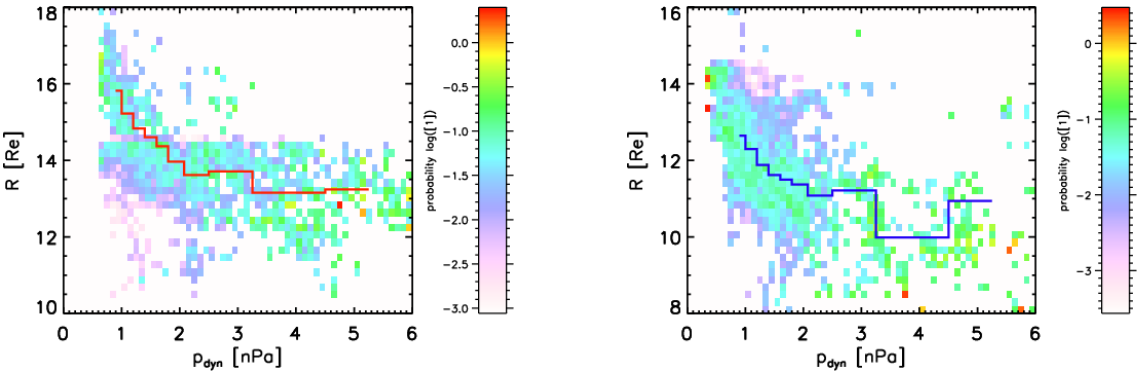

Figure 4.6: Normalized distributions of BS (left) and MP (right) crossings. The solid lines represent a mean position of particular boundaries as a function of the dynamic pressure.

and the inner magnetosphere (MS), and computed one-minute medians of the magnetic field magnitude, $|B_{Themis}|$ and density, n_{Themis}. As a solar wind monitor, we used ACE one-minute medians of the IMF magnitude, $|B_{ACE}|$, density, n_{ACE}, solar wind dynamic pressure, p, and plasma velocity, v_{ACE} shifted to THEMIS positions by convection along the X_{GSE} axis. We use two-step propagation algorithm that is described in Safrankova et al. [2002].

For all measurements of the THEMIS spacecraft at altitudes larger than 5 R_E in the period from March 2007 to September 2009, we computed the ratio of the magnetic fields, r_B

$$r_B = \frac{|B_{Themis}|}{|B_{ACE}|}$$

Because the compression ratio of the magnetic field in the magnetosheath decreases toward the flanks, we added the density compression factor, r_n

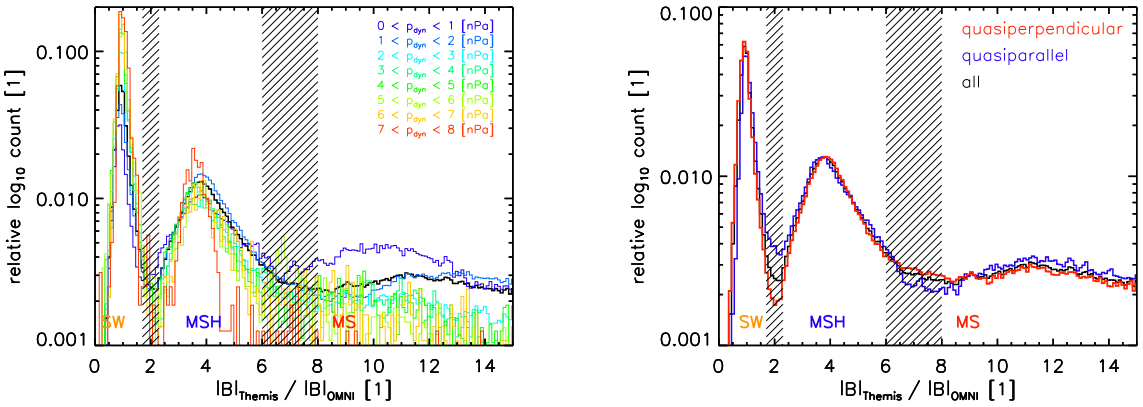

Figure 4.7: Identification of the subsolar solar wind, magnetosheath, and inner-magnetosphere by the magnetic field ratio r_B for different dynamic pressures (left) and different Θ_{Bn} (right). Data from the hatched regions were not included into the statistics.

$$r_n = \frac{n_{Themis}}{n_{ACE}}$$

These two ratios allowed us to identify SW, MSH, and MS regions on whole dayside parts of orbits and even toward the flanks in the range of ± 7 hours of local time around the local noon. In Fig. 4.7, the distributions of the magnetic field ratios (r_B) as a function of the solar wind dynamic pressure (Fig. 4.7, left) and different θ_{Bn} (Fig. 4.7, right) are shown. Fig. 4.7, left exhibits two peeks and a plateau. The first peak with maximum of r_B around 1 can be attributed to the solar wind (r_B is choosen from 0 to 1.7), the second peak around 3.8 is recognized as the magnetosheath ($2.3 < r_B < 6$). The transition between the magnetosheath and magnetopause is not so distinct but it still can be identified (r_B is between 6-8). Furthermore, we can eliminate shadowed regions in Fig. 4.7 that can contain a mixture of two regions.

Simultaneous application of both magnetic field and density ratios leads to even more distinct separation of the regions as it can be seen in a 2D histogram in Fig. 4.8 showing numbers of one–minute intervals in logarithmic scale. Our procedure provides three tables of times where the satellite was in the solar wind, in the magnetosheath, in the magnetosphere and we again build three p_{dyn}–R histograms from each table. One can clearly distinguish three regions: solar wind measurements are spread around $r_B = 1$ and $r_n = 1$ (it is not exactly the point for two reasons: shifting and comparison of distant data sources and foreshock fluctuations); the magnetosheath is specified by compression ratios of about $r_B \approx 4$ and $r_n \approx 3$ (the magnetosheath has a large spread of points around these ratios because its parameters depend on a particular position inside the magnetosheath and magnetosheath plasma and magnetic field are highly fluctuating). In many regions of the inner

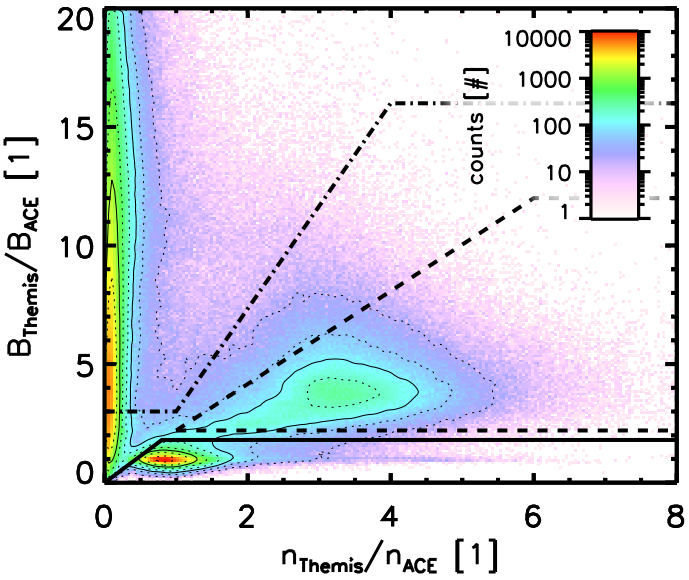

Figure 4.8: 2D histogram of the ratios of r_B vs r_n which were used to distinguish three regions: the solar wind at bottom and bounded with the solid line; the magnetosphere located at the left part and bounded with the dotted–dashed line; and the magnetosheath – a triangle distinguished with the dashed line in middle.

magnetosphere, the plasma density is small and the magnetic field does not depend on IMF and r_B can reach high values. It can be seen as a long ridge for $r_n < 1$. However, we processed all available THEMIS data regardless the spacecraft location and thus a part of magnetospheric observations was taken from the plasmasphere where the density can be higher than that in the solar wind.

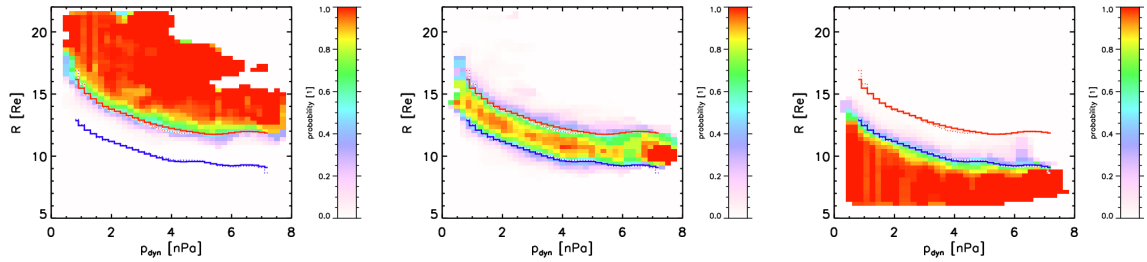

Figure 4.9: Results of the algorithm of automatic region identification represented as the R–p_{dyn} probability of the solar wind (left), the magnetosheath (middle) and the inner–magnetosphere (right) observations in the subsolar region. The red and blue curves are the bow shock and magnetopause, resp. determined on 50% probability of observations of a particular region.

Under assumption that the subsolar magnetopause and bow shock shapes can approximated by spherical surfaces with diameters controlled by the solar wind dynamic pressure, we demonstrate the performance of the algorithm of the boundary identification in Fig. 4.9. The identification in this figure is based on 50% probability of observations of a particular neighbouring regions. We tested also the method of

the maximum probability gradient but the results were well within statistical errors.

parameter	formulae
density ratio	$r_n = \frac{n_{local}}{n_{SW\ monitor}}$
magnetic field ratio	$r_B = \frac{B_{local}}{B_{SW\ monitor}}$
velocity ratio	$r_v = \frac{v_{local}}{v_{SW\ monitor}}$
magnetic field standard deviation	$std\, r_B = \sqrt{\frac{1}{N-1}\sum_{i=1}^{N}(B_i - \overline{B})}$

Table 4.1: Parameters and its definition which can be used in a procedure of region identification.

More reliable identification of different regions or identification of other regions can be based on employment of other parameters. Possible candidates are listed in the Table 4.1. Fig. 4.10 eventually shows the 2D histogram of different combinations of first three parameters of Table 4.1. It can be clearly seen that the combination we have used (left panel) provides the best tool for identification of SW, MSH and MS, identification of other regions (cups, low latitude boundary layer, foreshock) would require simultaneous application of 3 or more criteria.

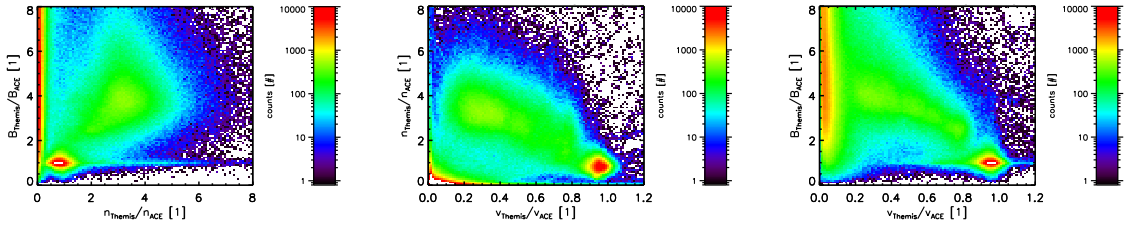

Figure 4.10: Mutual combinations of first three parameters from Table 4.1 which can be used for identification of different regions.

Chapter 5

Experimental results

5.1 Bow shock speed and small-scale motion

Multiple bow shock crossings occurring over intervals from minutes to several hours are usually interpreted in terms of bow shock motions with respect to the observing spacecraft [e.g., Nemecek et al., 1988; Zastenker et al., 1988]. Determined bow shock velocities typically range between a few km/s up to $\sim$ 100 km/s [e.g., Völk and Auer, 1974; Newbury et al., 1998]. Völk and Auer [1974] considered that bow shock velocities in the subsolar region of the order of 100 km/s can be induced by a bow shock interaction with solar wind discontinuities, while smaller velocities may be determined by smooth interplanetary disturbances such as Alfvén waves. Lepidi et al. [1996] examined a few periods of multiple bow shock crossings on IMP 8 and confirmed previous findings interpreting multiple crossings as response to changes in external solar wind conditions. They also found that an inward motion of the shock is accompanied by large magnetosheath densities just before shock sweeps across the spacecraft.

Based on the Interball-1/Magion-4 data, Safrankova et al. [2003] (App. C.10) and Jelinek et al. [2006] (WDS06, App. C.11) presented: (A) an analysis of the speed of the bow shock motion in a statistical sense, and (B) a case study of small-scale changes of the bow shock and magnetopause locations. Their results have shown that the bow shock motion is much more complicated than generally expected. The bow shock is in a permanent motion due to local changes of upstream and downstream parameters. The speed of this motion averaged over 0.5 – 1 R_E is less than 100 km/s; in a majority of observed crossings (75 %) it did not exceed 40 km/s (Fig. 5.1). The probability of observations of large speeds decreases with Θ_{Bn}.

In order to elucidate the problem of the bow shock response to upstream conditions, we have performed study of two intervals during which the bow shock crossings were registered many times by the Interball-1/Magion-4 closely separated satellite

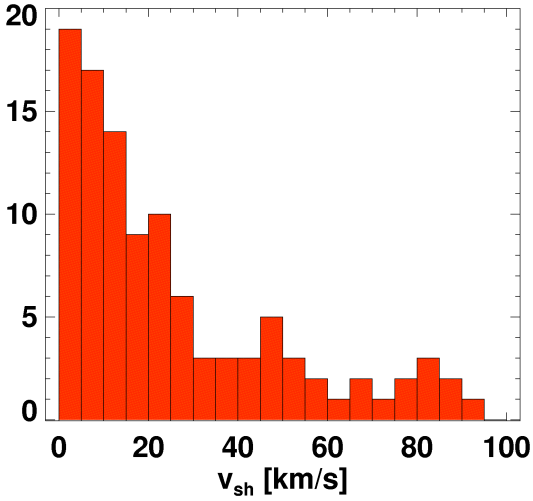

Figure 5.1: Histogram of BS velocities, v_{sh}, derived from simultaneous two-point INTERBALL-I and Magion-4 measurements adopted from Safrankova et al. [2003].

pair or the bow shock spent a notable time between both satellites. For our study of a small–scale motion of the bow shock, we have chosen relatively quiet solar wind conditions. Therefore, we deal with a small–scale motion of the bow shock location during a long time of stable upstream conditions. In order to determine the sources of this motion, two-point bow shock observations are complemented with simultaneous observations of the magnetopause displacement in one of intervals and by third point at the bow shock in the second interval (here, we used the Geotail data). We tried to find such intervals of measurements when one upstream quantity is changing far more than others to analyze an influence of a particular solar wind parameter. We have concerned with changes of several parameters controlling the bow shock position and dynamics - the plasma ram pressure, bow shock normals, the IMF magnitude, and a possible influence of the tilt angle. An example of such observations is presented in Fig. 5.2.

The study has shown that (1) the bow shock is in a permanent motion due to local changes of upstream and downstream parameters; (2) The bow shock location does not follow small magnetopause displacements; (3) Although the magnetopause location generally depends on IMF Bz, we do not see a direct correlation between the bow shock motion and IMF Bz changes [Jelinek et al., 2006]; (4) The bow shock motion during quiet solar wind intervals is not consistent with surface waves, rather "breathing" of the shock surface is observed. This finding is based on two-point observations of multiple crossings and further confirmed by an analysis of the local normals computed according to coplanarity theorem; and (5) The location of the high–latitude bow shock is probably a function of the tilt angle of the Earth dipole [Merka and Szabo, 2004]. From above results it follows that the peculiar

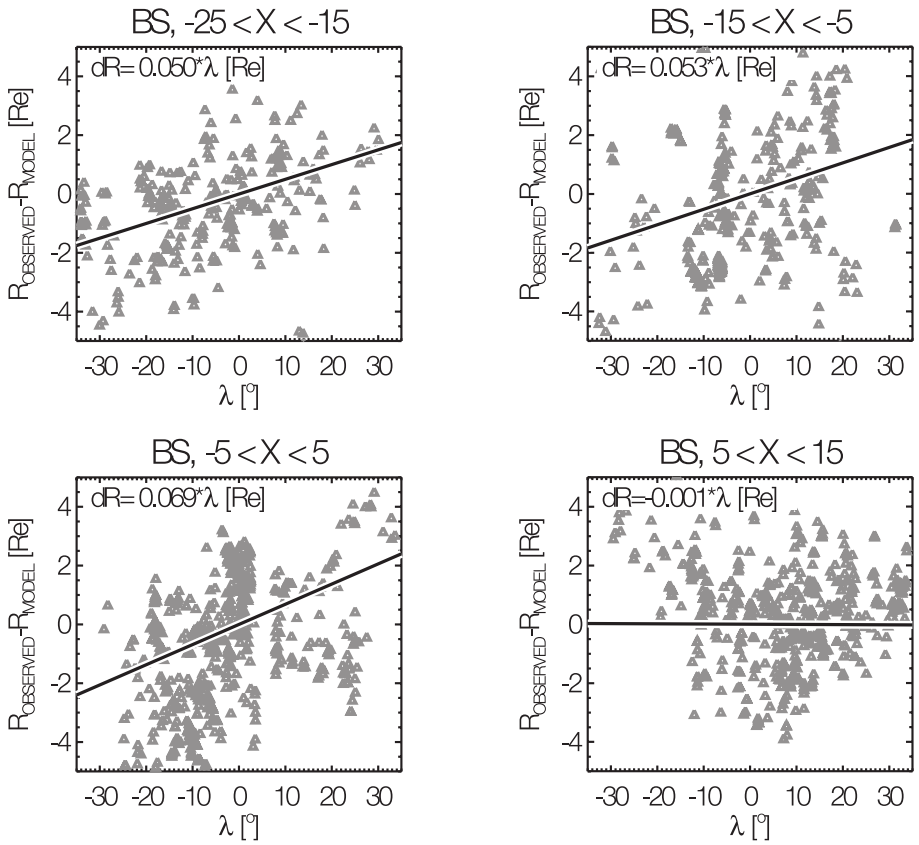

Figure 5.2: Differences between observed and predicted locations in the northern hemisphere at high latitudes as a function of the tilt angle; the panels represent four bins along the X_{GSM} coordinate. The heavy lines show the slope of the tilt–angle dependence in a particular range of X_{GSM}. The equation of the fit is given at the top of each panel according to Jelinek et al. [2008b].

magnetopause/bow shock behavior is currently not well understood and requires new observations and the development of new theories describing how the Earth's magnetosphere reacts to different IMF orientations. Moreover, despite a progress in bow shock/magnetopause modeling, the differences between predictions and observations remain often as large as several R_E. The bow shock crossing is observed mostly due to the changes of its position (from one stationary state to another) which is affected by variations of solar wind conditions. Such crossings assigned to solar wind parameters do not correspond to an equilibrium position of the bow shock and vice versa. Also, the magnetosheath thickness is changing due to magnetopause processes as well as due to changes of magnetosheath conditions. Thus, the results of above studies were a motivation for further investigations in two directions:

1) the case studies of locations of both boundaries through different orientations of IMF, and

2) the improvement of bow shock/magnetopause models.

5.2 Influence of near-radial IMF on the magnetopause position in the subsolar region

Fairfield et al. [1990] indicated that a radial IMF orientation can cause MP expansions. They have shown that pressure/density perturbations produced in the subsolar foreshock are correlated with dayside magnetospheric magnetic field variations. They inferred that foreshock pressure fluctuations convect through the subsolar bow shock into the magnetosheath and impinge on the subsolar magnetosphere. Other studies showed that this interaction is often unsteady and results in multiple MP crossings within times of the order of a few minutes [Fairfield et al., 1990; Sibeck, 1995; Russell et al., 1997; Nemecek et al., 1998].

The location of foreshock upstream from the bow shock is controlled by the Θ_{Bn} angle. In the subsolar region, this angle coincides with the cone angle between the IMF vector and the Earth-Sun line. When the Θ_{Bn} angle is small, the local bow shock is quasi-parallel. When the IMF is radial (i.e., aligned with the Sun-Earth line), the quasiparallel foreshock forms upstream of the whole dayside bow shock.

5.2.1 Case studies

Suvorova et al. [2010] presented MP expansions during long-lasting intervals of quasi-radial IMF and nearly constant solar wind dynamic pressure in Themis data (Fig. 5.3). In their case, magnetopause expansions result from significant decreases

of the total pressure of the high beta magnetosheath (with the low pressure). Their events were observed with upstream conditions characterized by IMF cone angles less than 20°–25°, high Mach numbers and proton plasma beta 1.3. The minimum value for the total pressure observed by THEMIS in the magnetosheath adjacent to the magnetopause was 0.16 nPa and the fraction of the solar wind pressure applied to the magnetopause was therefore 0.2, i.e., extremely small. The equilibrium location of the magnetopause was modulated by a nearly continuous wavy motion over a wide range of time and space scales.

A nearly radial IMF was also a subject of our second case study [Jelinek et al., 2010] that dealt with a significant deformation of the magnetopause surface. Such deformation of the magnetopause surface locally decreases its curvature radius that results in the decrease of the magnetosheath thickness to about half of its standard value in a particular observation point. In the paper, the observed phenomenon is attributed to a rotation of the IMF. Although it is generally expected that the bow shock and magnetopause move in accord, being driven mainly by the solar wind dynamic pressure, we found that the local and transient thinning of the magnetosheath can result from different responses of its boundaries to a sudden change of the pressure and/or IMF orientation. A possible scenario of this event is as it follows (Figs. 5.4 and 5.5):

1. The subsolar magnetopause was expanded until 2020 UT due to a radial IMF that causes the decreased magnetosheath pressure [Suvorova et al., 2010]

2. A tangential discontinuity shaped like that shown in Fig. 5.5 approaches the dawn bow shock flank at 2020 UT and brings the duskward pointing IMF to the parts of the bow shock dawnward of the discontinuity.

3. The magnetosheath pressure behind the discontinuity increases and pushes the affected parts of the magnetopause inward. This process is responsible for the decreasing curvature radius of the subsolar magnetopause inferred from THEMIS and Geotail observations.

4. The discontinuity proceeds along the bow shock surface duskward and approaches THB at 2032 UT. Its arrival causes a fast inward motion of both the magnetopause and bow shock.

5. At 2045 UT, the discontinuity crosses the Geotail location, the expanded magnetopause moves inward and the bow shock becomes quasiperpendicular at this point.

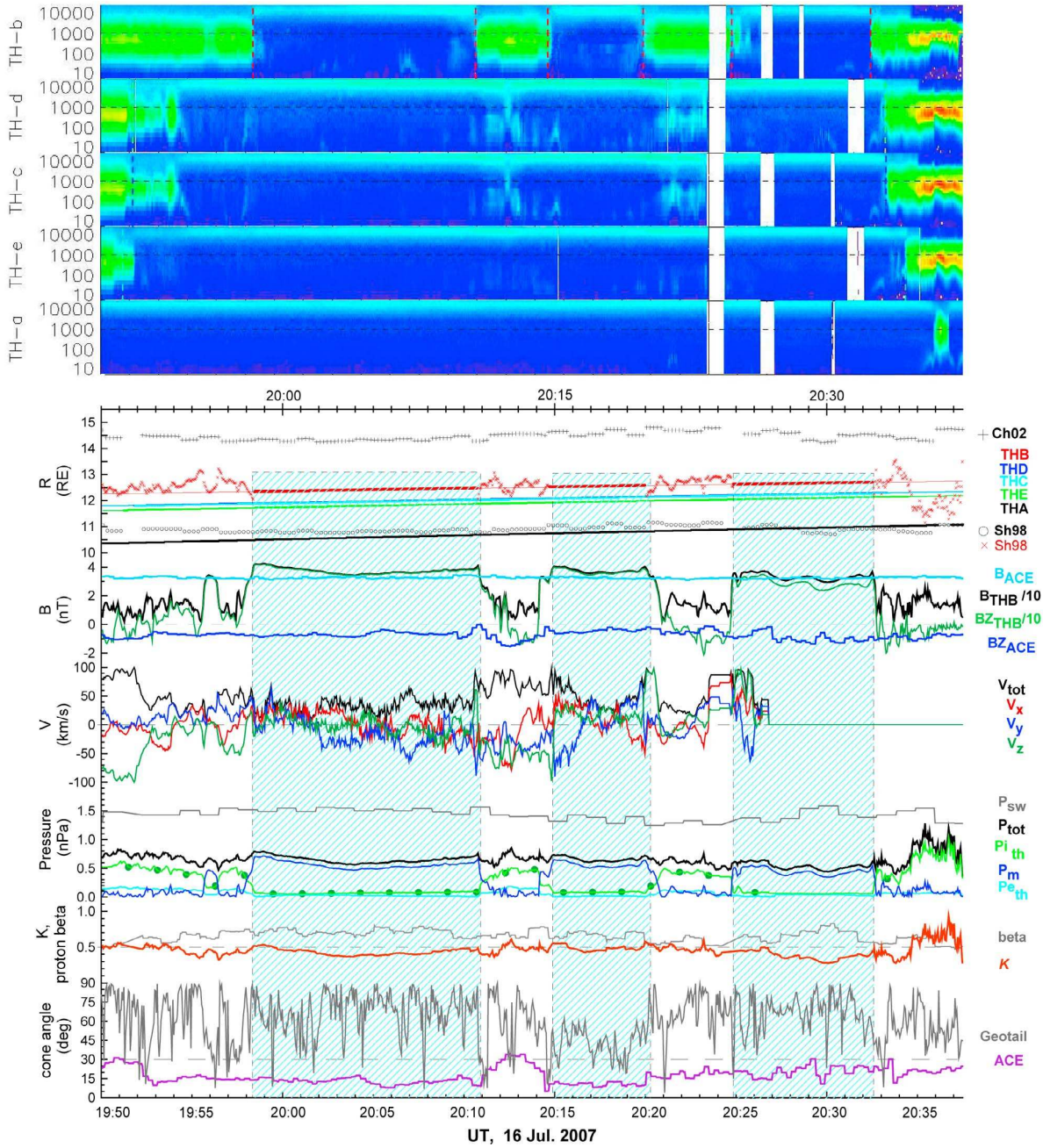

Figure 5.3: Plasma and magnetic fields observed on 16 July 2007 (from top to bottom): THEMIS ion spectrograms; Chao et al. [2002] bow shock model prediction; Shue et al. [1998] magnetopause model predictions calculated for the solar wind Psw (circles) and magnetosheath $Ptot$ (diagonal crosses) pressures; THEMIS radial distances (thick segments mark the magnetosphere encounters); ACE and THB measurements of magnetic field strength and Bz (divided by 10 for THB); THB plasma velocity (V_{tot}) and components Vx, Vy, and Vz; the upstream solar wind pressure Psw and THB magnetic (Pm), thermal ion Pi_{th}, thermal electron Pe_{th}, and total pressure (P_{tot}), circles depict the ion pressure Pi_{th} in ESA full mode; solar wind proton β and ratio K ($Ptot/Psw$); cone angles of ACE and Geotail magnetic field delayed by 41.5 and -1.5 min, respectively. Time intervals of THB magnetosphere encounters are marked by blue shadow bars (Fig 6. from Suvorova et al. [2010]).

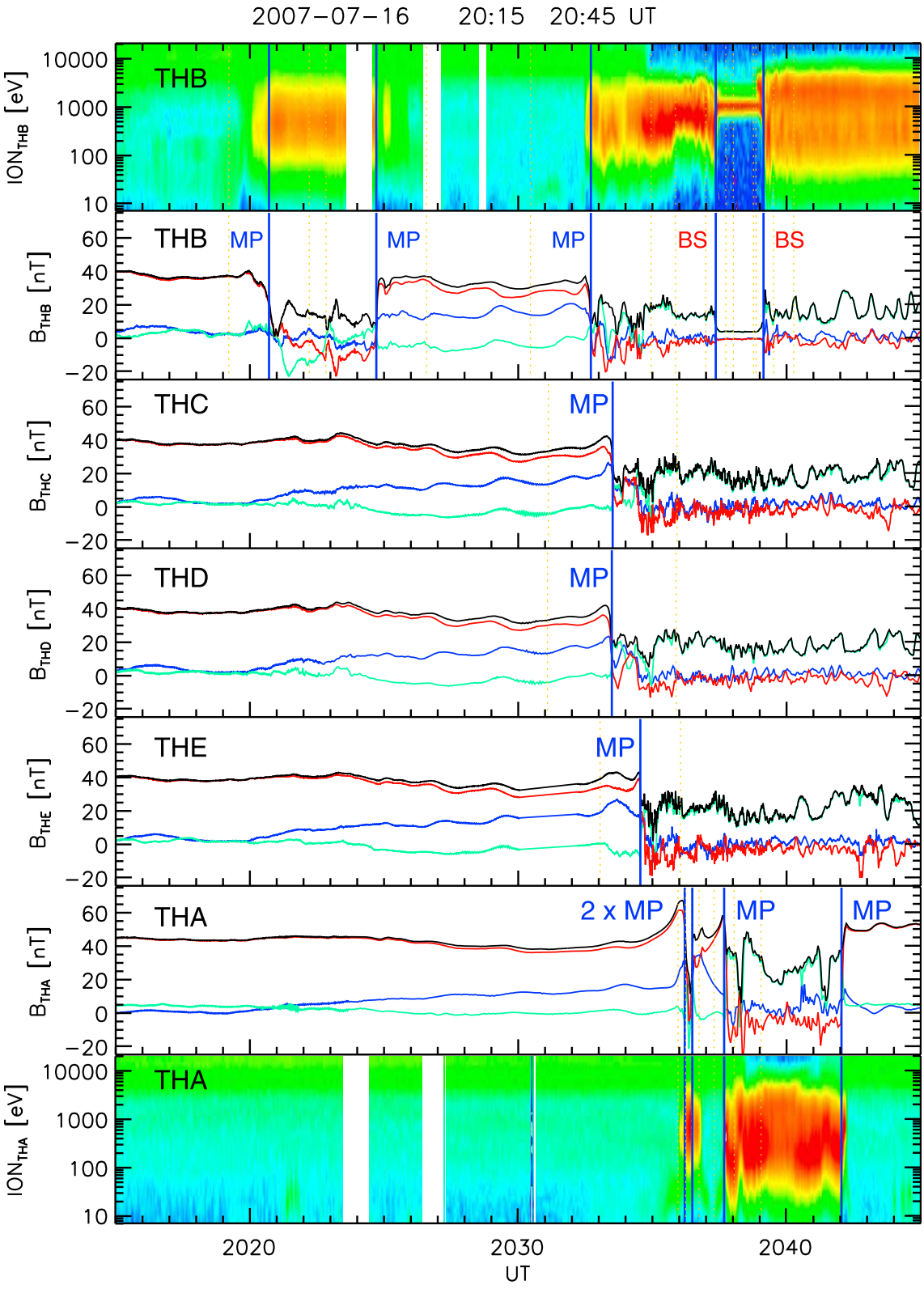

Figure 5.4: Measurements of THEMIS probes through the interval from 2015 to 2045 UT. From top to bottom: ion spectra from THB, five images of magnetic field observations ordered by the distance of probes from the Earth (THB, THC, THD, THE, THA), and ion spectra from THA. The vertical lines indicate the magnetopause and bow shock crossings. In magnetic field images, B_X, B_Y, B_Z components are marked by blue, green, and red colors, respectively (Fig 3. from Jelinek et al. [2010]).

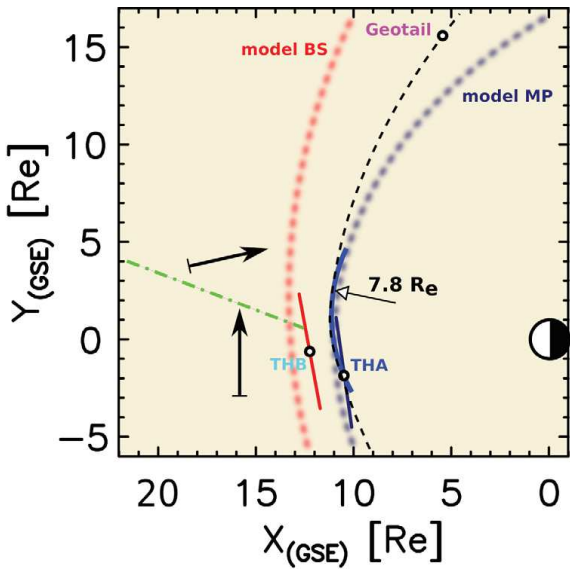

Figure 5.5: Projections of the observed situation onto the X–Y plane. The red and blue dotted curves show the model bow shock and magnetopause, respectively. The thin dashed curve presents estimated magnetopause shape at ≈2042 UT. The green dashed–dotted line stands for the IMF discontinuity estimated from THEMIS and Geotail observations, and IMF orientations shown by the black arrows correspond to those observed by ACE prior to (2015 UT) and by THB after (2038 UT) the discontinuity arrival (Fig 5. from Jelinek et al. [2010]).

5.2.2 Statistical study

Based on these two case studies and on the observations of Merka et al. [2003b] that reported larger amplitude magnetopause oscillations occurring during intervals of quasi-radial IMF, we performed a large statistical study of such conditions [Dusik et al., 2010]. This short study is devoted to an average magnetopause location through intervals of the IMF aligned with solar wind velocity. To distinguish between the influence of the IMF cone angle and the θ_{Bn} angle (the angle between the IMF vector and the vector of the normal to the bow shock just upstream of a particular magnetopause crossing), the analysis is carried out for the subsolar and flank magnetopauses separately. To the investigation, the five-spacecraft THEMIS mission [Angelopoulos, 2008] is used. Such approach yields the opportunity to identify many magnetopause crossings being registered by the same instruments with the same solar wind monitor. As the monitoring parameters, the WIND plasma moments [Ogilvie et al., 1995] and the ACE magnetic field [Smith et al., 1998] were used and these data were propagated by the two-step routine [Safrankova et al., 2002] to the location of a particular THEMIS magnetopause crossing.

Our analysis uses the differences between the radial distance of observed crossings, R_{obs} and the distance predicted by the Petrinec and Russell [1996] model, R_{mod}. The investigation of magnetopause locations observed by the Themis spacecraft in

2007–2008 brings a statistical evidence that the dayside magnetopause location is strongly influenced by the IMF cone angle as it was shown in the case studies [Merka et al., 2003b; Suvorova et al., 2010; Jelinek et al., 2010]. The difference between the IMF aligned with and IMF perpendicular to the solar wind flow is as large as 1 R_E (Fig. 5.6). This effect is attributed to a less effective transformation of the solar wind dynamic pressure to the pressure imposed onto the magnetopause during intervals of a radial IMF. We will return to this point in Section 5.4.1.

Another factor contributing to deviations of the observed crossings from their model predictions is a stronger dependence of the magnetopause location on the solar wind dynamic pressure than that usually suggested (Fig. 5.7). In this study, the scaling factor connected with the solar wind dynamic pressure was found to be 1/4.79 instead of 1/6 or 1/6.6 used in earlier studies of other authors. However, it is clear that used data were collected during a strong and long-lasting solar minimum, thus the exact quantification of the pressure effect requires a larger number of the crossings observed under pressures exceeding 2 nPa to be complemented into the data set. Newertheless, the value of 1/4.79 is in good agreement with findings of Lin et al. [2010] and Lu et al. [2011].

5.3 Bow shock model improvements

5.3.1 Bow shock dependence on the tilt angle

The bow shock position and shape are controlled by the obstacle size and shape, upstream Mach numbers, and the IMF orientation. Moreover, Merka and Szabo [2004] discussed the size and stability of the bow shock shape/position with respect to IMF and solar wind flow directions. The size and geometry of the obstacle – the magnetopause – are a result of combined solar wind ram pressure, IMF orientation, and dipole tilt angle effects as we already mentioned. The ram pressure effect scales the magnetopause size, while the IMF orientation and dipole tilt affect the geometry of the boundary. However, the changes of the bow shock shape and location with tilt angle variations were not reported, although Merka and Szabo [2004] noted that the tilt angle effect is likely to be also important for the estimation of the bow shock position.

In Jelinek et al. [2008b], we presented a short statistical study of bow shock locations for varying tilt angles. The study is based on a comparison of the bow shock model predictions with observations of several spacecraft. We have applied the Jerab et al. [2005] model for calculation of predicted distances. To distinguish high and low latitudes, the study employs a set of bow shock crossings registered during 1994–2002 by different spacecraft. The study shows that the night-side bow shock moves

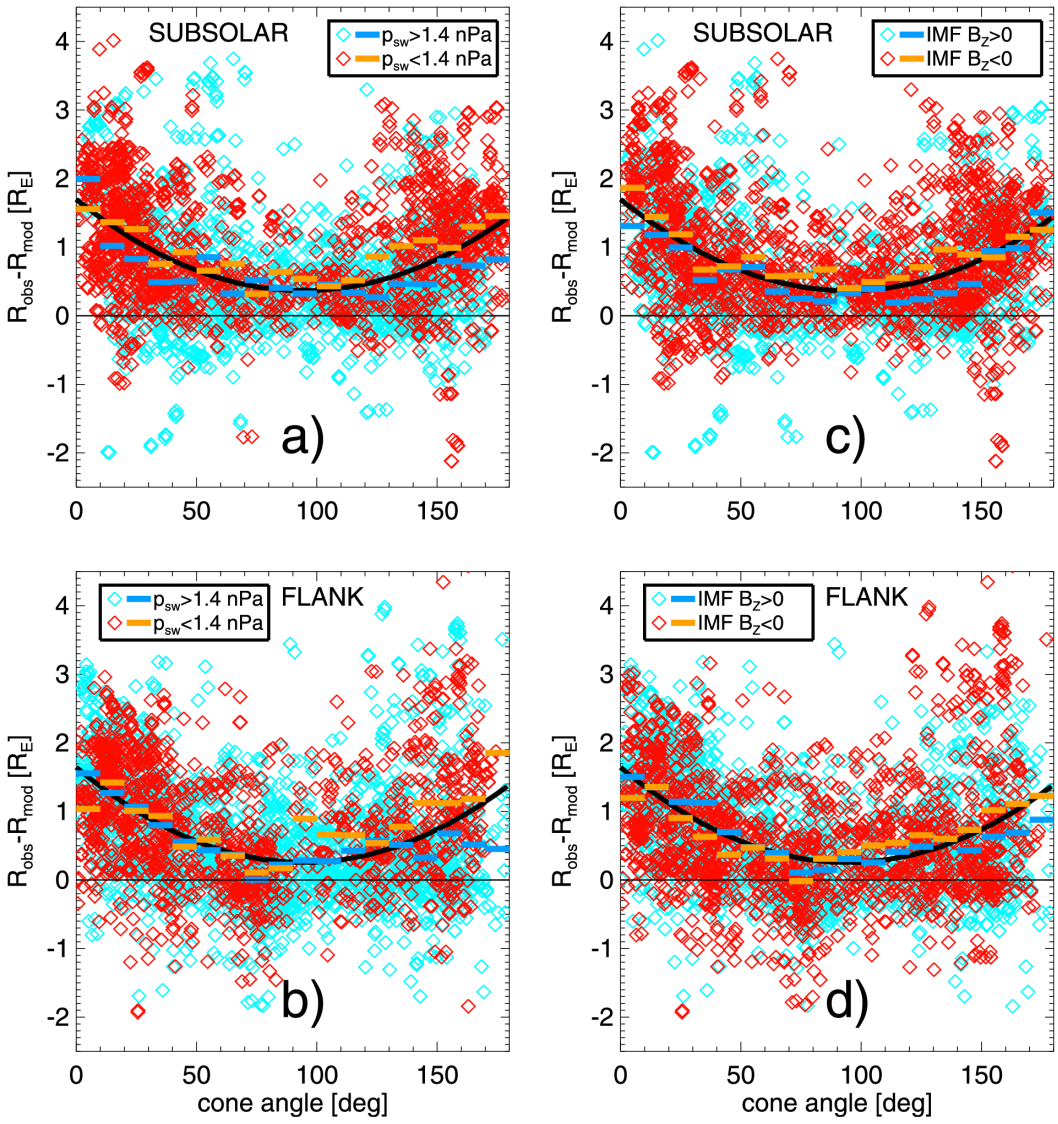

Figure 5.6: The difference between observed and predicted magnetopause locations as a function of the cone angle. (a) Subsolar set (red points and yellow bars are $p_{SW} < 1.4$ nPa; the blue points and bars are $p_{SW} > 1.4$ nPa). (b) Flank set (red points and yellow bars are $p_{SW} < 1.4$ nPa; the blue points and bars are $p_{SW} > 1.4$ nPa). (c) Subsolar set (red points and yellow bars are IMF $B_Z < 0$; the blue points and bars are IMF $B_Z > 0$). (d) Flank set (red points and yellow bars are IMF $B_Z < 0$; the blue points and bars are IMF $B_Z > 0$) (Fig 4. from [Dusik et al., 2010]).

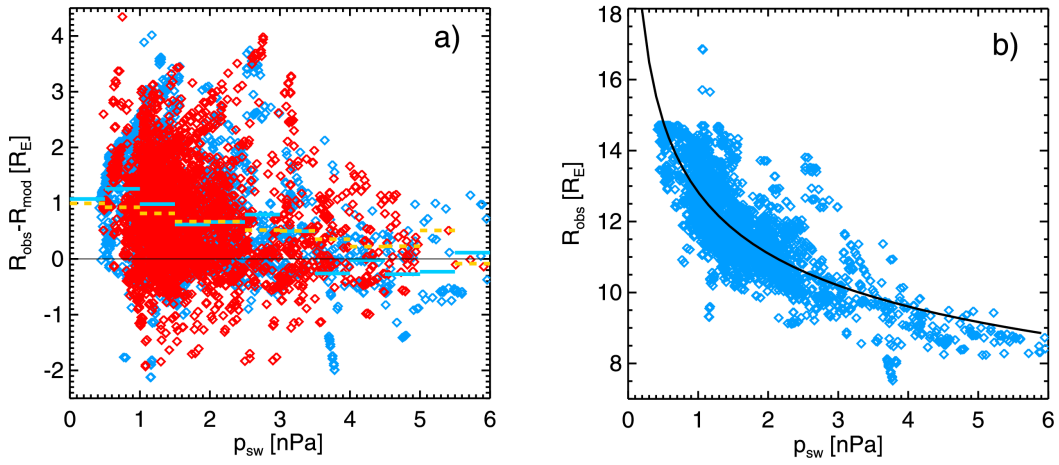

Figure 5.7: (a) Differences between observed and predicted magnetopause locations as a function of the upstream dynamic pressure, p_{SW}. The red points and yellow bars are flank crossings; the blue points and bars are subsolar crossings. (b) The radial distance of subsolar crossings as a function of p_{SW}. The equation of the fit is $y = 12.83x^{-1/4.79}$ (Fig 3. from Dusik et al. [2010]).

in the direction of the positive Z_{GSM} axis for positive tilt angles. The magnitude of the displacement can reach 3 R_E. The analysis also reveals that the high-latitude bow shock surface is significantly distorted near the dawn-dusk meridian. This effect was identified as a counterpart of the magnetopause indentation in the cusp region found by Safrankova et al. [2005].

They have shown that the tilt angle influences predominantly the location and shape of the high-latitude night-side magnetopause. For this reason, we have divided our set of bow shock crossings into high- and low-latitude parts with the breakpoint a = arctan $(Z_{GSM}/Y_{GSM}) = 30°$ (as in Safrankova et al. [2005]). Fig. 5.8 presents the difference between observed, $R_{OBSERVED}$ and predicted, R_{MODEL} bow shock locations are shown along the X_{GSM} axis for two groups of tilt angles: $\lambda > 10$, and $\lambda < -10$. To distinguish the changes of the bow shock shape with the tilt angle and to show that the results are statistically significant, we have shadowed the areas between 25% and 75% percentiles for both groups of tilt angles. The figure reveals that the high-latitude bow shock shape is heavily distorted near the dawn–dusk meridian. This distortion starts with an indentation that is followed by an overshoot. The shape of this distortion is similar for positive and negative tilts but it is shifted toward the Sun when the Earth's dipole points sunward (positive tilts in the northern hemisphere and vice versa). The deepness of the indentation is 1–2 R_E, the overshoot height is about 2–3 R_E and the width of both features is about 4 R_E. The difference between locations of the distortion for positive and negative tilts is 3 R_E along the X axis. Moreover, the figure suggests that the bow

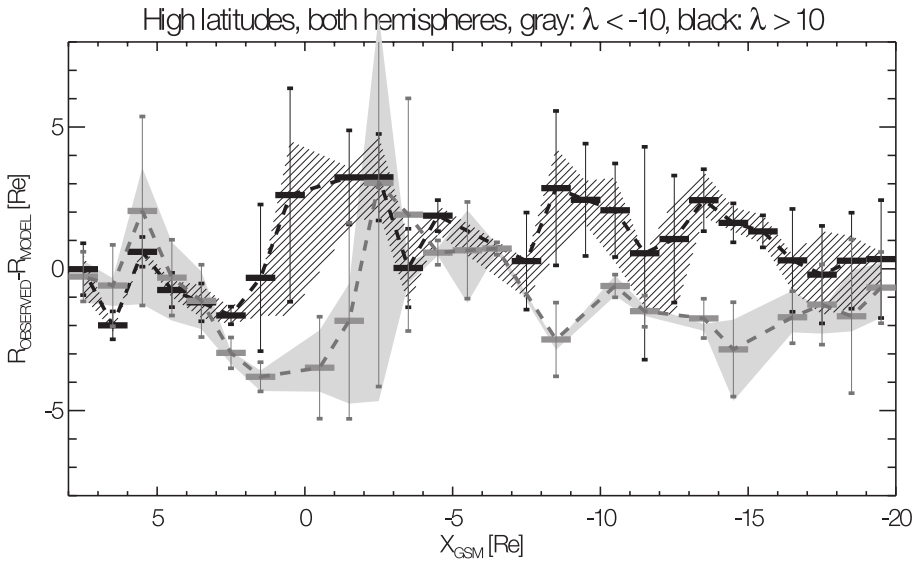

Figure 5.8: Differences between observed and predicted bow shock locations in both hemispheres at high latitudes along the X_{GSM} coordinate for two groups of tilt angles. Shadowing distinguishes the areas between 25% and 75% percentiles for both groups of tilt angles; positive tilts ($\lambda > 10°$): heavy lines and heavy shadowing; negative tilts ($\lambda < -10°$): gray lines and light shadowing (Fig 7. from [Jelinek et al., 2008b]).

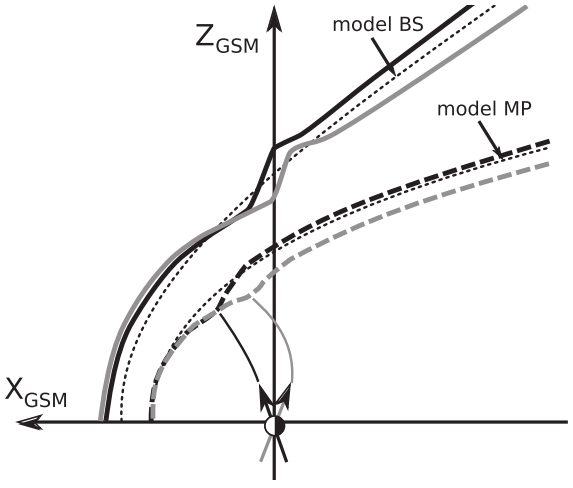

Figure 5.9: A sketch of the magnetopause and bow shock shapes for positive (black) and negative (gray) tilts. The Petrinec and Russell [1996] magnetopause and Jerab et al. [2005] bow shock models are shown for the sake of reference by the thin dotted lines (Fig 9. from Jelinek et al. [2008b]).

shock surface is undulated further downstream. The overshoot of the indentation is followed by surface waves with the wavelength 6–7 R_E and amplitude 1–2 R_E.

In order to discuss the bow shock distortion that follows from Fig. 5.8, a schematics of bow shock and magnetopause locations in the $X - Z$ plane is shown in Fig. 5.9. The Petrinec and Russell [1996] magnetopause and Jerab et al. [2005] bow shock models are shown for the sake of reference by the thin dotted lines. The magnetopause locations for positive and negative tilts are given by heavy dashed lines and follow the corrections of the magnetopause shape suggested by Safrankova et al. [2005]. The construction of the bow shock shape is based on differences from the previous figure. We can note that the magnitudes of the distortions of both bow shock and magnetopause surfaces are very similar and that these distortions move sunward on similar angles when the tilt increases. The distortion of the bow shock is located more tailward but it is consistent with the fact that the bow shock is built by waves generated at the magnetopause. These waves propagate radially in the magnetosheath plasma frame but they are blown downstream with the magnetosheath flow.

5.3.2 New model of bow shock and magnetopause locations

The models describing actual locations and shapes of the magnetopause and bow shock as a function of upstream parameters are based on a statistical processing of crossings observed by a single spacecraft and (usually distant) solar wind monitor. This approach implicitly assumes that the downstream parameters are proportional to their upstream values. Such assumption introduces many inaccuracies when, for example, a strong sudden change of solar wind conditions results in unusual boundary crossings, or multiple crossings follow in a short time and these effects could negatively affect statistical results. Moreover, a visual inspection of data plots is time consuming and subjective because the criteria for a boundary identification could vary. Another problem is the orbital bias of particular data sets as we discussed in the Section 4.2. These reasons result to the attempt to develop a new method of an automatic identification of both boundaries only from observations of the magnetic field and plasma density. One-minute averages of these parameters measured by a sounding spacecraft are normalized to corresponding values measured at the L1 point by the solar wind monitor and propagated to the sounding spacecraft location. The normalized values are then used for an identification of three regions: the solar wind, magnetosheath, and inner magnetosphere. The method of data preparation and their processing was described in the previous section.

In a first approximation, for we expect that bow shock and magnetopause lo-

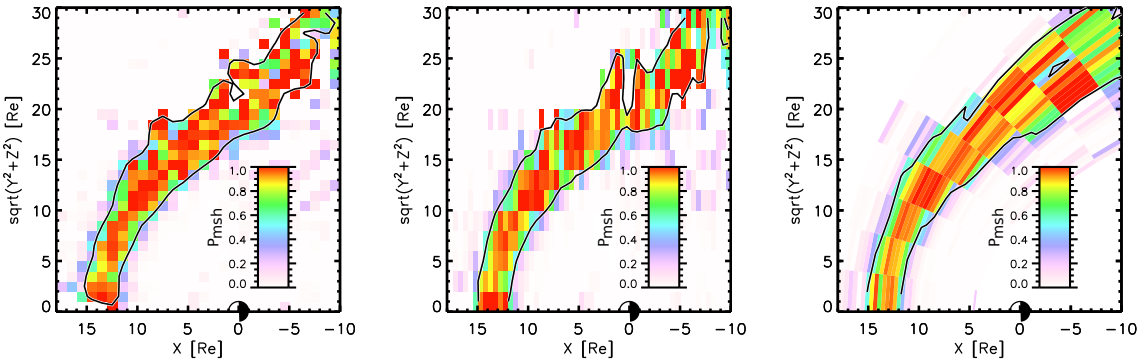

Figure 5.10: Possible examples of two rectangular and one parabolic binning of the magnetosheath occurrence probability.

cations are controlled exclusively by the solar wind dynamic pressure. We assume that both the magnetopause and bow shock are rotationally symmetric around the aberrated X_{GSE} axis. The aberration takes into account the Earth orbital motion; the perpendicular components of the solar wind velocity are omitted in accord with the study of Safrankova et al. [2002]. All data were sorted into bins described by two spatial coordinates X and Y and the upstream pressure, p and we computed the probability, P that we can find the SW, MSH or MS in a particular bin. The system does not expect any particular coordinate system. In principle, it is possible to use aberrated GSE coordinates, however, we applied non-Cartesian coordinates reflecting expected shapes of both boundaries. The differences between data binning in Cartesian and standard parabolic coordinates are shown in Fig. 5.10. It is seen that the parabolic coordinates provide better results but they still did not reflect different flaring angles of both boundaries. For this reason, we have introduced magnetosheath coordinates. The procedure is described in Jelinek et al. [2012] in detail and it is summarized in Appendix A.

As we already noted, we binned data of SW, MSH and MS according to the dynamic pressure non-linearly with increasing of pressure bins as:

$$\Delta p \approx p^{\frac{1+\epsilon}{\epsilon}}, \tag{5.1}$$

This is convenient especially for the magnetopause because the position of its subsolar point would depend as

$$R_{MP} = R_0 p^{-\frac{1}{\epsilon}}$$

where ϵ is according to current models between 4.5 and 6.7.

Under above defined conditions, we can write the locations of the bow shock and magnetopause surfaces in abberated GSE coordinates in the parametric form

	R_0	ϵ	λ
magnetopause	12.82	**5.26**	1.54
bow shock	15.02	6.55	1.17

Table 5.1: Scaling factors for the bow shock and magnetopause.

$$x = R_0 p^{-\frac{1}{\epsilon}} + \frac{1}{2}\tau^2 \tag{5.2}$$

$$R_{yz} = \frac{\sqrt{2R_0 p^{-\frac{1}{\epsilon}}}\,\tau}{\lambda} \tag{5.3}$$

Three scaling factors for each boundary are:

- R_0 – stand-off distance of the magnetopause and bow shock
- ϵ – scaling with the dynamic pressure
- λ – scaling of the flaring angle

The values of these factors are present in Table 5.1.

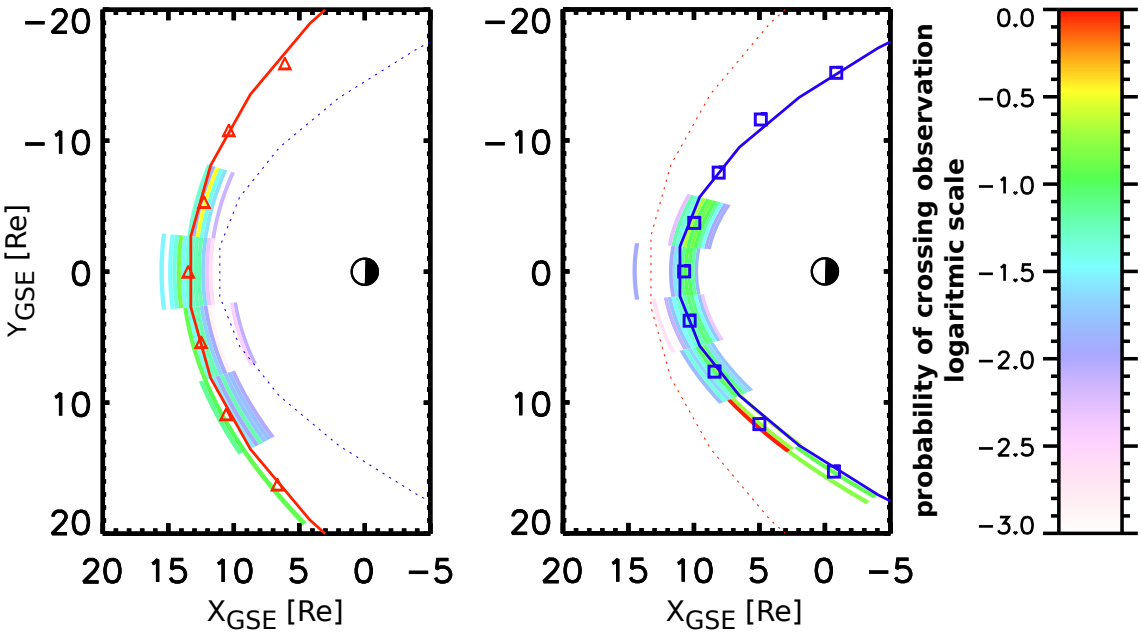

Figure 5.11: A comparison of the presented (left) bow shock and (right) magnetopause models with the observed bow shock and magnetopause crossings. The color scale shows the probability of observation of the particular boundary crossing in a given bin. The crossings from the pressure range of 1.0–1.1 nPa are shown and the full line stands for the model boundary location under 1.05 nPa of the dynamic pressure (left plot – red line, right plot – blue line). The second boundary (left plot – the magnetopause, right plot – the bow shock) is given by the dotted line for the sake of reference.

The described model was developed using probabilities of observations of particular regions and their performance can be tested by a comparison with real observed crossings of both boundaries. Thus, we used our sets of the magnetopause and bow shock crossings from Themis (see Section 4.1) and compared modeled results and experimental data in Fig. 5.11. The color scale shows the probability of observation of the particular boundary crossing in a given bin. The crossings from the pressure range of 1.0–1.1 nPa are shown and the full line stands for the model boundary location under 1.05 nPa of the dynamic pressure (left plot – red line, right plot – blue line). The second boundary (left plot – the magnetopause, right plot – the bow shock) is given by the dotted line for the sake of reference. One can note a good matching of crossings and model results. Histograms in Fig. 5.12 represent the differences between average positions of the bow shock (a) and the magnetopause (b) determined from boundary crossings and from the proposed model. Both distributions are almost centered and their width is comparable.

We can conclude that results of the new model are fully comparable with other empirical models [Petrinec and Russell, 1996; Shue et al., 1997, 1998] in the subsolar region at low latitudes.

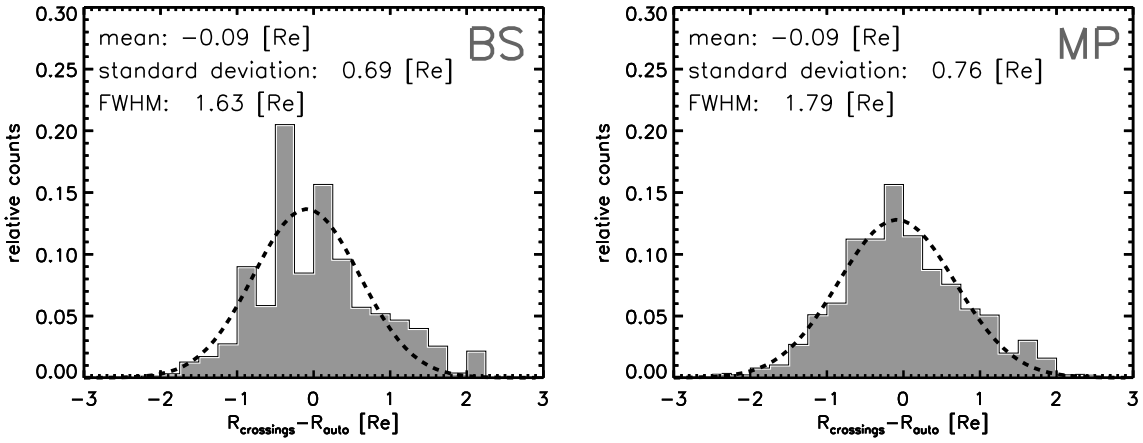

Figure 5.12: (left) Distributions of differences between positions of observed bow shock crossings and model positions. (right) The same plot for the magnetopause. The parameters of the Gaussian fit are given at the top of each panel.

Finally, we can note that the model is based on THEMIS observations that cover only very limited ranges of latitudes and tilt angles. In spite of its relatively good performance, the model cannot describe the dependence of the magnetopause location on the tilt angle [Boardsen et al., 2000; Safrankova et al., 2005; Jelinek et al., 2008b; Lin et al., 2010] or elliptical magnetopause cross-section suggested by, e.g., [Roelof and Sibeck, 1993; Boardsen et al., 2000; Lin et al., 2010] Such effects could be included after enlargement of the original data set with observations of other spacecraft like Cluster or earlier Prognoz type satellites that map the high-

latitude regions. Nevertheless, our model(s) can serve as a very useful tool for an analysis of any data from the region covered by the measurements used for its(their) development. An example of its/their application can be found in the next subsection.

5.4 Applications of the new bow shock and magnetopause model

5.4.1 Magnetopause pressure balance for radial and northward IMF

The paper by Samsonov et al. [2012] analyzes the distribution of different pressure components (dynamic, thermal, magnetic) in the magnetosheath along the Sun-Earth line for northward and radial interplanetary magnetic field (IMF) orientations with motivation to explain an unusual location and shape of the magnetopause often observed during the intervals of the radial IMF. The analysis employs isotropic and anisotropic MHD models and their results (Fig. 5.13) are compared with the statistical processing of THEMIS observations (Fig. 5.14). To the statistics, the results of the new model of magnetopause and bow shock locations and generalized parabolic magnetosheath coordinates were used. Both MHD models as well as the analysis of the THEMIS observations revealed that:

(i) The total pressure exerted onto the subsolar magnetopause is lower than the upstream dynamic pressure.

(ii) The pressure reduction depends on the IMF orientation being $\approx 5\%$ for a purely northward IMF and $\approx 24\%$ for the IMF aligned with the solar wind velocity.

(iii) The anisotropic MHD model should be employed for a realistic description of the pressure transformation inside the magnetosheath. The isotropic MHD solution underestimates the influence of the IMF orientation on the pressure transformation in the magnetosheath.

(iv) The temperature anisotropy in the magnetosheath only slightly exceeds the limits imposed by the plasma instabilities that were estimated in the solar wind.

The statistical and simulation results are documented in Figs. 5.14 and 5.13, respectively. The obtained values of the pressure reduction in the subsolar region are in a good agreement with the magnetopause expansion reported by Dusik et al. [2010].

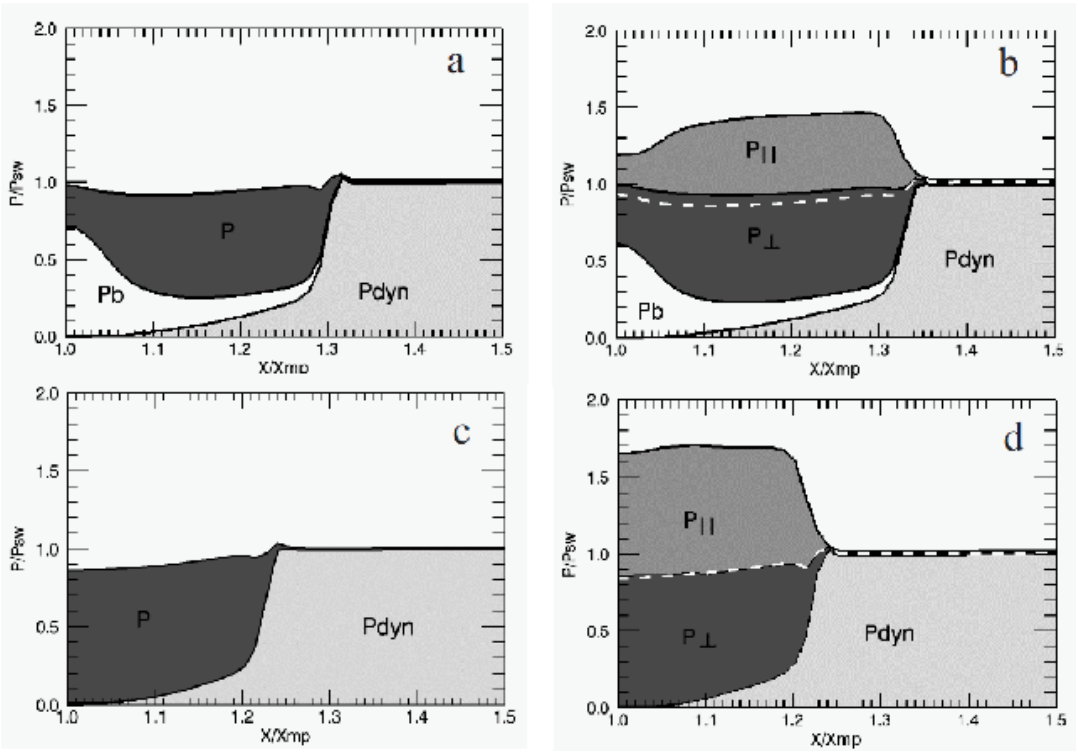

Figure 5.13: Results of the isotropic (a,c) and anisotropic (b,d) magnetosheath models at the Sun–Earth line for the northward (a,b) and radial IMF (c,d) according to Samsonov et al. [2012].

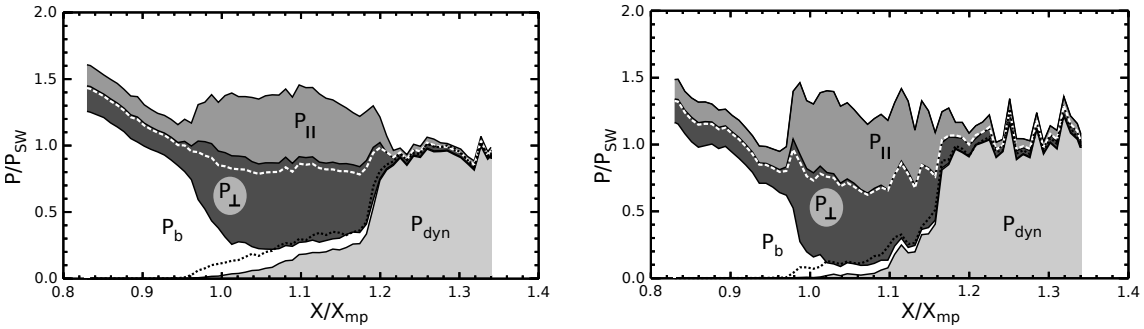

Figure 5.14: Pressure profiles from the experimental data for two cases: (left) $B_z \geq 2nT$; and (right) IMF in a cone of $\pm 15°$ from the Sun-Earth line (i.e., nearly radial). The gray areas: dynamic (P_{dyn} – light gray), magnetic (P_b – white) , thermal perpendicular ($P_\perp$ – dark gray) and parallel ($P_\parallel$ – middle gray) pressures at the Sun–Earth line. The lines show: dashed white - total pressure in the isotropic approximation, dotted line - total dynamic pressure including the velocity component parallel to the magnetopause.

5.4.2 Magnetosheath profiles in the model

The model of boundaries can be successfully applied to creation of spatial profiles of the magnetosheath. In Fig. 5.15, an example of the magnetosheath profile for the range of the dynamic pressure 1.0-1.1 nPa is shown in the magnetosheath coordinates rearranged to the GSE system (see Appendix A). The transformation supposed that $X_{MSH} = 0$ and 1 corresponds to the model magnetopause and bow shock locations and that the dynamic pressure is equal to 1 nPa. Such transformation of coordinates allows us to combine data with different dynamic pressures. Magnetosheath spatial distributions of the density ratio, r_n (Fig. 5.16, left) and magnetic field strength ratio, r_B (Fig. 5.16, right) plotted in Fig. 5.16 allow us to study properties of the magnetosheath and adjacent layers. An example of such a study is in Fig. 5.17. In the top panel, the green line defines the studied spatial profile and a series of panels in the bottom part shows an orthogonal projection of the density, velocity, temperature and magnetic field and their combinations along the green line.

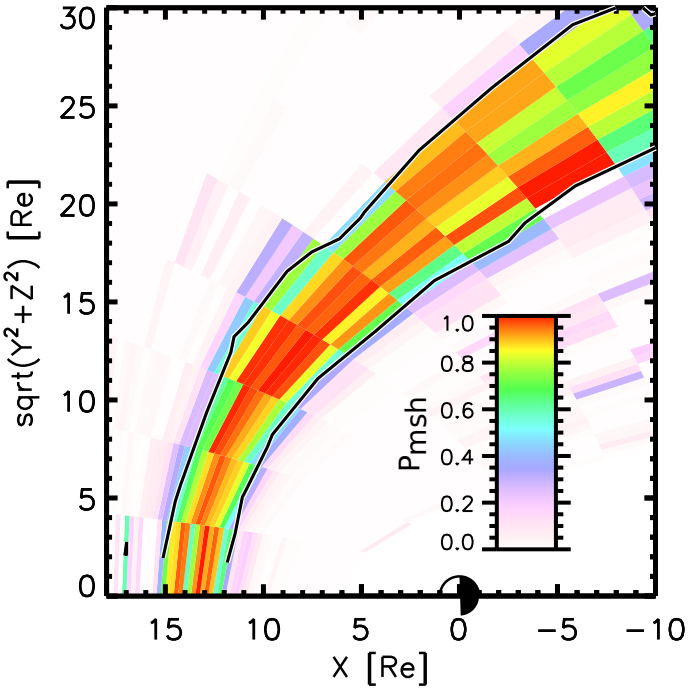

Figure 5.15: An example of the magnetosheath spatial profile for the range of the dynamic pressure 1.0 – 1.1 nPa in magnetosheath coordinates and rearranged to the GSE system in such way that $X_{MSH} = 0$ and 1 correspond to the model magnetopause, and bow shock, respectively for fixed dynamic pressure $p_{dyn} = 1$ nPa.

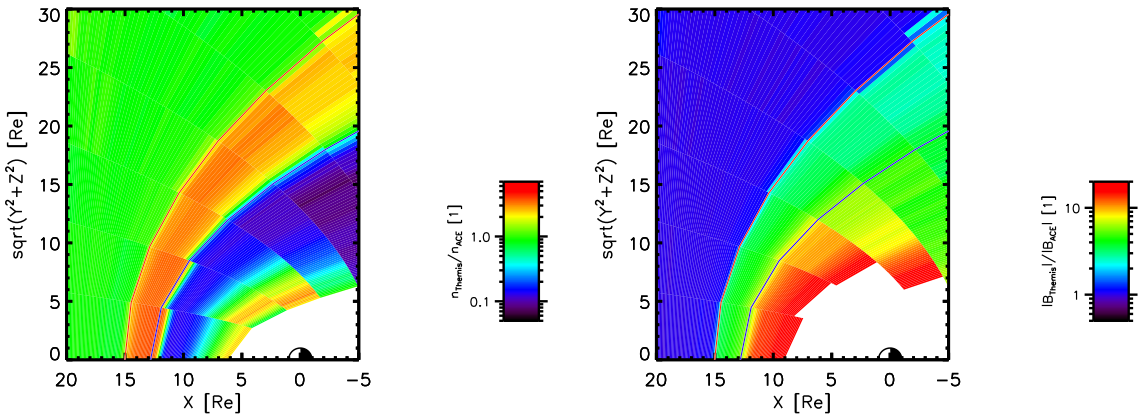

Figure 5.16: Spatial profiles of r_n (left) and r_B (right) in the magnetosheath.

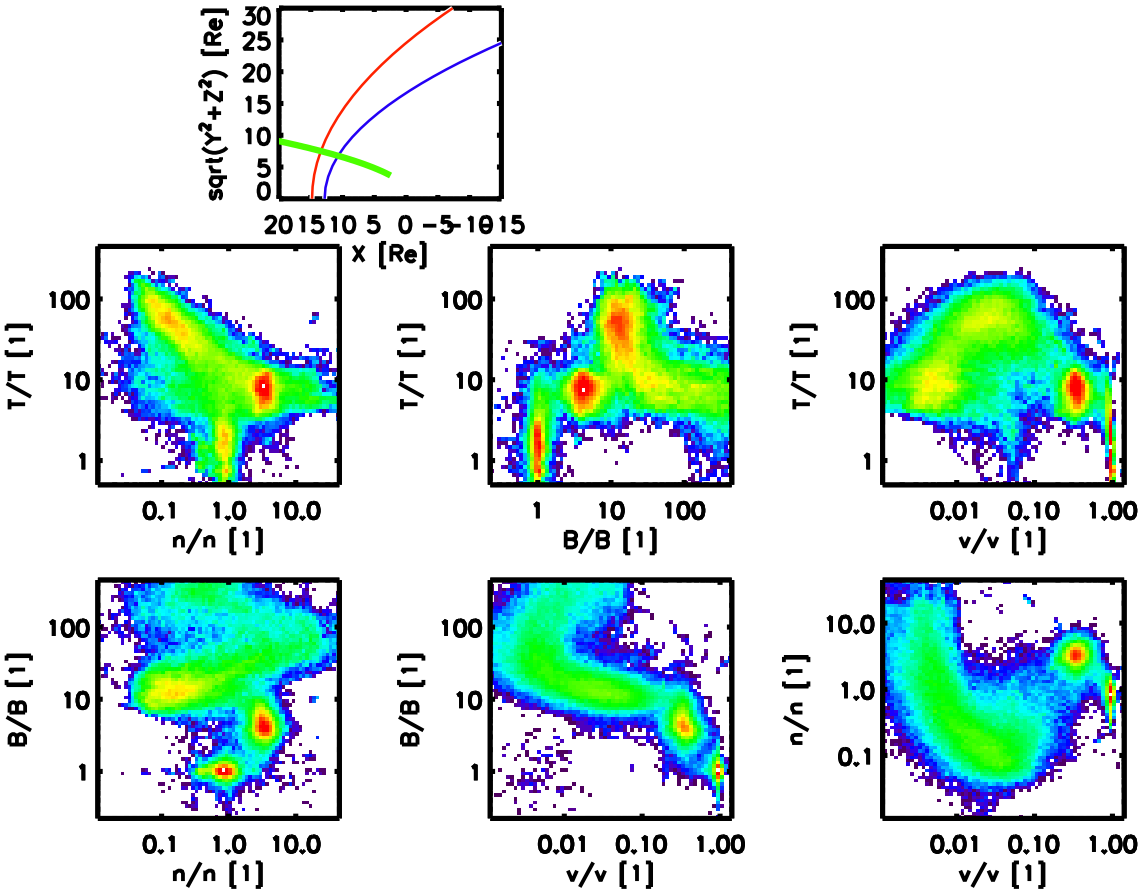

Figure 5.17: An example of different plasma parameter ratios observed at position colored by green (top panel). Six histograms show orthogonal 2D projections of four parameters. The last (right bottom) histogram shows a duck.

5.4.3 A comparison of model results and computer simulations

As the last step, we tried to apply spatial profiles of magnetosheath parameters from our model to comparison with numerical simulations. We used plasma and

magnetic field parameters and both compared with two simulations: Spreiter et al. [1966] gasdynamic model and with global MHD BATS-R-US model [Powell et al., 1999; Groth et al., 2000] under specific conditions.

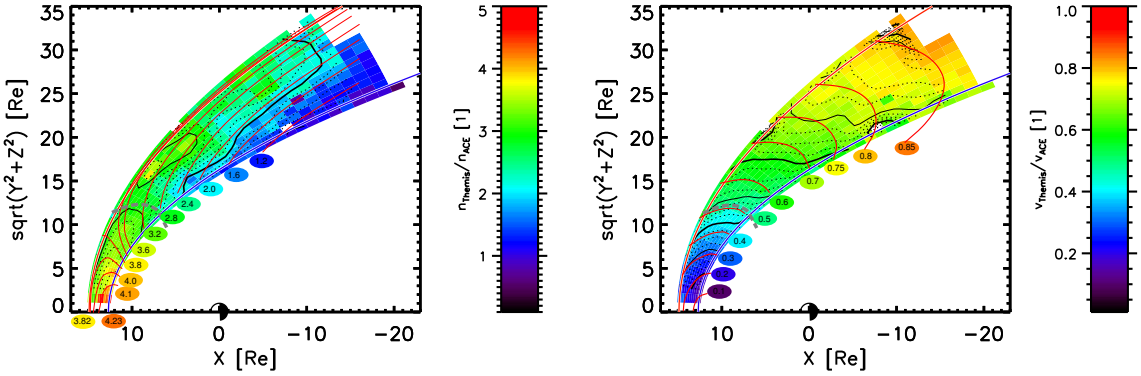

Figure 5.18: Magnetosheath's spatial profiles of the ion density (left panel) and velocity ratios (right panel), plotted in magnetosheath coordinates, and their comparison with the Spreiter gas dynamic model [Spreiter et al., 1966].

To comparison with the Spreiter model, we chose the Mach number, M = 8 and the ratio of specific heaths of 5/3. Results of comparison are present in Fig. 5.18. On the other hand, to comparison with the MHD model, we chose the model run with following solar wind conditions:

- Density: 5.0 n/cc
- Temperature: 232100.0 K
- Velocity: (-500.0, 0.0, 0.0) km/s
- IMF $\vec{B}$ = (-3.53, 3.53, 0.00) nT
- IMF $|B|$ = 4.99 nT

and results of comparison with our averaged profiles are shown in Figs. 5.19 and 5.20. In Fig. 5.19, the profiles of the magnetosheath density (left) and velocity (right) are compared. The experimental and model ion fluxes are shown in Fig. 5.20.

We can conclude a good overall agreement of our model with both gasdynamic and MHD models. We can see that the Spreiter model overestimates the subsolar density, BATS-R-US predicts maximal densities in the middle of the magnetosheath (not observed). Further, the Spreiter model overestimates and BATS-R-US slightly underestimates flank velocities. It is interesting to note that small spatial structures (most distinct in Fig. 5.20) are well reproduced by the BATS-R-US model. This effect will be a subject of a further study.

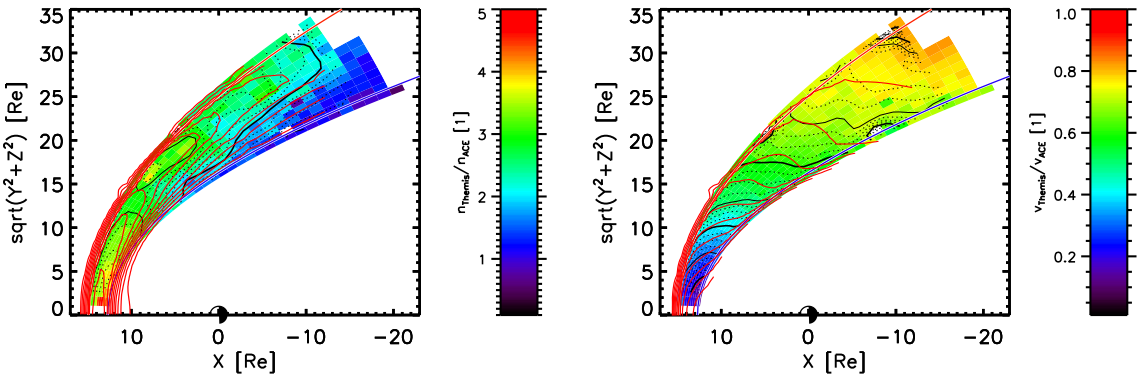

Figure 5.19: Magnetosheath's spatial profiles of the ion density (left panel) and velocity ratios (right panel) plotted in magnetosheath coordinates, and their comparison with the BATS-R-US model run.

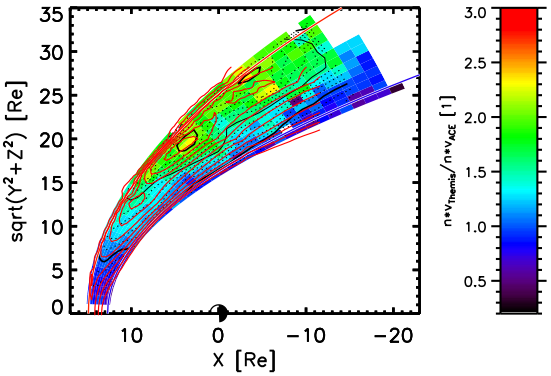

Figure 5.20: Magnetosheath's spatial profile of the ion flux ratio and its comparison with the BATS-R-US.

Chapter 6

Conclusion

The prediction of the location of the bow shock and magnetopause under various upstream conditions can be considered as a test of our understanding of the solar wind-magnetosphere interaction. The already suggested models of these boundaries are able to predict their average location with large uncertainties and thus the present thesis deals with the analysis of the sources of boundary motions and displacements. The analysis results in suggestion of a new method of the boundary determination that is then applied for construction of a new model for both boundaries. The model is tested against the sets of both boundary crossings identified by a visual inspection of plots of magnetic field and plasma parameters and, finally, used for finding of sources of unusual magnetopause location.

The results of the thesis can be briefly summarized as it follows:

1. Two-point observations of the bow shock motion revealed that its speed is less than 100 km/s; in a majority of observed crossings it did not exceed 40 km/s and the probability of observations of large speeds decreases with the θ_{Bn} angle ([Safrankova et al., 2003], Appendix C.10).

2. Although the magnetopause location is supposed to depend on the IMF B_Z orientation, the bow shock does not follow its changes ([Jelinek et al., 2008a], Appendix C.9).

3. The bow shock position is influenced by the tilt angle ([Jelinek et al., 2008b], Appendix C.8).

4. Both case and statistical studies demonstrated the radial IMF orientation as an important factor affecting the magnetopause location ([Suvorova et al., 2010], Appendix C.2; [Jelinek et al., 2010], Appendix C.3). The average magnetopause displacement was found to be approx 1 R_E for purely radial IMF

([Dusik et al., 2010], Appendix C.1) but the case studies have shown the magnetopause up to 4 R_E outward its nominal position.

5. Inspection of several thousands of magnetopause and bow shock crossings from the Themis project identified the problem of the orbital bias when the crossings of a low-apogee spacecraft are used for determination of averaged magnetopause and mainly bow shock locations. We have suggested a method that can suppress this bias and applied it on the set of Themis boundary crossings ([Jelinek et al., 2009], Appendix C.4; [Jelinek et al., 2012], Appendix C.5).

6. The above described activities have shown that the estimation of average boundary locations from their crossings by the spacecraft posses many unavoidable weakness. For this reason, we have applied a new approach and developed a method that can be used not only for finding of average boundary positions but it can be used for a variety of other studies of the magnetospheric regions.

7. This method was applied for development of the new magnetopause and bow shock model ([Jelinek et al., 2012], Appendix C.5). We should stress out that all previous models describe the bow shock and magnetopause surface separately, whereas the new model uses identical analytical expression with different parameters. It allows us to show that the pressure scaling factors for the bow shock and magnetopause are different.

8. The model was used for normalization of the parameters measured in the solar wind and magnetosheath. The normalization revealed that a way of transformation of the solar wind dynamic pressure into a total pressure in the magnetosheath depends on the IMF orientation ([Samsonov et al., 2012], Appendix C.6). This dependence was identified as the source of the magnetopause expansion for radial IMF (see point 4).

We believe that the developed method of the boundary identification can serve as a powerful tool for investigation of the solar wind-magnetosphere interaction. Several directions for such studies were suggested in the last two subsection of the thesis.

Bibliography

V. Angelopoulos. The themis mission. *Space Sci. Rev.*, 141:5–34, 2008. ISSN 0038-6308. doi: 10.1007/s11214-008-9336-1. URL http://dx.doi.org/10.1007/s11214-008-9336-1. 20, 34

R. L. Aptekar, D. D. Frederiks, S. V. Golenetskii, V. N. Ilynskii, E. P. Mazets, V. N. Panov, Z. J. Sokolova, M. M. Terekhov, L. O. Sheshin, T. L. Cline, and D. E. Stilwell. Konus-W Gamma-Ray Burst Experiment for the GGS Wind Spacecraft. *Space Sci. Rev.*, 71:265–272, feb 1995. ISSN 0038-6308. doi: 10.1007/BF00751332. 70

T. Armstrong, S. Krimigis, and R. Lepping. Magnetosheath bursts of predominantly medium nuclei observed with imp 8 on february 16, 1974. *J. Geophys. Res.*, 83(A11):5198, 1978. ISSN 0148-0227. doi: 10.1029/JA083iA11p05198. 79

M. P. Aubry, C. T. Russell, and M. G. Kivelson. Inward motion of the magnetopause before a substorm. *J. Geophys. Res.*, 75:7018–7031, 1970. ISSN 0148-0227. doi: 10.1029/JA075i034p07018. 8

H. U. Auster, K. H. Glassmeier, W. Magnes, O. Aydogar, W. Baumjohann, D. Constantinescu, D. Fischer, K. H. Fornacon, E. Georgescu, P. Harvey, O. Hillenmaier, R. Kroth, M. Ludlam, Y. Narita, R. Nakamura, K. Okrafka, F. Plaschke, I. Richter, H. Schwarzl, B. Stoll, A. Valavanoglou, and M. Wiedemann. The THEMIS Fluxgate Magnetometer. *Space Sci. Rev.*, 141: 235–264, dec 2008. ISSN 0038-6308. doi: 10.1007/s11214-008-9365-9. 20, 66

J. Bieber and E. Stone. Energetic electron bursts in the magnetopause electron layer and in interplanetary space. In *Proceedings of Magnetospheric Boundary Layers Conference, Alpbach, 11–15 June 1979*, pages 131–135. ESA SP-148, 1979. 12

S. A. Boardsen, T. E. Eastman, T. Sotirelis, and J. L. Green. An empirical model of the high-latitude magnetopause. *J. Geophys. Res.*, 105(A10):23193–23219, 2000. ISSN 0148-0227. doi: 10.1029/1998JA000143. URL http://dx.doi.org/10.1029/1998JA000143. 8, 10, 42

J. W. Bonnell, F. S. Mozer, G. T. Delory, A. J. Hull, R. E. Ergun, C. M. Cully, V. Angelopoulos, and P. R. Harvey. The Electric Field Instrument (EFI) for THEMIS. *Space Sci. Rev.*, 141: 303–341, dec 2008. ISSN 0038-6308. doi: 10.1007/s11214-008-9469-2. 67

J.-L. Bougeret, M. L. Kaiser, P. J. Kellogg, R. Manning, K. Goetz, S. J. Monson, N. Monge, L. Friel, C. A. Meetre, C. Perche, L. Sitruk, and S. Hoang. Waves: The Radio and Plasma Wave Investigation on the Wind Spacecraft. *Space Sci. Rev.*, 71:231–263, feb 1995. ISSN 0038-6308. doi: 10.1007/BF00751331. 69

D. Burgess. *Collisionless Shocks*, pages 129–163. Cambridge atmospheric and space science series. Cambridge University Press, 1995. ISBN 9780521457149. URL http://books.google.com/books?id=qWHSqXGfsfQC. 12

I. Cairns and C. Grabbe. Towards an mhd theory for the standoff distance of earth's bow shock. *Geophys. Res. Lett.*, 21(25):2781–2784, 1994. ISSN 0094-8276. doi: 10.1029/94GL02551. URL http://dx.doi.org/10.1029/94GL02551. 13

I. Cairns, D. Fairfield, R. Anderson, V. Carlton, K. Paularena, and A. Lazarus. Unusual locations of earth's bow shock on september 24 - 25, 1987: Mach number effects. *J. Geophys. Res.*, 100 (A1):47–62, 1995. ISSN 0148–0227. doi: 10.1029/94JA01978. URL http://dx.doi.org/10.1029/94JA01978. 12

I. H. Cairns and J. G. Lyon. Mhd simulations of earth's bow shock at low mach numbers: Standoff distances. *J. Geophys. Res.*, 100(A9):17173–17180, 1995. ISSN 0148–0227. doi: 10.1029/95JA00993. URL http://dx.doi.org/10.1029/95JA00993. 13

J. Chao, D. Wu, C.-H. Lin, Y.-H. Yang, X. Wang, M. Kessel, S. Chen, and R. Lepping. Models for the size and shape of the earth's magnetopause and bow shock. In L.-H. Lyu, editor, *Space Weather Study Using Multipoint Techniques Proceedings of the COSPAR Colloquium*, volume 12 of *COSPAR Colloquia Series*, pages 127–135. Pergamon, 2002. doi: 10.1016/S0964-2749(02)80212-8. URL http://www.sciencedirect.com/science/article/pii/S0964274902802128. 32

S. Chapman and V. Ferraro. A new theory of magnetic storms. *Nature*, 126:129–130, 1930. ISSN 0028-0836. doi: 10.1038/126129a0. 7

T. Doke, M. Fujii, M. Fujimoto, K. Fujiki, T. Fujui, F. Gliem, W. Güttler, N. Hasege, T. Hayashi, T. Ito, K. Itsumi, T. Kashiwagi, J. Kikuchi, T. Kohno, S. Kokubun, S. Livi, K. Maezawa, H. Moriya, K. Munakata, H. Murakami, Y. Muraki, H. Nagoshi, A. Nakamoto, K. Nagata, A. Nishida, R. Rathje, T. Shino, H. Sommer, T. Takashima, T. Terasawa, S. Ullaland, W. Weiss, B. Wilken, T. Yamamoto, T. Yanagimachi, and S. Yanagita. The energetic particle spectrometer hep onboard the geotail spacecraft. *J. Geomagn. and Geoelectr.*, 46:713–733, 1994. ISSN 0022-1392. 76

J. Dungey. A family of solutions of the magneto-hydrostatic problem in a conducting atmosphere in a gravitational field. *Mon. Not. Roy. Astron. Soc.*, 113(2):180–187, 1953. ISSN 0035-8711. 9

J. Dungey. Interplanetary magnetic field and the auroral zones. *Phys. Rev. Lett.*, 6:47–48, Jan 1961. doi: 10.1103/PhysRevLett.6.47. URL http://link.aps.org/doi/10.1103/PhysRevLett.6.47. 9

S. Dusik, G. Granko, J. Safrankova, Z. Nemecek, and K. Jelinek. Imf cone angle control of the magnetopause location: Statistical study. *Geophys. Res. Lett.*, 37(19):L19103, 2010. ISSN 0094-8276. doi: 10.1029/2010GL044965. 34, 36, 37, 43, 50

T. E. Eastman, S. A. Boardsen, S.-H. Chen, S. F. Fung, and R. L. Kessel. Configuration of high-latitude and high-altitude boundary layers. *J. Geophys. Res.*, 105(A10):23221–23238, 2000. ISSN 0148–0227. doi: 10.1029/1999JA900269. URL http://dx.doi.org/10.1029/1999JA900269. 10

D. Fairfield. Avarage and unusual locations of the earth's magnetopause and bow shock. *J. Geophys. Res.*, 76(28):6700–6716, 1971. ISSN 0148-0227. doi: 10.1029/JA076i028p06700. 8, 12

D. H. Fairfield and W. C. Feldman. Standing waves at low mach number laminar bow shocks. *J. Geophys. Res.*, 80(4):515–522, 1975. ISSN 0148-0227. doi: 10.1029/JA080i004p00515. URL http://dx.doi.org/10.1029/JA080i004p00515. 12

D. H. Fairfield, W. Baumjohann, G. Paschmann, H. Luehr, and D. G. Sibeck. Upstream pressure variations associated with the bow shock and their effects on the magnetosphere. *J. Geophys. Res.*, 95:3773–3786, apr 1990. ISSN 0148-0227. doi: 10.1029/JA095iA04p03773. 10, 30

M. Farris and C. Russell. Determining the standoff distance of the bow shock: Mach number dependence and use of models. *J. Geophys. Res.*, 99(A9):17,681–17,689, 1994. ISSN 0148-0227. doi: 10.1029/94JA01020. 12

M. H. Farris, S. M. Petrinec, and C. T. Russell. The thickness of the magnetosheath: Constraints on the polytropic index. *Geophys. Res. Lett.*, 18(10):1821–1824, 1991. ISSN 0094-8276. doi: 10.1029/91GL02090. URL http://dx.doi.org/10.1029/91GL02090. 12

C. J. Farrugia, F. T. Gratton, E. J. Lund, P. E. Sandholt, S. W. H. Cowley, R. B. Torbert, G. Gnavi, I. R. Mann, L. Bilbao, C. Mouikis, L. Kistler, C. W. Smith, H. J. Singer, and J. F. Watermann. Two-stage oscillatory response of the magnetopause to a tangential discontinuity/vortex sheet followed by northward imf: Cluster observations. *J. Geophys. Res.*, 113(A3):A03208–, mar 2008. ISSN 0148-0227. doi: 10.1029/2007JA012800. URL http://dx.doi.org/10.1029/2007JA012800. 14

W. Feldman, J. Asbridge, S. Bame, M. Montgomery, and S. Gary. Solar wind electrons. *J. Geophys. Res.*, 81(31):4181, 1975. ISSN 0148-0227. doi: 10.1029/JA080i031p04181. 77

V. Formisano. Orientation and shape of the earth's bow shock in three dimensions. *Planet. Space Sci.*, 27(9):1151–1161, 1979. ISSN 0032-0633. doi: 10.1016/0032-0633(79)90135-1. 12

V. Formisano, P. Hedgecock, G. Moreno, J. Sear, and D. Bollea. Observation of earth's bow shock for low mach numbers. *Planet. Space Sci.*, 19(11):1519–1531, 1971. ISSN 0032-0633. doi: 10.1016/0032-0633(71)90011-01519. 12

V. Formisano, P. Hedgecock, G. Moreno, F. Palmiotto, and J. Chao. Solar wind interaction with earth's magnetic field, 2.magnetohydrodynamic bow shock. *J. Geophys. Res.*, 78(19):3731–3744, 1973. ISSN 0148-0227. doi: 10.1029/JA078i019p03731. 8, 13

V. Formisano, V. Domingo, and K. Wenzel. The three-dimensional shape of the magnetopause. *Planet. Space Sci.*, 27(9):1137–1149, 1979. ISSN 0032-0633. doi: 10.1016/0032-0633(79)90134-X. 8

L. Frank, K. Ackerson, and R. Lepping. On hot tenuous plasmas, fireballs, and boundary layers in the earth's magnetotail. *J. Geophys. Res.*, 81(34):5859, 1976. ISSN 0148-0227. doi: 10.1029/JA081i034p05859. 78

L. Frank, K. Ackerson, W. Paterson, J. Lee, E. M.R., and G. Pickett. The comprehensive plasma instrumentation (cpi) for the geotail spacecraft. *J. Geomagn. and Geoelectr.*, 46:23–37, 1994. ISSN 0022-1392. 73

A. A. Galeev, Y. I. Gal'Perin, and L. M. Zelenyj. The INTERBALL project to study solar-terrestrial physics. *Kosmicheskie Issledovaniia*, 34:339–362, aug 1996. 81, 82

G. Gloeckler, H. Balsiger, A. Bürgi, P. Bochsler, L. A. Fisk, A. B. Galvin, J. Geiss, F. Gliem, D. C. Hamilton, T. E. Holzer, D. Hovestadt, F. M. Ipavich, E. Kirsch, R. A. Lundgren, K. W. Ogilvie, R. B. Sheldon, and B. Wilken. The Solar Wind and Suprathermal Ion Composition Investigation on the Wind Spacecraft. *Space Sci. Rev.*, 71:79–124, feb 1995. ISSN 0038-6308. doi: 10.1007/BF00751327. 69

R. E. Gold, S. M. Krimigis, S. E. Hawkins, III, D. K. Haggerty, D. A. Lohr, E. Fiore, T. P. Armstrong, G. HollAND, and L. J. Lanzerotti. Electron, Proton, and Alpha Monitor on the Advanced Composition Explorer spacecraft. *Space Sci. Rev.*, 86:541–562, jul 1998. ISSN 0038-6308. doi: 10.1023/A:1005088115759. 71

C. Grabbe. Low mach number predictions in an extended axially symmetric mhd theory of the magnetosheath. *Geophys. Res. Lett.*, 24(20):2495–2498, 1997. ISSN 0094-8276. doi: 10.1029/97GL02584. URL http://dx.doi.org/10.1029/97GL02584. 13

C. Groth, D. De Zeeuw, T. Gombosi, and K. Powell. Global three-dimensional mhd simulation of a space weather event: Cme formation, interplanetary propagation, and interaction with the magnetosphere. *J. Geophys. Res.*, 105(A11):25053–25078, 2000. ISSN 0148-0227. doi: 10.1029/2000JA900093. URL http://dx.doi.org/10.1029/2000JA900093. 47

K. S. Jacobsen, T. D. Phan, J. P. Eastwood, D. G. Sibeck, J. I. Moen, V. Angelopoulos, J. P. McFadden, M. J. Engebretson, G. Provan, D. Larson, and K.-H. Fornacon. Themis observations of extreme magnetopause motion caused by a hot flow anomaly. *J. Geophys. Res.*, 114(A8): A08210–, aug 2009. ISSN 0148–0227. doi: 10.1029/2008JA013873. URL http://dx.doi.org/10.1029/2008JA013873. 14

C. Jacquey, D. Williams, R. McEntire, A. Lui, V. Angelopoulos, S. Christon, S. Kokubun, T. Yamamoto, G. Reeves, and R. Belian. Tailward energetic ion streams observed at ∼100 r_e by geotail–epic associated with geomagnetic activity intensification. *Geophys. Res. Lett.*, 21(25): 3015–3018, 1994. ISSN 0094-8276. doi: 10.1029/94GL01606. 73

K. Jelinek, Z. Nemecek, and J. Safrankova. Simultaneous observations of the bow shock and magnetopause motions. In J. Safrankova and J. Pavlu, editor, *WDS'06 Proceedings of Contributed Papers, Part II*, pages 14–20. Prague, MATFYZPRESS, 2006. ISBN 80-86732-85-1. 27, 28

K. Jelinek, Z. Nemecek, and J. Safrankova. Small-scale deformation of the bow shock. *Adv. Space Res.*, 41(10):1519–1527, 2008a. ISSN 0273-1177. doi: 10.1016/j.asr.2007.04.050. 49

K. Jelinek, Z. Nemecek, J. Safrankova, and J. Merka. Influence of the tilt angle on the bow shock shape and location. *J. Geophys. Res.*, 113(A05):A05220, 2008b. ISSN 0148-0227. doi: 10.1029/2007JA012813. 19, 29, 35, 38, 42, 49

K. Jelinek, Z. Nemecek, and J. Safrankova. Themis: Locations of dayside bow shock and magnetopause. In J. Safrankova and J. Pavlu, editor, *WDS'09 Proceedings of Contributed Papers, Part II*, pages 15–21. Prague, MATFYZPRESS, 2009. ISBN 978-80-7378-102-6. 21, 50

K. Jelinek, Z. Nemecek, J. Safrankova, J.-H. Shue, A. Suvorova, and D. Sibeck. Thin magnetosheath as a consequence of the magnetopause deformation: Themis observations. *J. Geophys. Res.*, 115:A10203, 2010. ISSN 0148-0227. doi: 10.1029/2010JA015345. 31, 33, 34, 35, 49

K. Jelinek, Z. Nemecek, and J. Safrankova. A new approach to magnetopause and bow shock modeling based on automated region identification. *J. Geophys. Res.*, 117(A05):A05208, 2012. ISSN 0148-0227. doi: 10.1029/2011JA017252. 40, 50

M. Jerab, Z. Nemecek, J. Safrankova, K. Jelinek, and J. Merka. Improved bow shock model with dependence on the imf strength. *Planet. Space Sci.*, 53(1-3):85–93, 2005. ISSN 0032-0633. doi: 10.1016/j.pss.2004.09.032. 19, 35, 38, 39

A. D. Johnstone, C. Alsop, S. Burge, P. J. Carter, A. J. Coates, A. J. Coker, A. N. Fazakerley, M. GrANDe, R. A. Gowen, C. Gurgiolo, B. K. Hancock, B. Narheim, A. Preece, P. H. Sheather, J. D. Winningham, and R. D. Woodliffe. Peace: A plasma electron and current experiment. *Space Sci. Rev.*, 79:351–398, 1997. ISSN 0038-6308. doi: 10.1023/A:1004938001388. URL http://dx.doi.org/10.1023/A:1004938001388. 88

M. Kivelson and C. Russell. *Introduction to space physics*. Cambridge atmospheric and space science series. Cambridge University Press, 1995. ISBN 9780521457149. URL http://books.google.com/books?id=qWHSqXGfsfQC. 5, 6

S. Kokubun, T. Yamamoto, M. Acuna, K. Hayashi, K. Shiokawa, and H. Kawano. The geotail magnetic field experiment. *J. Geomagn. and Geoelectr.*, 46:7–21, 1994. ISSN 0022-1392. 74

H. Laakso, D. H. Fairfield, M. R. Collier, H. Opgenoorth, T. Phan, D. G. Sibeck, B. L. Giles, H. J. Singer, R. P. Lepping, R. P. Lin, F. S. Mozer, R. F. Pfaff, K. Tsuruda, and J. R. Wygant. Oscillations of magnetospheric boundaries driven by imf rotations. *Geophys. Res. Lett.*, 25(15): 3007–3010, 1998. ISSN 0094-8276. doi: 10.1029/98GL50916. URL http://dx.doi.org/10.1029/98GL50916. 14

B. Lavraud, A. Fedorov, E. Budnik, A. Grigoriev, P. Cargill, M. Dunlop, H. Rème, I. Dandouras, and A. Balogh. Cluster survey of the high-altitude cusp properties: a three-year statistical study. *Ann. Geophys.*, 22:3009–3019, aug 2004. ISSN 0992-7689. doi: 10.5194/angeo-22-3009-2004. 11

S. Lepidi, U. Villante, A. Lazarus, A. Szabo, and K. Paularena. Observations of bow shock motion during times of variable solar conditions. *J. Geophys. Res.*, 101(A5):11,107–11,123, 1996. ISSN 0148-0227. doi: 10.1029/96JA00478. 27

R. P. Lepping, M. H. Acũna, L. F. Burlaga, W. M. Farrell, J. A. Slavin, K. H. Schatten, F. Mariani, N. F. Ness, F. M. Neubauer, Y. C. Whang, J. B. Byrnes, R. S. Kennon, P. V. Panetta, J. Scheifele, and E. M. Worley. The wind magnetic field investigation. *Space Sci. Rev.*, 71: 207–229, feb 1995. ISSN 0038-6308. doi: 10.1007/BF00751330. 68

R. L. Lin, X. X. Zhang, S. Q. Liu, Y. L. Wang, and J. C. Gong. A three-dimensional asymmetric magnetopause model. *J. Geophys. Res.*, 115(A4):A04207–, apr 2010. ISSN 0148-0227. doi: 10.1029/2009JA014235. URL http://dx.doi.org/10.1029/2009JA014235. 8, 11, 35, 42

R. P. Lin, K. A. Anderson, S. Ashford, C. Carlson, D. Curtis, R. Ergun, D. Larson, J. McFadden, M. McCarthy, G. K. Parks, H. Rème, J. M. Bosqued, J. Coutelier, F. Cotin, C. D'Uston, K.-P. Wenzel, T. R. SANDerson, J. Henrion, J. C. Ronnet, and G. Paschmann. A Three-Dimensional Plasma and Energetic Particle Investigation for the Wind Spacecraft. *Space Sci. Rev.*, 71: 125–153, feb 1995. ISSN 0038-6308. doi: 10.1007/BF00751328. 70

J. Y. Lu, Z.-Q. Liu, K. Kabin, M. X. Zhao, D. D. Liu, Q. Zhou, and Y. Xiao. Three dimensional shape of the magnetopause: Global mhd results. *J. Geophys. Res.*, 116:A09237, 2011. ISSN 0148-0227. doi: 10.1029/2010JA016418. URL http://dx.doi.org/10.1029/2010JA016418. 8, 35

G. M. Mason, R. E. Gold, S. M. Krimigis, J. E. Mazur, G. B. Andrews, K. A. Daley, J. R. Dwyer, K. F. Heuerman, T. L. James, M. J. Kennedy, T. Lefevere, H. Malcolm, B. Tossman, and P. H. Walpole. The Ultra-Low-Energy Isotope Spectrometer (ULEIS) for the ACE spacecraft. *Space Sci. Rev.*, 86:409–448, jul 1998. ISSN 0038-6308. doi: 10.1023/A:1005079930780. 72

H. Matsumoto, I. Nagano, R. Anderson, H. Kojima, K. Hashimoto, M. Tsutsui, T. Okada, I. Kimura, Y. Omura, and M. ; Okada. Plasma wave observations with geotail spacecraft. *J. Geomagn. and Geoelectr.*, 46(1):59–95, 1994. ISSN 0022-1392. 74

D. J. McComas, S. J. Bame, P. Barker, W. C. Feldman, J. L. Phillips, P. Riley, and J. W. Griffee. Solar Wind Electron Proton Alpha Monitor (SWEPAM) for the Advanced Composition Explorer. *Space Sci. Rev.*, 86:563–612, jul 1998. ISSN 0038-6308. doi: 10.1023/A:1005040232597. 72

J. McFadden, C. Carlson, D. Larson, M. Ludlam, R. Abiad, B. Elliott, P. Turin, M. Marckwordt, and V. Angelopoulos. The THEMIS ESA Plasma Instrument and In-flight Calibration. *Space Sci. Rev.*, 141:277–302, dec 2008. ISSN 0038-6308. doi: 10.1007/s11214-008-9440-2. 20, 66

J. Merka and A. Szabo. Bow shock's geometry at the magnetospheric flanks. *J. Geophys. Res.*, 109(A12):A12224–, dec 2004. ISSN 0148-0227. doi: 10.1029/2004JA010567. URL http://dx.doi.org/10.1029/2004JA010567. 28, 35

J. Merka, A. Szabo, T. W. Narock, J. H. King, K. I. Paularena, and J. D. Richardson. A comparison of imp 8 observed bow shock positions with model predictions. *J. Geophys. Res.*, 108(A2):1077–, feb 2003a. ISSN 0148-0227. doi: 10.1029/2002JA009384. URL http://dx.doi.org/10.1029/2002JA009384. 12

J. Merka, A. Szabo, J. Safrankova, and Z. Nemecek. Earth's bow shock and magnetopause in the case of a field-aligned upstream flow: Observation and model comparison. *J. Geophys. Res.*, 108(A7):1269–, jul 2003b. ISSN 0148-0227. doi: 10.1029/2002JA009697. URL http://dx.doi.org/10.1029/2002JA009697. 10, 34, 35

R. Mewaldt, E. Stone, S. Vidor, and R. Vogt. Isotopic and elemental composition of the anomalous low-energy cosmic-ray fluxes. *Astrophys. J.*, 205:931–937, may 1976. ISSN 0004-637X. doi: 10.1086/154348. 80

E. Möbius, L. M. Kistler, M. A. Popecki, K. C. Crocker, M. Granoff, Y. Jiang, E. Sartori, V. Ye, H. Réme, J. A. Sauvaud, A. Cros, C. Aoustin, T. Camus, J.-L. Médale, J. Rouzaud, C. W. Carlson, J. P. McFadden, D. Curtis, H. Heetder, J. Croyle, C. Ingraham, B. Klecker, D. Hovestadt, M. Ertl, F. Eberl, H. Kästle, E. Künneth, P. Laeverenz, E. Seidenschwang, E. G. Shelley, D. M. Klumpar, E. Hertzberg, G. K. Parks, M. McCarthy, A. Korth, H. Rosenbauer, B. Gräve, L. Eliasson, S. Olsen, H. Balsiger, U. Schwab, and M. Steinacher. The 3-D Plasma Distribution Function Analyzers With Time-of-Flight Mass Discrimination for Cluster, FAST, and Equator-S. In R. F. Pfaff, J. E. Borovsky, & D. T. Young, editor, *Measurement Techniques in Space Plasmas – Particles*, page 243, 1998a. 88

E. Möbius, L. M. Kistler, M. A. Popecki, K. N. Crocker, M. Granoff, S. Turco, A. Anderson, P. Demain, J. Distelbrink, I. Dors, P. Dunphy, S. Ellis, J. Gaidos, J. Googins, R. Hayes, G. Humphrey, H. Kästle, J. Lavasseur, E. J. Lund, R. Miller, E. Sartori, M. Shappirio, S. Taylor, P. Vachon, M. Vosbury, V. Ye, D. Hovestadt, B. Klecker, H. Arbinger, E. Künneth, E. Pfeffermann, E. Seidenschwang, F. Gliem, K.-U. Reiche, K. Stöckner, W. Wiewesiek, A. Harasim, J. Schimpfle, S. Battell, J. Cravens, and G. Murphy. The Solar Energetic Particle Ionic Charge Analyzer (SEPICA) and the Data Processing Unit (S3DPU) for SWICS, SWIMS and SEPICA. *Space Sci. Rev.*, 86:449–495, jul 1998b. ISSN 0038-6308. doi: 10.1023/A:1005084014850. 71, 72

T. Mukai, S. Machida, Y. Saito, M. Hirahara, T. Terasawa, N. Kaya, T. Obara, M. Ejiri, and A. Nishida. The low energy particle (lep) experiment on board the geotail satellite. *J. Geomagn. and Geoelectr.*, 46:669–692, 1994. ISSN 0022-1392. 75

Z. Nemecek and J. Safrankova. The earths bow shock and magnetopause position as a result of the solar wind-magnetosphere interaction. *J. Atmos. Terr. Phys.*, 53(11-12):1049–1054, 1991. ISSN 0021-9169. doi: 10.1016/0021-9169(91)90051-8. 12, 19

Z. Nemecek, J. Safrankova, and G. Zastenker. Dynamics of the earth's bow shock position. *Adv. Space Res.*, 8(9-10):167–170, 1988. ISSN 0273-1177. doi: 10.1016/0273-1177(88)90127-5. 27

Z. Nemecek, J. Safrankova, L. Prech, D. G. Sibeck, S. Kokubun, and T. Mukai. Transient flux enhancements in the magnetosheath. *Geophys. Res. Lett.*, 25(8):1273–1276, 1998. ISSN 0094-8276. doi: 10.1029/98GL50873. URL http://dx.doi.org/10.1029/98GL50873. 30

J. Newbury, C. Russell, and M. Gedalin. The ramp widths of high-mach-number, quasi-perpendicular collisionless shocks. *J. Geophys. Res.*, 103(A12):29,581–29,593, 1998. ISSN 0148-0227. doi: 10.1029/1998JA900024. 27

K. W. Ogilvie, D. J. Chornay, R. J. Fritzenreiter, F. Hunsaker, J. Keller, J. Lobell, G. Miller, J. D. Scudder, E. C. Sittler, Jr., R. B. Torbert, D. Bodet, G. Needell, A. J. Lazarus, J. T. Steinberg, J. H. Tappan, A. Mavretic, and E. Gergin. SWE, A Comprehensive Plasma Instrument for the Wind Spacecraft. *Space Sci. Rev.*, 71:55–77, feb 1995. ISSN 0038-6308. doi: 10.1007/BF00751326. 34, 68

A. Owens, R. Baker, T. L. Cline, N. Gehrels, J. Jermakian, T. Nolan, R. Ramaty, H. Seifert, D. A. Shephard, G. Smith, D. E. Stilwell, B. J. Teegarden, C. P. Cork, D. A. LANDis, P. N. Luke, N. W. Madden, D. Malone, R. H. Pehl, H. Yaver, K. Hurley, S. Mathias, and A. H. Post, Jr. A High-Resolution GE Spectrometer for Gamma-Ray Burst Astronomy. *Space Sci. Rev.*, 71: 273–296, feb 1995. ISSN 0038-6308. doi: 10.1007/BF00751333. 69

E. N. Parker. Kinematical Hydromagnetic Theory and its Application to the Low Solar Photosphere. *Astrophys. J.*, 138:552, aug 1963. doi: 10.1086/147663. 9

G. Paschmann, J. M. Quinn, R. B. Torbert, H. Vaith, C. E. McIlwain, G. Haerendel, O. H. Bauer, T. Bauer, W. Baumjohann, W. Fillius, M. Förster, S. Frey, E. Georgescu, S. S. Kerr, C. A. Kletzing, H. Matsui, P. Puhl-Quinn, and E. C. Whipple. The electron drift instrument on cluster: overview of first results. *Ann. Geophys.*, 19(10/12):1273–1288, 2001. ISSN 0992-7689. doi: 10.5194/angeo-19-1273-2001. URL http://www.ann-geophys.net/19/1273/2001/. 87

M. Peredo, J. Slavin, E. Mazyr, and S. Curtis. Tree-dimensional position and shape of the bow shock and their variation with alfvénic, sonic and magnetosonic mach numbers and interplanetary magnetic field orientation. *J. Geophys. Res.*, 100(A5):7907–7916, 1995. ISSN 0148-0227. doi: 10.1029/94JA02545. 12

S. M. Petrinec and C. T. Russell. Near-earth magnetotail shape and size as determined from the magnetopause flaring angle. *J. Geophys. Res.*, 101(A1):137–152, 1996. ISSN 0148-0227. doi: 10.1029/95JA02834. URL http://dx.doi.org/10.1029/95JA02834. 8, 9, 10, 34, 38, 39, 42

H. E. Petschek. Magnetic Field Annihilation. *NASA Special Publication*, 50:425, 1964. 9

T.-D. Phan, J. T. Gosling, G. Paschmann, C. Pasma, J. F. Drake, M. Øieroset, D. Larson, R. P. Lin, and M. S. Davis. The dependence of magnetic reconnection on plasma β and magnetic shear: Evidence from solar wind observations. *Astroph. J. Lett.*, 719(2):L199, 2010. ISSN 2041-8213. URL http://stacks.iop.org/2041-8205/719/i=2/a=L199. 9

K. Powell, P. Roe, T. Linde, T. Gombosi, and D. De Zeeuw. A solution-adaptive upwind scheme for ideal magnetohydrodynamics. *J. Comp. Phys.*, 154(2):284–309, 1999. ISSN 0021-9991. doi: 10.1006/jcph.1999.6299. URL http://www.sciencedirect.com/science/article/pii/S002199919996299X. 47

M. I. Pudovkin, V. V. Lebedeva, and M. F. Heyn. Magnetosheath's parameters and their dependence on intensity and direction of the solar wind magnetic field. *J. Geophys. Res.*, 87: 8131–8138, oct 1982. ISSN 0148-0227. doi: 10.1029/JA087iA10p08131. 14

E. Roelof and D. Sibeck. Magnetopause shape as a bivariate function of interplanetary magnetic field bz and solar wind dynamic pressure. *J. Geophys. Res.*, 98(A12):21421–21450, 1993. ISSN 0148-0227. doi: 10.1029/93JA02362. URL http://dx.doi.org/10.1029/93JA02362. 8, 9, 42

A. Roux, O. Le Contel, C. Coillot, A. Bouabdellah, B. de La Porte, D. Alison, S. Ruocco, and M. C. Vassal. The Search Coil Magnetometer for THEMIS. *Space Sci. Rev.*, 141:265–275, dec 2008. ISSN 0038-6308. doi: 10.1007/s11214-008-9455-8. 66

C. T. Russell and T.-L. Zhang. Unusually distant bow shock encounters at venus. *Geophys. Res. Lett.*, 19(8):833–836, 1992. ISSN 0094-8276. doi: 10.1029/92GL00634. URL http://dx.doi.org/10.1029/92GL00634. 13

C. T. Russell, S. M. Petrinec, T. L. Zhang, P. Song, and H. Kawano. The effect of foreshock on the motion of the dayside magnetopause. *Geophys. Res. Lett.*, 24(12):1439–1441, 1997. ISSN 0094-8276. doi: 10.1029/97GL01408. URL http://dx.doi.org/10.1029/97GL01408. 30

J. Safrankova, G. Zastenker, A. Fedorov, Z. Nemecek, M. Simersky, O. Vaisberg, L. Prech, Y. Sharko, T. Romasenko, A. Leibov, M. Richter, T. Lesina, N. Plusnina, and N. Yanovskaja. Omnidirectional plasma sensor VDP, in: INTERBALL Mission and Payload, ed. by Yu. Galperin et al. *CNES–IKI–RSA*, pages 195–198, 1995. 82

J. Safrankova, Z. Nemecek, S. Dusik, L. Prech, D. Sibeck, and N. Borodkova. The magnetopause shape and location: a comparison of the interball and geotail observations with models. *Ann. Geophys.*, 20(3):301–309, 2002. ISSN 0992-7689. 23, 34, 40

J. Safrankova, K. Jelinek, and Z. Nemecek. The bow shock velocity from two-point measurements in frame of the interball project. *Adv. Space Res.*, 31(5):1377–1382, 2003. ISSN 0273-1177. doi: 10.1016/S0273-1177(02)00951-1. 14, 27, 28, 49

J. Safrankova, S. Dusik, and Z. Nemecek. The shape and location of the high-latitude magnetopause. *Adv. Space Res.*, 36(10):1934–1939, 2005. ISSN 0273-1177. doi: 10.1016/j.asr.2004.05.009. 10, 37, 39, 42

A. Samsonov, Z. Nemecek, J. Safrankova, and K. Jelinek. Why does the subsolar magnetopause move sunward for radial interplanetary magnetic field? *J. Geophys. Res.*, 117(A05):A05221, 2012. ISSN 0148-0227. doi: 10.1029/2011JA017429. 43, 44, 50

A. Seiff and E. Whiting. Correlation study of bow-wave profiles on blunt bodies. *62N10002, Report Number: NASA-TN-D-1148*, 1962. 13

J.-H. Shue, J. K. Chao, H. C. Fu, C. T. Russell, P. Song, K. K. Khurana, and H. J. Singer. A new functional form to study the solar wind control of the magnetopause size and shape. *J. Geophys. Res.*, 102(A5):9497–9511, 1997. ISSN 0148-0227. doi: 10.1029/97JA00196. URL http://dx.doi.org/10.1029/97JA00196. 8, 9, 42

J.-H. Shue, J. Chao, H. Fu, K. Khurana, C. Russel, H. Singer, and P. Song. Magnetopause location under extreme solar wind conditions. *J. Geophys. Res.*, 103(A8):17,691–17,700, 1998. ISSN 0148-0227. doi: 10.1029/98JA01103. 8, 9, 32, 42

D. G. Sibeck. *The Magnetospheric Response to Foreshock Pressure Pulses*, page 293. the American Geophysical Union, 1995. 30

D. G. Sibeck, R. E. Lopez, and E. C. Roelof. Solar wind control of the magnetopause shape, location, and motion. *J. Geophys. Res.*, 96(A4):5489–5495, 1991. ISSN 0148-0227. doi: 10.1029/90JA02464. URL http://dx.doi.org/10.1029/90JA02464. 8, 9

D. G. Sibeck, N. L. Borodkova, S. J. Schwartz, C. J. Owen, R. Kessel, S. Kokubun, R. P. Lepping, R. Lin, K. Liou, H. Luhr, R. W. McEntire, C.-I. Meng, T. Mukai, Z. Nemecek, G. Parks, T. D. Phan, S. A. Romanov, J. Safrankova, J.-A. Sauvaud, H. J. Singer, S. I. Solovyev, A. Szabo, K. Takahashi, D. J. Williams, K. Yumoto, and G. N. Zastenker. Comprehensive study of the magnetospheric response to a hot flow anomaly. *J. Geophys. Res.*, 104(A3):4577–4593, 1999. ISSN 0148-0227. doi: 10.1029/1998JA900021. URL http://dx.doi.org/10.1029/1998JA900021. 14

D. G. Sibeck, K. Kudela, R. P. Lepping, R. Lin, Z. Nemecek, M. N. Nozdrachev, T.-D. Phan, L. Prech, J. Safrankova, H. Singer, and Y. Yermolaev. Magnetopause motion driven by interplanetary magnetic field variations. *J. Geophys. Res.*, 105(A11):25155–25169, 2000. ISSN 0148-0227. doi: 10.1029/2000JA900109. URL http://dx.doi.org/10.1029/2000JA900109. 14

J. Slavin and R. Holzer. Solar wind flow about the terrestrial planets, 1. modeling bow shock position and shape. *J. Geophys. Res.*, 86(A13):11401–11418, 1981. ISSN 0148-0227. doi: 10.1029/JA086iA13p11401. URL http://dx.doi.org/10.1029/JA086iA13p11401. 12

C. W. Smith, J. L'Heureux, N. F. Ness, M. H. Acuña, L. F. Burlaga, and J. Scheifele. The ACE Magnetic Fields Experiment. *Space Sci. Rev.*, 86:613–632, jul 1998. ISSN 0038-6308. doi: 10.1023/A:1005092216668. 34, 71

J. Spreiter and S. Stahara. A new predictive model for determining solar wind-terrestrial planet interactions. *J. Geophys. Res.*, 85(A12):6769–6777, 1980. ISSN 0148-0227. doi: 10.1029/JA085iA12p06769. 14

J. R. Spreiter, A. L. Summers, and A. Y. Alksne. Hydromagnetic flow around the magnetosphere. *Planet. Space Sci.*, 14:223–+, mar 1966. ISSN 0032-0633. doi: 10.1016/0032-0633(66)90124-3. 13, 14, 15, 47

E. C. Stone, C. M. S. Cohen, W. R. Cook, A. C. Cummings, B. Gauld, B. Kecman, R. A. Leske, R. A. Mewaldt, M. R. Thayer, B. L. Dougherty, R. L. Grumm, B. D. Milliken, R. G. Radocinski, M. E. Wiedenbeck, E. R. Christian, S. Shuman, and T. T. von Rosenvinge. The Solar Isotope Spectrometer for the Advanced Composition Explorer. *Space Sci. Rev.*, 86:357–408, jul 1998a. ISSN 0038-6308. doi: 10.1023/A:1005027929871. 71

E. C. Stone, A. M. FrANDsen, R. A. Mewaldt, E. R. Christian, D. Margolies, J. F. Ormes, and F. Snow. The Advanced Composition Explorer. *Space Sci. Rev.*, 86:1–22, jul 1998b. ISSN 0038-6308. doi: 10.1023/A:1005082526237. 70

A. Suvorova, J.-H. Shue, A. Dmitriev, D. Sibeck, J. McFadden, H. Hasegawa, K. Ackerson, K. Jelinek, J. Safrankova, and Z. Nemecek. Magnetopause expansions for quasi-radial interplanetary magnetic field: Themis and geotail observations. *J. Geophys. Res.*, 115:A10216, 2010. ISSN 0148-0227. doi: 10.1029/2010JA015404. 30, 31, 32, 35, 49

P. A. Sweet. The Neutral Point Theory of Solar Flares. In *Electromagnetic Phenomena in Cosmical Physics*, editor, B. Lehnert, volume 6 of *IAU Symposium*, page 123, 1958. 9

S. Szita, A. N. Fazakerley, P. J. Carter, A. M. James, P. Trávnícek, G. Watson, M. André, A. Eriksson, and K. Torkar. Cluster peace observations of electrons of spacecraft origin. *Ann. Geophys.*, 19(10/12):1721–1730, 2001. ISSN 0992-7689. doi: 10.5194/angeo-19-1721-2001. URL http://www.ann-geophys.net/19/1721/2001/. 87

B. J. Teegarden, T. T. von Rosenvinge, F. B. McDonald, J. H. Trainor, and W. R. Webber. Measurement of the fluxes of galactic cosmic-ray H-2 and He-3 in 1972-1973. *Astrophys. J.*, 202: 815–822, dec 1975. ISSN 0004-637X. doi: 10.1086/154036. 79

K. Tsubouchi, T. Terasawa, T. Mukai, Y. Saito, T. Yamamoto, S. Kokubun, H. Kojima, and H. Matsumoto. Motion of the earth's bow shock in the deep-tail flank. *J. Geophys. Res.*, 105 (A11):25097–25112, 2000. ISSN 0148-0227. doi: 10.1029/1999JA000454. URL http://dx.doi.org/10.1029/1999JA000454. 14

K. Tsuruda, H. Hayakawa, M. Nakamura, T. Okada, A. Matsuoka, F. Mozer, and R. Schmidt. Electric field measurements on the geotail satellite : Geotail instruments and initial results. ii. *J. Geomagn. and Geoelectr.*, 46(8):693–711, 1994. ISSN 0022-1392. 75

N. A. Tsyganenko. Modeling of twisted/warped magnetospheric configurations using the general deformation method. *J. Geophys. Res.*, 103(A10):23551–23563, 1998. ISSN 0148-0227. doi: 10.1029/98JA02292. URL http://dx.doi.org/10.1029/98JA02292. 10

M. Verigin, G. Kotova, V. Bezrukikh, G. Zastenker, and N. Nikolaeva. Analytical model of the near-earth magnetopause according to the data of the prognoz and interball satellite data. *Geomagnetism and Aeronomy*, 49:1176–1181, 2009. ISSN 0016-7932. doi: 10.1134/S0016793209080283. URL http://dx.doi.org/10.1134/S0016793209080283. 9

H. Völk and R. Auer. Motions of the bow shock induced by interplanetary disturbances. *J. Geophys. Res.*, 79(1):40–48, 1974. ISSN 0148-0227. doi: 10.1029/JA079i001p00040. 27

T. T. von Rosenvinge, L. M. Barbier, J. Karsch, R. Liberman, M. P. Madden, T. Nolan, D. V. Reames, L. Ryan, S. Singh, H. Trexel, G. Winkert, G. M. Mason, D. C. Hamilton, and P. Walpole. The Energetic Particles: Acceleration, Composition, and Transport (EPACT) investigation on the WIND spacecraft. *Space Sci. Rev.*, 71:155–206, feb 1995. ISSN 0038-6308. doi: 10.1007/BF00751329. 68

Wikipedia. Parabolic coordinates — wikipedia, the free encyclopedia, 2012. URL http://en.wikipedia.org/w/index.php?title=Parabolic_coordinates&oldid=485422876. [Online; accessed 11-May-2012]. 61

B. Wilken, W. I. Axford, I. Daglis, P. Daly, W. Guttler, W. H. Ip, A. Korth, G. Kremser, S. Livi, V. M. Vasyliunas, J. Woch, D. Baker, R. D. Belian, J. B. Blake, J. F. Fennell, L. R. Lyons, H. Borg, T. A. Fritz, F. Gliem, R. Rathje, M. Grande, D. Hall, K. Kecsuemety, S. Mckenna-Lawlor, K. Mursula, P. Tanskanen, Z. Pu, I. Sandahl, E. T. Sarris, M. Scholer, M. Schulz, F. Sorass, and S. Ullaland. Rapid – the imaging energetic particle spectrometer on cluster. *Space Sci. Rev.*, 79:399–473, 1997. ISSN 0038-6308. doi: 10.1023/A:1004994202296. URL http://dx.doi.org/10.1023/A:1004994202296. 88

D. Williams. The ion-electron magnetic separation and solid state detector detection system flown on imp 7 and 8: e/sub p/ greater than or equal to 50 kev, e/sub e/ greater than or equal to 30 kev. Technical report, National Oceanic and Atmospheric Administration, Boulder, CO (USA). Space Environment Lab., 1977. 81

T. Yeh and W. I. Axford. On the re-connexion of magnetic field lines in conducting fluids. *J. Plasma Phys.*, 4:207, may 1970. doi: 10.1017/S0022377800004967. 9

Y. I. Yermolaev, A. O. Fedorov, O. L. Vaisberg, V. M. Balebanov, Y. A. Obod, R. Jimenez, J. Fleites, L. Llera, and A. N. Omelchenko. Ion distribution dynamics near the earth's bow shock: first measurements with the 2d ion energy spectrometer corall on the interball/tail-probe satellite. *Ann. Geophys.*, 15(5):533–541, 1997. ISSN 0992-7689. doi: 10.1007/s00585-997-0533-0. URL http://www.ann-geophys.net/15/533/1997/. 82, 83

G. N. Zastenker, V. N. Smirnov, C. T. Russell, H. S. Bridge, and A. Lazarus. Bow shock motion with two-point observations - Prognoz 7, 8 and ISEE 1, 2; Prognoz 10 and IMP 8. *Adv. Space Res.*, 8:171–174, 1988. ISSN 0273-1177. doi: 10.1016/0273-1177(88)90128-7. 27

H. Zhang, Q.-G. Zong, D. G. Sibeck, T. A. Fritz, J. P. McFadden, K.-H. Glassmeier, and D. Larson. Dynamic motion of the bow shock and the magnetopause observed by themis spacecraft. *J. Geophys. Res.*, 114(A1):A00C12–, jan 2009. ISSN 0148–0227. doi: 10.1029/2008JA013488. URL http://dx.doi.org/10.1029/2008JA013488. 14

X.-W. Zhou and C. T. Russell. The location of the high-latitude polar cusp and the shape of the surrounding magnetopause. *J. Geophys. Res.*, 102(A1):105–110, 1997. ISSN 0148–0227. doi: 10.1029/96JA02702. URL http://dx.doi.org/10.1029/96JA02702. 11

Appendix A

Magnetosheath coordinates

The magnetosheath coordinate system is defined for easy and suitable description of the magnetopause, magnetosheath, and bow shock regions.

In this appendix, a source code in IDL (Interactive Data Language) dedicated to transform aberated GSE coordinates into relative magnetosheath coordinates is described. Transformation is based on simplified magnetopause and bow shock model (see Section 5.3.2), where the only scaling parameter of the model is the solar wind dynamic pressure.

The magnetosheath coordinates expect a rotational symetry and thus, the angular coordinate is not used. The coordinate τ in magnetosheath coordinates represents the distance from the subsolar point ($\tau = 0$) to a point in the space and it has the same value in both magnetosheath and parabolic coordinate systems [Wikipedia, 2012]. The last coordinate is defined to be equal to 0 at the magnetopause and to 1 at the bow shock. However, the bow shock and magnetopause have different flaring factor λ_{BS} and λ_{MP} and their locations depend on the solar wind dynamic pressure. For this reason, the solar wind dynamic pressure would be considered as another scaling factor. For a given pressure, the coordinate σ can be writen as

$$\sigma \sim \sqrt{r + \lambda x}$$

where the flaring parameter λ changes linearly from the bow shock to the magnetopause being equal to λ_{MP} at the magnetopause and λ_{BS} at the bow shock. Thus σ coordinate can be used as the last coordinate of the magnetosheath coordinate system but, as noted abowe, we use rather the index of this linear dependence that can be writen as

$$X_{MSH} = \frac{R - R_{MP}}{R_{BS} - R_{MP}}$$

which is output of a function described below.

The function "im_msh_position" takes the position of a sounding spacecraft (aberated GSE coordinates) and the solar wind dynamic pressure (data of solar

wind monitor shifted to position of a sounding spacecraft) and returns the position relative to model of the magnetopause and bow shock. We would like to note that although these coordinates are primarly designed for the magnetosheath, they can be extend beyond the magnetopause or bow shock positions.

Description: *x, y, z* are aberated GSE coordinates, *pdyn* is a propagated solar wind dynamic pressure, *tau* is one component of parabolic coordinates, *mshr* is the resulting range where binning of transversal component of relative magnetosheath coordinates is constructed, *resol* controls how many bins would be between the MP and BS.

- Lines 02 and 03 define parameters of the bow shock and magnetopause model.
- Line 04 – 08 convert x, y and z GSE into parabolic coordinates.
- Line 09 defines transversal binning and in fact a resolution of conversion.
- Lines 13 and 14 define the stand-off distance of the bow shock and magnetopause, respectively.
- Lines 15 to 19 provide a linear interpolation of the model between MP and BS and convert interpolated subsolar magnetosheath R into the parabolic σ component (ss_n).
- Line 20 computes all intersections of interpolated magnetosheath lines of constant σ (ss_n) with τ (parabolic coordinate of the position).
- Lines 21 to 24 find the closest intersection of interpolated magnetosheath location with the σ component of parabolic coordinates.

```
01 function im_msh_position,x,y,z,pdyn,tau=tau,mshr=iii,$
     resol=resol
;constants of models
02   r_0bs=15.02 & power_bs=6.55 & lambda_bs=1.17
03   r_0mp=12.82 & power_mp=5.26 & lambda_mp=1.54

;number of bins in MSH
04   if ~ keyword_set(resol) then ni=10 else ni=resol
;converting to the parabolic coordinates
05   r=sqrt(y^2.0+z^2.0+x^2.0)
06   tau=sqrt(r-x)
```

```
07   sig=sqrt(r+x)
08   phi=atan(z,y)

;model position for BS and MP boundaries
09   iii=[-2,2.0*findgen(2*ni+1)/(2*ni)-0.5-1.0/(2*ni),3]
10   nnn=n_elements(pdyn)
11   out=replicate(-10.0,nnn)
12   for i=0L,nnn-1 do begin
13     r_bs=r_0bs*pdyn[i]^(-1.0/power_bs)
14     r_mp=r_0mp*pdyn[i]^(-1.0/power_mp)
15     rr=[r_mp,r_bs]
16     ll=[lambda_mp,lambda_bs]
17     rr_n=interpol(rr,[0.0,1.0],iii)
18     ll_n=interpol(ll,[0.0,1.0],iii)
19     ss_n=sqrt(2*rr_n)
20     sigma_p=sqrt((ss_n^4.0+ss_n^2*tau[i]^2.0)/(ss_n^2.0+ll_n^2*tau[i]^2.0))
21     d_sig=abs(sigma_p-sig[i])
22     min_dsig=min(d_sig)
23     ind=where(d_sig eq min_dsig,cnt)
24     if cnt gt 0 then out[i]=iii[ind[0]]
25   endfor

;rearrangement of output variables
26   out=reform(out)
27   if n_elements(out) eq 1 then out=out[0]
28   iii=iii[1:n_elements(iii)-2]
29   return,out
30 end
```

Appendix B

Data sources

In this Appendix, we present data sources used in this work and brief summarize spacecraft scientific instruments.

As the topic of this thesis is to study processes in the solar wind–magnetosphere coupling, we used data from the spacecraft which orbits cross the magnetopause or bow shock and their instruments were dedicated to measure at least the magnetic field and plasma parameters; these spacecraft are: IMP-8, WIND, GEOTAIL, INTERBALL-I, MAGION-4, CLUSTER and THEMIS.

B.1 THEMIS project

NASA's Time History of Events and Macroscale Interactions during Substorms (THEMIS) aims to determine what physical processes in the near-Earth space initiate the violent eruptions of the aurora that occur during substorms in the Earth's magnetosphere.

The THEMIS project consists of five identical spacecraft which are capable to measure magnetic field, plasma parameters, energetic particles and electric field. Table B.1 summarizes instruments (its parameters) placed onboard of each THEMIS satellite. The project also involves ground stations for the magnetic field measurement and all-sky camera stations for recording visible aurora lightening.

Table B.1: Scientific instrument placed on board of THEMIS spacecraft.

Instrument	Description	
FGM [Auster et al., 2008]	Flux Gate Magnetometer measures the background magnetic field and its low frequency fluctuations in the near-Earth space.	
	range	± 25000 nT
	frequency range:	DC – 64 Hz
	resolution:	3 pT (digitization: 12 pT)
	stability:	<1 nT/yr (0.02 nT/12 hrs)
	noise:	10 pT/$\sqrt{\text{Hz}}$ @ 1 Hz
SCM [Roux et al., 2008]	Search Coil Magnetometer measures low-frequency magnetic field fluctuations and waves in three directions.	
	frequency range:	1 Hz – 4 kHz
	sensitivity:	0.8 pT/$\sqrt{\text{Hz}}$ @ 10 Hz 0.08 pT/$\sqrt{\text{Hz}}$ @ 100 Hz 0.022 pT/$\sqrt{\text{Hz}}$ @ 1 kHz
	dynamic range:	10^{-5}–1 nT/$\sqrt{\text{Hz}}$ [spectra]
ESA [McFadden et al., 2008]	Ion and electron ElectroStatic Analyzers (iESA and eESA) measures 3D particle distribution function of thermal plasma. On-board moments are also calculated and processing includes corrections for the spacecraft potential.	
	energy resolution	i: 5 eV – 25 keV e: 5 eV – 30 keV
	δE/E Inherent:	i: ≈19% e: ≈15% Transmitted: 35% (32 energy steps)
	angular resolution Elev. × Azim.	e: 22.5° × 11.25° i: (5.625° × 5.625° max) typical: 22.5° × 22.5°, 4π str
	eflux, per anode	i: 10^3–10^9 eV/(cm^2 s str eV) e: 10^4–10^{10} eV/(cm^2 s str eV)
SST	Solid State Telescope (SST) measures suprathermal particle distribution functions, namely the number of ions and electrons coming towards the spacecraft from specified directions with specified energies.	
	energy range	i: 25 eV – 6 MeV e: 25 eV – 1 MeV
	energy steps	16 (transmitted)
	angular resolution Elev. × Azim.	inherent: 30° × 11.25° transmitted: 30° × 22.5°
	eflux, per detector	i, e: 0.5–5 10^8 eV/(cm^2 s str eV)

Continued on next page

Table B.1 – THEMIS spacecraft – continued from previous page

Instrument	Description
EFI [Bonnell et al., 2008]	Electric Field Instrument measures the electric fields in three directions. One pair of sensors is deployed to 20 meters, the other pair to 25 meters. Two stiff telescopic booms extend sensors perpendicular to the four spinning cables and along the spacecraft's spin axis.
	frequency range: DC–8 kHz; AKR band: 100–300 kHz
	sensitivity: 10^{-4} mV/m/$\sqrt{\text{Hz}}$ @ 10 Hz
	dynamic range: 10^{-4}–10^{2} mV/m/$\sqrt{\text{Hz}}$ [spectra]
	time series range; resolution: ±300 mV/m; 0.009 mV/m [DC coupled]; ±100 mV/m; 0.003 mV/m [AC coupled]
	noise: $3\,10^{-6}$ mV/m (SpB); $3\,10^{-5}$ mV/m (AxB)
	DC offset error: 0.1 mV/m (SpB); 1 mV/m (AxB)
	antenna lengths: 50 m (12), 40 m (34), 7 m (56) tip-to-tip

B.2 WIND

The WIND spacecraft is the NASA project involved in GGS (Global Geospace Science); it was launched 1. December 1994. A trajectory of WIND was many times changed (see http://cdaweb.gsfc.nasa.gov/istp_public/). Onboard it is placed 8 measuring instruments designated for a detection of charged particles and electric and magnetic field measurements; for our study, we use namely instruments MIF, SWE and 3DP.

Table B.2: Scientific instrument placed onboard of WIND.

Instrument	Description
EPACT [von Rosenvinge et al., 1995]	The Energetic Particles: Acceleration, Composition and Transport investigation is designed to make comprehensive observations of solar, interplanetary, and galactic particles over wide ranges of charge, mass, and intensity using a combination of 8 different particle telescopes. **spices** — **energy range** e^- — 0.2 MeV–10 MeV H^+ — 1.4 MeV–120 MeV He^{++} — 0.04 MeV–500 MeV/nucleon - large collecting capability ideal for observing ^{3}He, ^{4}He; - isotopes measurement from He to Fe
MIF [Lepping et al., 1995]	Magnetic Field Investigation consists of two 3D fluxgate magnetometers dedicated to measure the magnetic field in the wide range with rapid sampling which is suitable to measure fluctuations. range — from ±4 nT to ±65536 nT digital resolution — from ±0.001 nT to ±16.0 nT measurement frequency — 44 vectors/s
SWE [Ogilvie et al., 1995]	Solar Wind Experiment consists of three instruments: Faraday Cup (FC) ion instruments, Vector electron ion spectrometer (VEIS) and Strahl detector. FC — energy/q range — 150 V – 8.0 kV VEIS — energy/q range — 7 V – 24.8 kV analyzer FOV — 7.5° × 6.5° strahl — energy/q range — 5 V – 5 kV analyzer FOV — ≈ 3° × ±30°

Continued on next page

Table B.2 – WIND spacecraft – continued from previous page

Instrument	Description
WAVES [Bougeret et al., 1995]	Waves provides a comprehensive coverage of radio and plasma wave phenomena in the frequency range from a fraction of a Hertz up to about 14 MHz for the electric field and 3 kHz for the magnetic field. The WAVES form three electric dipole antenna systems supplied by Fairchild Space (two are coplanar, orthogonal wire dipole antennas in the spin-plane, the other a rigid spin-axis dipole) and three magnetic search coils mounted orthogonally. FFT - Low Frequency FFT Receiver: low band - 0.3 Hz – 170 Hz; mid band - 7 Hz – 3.5 kHz; high band - 20 Hz – 10 kHz TNR - Thermal Noise Receiver: range 4 kHz - 256 kHz RAD1 - Radio Receiver Band 1: range 20 kHz - 1,040 kHz RAD2 - Radio Receiver Band 2: range 1.075 MHz - 13.825 MHz TDS - Time Domain Sampler: fast: sample rate 120kS/s; slow: sample rate 7.5kS/s
SMS [Gloeckler et al., 1995]	SMS instrument consists of three different sensors: - SWICS measures the mass and charge composition of the solar wind ions from H to Fe over the energy/charge range of 0.5 to 30 keV/q. - MASS measures the elemental and isotopic composition of the solar wind from 0.5 to 12 keV/q with mass resolutions of M/δM ~100. - STICS measures the mass and mass/charge of suprathermal ions. It covers a range of 6 to 223 keV/q in 30 logarithmic steps (1 step per rotation of the spacecraft).
TGRS [Owens et al., 1995]	The Transient Gamma-Ray Spectrometer detects transient gamma-ray burst events and provides high-resolution spectroscopic survey of cosmic gamma-ray bursts, and also make measurements of gamma-ray lines in solar flares. - gamma energy spectrum (15 keV - 10 MeV); - energy resolution 2 keV - 1 MeV ($E/\delta E = 500$).

Continued on next page

Table B.2 – WIND spacecraft – continued from previous page

Instrument	Description
3DP [Lin et al., 1995]	Three-Dimensional Plasma and Energetic Particle Investigation experiment consists of three basic detector systems: - electron electrostatic analyzers (EESA) - ion electrostatic analyzers (PESA) - semiconductor telescopes (SST) Each of these is designed to cover a different part of the suprathermal particle population.
KONUS [Aptekar et al., 1995]	KONUS experiment provides omnidirectional and continuous coverage of the sky in the hard X- and gamma-ray domain. - measurement of X-ray in range 10 keV - 10 MeV; - continuous measurement of gama and X background; - high temporal resolution in X spectra during solar flare.

EESA	energy range	3 eV – 30 keV
PESA	energy range	3 eV – 30 keV
SST	Foil F	species - electrons energy range - 25 eV to 400 keV
	Magnetic O	species - protons energy range - 20 keV to 6 MeV
	Telescope FT	species - electrons energy range - 400 keV to 1 MeV
	Telescope OT	species - protons energy range - 6 MeV to 11 MeV

B.3 ACE

The Advanced Composition Explorer (ACE) [Stone et al., 1998b] spacecraft carries six high-resolution sensors and three monitoring instruments sample low-energy particles of solar origin and high-energy galactic particles at orbits of the L1 libration point which is a point of Earth-Sun gravitational equilibrium.

ACE provides a continuous coverage of solar wind parameters and solar energetic particle intensities (space weather). When reporting Space Weather, ACE provides an advance warning (about one hour) of geomagnetic storms that can overload power grids, disrupt communications on Earth, and present a hazard to astronauts.

Table B.3: Scientific instrument placed on board of ACE spacecraft.

Instrument	Description
CRIS	The Cosmic Ray Isotope Spectrometer (CRIS) is intended to ascertaining the isotopic composition of the cosmic rays and hence determining their origin. The heavier nuclei (1% of interstellar medium composition) provide information about cosmic-ray origin through their elemental and isotopic composition. CRIS is designed to have high collection power (≈250 cm^2 sr) while still maintaining excellent isotopic resolution up through Z=30 (Zinc) and beyond.
MAG [Smith et al., 1998]	MAG is twin, triaxial fluxgate magnetometers (boom mounted) range: from ±4 nT to ±65536 nT digital resolution: from ±0.001 nT to ±16.0 nT measurement frequency: 3,4 or 6 vectors/s; 24 vectors/s in snapshot memory noise level: < 0.006 nT RMS. @ 0-10 Hz
EPAM [Gold et al., 1998]	Electron, Proton, and Alpha Monitor (EPAM) particle instrument is composed of five telescope apertures of three different types. Two Low Energy Foil Spectrometers (LEFS) measure the flux and direction of electrons above 30 keV, two Low Energy Magnetic Spectrometers (LEMS) measure the flux and direction of ions greater than 50 keV, and the Composition Aperture (CA) measures the elemental composition of the ions.
SEPICA [Möbius et al., 1998b]	The Solar Energetic Particle Ionic Charge Analyzer determines the ionic charge states of solar and interplanetary energetic particles. The charge state of energetic ions is key data needed to determine source temperatures, acceleration, fractionation, and transport processes for these particle populations. 0.3 – 6 MeV/N (He): isotopic: He 0.2 – 18 MeV/N (O): individual elements: up to O 0.1 – 5.4 MeV/N (Fe): groups, $\delta Z/Z$ approximately equals 2-3: up to Fe
SIS [Stone et al., 1998a]	The Solar Isotope Spectrometer is designed to provide high-resolution measurements of the isotopic composition of energetic nuclei from He to Ni (Z=2 to 28) over the energy range from ≈ 10 to ≈ 100 MeV/nucleon.

Continued on next page

Table B.3 – ACE spacecraft – continued from previous page

Instrument	Description
SWEPAM [McComas et al., 1998]	The Solar Wind Electron, Proton, and Alpha Monitor (SWEPAM) measures the solar wind plasma electron and ion fluxes (rates of particle flow) as functions of direction and energy. These data provide detailed knowledge of the solar wind conditions and internal state every minute. SWEPAM also provides real-time solar wind observations which are continuously telemetred to the ground for Space Weather purposes.
SWICS [Möbius et al., 1998b]	The Solar Wind Ion Composition Spectrometer (SWICS) is optimized for measurements of the chemical and isotopic compositions of solar and interstellar matter. The instrument is time-of-flight mass spectrometer with electrostatic analyzers and determines the chemical and ionic charge state composition of the solar wind and resolves H and He isotopes of both solar and interstellar sources.
SWIMS [Möbius et al., 1998b]	The Solar Wind Ion Mass Spectrometer (SWIMS) instruments is similar to SWICS, however, is optimized for measurement of the chemical and isotopic compositions of the solar wind for every element between He and Ni, up to 10 keV/nucleon.
ULEIS [Mason et al., 1998]	The Ultra Low Energy Isotope Spectrometer (ULEIS) measures ion fluxes over the charge range from He through Ni from about 20 keV/nucleon to 10 MeV/nucleon, thus covering both suprathermal and energetic particle energy ranges.

B.4 GEOTAIL

The GEOTAIL spacecraft is a collaborative project undertaken by the Institute of Space and Astronautical Science (ISAS), Japan Aerospace Exploration Agency (JAXA), and the National Aeronautics and Space Administration (NASA). The Geotail spacecraft was designed and built by ISAS and was launched on July 24, 1992. After fulfilling its original objective of studying the dynamics of the Earth's magnetotail over a wide range of distance, extending from the near-Earth region ($\approx$ 8 R_E) from the Earth) to the distant tail (about 200 R_E), its orbit was changed. Since February 1995, Geotail has been in an elliptical 9 by 30 R_E orbit where it has provided data on most aspects of the solar wind interaction with the magnetosphere.

Table B.4: Scientific instrument placed on board of GEOTAIL spacecraft.

Instrument	Description
CPI [Frank et al., 1994]	The Comprehensive Plasma Instrumentation observes the 3D velocity distributions of electrons and ions. Three sets of analyzers are employed to provide resolution of particle energies, directions, and Mass/Charge composition. - The Solar Wind analyzer (CPI- SW) measures ions with energies/charge 150 V to 7 kV with high-resolution of directions to characterize the plasma of the solar wind. - The Hot Plasma analyzer (CPI-HP) provides 3D coverage of electrons and ions with energies/charge 1 V - 50 kV to cover distributions typical in the magnetosphere. - The Ion Composition analyzer (CPI-IC) includes five miniature imaging mass spectrometers at the exit aperture of the analyzer for discrimination of ion Mass/Charge.
EPIC [Jacquey et al., 1994]	Energetic Particles and Ion Composition investigation is to explore the outer magnetosphere and the distant magnetotail region. The instrument contains two main sensor heads. - The STICS assembly (Supra-Thermal Ion Composition Spectrometer) uses a quadrispherical electrostatic analyzer followed by a foil/solid state detector time-of-flight (TOF) telescope to measure charge state, mass and energy of ions with energies of 10 - 230 keV/q. - The ICS assembly (Ion Composition Subsystem) measures the mass and energy of energetic ions with energies of less than 50 keV to 3 MeV. It uses a pair of collimators with sweeping magnets to reject electrons, followed by TOF and energy analysis. A thin foil/solid state electron telescope measures electrons higher than 30 keV. Directional measurements with a time resolution < 3 s for all species are possible.

Continued on next page

Table B.4 – GEOTAIL spacecraft – continued from previous page

Instrument	Description
MGF [Kokubun et al., 1994]	The MGF experiment consists of dual three-axis fluxgate magnetometers and a three-axis search coil magnetometer. The fluxgate magnetometers are of standard design and consist of an amplifier, filter, phase sensitive detector, integrator, and a voltage-current converter. dynamic range: 7 ranges; from ±16 nT to ±65536 nT digital resolution: 15-bit A/D conversion; from ±1 pT to ±4 nT measurement frequency: 16 vectors/s The search coil magnetometer system consists of three sensors, preamplifier, amplifier, filter, multiplexer, and an A/D converter. The search coil magnetometers operate in a frequency range of 0.5 kHz to 1 kHz, and supply 128 vectors/sec. The fluxgate magnetometer operates in both real time and record modes, while the search coil data are used only in real time mode.
PWI [Matsumoto et al., 1994]	The Plasma Waves Instrument measures electric fields over the range 5.6 Hz to 800kHz, and magnetic fields over the range 5.6 Hz to 12.5 kHz. Triaxial magnetic search coils are utilized in addition to two sets of electric dipole antennas. The instrument contains: - the sweep-frequency analyzer (SFA) (24 Hz to 800 kHz for the electric field and 24 Hz to 12.5 kHz for the magnetic field), - the multichannel analyzer (MCA) (5.6 Hz to 311 kHz for the electric field and 5.6 Hz to 10 kHz for the magnetic field) - wideband waveform capture receiver (WFC)(10 Hz to 4 kHz).

Continued on next page

Table B.4 – GEOTAIL spacecraft – continued from previous page

Instrument	Description
LEP [Mukai et al., 1994]	LEP consists from three instrument the Energy Analyzer for electrons (EA-e), the Energy Analyzer for ions (EA-i), and the Solar Wind analyzer (SW). - LEP-EA measures 3D velocity distributions of hot plasmas in the magnetosphere. EA consists of two nested sets of quadrispherical electrostatic analyzers. LEP-SW measures 3D velocity distributions of solar wind ions in the energy range from 0.3 keV/Q to 8 keV/Q with a 270° spherical electrostatic analyzer with a FOV of 5° × 60°. - (EA-e) measures electrons in the energy range from 60 eV to 38 keV (or, 8 eV to 8 keV in the other mode). - (EA-i) measures positive ions from 32 eV/Q to 39 keV/Q (or, 5 keV/Q to 43 keV/Q in the solar wind region). The field of view for each quadrispherical analyzer with FOV 10° × 145°.
EFD [Tsuruda et al., 1994]	The Electric Field Detector antenna part consists of two orthogonal double probes. One of the pairs (PANT) has spherical probes at the tips of the antennas for the constant photoelectron emission. The other (WANT) has smaller masses at the tips. The separation distances between the pair of sensors are 100 m tip-to-tip. The electric field is measured in the spin plane which is nearly parallel to the ecliptic plane.

Continued on next page

Table B.4 – GEOTAIL spacecraft – continued from previous page

Instrument	Description
HEP Doke et al. [1994]	There are five instruments that make up this investigation: Low-energy particle Detector (LD), Burst Detector (BD), Medium-energy Isotope detectors (MI-1 and MI-2), and High energy Isotope detector (HI). LD and BD are mainly dedicated to magnetospheric studies. MI and HI concentrate on solar flare and cosmic ray studies. - The LD sensor consists of three time-of-flight/energy detectors, and covers 180 degrees in polar angle over the energy range: energy range – elements 20–300 keV – e^- 2 keV–1.5 MeV – p^+ 2 keV–1.5 MeV/q – Ions - The BD sensor consists of three delta-E x E telescopes which identify particles by their energy loss and residual energy: energy range – elements 0.12–2.5 MeV – e^- 0.7–35 MeV – p^+ 0.7–140 MeV – He - The MI and HI instruments are all silicon semiconductor detector telescopes utilizing the well-known dE/dx x E algorithm for isotope identification: mass and nuclear charge. – The MI instrument measures elemental and isotopic compositions of solar energetic particles and energetic particles in the heliosphere with $2 < Z < 28$ in the 2.4–80 MeV/nucleon energy range, and measures the elemental composition of solar energetic particles heavier than iron. – The HI instrument also measures elemental and isotopic compositions of solar energetic particles and galactic cosmic rays with $2 < Z < 28$ in the 10–210 MeV/nucleon energy range.

B.5 IMP 8

IMP-8 (IMP-J) was launched by NASA on October 26, 1973 to measure the magnetic field, plasma, and energetic charged particles (e.g., cosmic rays) of the Earth's

magnetotail and magnetosheath and of the near-Earth solar wind. IMP-8, the last of ten IMP (Interplanetary Monitoring Platform) or AIMP (Anchored-IMP) spacecraft launched in 10 years, operated for 33 years in its near-circular, 35 Earth Radii, 12-day orbit. It was an important adjunct to the International Solar Terrestrial Physics program, provided in-ecliptic, one Astronomical Unit baseline data for the deep space Voyager and Ulysses missions, and accumulated a long-timeseries database useful in understanding long-term solar processes. Last available data are for October 7, 2006.

Table B.5: Scientific instrument placed onboard of the IMP 8 spacecraft.

Instrument	Description
MFE	The Magnetic Field Experiment is a triaxial fluxgate magnetometer designed to study the interplanetary and geomagnetic tail magnetic fields. dynamic range: from ±12 nT to ±108 nT digital resolution: 0.3 for ±36 nT measurement frequency: 25 vectors/s The magnetometer failed June 10, 2000.
SPCF	Solar Plasma Faraday Cup A modulated split-collector Faraday cup, perpendicular to the spacecraft spin axis, was used to study the directional intensity of positive ions and electrons. energy range: e: 17 – 7 keV; i: 50 – 7 keV angular resolution: 24° A spectrum was obtained every eight spacecraft revolutions. Angular information was obtained in either 15 equally spaced intervals during a 360-deg revolution of the satellite or in 15 angular segments centered more closely about the spacecraft-sun line. Operations were continuing as of August 2005.
SPEA [Feldman et al., 1975]	Solar Plasma Electrostatic Analyzer is a hemispherical electrostatic analyzer that measures the directional intensity of positive ions and electrons in the solar wind, magnetosheath, and magnetotail. Ions as heavy as oxygen were resolved when the solar wind temperature was low. No data were obtained from this experiment past October 2001.

Continued on next page

Table B.5 – IMP 8 spacecraft – continued from previous page

Instrument	Description
EWRN	Electrostatic Waves and Radio Noise A wide-band receiver was used to observe high-resolution frequency-time spectra, and a six-channel narrow-band receiver with a variable center frequency was used to observe wave characteristics. The frequency range for electric fields was 0.3 Hz to 200 kHz, and for magnetic fields it was 20 Hz to 200 kHz.
LEPE [Frank et al., 1976]	Measurement of Low-Energy Protons and Electrons (LEPE) the detector was a dual-channel, curved-plate electrostatic analyzer energy range: 5 eV –d 50 keV angular FOV: $9° \times 25°$ energy levels: 16 mode 1: 16 ang. sect. per 272 s mode 2: 4 ang. sect. per 68 s
SSD	Solid-State Detectors (SSD) was designed to determine the composition and energy spectra of low-energy particles observed during solar flares and 27-d recurrent events. The detectors included (1) an electrostatic analyzer (to select particles of the desired energy per charge) combined with an array of windowless solid-state detectors (to measure the energy loss) and surrounded by an anticoincidence shield, and (2) a thin-window proportional counter, solid-state particle telescope. energy/charge range: 0.1 – 10 MeV/q; elements: e^-, e^+ and Ions (for $1 < Z < 8$ with charge resol.) Two 1000-channel pulse-height analyzers, one for each detector, were included in the experiment payload.

Continued on next page

Table B.5 – IMP 8 spacecraft – continued from previous page

Instrument	Description
CPME [Armstrong et al., 1978]	Charged Particle Measurements Experiment (CPME) was three solid-state detectors in an anticoincidence plastic scintillator observed particles in the energy range: energy range: 0.2 – 2.5 MeV; elements: e^- energy range: 0.3 – 500 MeV; elements: p^+ energy range: up to 8 MeV/q; elements: $2 \leq Z \leq 5$ energy range: up to 32 MeV/q; elements: $6 \leq Z \leq 8$ energy range: 50 MeV/nucleon; elements: $\Sigma(p^+ + \alpha)$ Five thin-window Geiger-Mueller tubes observed: energy range: $>$ 15 keV; elements: e^- energy range: $>$ 250 keV; elements: p^+ energy range: 2 – 10 Å; elements: X-rays
GSFC [Teegarden et al., 1975]	Solar and Cosmic-Ray Particles instrument was designed to measure energy spectra, composition, and angular distributions of solar and galactic electrons, protons, and heavier nuclei up to Z=30. Three distinct detector systems were used. (1) pair of solid-state telescopes that measured integral fluxes elements: e^-; energy treshold: 150, 350 and 700 keV elements: p^+; energy treshold: 0.05, 0.15, 0.50, 0.70, 1.0, 1.2, 2.0, 2.5, 5.0, 15, and 25 MeV (2) solid-state dE/dx vs E telescope that looked perpendicular to the spin axis. This telescope measured Z=1 to 16 nuclei with energies between 4 and 20 MeV/nucleon. (3)three-element telescope whose axis made an angle of 39 deg with respect to the spin axis. The middle element was a CsI scintillator, while the other two elements were solid-state sensors. The instrument responded to electrons between 2 and 12 MeV and to Z=1 to 30 nuclei in the energy range 20 to 500 MeV/nucleon.

Continued on next page

Table B.5 – IMP 8 spacecraft – continued from previous page

Instrument	Description
CRNC	This experiment used two telescopes to measure the composition and energy spectra of solar (and galactic) particles above about 0.5 MeV/nucleon. The main telescope consisted of five collinear elements (three solid state, one CsI, and one sapphire Cerenkov) surrounded by a plastic anticoincidence shield. The telescope had a 60-deg, full-angle acceptance cone with its axis approximately normal to the spacecraft spin axis, permitting eight-sectored information on particle arrival direction. The low-energy telescope was essentially a two-element shielded solid-state detector with a 70-deg full-angle acceptance cone. The first element was pulse-height analyzed, and data were recorded by sectors.
EHHI [Mewaldt et al., 1976]	Electrons and Hydrogen and Helium Isotopes experiment was designed to measure the differential energy spectra energy range – elements 2 – 40 MeV/nucleon – Isotopes (from H to O) 0.5 – 5 MeV – e^- The instrument consisted of a stack of 11 fully depleted silicon solid-state detectors surrounded by a plastic scintillator anticoincidence cup.

Continued on next page

Table B.5 – IMP 8 spacecraft – continued from previous page

Instrument	Description
EEP [Williams, 1977]	The purposes of Energetic Electrons and Protons investigation were (1) to study the propagation characteristics of solar cosmic rays through the interplanetary medium over the energy ranges indicated below, (2) to study electron and proton fluxes throughout the geomagnetic tail and near the flanks of the magnetosphere, and (3) to study the entry of solar cosmic rays into the magnetosphere. The instrumentation consisted of a three-element telescope employing fully depleted surface-barrier solid-state detectors and a magnet to deflect electrons. Two additional detectors in separate mounts were used to measure energy range: elements (F) > 15 keV: charged particles (G1) > 0.6 MeV: $Z \geq 2$ (G2) > 2.0 MeV: $Z \geq 2$ (G3) > 2.0 MeV: $Z \geq 3$ 0.5 – 5 MeV: e^- The telescope measured: energy range / chan. num. / elements 2.1 – 25 MeV / 3 / p^+ 0.05 – 2.1 MeV / 3 / $Z \geq 1$ 8.4 – 35.0 MeV / 2 / α 30 – 200 keV / 2 / deflected e^-

B.6 INTERBALL project

The INTERBALL project Galeev et al. [1996] was dedicated to the detailed study of a wide range of plasma processes arise as a result of interaction of the solar wind with the Earth's magnetosphere. The project was conceived as a four-satellite mission of two closely spaced pairs of the spacecraft on different high-altitude orbits. The spacecraft were placed on orbits with different apogee:

- pair of "Tail" satellites (Interball-1 + Magion 4) $\sim$ 200.000 km
- pair of "Auroral" satellites (Interball-2 + Magion 5) $\sim$ 20.000 km

Inclinations for both pairs were 62.8°. The spacecraft were spin stabilized (one spin lasts $\approx$ 120 s) when the spin axis was positioned to point to the Sun.

The Tail spacecraft had such a orbit that covers many regions such cusps (in different locations), the subsolar and tail magnetopause and bow shock, the neutral region and another.

INTERBALL-1

Spacecraft included many scientific instrument to measure thermal and cold plasma, waves, energetic particles, electric and magnetic fields, particle compositions, etc. Table B.6 lists a brief overview of instrumental payloads (for more detailed description see Galeev et al. [1996]).

Table B.6: Scientific instruments placed onboard of the INTERBALL-1 spacecraft.

Instrument	Description
SKA-1	Measurements of three-dimensional distribution of ions in the energy range 50-5000 eV/q. Measurements of energy spectra of ions with M/Q selection (M=1,2,4,16) in the energy range 5-40 keV/q in the antisolar direction.
ELECTRON [Yermolaev et al., 1997]	This instrument was based on hemispheric electrostatic analyser for measurements of a 3D energetic distribution of electrons. It consisted of a window aperture ($180^o \times 6^o$), hemispheric electrostatic analyser and microchannel plate detector (8 segments) energy resolution: 10 eV – 25 keV energy steps: 2,4,16 or 32 angular resolution Elev. × Azim.: 22.5° × 6° During one spin, it was possible to obtain 16 or 32 spectra.
PROMICS-3	Measurements of composition of charged particles in the range $1 \leq Z \leq 32$ and 3D energetic distribution in range 0.01–30 keV/q
VDP [Safrankova et al., 1995]	Fast measurements of integral ion flux vector or an integral energetic spectrum of ions and electrons. The instrument consists of six identical Faraday cup detectors with an input angular aperture of 134°. The Faraday cup has five grid when two were used to select electrons or ions and one to change energy threshold of integral spectra (0.2 – 2.4 keV).
AMEI-2	Energy spectra of H^+, He^+, He^{++}, O^+ and heavier ion in the range 0.1-8 keV/q at all directions.
MONITOR-3	Measurements of the solar wind ion fluxes and energy-angular distributions of H^+ and He^{++} around the Sun direction with high-time resolution.

Continued on next page

Table B.6 – INTERBALL-1 spacecraft – continued from previous page

Instrument	Description
CORALL [Yermolaev et al., 1997]	The CORALL instrument measured 3D ion energy distribution function and its scientific goal was (1) to investigate dissipative and transport processes and processes accelerating ions; (2) to provide measurements of presence of magnetospheric ions, especially in plasma layer and in the tail and measurements of dynamics of accelerated plasma. The instrument consisted of an input window (5° × 110°), hemispheric electrostatic analyser and collector divided into five parts for angular resolution. energy resolution: 30 eV – 24 keV angular resolution: 6° × 24° number of channel: 32 temporal resolution: one spectra snapshot 4 s
ALPHA-3	Thermal plasma ion flux E < 25 eV/q.
SKA-2	Charged energetic particles (E_e = 40 – 200 keV; E_i = 0.05 – 150 keV) composition and anisotropy.
DOK-2	Energy spectra, angular distributions and time variations of electrons (E_e = 15 - 400 keV) and ions (E_i = 20 - 1000 keV).
RF-15-1	Solar X-ray burst spectra and time profile measurements in the range 2–240 keV and tomography imaging of solar flares in the range 2–8 keV.
SOSNA-2	Dosimetric measurements.
RKI-2	Ionizing radiation (5,15,40,100,500 MeV) and UV radiation from the Sun.
OPERA	Measurement of three components of fluctuations of the electric field in the frequency range of 0 – 50 kHz.
MIF-M	Fluxgate 3-axe compensation magnetometer dynamic range: DC: 0,3 – 37,5 nT; AC: 0,005 – 30 nT frequency band: DC: 0 – 2 Hz; AC: 2 – 25 Hz
IFPE	Measurement of ion and electron flux fluctuations in the range of 0.1Hz – 1kHz.
FGM-I	3D magnetic field detector; temporal resolution 0 - 25 Hz in the range 0.25-256 nT.
KEM-3	Measurement of the electric field (0.1 Hz – 400 kHz), the magnetic field (1 – 50 kHz) and two components of the electric current (0.1 Hz – 40 kHz).

Continued on next page

Table B.6 – INTERBALL-1 spacecraft – continued from previous page

Instrument	Description
FM-3I	Magnetic field measurements onboard the Interball Tail spacecraft were carried out by the FM-3I instrument which consists of two flux-gate magnetometers covering two different ranges: ±200 nT and ±1000 nT in frequency band 0 - 0.1 Hz. Besides scientific goals, the FM-3I experiment data was used to perform the attitude control of the Interball Tail spacecraft.
AKR-X	Radioemission in the range 100 kHz - 1.5 MHz.

MAGION-4

MAGION-4 was a sub-satellite (weight 50 kg) of the INTERBALL-1 main spacecraft (1000 kg) and it was placed on the same orbit as the main satellite but with time delay between each other. This delay was several times changed to observe different regions or boundaries with different temporal distance. Because MAGION-4 was a part of the multisatellite project and had limited weight, it contained similar, however, simplified type of instruments as the main satellite.

Table B.7: Scientific instruments placed on board of the MAGION-4 spacecraft.

Instrument	Description
KEM-3	Measurements of parameters of the electromagnetic field in the frequency band of VLF and ULF. Measurements of one component of the electric field and three components of the magnetic field (E_x = 0.1 Hz - 400 kHz; B_x = 1.0 kHz - 50 kHz; $B_{x,y,z}$ = 1.0 Hz - 2 kHz).
SG-R8	Fluxgate triaxial magnetometer (dynamic range ±128, ±1024, ±8196 a ±65536 nT).
DOK-S	Solid state detector measured energy spectra, angular distributions and time variations of electrons (E_e = 20 - 180 keV) and ions (E_i = 20 - 1300 keV).

Continued on next page

Table B.7 – MAGION-4 spacecraft – continued from previous page

Instrument	Description
MPS, SPS	These instruments were as a counter-part of CORAL and ELECTRON instruments placed on the INTERBALL-1 spacecraft. MPS consisted of two identical cylindrical electrostatic energetic analyzers of ions. They were designed to measure the solar wind and to detect charged particles reflected by the bow shock. MPS collected data only from narrow angle ($\approx 5°$) from sunward and anti-sunward directions. SPS included two hemispheric electrostatic analysers with segmented collectors, one for electrons with two channels parallel to spin axes and one for ions with three channels. energy resolution: SW mode: 0.04 – 5 keV; MS mode: 0.2 – 25 keV # of energy steps: 16 temporal resolution: 12.8 s/spectra angular resolution: MPS: $4° \times 4°$; SPS e: $4° \times 67°$; SPS i: $4° \times 45°$
VDP-S	The VDP-S instrument was designed for determination of the integral flux vector of ions and electrons with energies above 170 eV. The instrument consists of four identical Faraday cups with an input angular aperture of 100°. Depending on the telemetry mode, the sampling frequency was 1, 2, 4 or 8 Hz.
RF	The X-ray photometer was dedicated to measure the solar X-ray radiation in the soft spectral range. The output signal of the detector was passed to the two-channel amplitude analyzer where it is selected in two ranges: 10–15 keV and 15–60 keV. The maximum capacity of the detector is 183441 imp/0.8 sec.
ULF	The ULF instrument was designed for the magnetic field (3 components) and electric fields (one component) in the ULF frequency band. dynamic range: -76 dB – +30 dB number of analyzed components: 4
SAS	The SAS instrument consisted of two SFA analyzers, time transformer and analog telemetry unit. The instrument was designed as the well-known step-frequency analyzer with two intermediate frequencies: 465 kHz and 5 kHz.

Continued on next page

Table B.7 – MAGION-4 spacecraft – continued from previous page

Instrument	Description	
KM-14	Measurements of density and temperature of cold plasma.	
	electron temperature	1,000 - 60,000 K
	ion density	$> 10^7\ m^{-3}$ (for velocity ≈ 3 km/s) $< 5 \cdot 10^{12}\ m^{-3}$ (for velocity ≈ 8 km/s)

B.7 Cluster

The current mission, Cluster II is a collection of four spacecraft flying in a tetrahedral configuration and named Samba, Tango, Rumba, and Salsa. They investigate the small-scale structures of the Earth's plasma environment, such as those involved in the interaction between the solar wind and the magnetospheric plasma, in global magnetotail dynamics, in cross-tail currents, and in the formation and dynamics of the neutral line and plasmoids.

The four spacecraft have been collected the most detailed data on small-scale changes in the near-Earth space and the interaction between the charged particles of the solar wind and Earth's magnetosphere. This enables scientists to build a three-dimensional model of the magnetosphere and to better understand the processes taking place inside it. The Cluster mission control centre is located at ESOC, Darmstadt, Germany.

Each of four spacecraft carries an identical set of 11 instruments to investigate charged particles, electrical and magnetic fields. These were built by European and American teams led by Principal Investigators.

Table B.8: Scientific instruments placed onboard of CLUSTER II spacecraft.

Instrument	Description	
FGM	Fluxgate Magnetometer	
	range	from ± 64 to ± 65536 nT
	resolution	7.5 pT
	offset drift	<0.03 nT/° (temperature range $-35°C$ to $25°C$)
	noise	<10 pT/$\sqrt{\text{Hz}}$ @ 1 Hz

Continued on next page

Table B.8 – CLUSTER II spacecraft – continued from previous page

Instrument	Description
EDI [Paschmann et al., 2001]	Electron Drift Instrument measures the displacement of a weak (¡ 1 μA, 1.0 or 0.5 keV) beam of test electrons, after one gyration in the ambient magnetic field that is induced by electric fields or magnetic gradients. This displacement (the drift step) causes the beam to return to a detector on the spacecraft only when emitted in one of two precisely determined directions. By employing two beams and two detectors, these directions can be monitored continuously and the displacement obtained by triangulation.
ASPOC [Szita et al., 2001]	Active Spacecraft Potential Control experiment. A problem with accurate measurements of charged particles and electric fields in space is electrical charging of the spacecraft. This charging is created by ultraviolet radiation from the Sun that knocks off electrons from the surface of the spacecraft. A solution to this problem is the active emission of positive charges through a beam of high-energy ions. The objective of the ASPOC (Active Spacecraft Potential Control) instrument is to investigate this ion beam and its interaction with the surrounding particles, connected with the reduction efficiency of the spacecraft charge to acceptable levels.
STAFF	Spatio-Temporal Analysis of Field Fluctuation experiment Magnetic field B magnitude and direction of EM fluctuations, cross-correlation of E and B
EFW	Electric Field and Wave experiment Electric field E magnitude and direction E vector, spacecraft potential, electron density and temperature
WHISPER	Waves of High frequency and Sounder for Probing of Electron density by Relaxation experiment Electric field E spectrogram of terrestrial plasma waves and radio emissions in the 2–80 kHz range; triggering of plasma resonances by an active sounder. Source location of waves by triangulation; electron density within the range 0.2–80 cm^{-3}

Continued on next page

Table B.8 – CLUSTER II spacecraft – continued from previous page

Instrument	Description
WBD	Wide Band Data instrument As part of the Cluster Wave Experiment Consortium (WEC), the Wideband (WBD) Plasma Wave Investigation is designed to provide high-resolution measurements of both electric (two electric-field components Ey, Ez) and magnetic (two magnetic-field components Bx,By) fields in selected frequency bands from 25 Hz to 577 kHz. Continuous waveforms are digitized and transmitted in either a 220 kbit/s real-time mode or a 73 kbit/s burst mode. The real-time data are received directly by a NASA Deep-Space Network (DSN) receiving station, and the burst-mode data are transferred to the spacecraft solid-state recorder for later playback.
PEACE [Johnstone et al., 1997]	PEACE is a top-hat electrostatic electron analyser. It is designed to measure the 3D electron velocity distribution in the energy range 0.7 eV to 32 keV in the vicinity of the Cluster spacecraft.
CIS [Möbius et al., 1998a]	The Cluster Ion Spectrometer (CIS) is a comprehensive ionic plasma spectrometry package onboard the four Cluster spacecraft, capable of obtaining full three-dimensional ion distributions with one spin (4 second) time resolution and with mass-per-charge composition determination. The CIS package consists of two different instruments, the time-of-flight ion Composition Distribution Function analyzer (CODIF, CIS-1), and the Hot Ion Analyzer (HIA, CIS-2). energy range per charge: 15 – 40000 keV/e δE/E: ≈ 0.13 angular resolution Elev. × Azim.: $22.5° \times 11.25°$, 4π str
RAPID [Wilken et al., 1997]	The RAPID spectrometer for the Cluster mission is an advanced particle detector for the analysis of suprathermal plasma distributions in the energy range: e^-: 20 – 400 keV p^+: 40 – 1500 keV heavier ions: 10 – 1500 keV/nuc

Appendix C

Attached articles

C.1 IMF cone angle control of the magnetopause location: Statistical study

GEOPHYSICAL RESEARCH LETTERS, VOL. 37, L19103, doi:10.1029/2010GL044965, 2010

IMF cone angle control of the magnetopause location: Statistical study

Š. Dušík,[1] G. Granko,[1] J. Šafránková,[1] Z. Němeček,[1] and K. Jelínek[1]

Received 2 August 2010; revised 31 August 2010; accepted 1 September 2010; published 9 October 2010.

[1] We investigate the dependence of the magnetopause location on the interplanetary magnetic field (IMF) cone angle (the angle between the IMF and solar wind velocity vectors) in a statistical study based on ≈6500 magnetopause crossings observed by the five THEMIS spacecraft, both at the dayside and flanks. To remove other well-known effects, we analyze the difference between observed magnetopause radial distances and those predicted by an empirical magnetopause model (scalable by the solar wind dynamic pressure and IMF B_Z component). The results demonstrate a systematic increase of the magnetopause distance for radial IMF directions, from ≈0.3 R_E at 90° to ≈1.7 R_E at 0° or 180° cone angle. Moreover, a stronger dependence of the magnetopause location on the solar wind dynamic pressure than predicted by the current models was observed. **Citation:** Dušík, Š., G. Granko, J. Šafránková, Z. Němeček, and K. Jelínek (2010), IMF cone angle control of the magnetopause location: Statistical study, *Geophys. Res. Lett.*, *37*, L19103, doi:10.1029/2010GL044965.

1. Introduction

[2] The magnetopause is a layer/region determined by the pressure balance between the total pressure on the magnetosheath side and the magnetic pressure on the magnetospheric side. A strong dependence of the magnetopause shape and location on the solar wind dynamic pressure was established and also the dependence on the strength and orientation of the interplanetary magnetic field (IMF) has been noted by *Aubry et al.* [1970].

[3] During following years, many quantitative empirical models of the magnetopause location and its shape under various solar wind conditions have been developed based on *in situ* satellite measurements [e.g., *Fairfield*, 1971; *Sibeck et al.*, 1991; *Roelof and Sibeck*, 1993; *Petrinec and Russell*, 1996; *Shue et al.*, 1997, 1998].

[4] For the shape of the near-Earth high-latitude magnetopause, *Boardsen et al.* [2000] prepared an empirical model which is parameterized by the solar wind dynamic pressure, IMF B_Z, and dipole tilt angle in a limited range of the X_{GSE} coordinate and found that the dipole tilt angle and solar wind dynamic pressure are the most significant factors influencing the shape of the high-latitude magnetopause, whereas the IMF B_Z dependence is separable only when the effects of the pressure and dipole tilt angle are removed. Moreover, these authors have shown that the low-latitude subsolar magnetopause is a function of the tilt angle and that this dependence becomes weaker towards the flanks. The cusp magnetopause indentation was suggested by a number of the authors [e.g., *Petrinec and Russell*, 1995; *Sotirelis and Meng*, 1999; *Eastman et al.*, 2000] and its deepness and location were associated with the dipole tilt angle [*Šafránková et al.*, 2002, 2005; *Lin et al.*, 2010]. On the other hand, the presence of this indentation was questioned in several papers [e.g., *Zhou and Russell*, 1997; *Lavraud et al.*, 2004].

[5] *Fairfield et al.* [1990] indicated that a radial IMF orientation may be an alternative dominant factor which can cause the magnetopause expansion in the subsolar region. They supposed that foreshock pressure fluctuations convect through the subsolar bow shock into the magnetosheath and influence the subsolar magnetopause location. The position of the foreshock behind the bow shock is controlled by the θ_{BN} angle (the angle between the IMF and local normal to the bow shock). In the subsolar region, this angle coincides with the angle between the IMF vector and the Earth-Sun line. In the case of a radial IMF, the foreshock is located upstream of the subsolar quasiparallel bow shock. Under this condition, *Merka et al.* [2003] reported larger amplitude magnetopause oscillations occurring during intervals of quasi-radial IMF. Also the case studies by *Suvorova et al.* [2010] and *Jelínek et al.* [2010] mentioned an unusual location of the magnetopause caused by the radial IMF. Thus, our short statistical study is devoted to an average magnetopause location through intervals of the IMF aligned with solar wind velocity. To distinguish between the influence of the IMF cone angle (the angle between solar wind velocity and IMF vectors) and the θ_{BN} angle (the angle between the IMF vector and the vector of the normal to the bow shock just upstream of a particular magnetopause crossing), the analysis is carried out for the subsolar and flank magnetopauses separately. The investigation is based on the five-spacecraft THEMIS mission [*Angelopoulos*, 2008] that yields the opportunity to identify many magnetopause crossings being registered by the same instruments with the same solar wind monitor.

2. Data Set and Methodology

[6] All five THEMIS probes were launched on 17 February 2007 into very similar elliptical and near-equatorial orbits. Our analysis uses magnetopause crossings identified by a visual inspection of the plots containing plasma moments, ion, and electron spectra [*McFadden et al.*, 2008], and magnetic field data [*Auster et al.*, 2008] with the best available time resolution. The inspected periods were June–August and November 2007 and May–August 2008; altogether we collected 6649 magnetopause crossings for which the upstream data were available. Many of these crossings

[1]Faculty of Mathematics and Physics, Charles University, Prague, Czech Republic.

0094-8276/10/2010GL044965

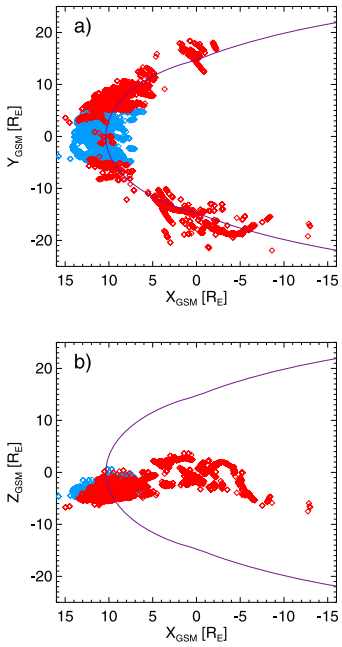

Figure 1. A projection of the observed THEMIS magnetopause crossings onto the (a) *XY* and (b) *XZ* GSM planes. The blue points stand for crossings observed inside a region $X_{GSM} > 5$, $-5 < Y_{GSM} < 5$, $-5 < Z_{GSM} < 5$; the rest of the crossings are shown by the red points. The PR96 magnetopause model for $B_Z = 0$ and $p_{SW} = 2$ nPa is given for reference.

were multiple but we treated each in a series as a single crossing. The locations of all crossings are shown in Figure 1. The *Petrinec and Russell* [1996] (PR96 hereafter) magnetopause surface calculated for IMF $B_Z = 0$ and the solar wind dynamic pressure, $p_{SW} = 2$ nPa is given for reference.

[7] To further analysis, the crossings were divided into two groups of approximately equal sizes: subsolar crossings ($5 < X_{GSM}$; $-5 < Y_{GSM} < +5$, $-5 < Z_{GSM} < 5$) and the rest of them. The latter group will be called the flank crossings hereafter.

[8] The WIND plasma moments [*Ogilvie et al.*, 1995] and the ACE magnetic field [*Smith et al.*, 1998] were used as input parameters for model predictions. These data were propagated by the two-step routine [*Šafránková et al.*, 2002] to the location of a particular THEMIS magnetopause crossing; the deceleration in the magnetosheath was omitted. Five-minute averages of both the plasma and magnetic field centered around the time of the magnetopause crossing were then used as a proxy of the upstream conditions. The locations of observed crossings should be transformed into aberrated coordinates. The aberration is widely discussed by *Šafránková et al.* [2002] with the conclusion that the best ordering of the data provides the procedure taking into account the Earth's orbital motion and omitting the transversal components of the solar wind velocity, thus we use this approach.

[9] Our analysis uses the differences between the radial distance of observed crossings, R_{obs} and the distance predicted by the PR96 model, R_{mod}. To ensure that the results do not depend on the model used, we performed the same analysis applying the residuals of *Shue et al.* [1997], *Roelof and Sibeck* [1993], and *Boardsen et al.* [2000] models; the results were even quantitatively very similar.

3. Data Analysis and Its Discussion

[10] The PR96 model includes the IMF B_Z and p_{SW} as parameters, thus we check its performance with respect to these parameters. Figure 2 shows the differences, $R_{obs} - R_{mod}$ as a function of IMF B_Z. One can note that the average value of deviations is nearly constant and equal to $\approx 0.5\ R_E$ for -10 nT $< B_Z < 4$ nT. It drops down to $\approx -0.3\ R_E$ for larger IMF B_Z but the number of crossings for such large B_Z is small and they cannot spoil a further analysis.

[11] The differences $R_{obs} - R_{mod}$ are plotted as a function of p_{SW} in Figure 3a. The average values shown as the yellow and blue bars reveal a systematic dependence of the difference on p_{SW}. The crossings observed under low p_{SW} are on $\approx 1\ R_E$ farther from the Earth than the predictions for both subsolar (blue points) and flank (red points) groups of crossings. From this it follows that the dependence of the magnetopause location on p_{SW} is stronger than the sixth root that is usually expected. To show it, we plot the radial distance of subsolar crossings as a function of p_{SW} in Figure 3b. The best fit is $12.8 \times p_{SW}^{1/4.8}$. The value of the exponent is rather high, however, *Lin et al.* [2010] published a 3D magnetopause model and found this exponent $\approx 1/5.2$ for the whole magnetopause surface. We assume that the presence of plasma in the low-latitude boundary layer can further increase the value of the exponent for the subsolar region. Consequently, the whole problem needs a deep analysis that is out of the present paper that is concentrated on the influence of the IMF direction. We think that the reason why this effect was not found in earlier studies [e.g., *Šafránková et al.*, 2002] is an unusually low p_{SW} in 2007–2008. The distribution of p_{SW} in our set peaks at 1.4 nPa (not shown), whereas 2 nPa is considered as a typical pressure.

[12] Nevertheless, to account for the pressure and possible IMF B_Z effects, we have divided both our sets (subsolar and flank) into two sub-sets according to p_{SW} (the break point is

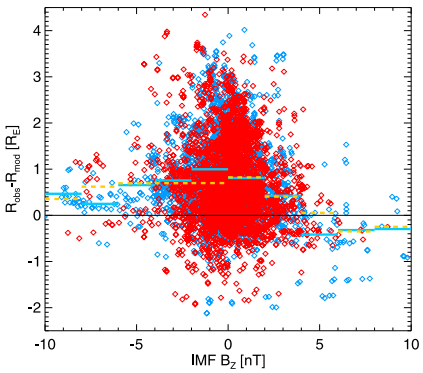

Figure 2. Differences between observed and predicted magnetopause locations $R_{obs} - R_{mod}$ as a function of IMF B_Z. The red points and yellow bars are flank crossings; the blue points and bars are subsolar crossings.

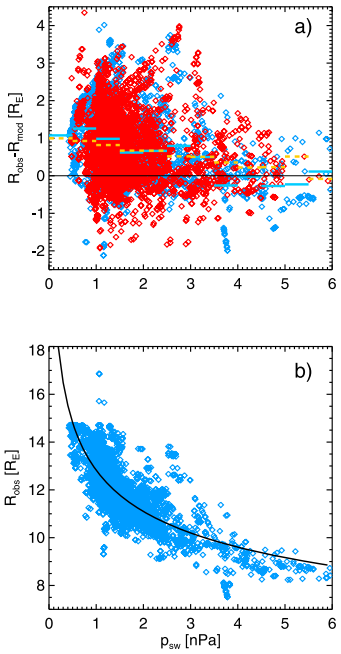

Figure 3. (a) Differences between observed and predicted magnetopause locations as a function of the upstream dynamic pressure, p_{SW}. The colors have the same meaning as in Figure 2. (b) The radial distance of subsolar crossings as a function of p_{SW}. The equation of the fit is $y = 12.83\ x^{-1/4.79}$.

1.4 nPa) and then according to the IMF B_Z sign. The differences, $R_{obs} - R_{mod}$ as a function of the IMF cone angle are plotted in Figure 4. As mentioned, the cone angle is defined as the angle between the IMF and solar wind velocity vectors. In Figure 4, the red points stand for low p_{SW} and blue points for the high p_{SW} in a) and b) panels, whereas the same colors distinguish positive (blue) and negative (red) IMF B_Z in c) and d) panels, respectively. The average values are shown by the horizontal bars of corresponding colors. The top panels show the distribution of the subsolar crossings, the flank crossings are given in the bottom panels. The black parabolic curves that emphasize the trends are the fits of all data in the corresponding panel. In spite of a large spread of experimental points, one can clearly see that the crossings observed during a radial IMF (aligned with the solar wind flow) are on average about 1 R_E outward from the Earth than the crossings observed during the IMF perpendicular to the solar wind velocity. This trend is clearly observed in all subsets.

[13] We assume that the dependence is connected with a different way of transformation of the upstream pressure to the pressure imposed onto the magnetopause behind the quasiparallel and quasiperpendicular bow shocks. There is no compression of the magnetic field at the parallel bow shock and *Verigin et al.* [2009] pointed out an important role of the magnetic field tension that is vanishing behind the parallel bow shock. Moreover, *Suvorova et al.* [2010] have shown that the magnetosheath plasma pressure is by a factor of ≈2 lower for such shock. For this reason, we made the plots of $R_{obs} - R_{mod}$ vs the θ_{BN} angle (not shown) but the ordering of the data was much worse, especially at the flanks. Nevertheless, the parallel subsolar bow shock is the proper cause of the magnetopause displacement. Taking into account the shape of the magnetosheath streamlines [e.g., *Spreiter et al.*, 1966], the magnetopause is influenced by the solar wind entering close to the subsolar point and the θ_{BN} angle is equal to the cone angle at this point. The average amplitude of the cone angle effect (≈1 R_E) is smaller than that following from the case studies [*Suvorova et al.*, 2010; *Jelínek et al.*, 2010] but as it can be seen in Figure 4, we have a large number of crossings that lie 3 or more R_E from the predicted location. The large spread of the points can be partly connected with the fact that the radial IMF is difficult to propagate [e.g., *Jelínek et al.*, 2010, and references therein] and partly with other factors. We should point out that we made the plots similar to those in Figure 4 for other quantities (e.g., in-ecliptic IMF angle, solar wind speed and density, upstream β, tilt angle, and geomagnetic indices) but without any clear effect. We believe that a possible influence of these quantities would be separable when the cone angle effect will be removed by an improved magnetopause model.

4. Conclusion

[14] The analysis of magnetopause locations observed by the Themis spacecraft in 2007–2008 is present. It brings a statistical evidence that the dayside magnetopause location is strongly influenced by the IMF cone angle as it was shown in

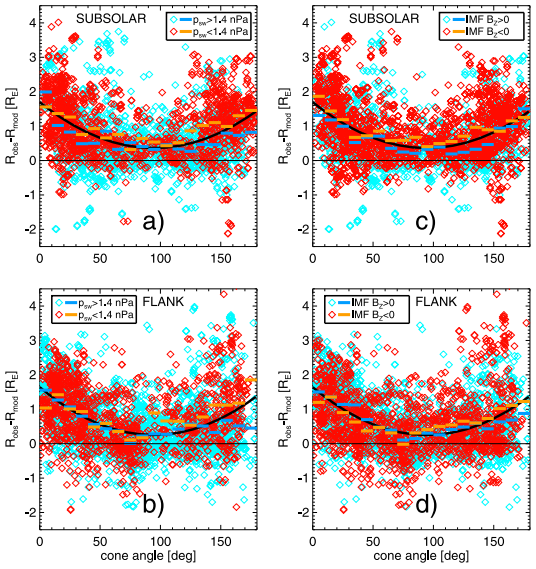

Figure 4. The difference between observed and predicted magnetopause locations as a function of the cone angle. (a) Subsolar set (red points and yellow bars are p_{SW} < 1.4 nPa; the blue points and bars are p_{SW} > 1.4 nPa). (b) Flank set (red points and yellow bars are p_{SW} < 1.4 nPa; the blue points and bars are p_{SW} > 1.4 nPa). (c) Subsolar set (red points and yellow bars are IMF B_Z < 0; the blue points and bars are IMF B_Z > 0). (d) Flank set (red points and yellow bars are IMF B_Z < 0; the blue points and bars are IMF B_Z > 0).

the case studies [*Merka et al.*, 2003; *Suvorova et al.*, 2010; *Jelínek et al.*, 2010]. The difference between the IMF aligned with and IMF perpendicular to the solar wind flow is as large as 1 R_E. This effect is attributed to a less effective transformation of the solar wind dynamic pressure to the pressure imposed onto the magnetopause during intervals of a radial IMF. Another factor contributing to deviations of the observed crossings from their model predictions is a stronger dependence of the magnetopause location on the solar wind dynamic pressure than that usually suggested. However, the exact quantification of the pressure effect requires a larger number of the crossings observed under pressures exceeding 2 nPa to be complemented into the data set.

[15] **Acknowledgments.** The authors acknowledge the NASA contract NAS5-02099 and V. Angelopoulos for use of data from the THEMIS mission. Specifically, the authors thank C. W. Carlson and J. P. McFadden for use of ESA data and K. H. Glassmeier, U. Auster, and W. Baumjohann for the use of FGM data provided under the lead of the Technical University of Braunschweig and with financial support through the German Ministry for Economy and Technology and the German Center for Aviation and Space (DLR) under contract 50 OC 0302. The present work was partly supported by the Czech Grant Agency under contract 205/09/0112 and partly by the Research Plan MSM 0021620860 that is financed by the Ministry of Education of the Czech Republic. G. Granko thanks the Charles University Grant Agency (GAUK 163810) for support.

References

Angelopoulos, V. (2008), The THEMIS mission, *Space Sci. Rev.*, *141*, 5–34, doi:10.1007/s11214-008-9336-1.

Aubry, M. P., C. T. Russell, and M. G. Kivelson (1970), Inward motion of the magnetopause before a substorm, *J. Geophys. Res.*, *75*, 7018–7031.

Auster, H. U., et al. (2008), The THEMIS fluxgate magnetometer, *Space Sci. Rev.*, *141*, 235–264, doi:10.1007/s11214-008-9365-9.

Boardsen, S. A., T. E. Eastman, T. Sotirelis, and J. L. Green (2000), An empirical model of the high-latitude magnetopause, *J. Geophys. Res.*, *105*, 23,193–23,219.

Eastman, T. E., S. A. Boardsen, S.-H. Chen, S. F. Fling, and R. L. Kessel (2000), Configuration of high-latitude and high-altitude boundary layers, *J. Geophys. Res.*, *105*, 23,221–23,238.

Fairfield, D. H. (1971), Average and unusual locations of the Earth's magnetopause and bow shock, *J. Geophys. Res.*, *76*, 6700–6716.

Fairfield, D. H., W. Baumjohann, G. Paschmann, H. Luehr, and D. G. Sibeck (1990), Upstream pressure variations associated with the bow shock and their effects on the magnetosphere, *J. Geophys. Res.*, *78*, 3731–3744.

Jelínek, K., Z. Němeček, J. Šafránková, J.-H. Shue, A. V. Suvorova, and D. G. Sibeck (2010), Thin magnetosheath as a consequence of the magnetopause deformation: THEMIS observations, *J. Geophys. Res.*, doi:10.1029/2010JA015345, in press.

Lavraud, B., A. Fedorov, E. Budnik, A. Grigoriev, P. J. Cargill, M. W. Dunlop, H. Reme, I. Dandouras, and A. Balogh (2004), Cluster survey of the high-altitude cusp properties: A three-year statistical study, *Ann. Geophys.*, *22*, 3009–3019.

Lin, R. L., X. X. Zhang, S. Q. Liu, Y. L. Wang, and J. C. Gong (2010), A three-dimensional asymmetric magnetopause model, *J. Geophys. Res.*, *115*, A04207, doi:10.1029/2009JA014235.

McFadden, J. P., C. W. Carlson, D. Larson, M. Ludlam, R. Abiad, B. Elliott, P. Turin, M. Marckwordt, and V. Angelopoulos (2008), The THEMIS ESA plasma instrument and in-flight calibration, *Space Sci. Rev.*, *141*, 277–302, doi:10.1007/s11214-008-9440-2.

Merka, J., A. Szabo, J. Šafránková, and Z. Němeček (2003), Earth's bow shock and magnetopause in the case of a field-aligned upstream flow: Observation and model comparison, *J. Geophys. Res.*, *108*(A7), 1269, doi:10.1029/2002JA009697.

Ogilvie, K. W., et al. (1995), SWE, a comprehensive plasma instrument for the Wind spacecraft, *Space Sci. Rev.*, *71*, 41–54.

Petrinec, S. M., and C. T. Russell (1995), An examination of the effect of dipole tilt angle and cusp regions on the shape of the dayside magnetopause, *J. Geophys. Res.*, *100*, 9559–9566.

Petrinec, S. M., and C. T. Russell (1996), Near-Earth magnetopause shape and size as determined from the magnetopause flaring angle, *J. Geophys. Res.*, *101*, 137–152.

Roelof, E. C., and D. G. Sibeck (1993), Magnetopause shape as a bivariate function of interplanetary magnetic field *Bz* and solar wind dynamic pressure, *J. Geophys. Res.*, *98*, 21,421–21,450.

Šafránková, J., Z. Němeček, Š. Dušík, L. Přech, D. G. Sibeck, and N. N. Borodkova (2002), The magnetopause shape and location: A comparison of the Interball and Geotail observations with models, *Ann. Geophys.*, *20*, 301–309.

Šafránková, J., Š. Dušík, and Z. Němeček (2005), The shape and location of the high-latitude magnetopause, *Adv. Space Res.*, *36*(10), 1934–1939.

Shue, J.-H., J. K. Chao, H. C. Fu, K. K. Khurana, C. T. Russell, H. J. Singer, and P. Song (1997), A new functional form to study the solar wind control of the magnetopause size and shape, *J. Geophys. Res.*, *102*, 9497–9511.

Shue, J.-H., et al. (1998), Magnetopause location under extreme solar wind conditions, *J. Geophys. Res.*, *103*(A8), 17,691–17,700.

Sibeck, D. G., R. E. Lopez, and E. C. Roelof (1991), Solar wind control of the magnetopause shape, location, and motion, *J. Geophys. Res.*, *96*, 5489–5495.

Smith, C. W., et al. (1998), The ACE magnetic fields experiment, *Space Sci. Rev.*, *86*, 613–632.

Sotirelis, T., and C.-I. Meng (1999), Magnetopause from pressure balance, *J. Geophys. Res.*, *104*, 6889–6898.

Spreiter, J. R., A. L. Summers, and A. Y. Alksne (1966), Hydromagnetic flow around the magnetosphere, *Planet. Space Sci.*, *14*, 223–253.

Suvorova, A. V., J.-H. Shue, A. V. Dmitriev, D. G. Sibeck, J. P. McFadden, H. Hasegawa, K. Ackerson, K. Jelínek, J. Šafránková, and Z. Němeček (2010), Magnetopause expansions for quasi-radial interplanetary magnetic field: THEMIS and Geotail observations, *J. Geophys. Res.*, doi:10.1029/2010JA015404, in press.

Verigin, M. I., G. A. Kotova, V. V. Bezrukikh, G. N. Zastenker, and N. Nikolaeva (2009), Analytical model of the near-Earth magnetopause according to the data of the Prognoz and Interball satellite data, *Geomagn. Aeron.*, *49*(8), 1176–1181.

Zhou, X. W., and C. T. Russell (1997), The location of the high-latitude polar cusp and the shape of the surrounding magnetopause, *J. Geophys. Res.*, *102*, 105–110.

Š. Dušík, G. Granko, K. Jelínek, Z. Němeček, and J. Šafránková, Faculty of Mathematics and Physics, Charles University, V Holešovičkách 2, 180 00 Prague 8, Czech Republic.

C.2 Magnetopause expansions for quasi-radial interplanetary magnetic field: THEMIS and Geotail obser vations

JOURNAL OF GEOPHYSICAL RESEARCH, VOL. 115, A10216, doi:10.1029/2010JA015404, 2010

Magnetopause expansions for quasi-radial interplanetary magnetic field: THEMIS and Geotail observations

A. V. Suvorova,[1,2] J.-H. Shue,[1] A. V. Dmitriev,[1,2] D. G. Sibeck,[3] J. P. McFadden,[4] H. Hasegawa,[5] K. Ackerson,[6] K. Jelínek,[7] J. Šafránková,[7] and Z. Němeček[7]

Received 26 February 2010; revised 23 April 2010; accepted 12 May 2010; published 9 October 2010.

[1] We report Time History of Events and Macroscale Interactions during Substorms (THEMIS) and Geotail observations of prolonged magnetopause (MP) expansions during long-lasting intervals of quasi-radial interplanetary magnetic field (IMF) and nearly constant solar wind dynamic pressure. The expansions were global: The magnetopause was located more than 3 R_E and ~7 R_E outside its nominal dayside and magnetotail locations, respectively. The expanded states persisted several hours, just as long as the quasi-radial IMF conditions, indicating steady state situations. For an observed solar wind pressure of ~1.1–1.3 nPa, the new equilibrium subsolar MP position lay at ~14.5 R_E, far beyond its expected location. The equilibrium position was affected by geomagnetic activity. The magnetopause expansions result from significant decreases in the total pressure of the high-β magnetosheath, which we term the low-pressure magnetosheath (LPM) mode. A prominent LPM mode was observed for upstream conditions characterized by IMF cone angles less than 20°–25°, high Mach numbers and proton plasma $\beta \leq 1.3$. The minimum value for the total pressure observed by THEMIS in the magnetosheath adjacent to the magnetopause was 0.16 nPa and the fraction of the solar wind pressure applied to the magnetopause was therefore 0.2, extremely small. The equilibrium location of the magnetopause was modulated by a nearly continuous wavy motion over a wide range of time and space scales.

Citation: Suvorova, A. V., J.-H. Shue, A. V. Dmitriev, D. G. Sibeck, J. P. McFadden, H. Hasegawa, K. Ackerson, K. Jelínek, J. Šafránková, and Z. Němeček (2010), Magnetopause expansions for quasi-radial interplanetary magnetic field: THEMIS and Geotail observations, *J. Geophys. Res.*, *115*, A10216, doi:10.1029/2010JA015404.

1. Introduction

[2] Global expansions of the magnetopause (MP), formed in response to the interaction between the solar wind (SW) and the Earth's magnetosphere, are mainly associated with low dynamic pressures (<1 nPa) in tenuous solar wind flows [*Richardson et al.*, 2000; *Terasawa et al.*, 2000; *Lockwood*, 2001]. This fundamental interaction mode can be quasi-steady when SW conditions are nearly constant for a long time (about 1 h or more). However, *Fairfield et al.* [1990] indicated that radial interplanetary magnetic field (IMF) orientations can also cause MP expansions. They have shown that pressure/density perturbations produced in the subsolar foreshock correlate with dayside magnetospheric magnetic field variations. They infer that the foreshock pressure fluctuations convect through the subsolar bow shock into the magnetosheath and impinge on the subsolar magnetosphere. Other studies showed that this interaction mode is often unsteady, resulting in multiple MP crossings with interarrival times on the order of a few minutes [*Fairfield et al.*, 1990; *Sibeck*, 1995; *Russell et al.*, 1997; *Němeček et al.*, 1998].

[3] The location of foreshock upstream from the bow shock is controlled by the angle θ_{Bn} between the IMF and the local normal to the bow shock. In the subsolar region, this angle coincides with the cone angle between the IMF vector and the Earth-Sun line. When the angle θ_{Bn} is small, the local bow shock is quasi-parallel ($Q_{||}$). When the IMF is radial (aligned with the Sun-Earth line), the $Q_{||}$ foreshock forms upstream of the subsolar bow shock. The $Q_{||}$ foreshock exhibits strong wave activity that is swept downstream into the magnetosheath turbulence, but contrast with the much quieter quasi-perpendicular ($Q_{\perp}$) shock for IMF orientations perpendicular to the local bow shock normal

[1]Institute of Space Science, National Central University, Jhongli, Taiwan.
[2]Skobeltsyn Institute of Nuclear Physics, Moscow State University, Moscow, Russia.
[3]NASA Goddard Space Flight Center, Greenbelt, Maryland, USA.
[4]Space Sciences Laboratory, University of California, Berkeley, California, USA.
[5]Institute of Space and Astronautical Science, JAXA, Sagamihara, Japan.
[6]Department of Physics and Astronomy, University of Iowa, Iowa City, Iowa, USA.
[7]Faculty of Mathematics and Physics, Charles University, Prague, Czech Republic.

0148-0227/10/2010JA015404

[*Wilkinson*, 2003]. *Fairfield et al.* [1990] demonstrated that plasma densities and dynamic pressures diminish within the foreshock and suggested that this might result in a decrease in the subsolar magnetosheath pressure. If so, the IMF orientation may control the pressure applied to the dayside magnetosphere. According to this hypothesis, during radial (transverse) IMF the magnetosheath pressure applied to the magnetopause should be smaller (higher). Careful study of magnetopause positions as a function of IMF cone angle can verify this hypothesis.

[4] Comprehensive studies of foreshock effects on the magnetosheath, magnetopause, and magnetosphere were presented by numerous authors [*Sibeck et al.*, 1989; *Sibeck*, 1992, 1995; *Sibeck and Gosling*, 1996; *Russell et al.*, 1997; *Němeček et al.*, 1998; *Zastenker et al.*, 1999, 2002; *Shevyrev and Zastenker*, 2005; *Shevyrev et al.*, 2007]. The dayside MP moves in response to variations of the IMF cone angle [*Sibeck*, 1995]. MP motion attains greater amplitudes behind the foreshock, where amplitudes vary from 0.2 to 0.8 R_E [*Russell et al.*, 1997]. *Laakso et al.* [1998] and *Merka et al.* [2003] reported examples of even larger amplitude (~2 R_E) MP oscillations for quasi-radial IMF orientations. On the basis of indirect estimates, *Merka et al.* [2003] proposed a bullet-like shape for the expanded magnetopause. They assumed that the unusual MP motion was related to a decrease of the magnetosheath pressure behind the $Q_{\|}$-shock. This assumption followed the ideas of *Fairfield et al.* [1990]. However, there were no magnetosheath data, which could confirm or disprove that assumption.

[5] These results lead one to expect depressed total pressures within the magnetosheath during intervals when the IMF has a radial orientation. Two important questions remain open: (1) What fraction of the solar wind dynamic pressure is applied to the magnetosphere by the magnetosheath during intervals of radial IMF orientation? (2) What is the average location of the magnetopause under these conditions? These effects are absent from global MHD codes and have not yet been addressed by global kinetic or hybrid codes. MP dynamics and the properties of the adjacent magnetosheath for radial IMF conditions remain almost unexplored mainly because of insufficient experimental data in the subsolar region.

[6] The Time History of Events and Macroscale Interactions during Substorms (THEMIS) mission [*Angelopoulos*, 2008] provides a large database of observations for detailed studies of the MP and magnetosheath. Using THEMIS and Geotail, we investigate three cases of very large MP expansion occurring for prolonged quasi-radial IMF and nearly steady SW dynamic pressures. We demonstrate that the bow shock and magnetopause lie far beyond their expected positions. The MP expansions are found to be quasi-steady and long lasting. We show and quantify dramatic decreases in the magnetosheath total pressure induced by rotations to quasi-radial IMF orientations rather than by decreases in the SW dynamic pressure.

2. Experimental Data

[7] We analyze three events on 16 July, 4 August, and 8 August 2007, which are accompanied by long-lasting (up to a few hours) quasi-radial IMF orientations (the cone angle is less than 30°). Solar wind and geomagnetic conditions for these time intervals are presented in Figures 1–3. During these intervals, ACE was located at GSM (225, −2, 23), (227, 28, 4), and (226, 23, 13) R_E, respectively, while Wind was located at (253, −67, 16), (228, −95, 33), and (232, −97, 13) R_E, respectively. Comparing the Wind and ACE data, we find that averaged values for SW dynamic pressure agree to within ~20%, although the two spacecrafts often observe different transient variations in the plasma parameters. The IMF demonstrates higher variability and larger differences. However, the clock and cone angles measured by ACE and Wind coincide well within some intervals. The observed differences in SW plasma and IMF parameters are due to the very large distance between the monitors [e.g., *Richardson and Paularena*, 2001]. We use ACE to determine SW plasma and IMF conditions because Wind was located very far from the Earth-Sun line.

[8] The duration of the quasi-radial IMF intervals was about 1.5 h (Figure 1), 2 h (Figure 2), and 14 h (Figure 3), respectively. Here we should talk about geomagnetic activity as an internal factor affecting the magnetopause location [*Petrinec and Russell*, 1993; *Sibeck*, 1994]. As one can see in Figures 1–3, there were no geomagnetic storms during these 3 days (minimum value $Dst_{\min}$ ~−25 nT). Hence, the ring current effect, which would lead to an inflated magnetosphere, is negligibly small, if any. Therefore, we will rule out the *Dst* index from the following consideration. Auroral activity, represented by the *AE* index, was quiet on 16 July and 4 August with maximum value $AE_{\max}$ ~150 nT, while moderate auroral activity was observed on 8 August with $AE_{\max}$ ~600 nT. We will consider last event in relation with dayside magnetopause erosion due to the field-aligned currents.

[9] Figure 4 shows THEMIS locations in the GSM coordinate system during time intervals from 1950–2037 UT on 16 July 2007, 0400–0600 UT on 8 August 2007, and 0400–1200 UT on 4 August 2007. At the beginning of each interval, the five THEMIS probes were located in the subsolar region, moving outward in the string-of-pearls configuration with THB leading and THA trailing. Geotail was located in the duskside magnetosheath at GSM (6, 15, 1.5) R_E on 16 July, in the nightside magnetosheath at GSM (−10, 24, −13) R_E on 8 August, and inside the magnetotail at GSM (−23, 10, −12 R_E) on 4 August.

[10] We compare clock angles of the magnetosheath and interplanetary magnetic fields observed by Geotail, ACE, and THEMIS to estimate the time delay for SW propagation (Figure 5). We obtain a 43 min lag from ACE to Geotail on 16 July (Figure 5a). Taking into account the time for plasma to propagate from the THEMIS probes to Geotail results in a 41.5 min time lag from ACE to THEMIS. On 8 August (Figure 5b), the SW propagation times from ACE to THEMIS and from ACE to Geotail was determined to be 38.5 min and 43.5 min, respectively. On the morning of 4 August, there was no spacecraft in the magnetosheath. We considered an interval from 1400 to 1900 UT when THA was located in the magnetosheath (Figure 5c). During this interval, THB magnetic field variations lagged those at ACE by 63 to 68 min, while a direct solar wind propagation technique yields a similar delay of ~65 min. For the interval from 0200 to 1200 UT on 4 August, we suppose that the direct propagation technique is also reliable and hence the average time delay is estimated to be ~63 min.

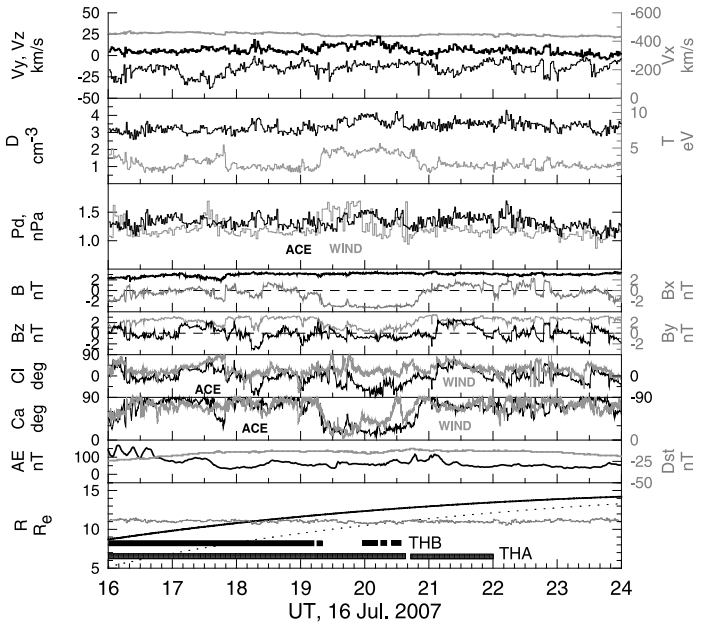

Figure 1. Upstream solar wind parameters observed by ACE at 1600–2400 UT on 16 July 2007 (from top to bottom): velocity components *Vx* (gray line), *Vy* (thick black line), and *Vz* (thin line); proton density *D* (thin) and temperature *T* (gray); SW dynamic pressure *Pd* observed by ACE (black) and Wind (gray); IMF strength *B* (black) and *Bx* component (gray); IMF component B*y* (gray) and B*z* (black); IMF clock (Cl) and cone (Ca) angles observed by ACE (black) and Wind (gray). The two bottom panels show geomagnetic indices *AE* (black) and *Dst* (SYM index; gray) and distances to the THB probe (solid line) and THA probe (dotted line). *Shue et al.*'s [1998] magnetopause model prediction is shown by a gray line and magnetosphere intervals observed by THB and THA are shown by black and shaded bars, respectively. The time of upstream parameters is delayed on SW propagation to THEMIS (see explanation in section 2).

[11] *Shue et al.* [1998, hereafter Sh98] and *Chao et al.* [2002, hereafter Ch02] provide reference models for the location of the MP and bow shock, respectively, as functions of solar wind conditions. Note that the bow shock predicted by the Ch02 model does not depend on the MP location. The Ch02 model predicts a decrease in the distance to the $Q_{||}$ bow shock caused by a decrease in the fast magnetosonic velocity for small cone angles. Among a number of bow shock models, the Ch02 model demonstrates the highest prediction capabilities for a wide range of upstream conditions [*Dmitriev et al.*, 2003].

[12] We also correct an aberration of up to 6° due to the Earth's revolution around the Sun and fluctuations in the SW direction. The correction was performed on a point-by-point basis. The upstream and THEMIS data have been converted into aberrated GSM (aGSM) coordinates, in which the *x* axis is aligned with the SW velocity [e.g., *Dmitriev et al.*, 2003]. In the aGSM coordinate system, the radial IMF is aligned with the SW flow and *x* axis. SW dynamic pressure is calculated as $Pd = 1.67 \times 10^{-6}\, D{\cdot}V^2$ (in nPa), where *V* is bulk velocity (in km/s) and $D = N_p + 4N\alpha$ (in cm^{-3}) is corrected SW density including a *He* contribution. The *He* content was nearly constant at 4~5% on 16 July and 8 August and ~3% on 4 August. The total SW pressure *Psw* is calculated as a sum of the dynamic pressure, thermal proton pressure, and magnetic pressures of the solar wind.

3. Geomagnetically Quiet Event on 16 July 2007

[13] An interval of prolonged quasi-radial IMF at 1950–2037 UT on 16 July 2007 is presented in Figure 6. The SW and geomagnetic conditions are quiet: the SW velocity (~450 km/s) is stable, the SW pressure *Psw* varies slightly about 1.5 nPa, and IMF *Bz* is small (~−1 nT). The top panel in Figure 6 displays ion spectrograms from THEMIS electrostatic analyzers (ESA) plasma instruments [*McFadden et al.*, 2008]. The presence of $Q_{||}$ mode is supported by intense fluxes in the high-energy channels of ion spectrograms as well as by enhanced fluxes of energetic particles (not shown) observed by THB in the magnetosheath until ~2035 UT. The magnetosheath is identified as a region of relatively dense plasma with a very wide energy spectrum of ions. Note that after ~2035 UT the small cone angle is unreliable because of a different time shifting for the solar wind propagation in the trailing edge of the interval. That shifting is associated with the arrival of another solar wind structure led by a discontinuity, which propagation in the magnetosheath is observed by the THEMIS probes at

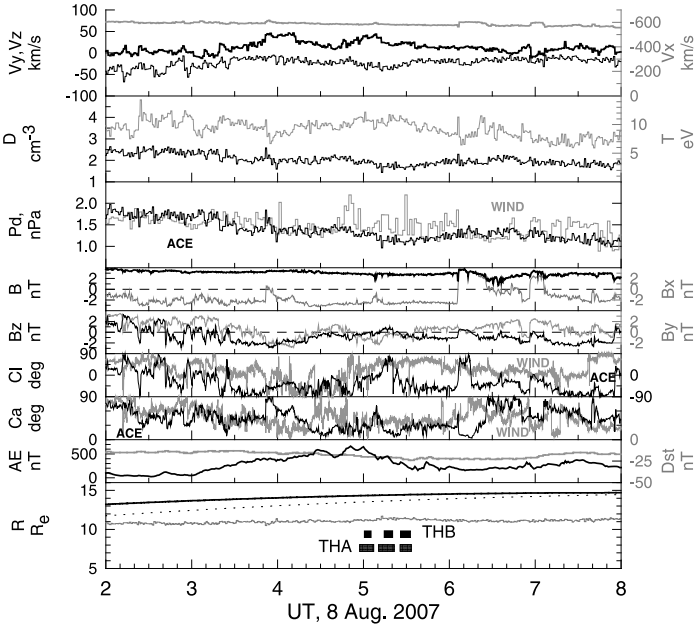

Figure 2. The same as in Figure 1 but on 8 August 2007 at 0200–0800 UT.

~2035 UT. Hence, we cut our consideration of the $Q_{||}$ interval at 2035 UT.

[14] At the beginning of the event at ~1950 UT, all the THEMIS probes except for THA are located in the magnetosheath. The innermost THA probe is inside the magnetosphere that is in good agreement with the Sh98 model prediction. From 1952 UT the MP starts to expand and reaches distances of >12.7 R_E, such that the outer probes

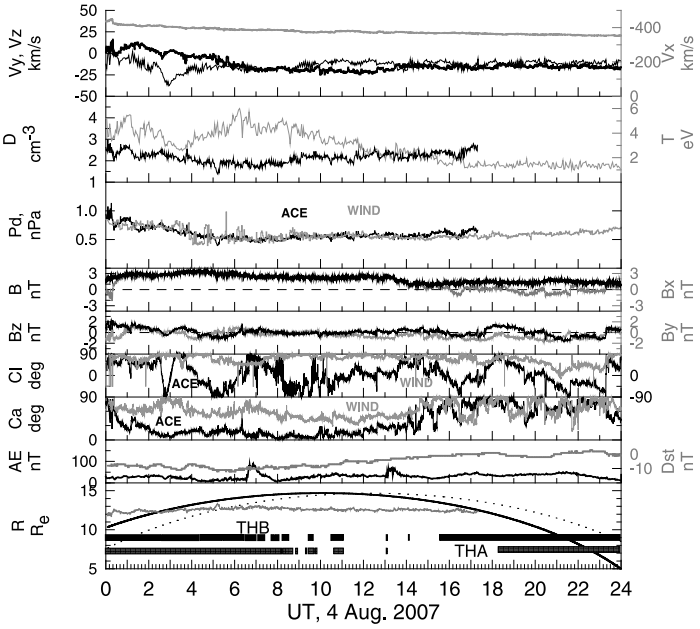

Figure 3. The same as in Figure 1 but on 4 August 2007 at 0000–2400 UT.

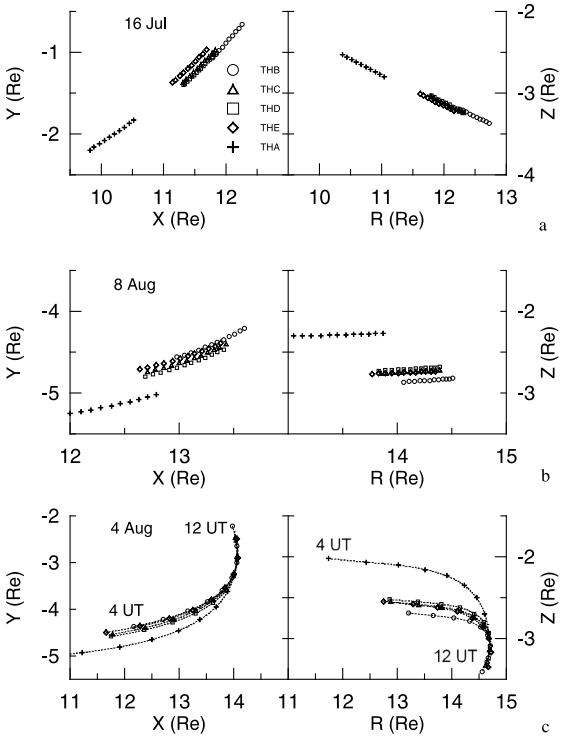

Figure 4. GSM coordinates of the THEMIS probes for the time intervals: (a) 1950–2037 UT on July 16 2007; (b) 0400–0600 UT on August 8 2007; (c) 0400–1200 UT on August 4 2007.

THC, THD, and THE enter inside the magnetosphere for a period of ~40 min. The expansion is large; THB observes the magnetopause at distances of ~2 R_E above the Sh98 model prediction. Note that application of other magnetopause models gives similar a result within one standard deviation σ (~0.5 R_E) for $Psw \geq 1$ and 2σ for $Psw < 1$; all the models are unable to predict such distant magnetopause. We have to emphasize that the total SW pressure and IMF *Bz* are almost constant during that time and thus the expansion cannot be caused by variations of those parameters. It is reasonable to attribute the expansion to a decrease of the cone angle from ~30° to ~10° that occurred at 1950 to 1953 UT.

[15] The expanding magnetopause propagates outward from THE to THD with velocity of 26 km/s, then the MP decelerates to 9 km/s on its path from THD to THB. On average, the MP takes ~7 min to pass the distance of ~0.72 R_E between THE and THB (average speed of ~11 km/s). The MP velocities estimated by such method are presented in Table 1. The estimation error of about 15% is originated mainly from the limited ~3 s time resolution of the magnetic field and plasma data and also from uncertainty in determining the moment when a probe crosses the MP current sheet.

[16] The MP and adjacent magnetosheath plasma should move with similar velocities. Magnetosheath layer adjacent to the MP passes THEMIS probes during ~30 s. In Figure 7, one can see that the ambient plasma in this layer moves outward mostly in X direction with the velocities of V_x ~20 km/s as measured by THE at 1950:40 UT, ~2 to 10 km/s (THD and THC at 1951:20 UT), and ~15 to 30 km/s as observed by THB at 1958:00 UT. These values agree very well with the estimated MP velocities of 26 and 9 km/s (two upper rows in Table 1). Thus, our estimations are reasonable and we can conclude that within one error the MP velocities are consistent with the velocities V_x of magnetosheath plasma adjacent to the MP.

[17] Magnetic field was measured by THEMIS/FGM instrument [*Auster et al.*, 2008]. During the MP crossings, the magnetospheric field, observed just inbound the magnetopause, is 2.4 times larger than the dipole value calculated from International Geomagnetic Reference Field model. Such a value is expected from the shielding effect of the Chapman-Ferraro current. Note that the crossings observed at ~1951, ~1954, and ~1958 UT are caused by the outward MP moving (i.e., the magnetopause position is not of equilibrium). From the THB observations of the MP crossing at ~1958 UT (see Figure 6), one can see that the total pressure in the adjacent magnetosheath layer is slightly smaller than the *Ptot* in the magnetospheric boundary layer and there is a little jump from *Ptot* = 0.6 nPa in the magnetosheath to *Ptot* = 0.8 nPa in the magnetosphere. We suggest that this jump is owing to the MP moving outward to a new equilibrium position corresponding to lower pressure in the magnetosheath. From 2004 UT, when THB observes minimum magnetospheric field and *Ptot* ~ 0.6 nPa, the magnetopause starts to move back.

[18] At 2011–2015 UT, the outermost probe THB observes a magnetosheath rebound, which is accompanied by an enhancement of cone angle from ~10° to ~35° and southward IMF from ~0 to −2 nT. According to the Sh98 model prediction, the small change of IMF *Bz* does not affect the magnetopause location. However, it is important to note that the geomagnetic field in the vicinity of distant magnetopause is weak, ~20 to 40 nT. Because of that weak

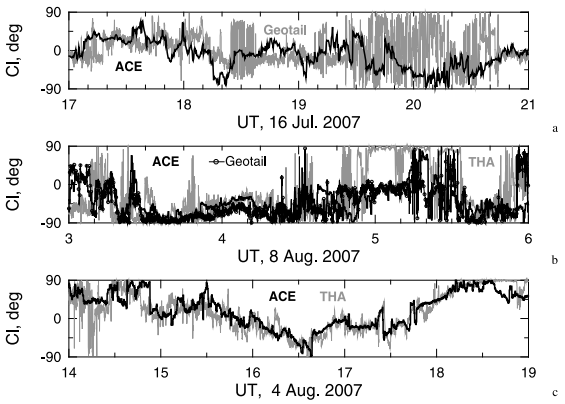

Figure 5. Clock angle of magnetic fields (a) on 16 July observed by Geotail (gray line) and ACE (black line), delayed by 43 min; (b) on 8 August observed by THA (gray line) and Geotail (circles), delayed by −5 min, and ACE (black line), delayed by 38.5 min; (c) on 4 August observed by THA (gray line) and ACE (black line), delayed by 63 min.

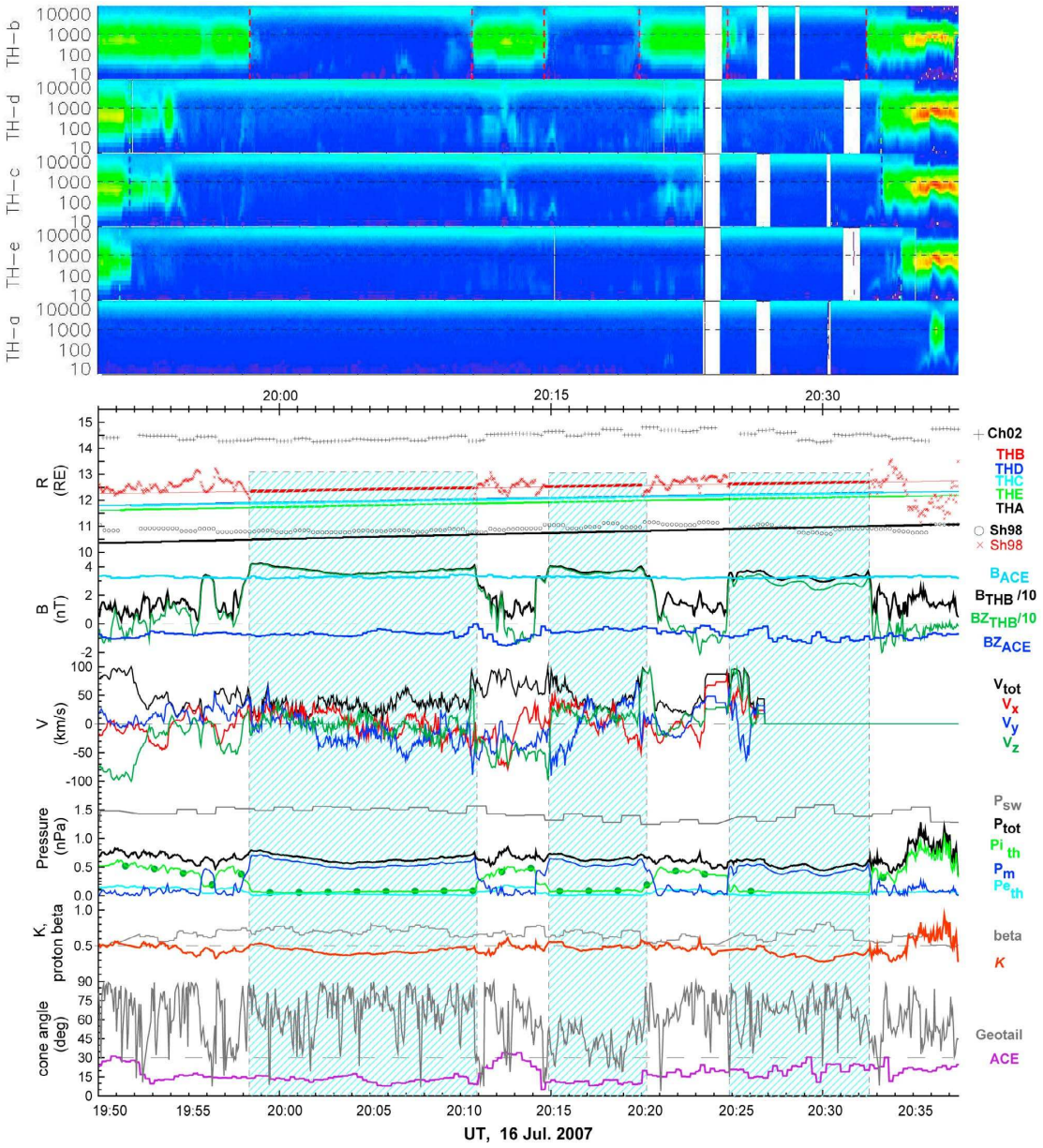

Figure 6. Plasma and magnetic fields observed on 16 July 2007 (from top to bottom): THEMIS ion spectrograms; *Chao et al.*'s [2002] bow shock model prediction; *Shue et al.*'s [1998] magnetopause model predictions calculated for the solar wind *Psw* (circles) and magnetosheath *Ptot* (diagonal crosses) pressures; THEMIS radial distances (thick segments mark the magnetosphere encounters); ACE and THB measurements of magnetic field strength and *Bz* (divided by 10 for THB); THB plasma velocity (V_{tot}) and components *Vx*, *Vy*, and *Vz*; the upstream solar wind pressure *Psw* and THB magnetic (*Pm*), thermal ion Pi_{th}, thermal electron Pe_{th}, and total pressure (P_{tot}), circles depict the ion pressure Pi_{th} in ESA full mode; solar wind proton β and ratio *K* (*Ptot*/*Psw*); cone angles of ACE and Geotail magnetic field delayed by 41.5 and −1.5 min, respectively. Time intervals of THB magnetosphere encounters are marked by blue shadow bars.

Table 1. Magnetopause and Plasma Velocities

16 Jul	UT	Probes	V_{MP} (km/s)
1	1952	E-D	26 ± 7
2	1958	D-B	9 ± 1
3	2032	B-D	−55 ± 4
4	2033	D-E	−14 ± 3
5	2037	E-A	−35 ± 4
08 Aug	0500	A-B	25 ± 5
2	0505	B-E	−105 ± 30
3	0507	E-A	−33 ± 5
4	0511	A-E	180 ± 50
5	0514	E-B	8 ± 1
6	0520	B-A	−48 ± 3
7	0525	A-B	230 ± 80
8	0532	B-A	−100 ± 10

magnetic field, the expanded magnetopause is very sensitive to small variations of both major driving parameters (*Psw* and *Bz*) and other parameters affecting the bow shock and magnetosheath formation, such as the IMF cone angle. Probably, in the present case, both effects of southward IMF and increasing cone angle are responsible for the inward magnetopause motion.

[19] Magnetosheath rebound, observed by THB at 2020–2025 UT, is not accompanied by any substantial enhancement of the SW pressure or southward IMF. Even worse, the SW pressure decreases to 1.3 nPa, which that should push the magnetopause outward. That is not the case. In addition, we observe an enhancement of the cone angle up to >20°, which persists until the end of the interval at ~2034 UT. Hence, the observed dynamics of upstream parameters hardly explains the magnetosheath rebound at 2020–2025 UT as well as the magnetospheric rebound at 2025–2033 UT. There should be another process driving the magnetopause.

[20] During the interval on 16 July 2007, we find variations of the magnetosheath and magnetospheric parameters over a wide range of timescales. We calculate thermal ion Pi_{th} and electron Pe_{th} pressures using 3 s data of reduced distribution from the THB/ESA instrument, which was operating in fast survey mode until 2027 UT, and then it was turned to slow mode. We also calculate the ion thermal pressures Pi_{th} using data from full distribution, which has lower time resolution of ~1.5 min. One can see a good consistency between the two data products. The total magnetosheath pressure is obtained as a sum of Pi_{th}, Pe_{th}, and magnetic pressure *Pm*.

[21] From 1950 to 2035 UT, the THEMIS probes observe 1~2 min oscillations of the total pressure in the magnetosheath as well as in the magnetosphere. Those specific quasi-regular variations clearly indicate oscillating MP motion. The multiple magnetopause crossings observed from 1951 to 2011 UT can be also considered a result of a long period (~10 min) of MP undulation. Similar wavy motions (oscillations) of the MP were reported earlier as transient events [*Sibeck*, 1995; *Sibeck and Gosling*, 1996].

[22] On the basis of the THEMIS observations, we can estimate the average MP location by two independent methods. In the first one, we assume nearly constant MP velocity of 9 km/s for propagation from THB to the new equilibrium location (i.e., during 6 min from 1958 to 2004 UT). Hence, we obtain that at 2004 UT the expanding MP approaches to a distance of ~12.85 R_E. The other method is based on the magnetopause model. As we can see in Figure 6, the magnetopause location is predicted much better when the Sh98 model is applied for the magnetosheath pressure *Ptot* and IMF *Bz*. The inconsistencies can be explained by the fact that the Sh98 model as well as any other MP model has shortcomings at very low pressures. We consider the magnetosheath pressure *Ptot* = 0.6 nPa, detected by THB at 1958 UT, as a lower pressure limit and calculate the upper limit for the MP expansion of ~12.4 ± 0.5 R_E. Thus, two different ways give similar estimations of the MP expansion.

[23] After 2004 UT, the MP starts to move back and at 2012 UT approaches a distance somewhere between THD and THB, which are located at 12 and 12.5 R_E, respectively. Hence, we can estimate the MP equilibrium location somewhere between 12.5 and 12.7 R_E, which is an average distance between the two extreme points of 12~12.5 and 12.85 R_E.

[24] Considering upstream conditions, we do not find any substantial changes or quasi-periodic variations of the solar wind parameters except for the cone angle. At the beginning (~1952 UT), the outward motion of MP is rather related to a fast decrease of the cone angle from ~30° to ~15°. This decrease is accompanied by a gradual decrease of the magnetosheath total pressure *Ptot* from 0.8 to 0.5 nPa, as observed by the THB probe. Here we point out that during the time interval of small cone angles (1952–2035 UT), the THB probe observes very low magnetosheath pressure, which is almost balanced by the magnetospheric pressure. This quasi-balance is clearly seen during the THB magnetopause crossings, which are revealed as significant jumps of all parameters except the total pressure across the MP. Inside the magnetosphere, the magnetic pressure (*Pm*)

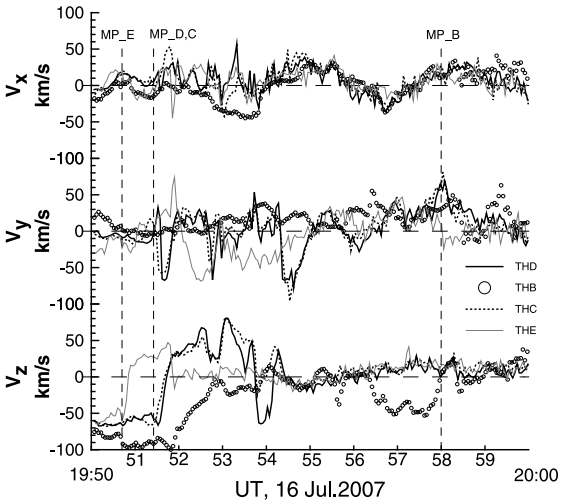

Figure 7. Components *Vx*, *Vy*, and *Vz* of plasma velocity observed by THEMIS probes (THB, THC, THD, THE) on 16 July 2007 near the magnetopause crossings (indicated by vertical dashed lines) during transition from the magnetosheath to the magnetosphere at 1950–2000 UT.

dominates and has a low value, consistent with MP distances of 12.3–12.9 R_E.

[25] The total pressure in the magnetosheath *Ptot* is by a factor of 2 lower than the SW pressure *Psw* as indicated by a ratio $K = Ptot/Psw$ in Figure 6. Near the magnetopause, the value of *Ptot* is found to be ~0.5 nPa. The total pressure in the low-pressure magnetosheath (LPM) is mainly contributed by the thermal pressure, a sum of ion Pi_{th} and electron Pe_{th} thermal pressures. The pressure of turbulent magnetic field *Pm* is very weak as observed by THB. Hence, the magnetosheath plasma β is high. We examined simultaneous Geotail observations of the post-noon magnetosheath (Figures 5a and 6) and also found weak magnetic field of ~5 nT, which is characterized by fast variations in the orientation and magnitude. Hence, in the dayside magnetosheath, THEMIS and Geotail observed similar conditions proper for $Q_{||}$ bow shock.

[26] During the LPM mode, we do not find correlation for rapid (~minute) variations of the magnetosheath pressure *Ptot* with the SW pressure *Psw* and cone angle. We have to emphasize that the MP expansion associated with the LPM mode is observed by THEMIS for an unusually long time (~45 min).

4. Disturbed Event on 8 August 2007

[27] Figure 8 shows multiple magnetosphere encounters of THEMIS at unusually large distances of 13.5 to 14.5 R_E accompanied by quasi-radial IMF at 0400–0600 UT on 8 August 2007. The SW conditions (Figure 2) were slightly disturbed: IMF *Bz* varied between −2 and 1 nT, SW velocity was ~600 km/s, and *Psw* varied around 1.3 nPa. The THB/ESA instrument operated in the slow survey mode. The ion thermal pressures calculated for the full and reduced data products show good agreement in the magnetosheath/magnetosphere region.

[28] As we see in Figure 2, the cone angle decreases below 30° after 0420 UT, and the quasi-radial IMF lasts for ~2 h. In Figure 8, we can see that THA observes intense fluxes of energetic particles (>10 keV) and strong magnetosheath pressure variations indicated by the K_A ratio. Those features confirm the presence of $Q_{||}$ bow shock. It is interesting to note a decrease of the energetic particle fluxes and pressure variations at 0439 to 0444 UT when the cone angle increases up to 25° and conditions for the $Q_{||}$ bow shock are broken.

[29] From ~0330 to 0420 UT, the IMF was mostly southward with $Bz = -2$ nT, which caused substorm activity with *AE* of ~600 nT that continued until 0520 UT. Therefore, from 0420 to 0520 UT, the magnetopause is driven by two opposite effects: the small cone angle and enhanced geomagnetic activity. Because of decreasing cone angle, one can expect an expansion of the magnetopause. Simultaneously, the substorm activity results in earthward motion of the dayside magnetopause because of a depression of the dayside geomagnetic field by the intensified field-aligned currents [*Sibeck*, 1994].

[30] A response of the magnetopause and bow shock to the enhanced substorm activity is demonstrated in Figure 8. By ~0408 UT, all THEMIS probes were located inside the magnetosheath at distances of 13~14 R_E, which is in agreement with model predictions of the magnetopause and bow shock. After ~0408 UT, the outermost probes successively observe the bow shock moving inward and entering the interplanetary medium, which is characterized by very narrow ion spectrum with mean energy of several keV. From 0418 to 0438 UT, the bow shock is located between THA and THE, somewhere at ~13.5 R_E, which is ~1 R_E less than the Ch02 model prediction. The THEMIS encounter with interplanetary medium might result from the substorm-associated earthward motion of the dayside magnetopause, which is followed by the bow shock.

[31] From ~0446 UT, the SW pressure gradually decreases, which leads to outward bow shock moving. The outermost THEMIS probes return to the magnetosheath at a distance of ~14.2 R_E, which is close to the modeled bow shock location. At 0453 UT, the SW pressure decreases to ~1.2 nPa, the IMF *Bz* starts to turn northward, and the substorm activity weakens. At that time, the innermost THA observed a short (~1 min) magnetopause rebound at 13.5 R_E, which means that the magnetopause has expanded by more than 2 R_E from the modeled location. During this crossing, an extreme LPM with *Ptot* of 0.2~0.3 nPa (<30% of the SW pressure *Psw*~1.3 nPa) is observed by all the probes. At ~0457 to 0500 UT, the THEMIS probes successively cross the magnetopause, which is moving outward with velocity of ~25 km/s (Table 1) up to distances of ~14.5 R_E. Unfortunately, THEMIS did not provide high-resolution data on plasma velocities at that time.

[32] The LPM pressure is balanced by the small pressure of magnetic field of ~20 nT in the magnetosphere. From 0500 to 0533 UT, we can distinguish three magnetospheric intervals lasting for 4–8 min and recurred every 5–8 min. It is interesting to note that during the first and second intervals, when the *AE* index is still high, the observed geomagnetic field is only 1.5 times higher (even not double) than the dipole magnetic field. The pressure balance during ±30 s of those crossings almost conserves for the outward MP motions at 0500 and 0515 UT when the MP passes THB. This balance indicates that the magnetopause would not move far away and stops near the THB orbit at ~14.5 R_E. On the other hand, for the observed minimal magnetosheath pressure of 0.16 nPa, we can determine the modeled MP distance of ~15.7±0.5 R_E (i.e., ~1.3 R_E above THB). These two features (diminished geomagnetic field and smaller MP distance) can be attributed to a suppressing magnetic effect of the substorm activity at the restoring phase.

[33] The magnetosheath encounter at 0506–0515 UT is accompanied with substantial increase of the cone angle. The MP moves very fast during this transient event (Table 1). At 0520–0525 UT, the THEMIS probes are located in the magnetosheath and observe enhanced plasma and magnetic pressure and large negative *Bz*. It is rather difficult to determine unambiguously solar wind sources for those magnetosheath features. Hence, that magnetosheath rebound might be related to MP undulation with a period of ~10 min.

[34] At 0525–0533 UT, the SW pressure decreases to 1.1 nPa and the THEMIS probes reenter to the magnetosphere, where they observe magnetic pressure of 0.17 nPa. During the third magnetospheric interval, the *AE* index decreases substantially and geomagnetic field approaches to the 2.4 dipole value. A minimum in the geomagnetic field profile at ~0529 UT indicates that the MP continues to move after the crossings and might reach even 16 R_E, against the

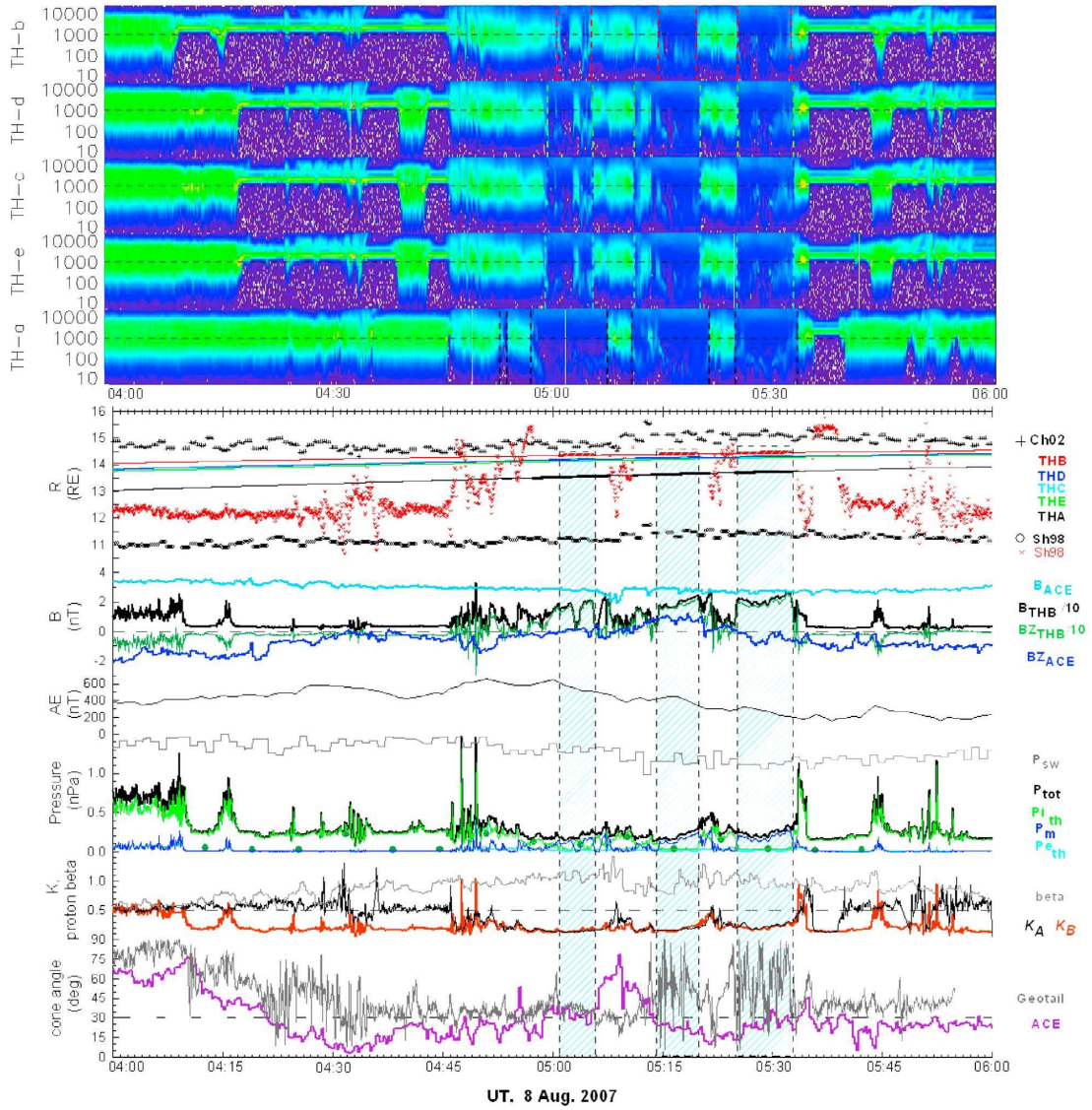

Figure 8. The same as Figure 6, but for 0400–0600 UT on 8 August 2007. Instead of the panel with THB velocity components, we show a panel with *AE*. Ratio *K* is shown for THA (K_A) by a black line and for THB (K_B) by a red line. The ACE and Geotail magnetic field cone angles are delayed by 38.5 and −5 min, respectively.

11.5 R_E predicted by the Sh98 model. Note that the model prediction is substantially improved by using the magnetosheath pressure *Ptot* measured by the THA probe.

[35] We should note that the observed MP is located very close (within 0.5 R_E) to the bow shock predicted by the Ch02 model. It is very unlikely that the magnetosheath has such a small thickness. Hence, we expect more distant bow shock during the LPM. We can estimate the magnetosheath thickness and bow shock distance from THEMIS observations of the magnetopause crossings at 0533 UT and bow shock crossings at 0535 UT. Using the time delay technique, we find that at 0533 UT the MP moves inward with a velocity of ~100 km/s (see Table 1). In a similar manner, we can determine the velocity of bow shock of ~100 km/s at 0535 UT. Taking into account the 2 min time delay between the magnetopause and bow shock crossings, we estimate the path of ~1.9 R_E passed by the bow shock until the crossing with THB. That path should be close to the thickness of magnetosheath. Hence, at 0533 UT the bow shock might be located at ~14.5 + 1.9 = 16.4 R_E and the thickness of the magnetosheath is estimated to be ~1.9 R_E. Such a thin magnetosheath is reported by *Jelinek et al.* [2010].

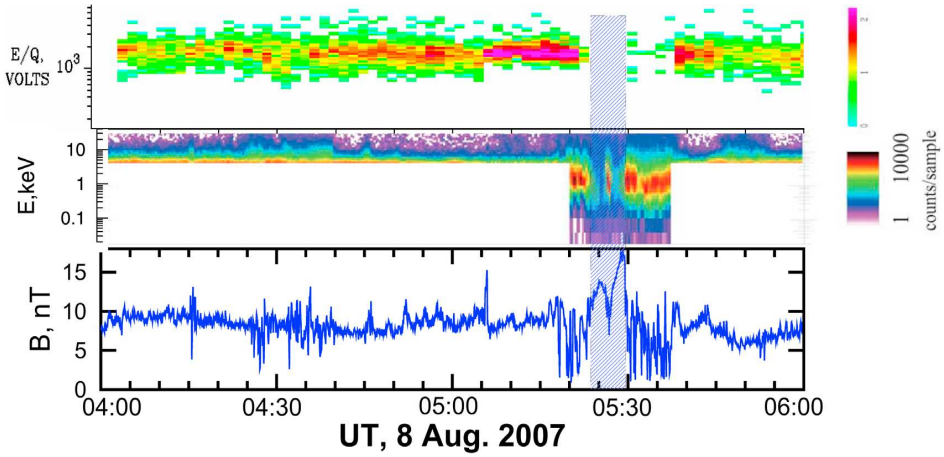

Figure 9. Geotail observations in the tail region on 8 August 2007 (from top to bottom): comprehensive plasma instrument and low-energy particle plasma ion spectrograms and magnetic field strength (Geotail time). The blue shadow bar indicates the magnetosphere encounter.

[36] In the tail region, Geotail also observes an unusual MP expansion. The ion spectrograms presented in Figure 9 show that most of time Geotail is located in the magnetosheath, which is characterized by a very variable magnetic field. During that interval, the low-energy particle plasma instrument operated in a solar wind mode, which was switched to the magnetospheric mode only for a short time from 0520 to 0545 UT. At ~0523 to ~0530 UT, Geotail enters the magnetosphere at a very large distance of ~28 R_E from the x axis. At that time, the SW pressure is Psw ~ 1.1 and the Sh98 model predicts the magnetopause distance of 21 R_E (i.e., ~7 R_E smaller than the observed one). The magnetosphere encounter is revealed as a strong decrease of the ion density and enhancement of the magnetic field that are proper to conditions in the southern lobe/mantle. The surrounding regions, where the magnetic field magnitude is depressed and strongly fluctuating, can be attributed to the magnetosheath region downstream of the $Q_{||}$ bow shock.

[37] Here we have to point out very good correlation of the variations of magnetic field orientation (clock and cone angles) observed by Geotail and THA in the magnetosheath and by ACE in the far upstream region (see Figures 5b, 8, and 9). The correlation is broken when magnetopause approaches THA (at 0500–0530 UT) or Geotail (at 0515–0530 UT). The coincidence of magnetosheath magnetic field orientation with the IMF orientation supports our suggestion that the magnetosphere is indeed affected by the solar wind structure with quasi-radial IMF as observed by ACE.

[38] From ~0535 UT, the IMF gradually turns southward, the SW pressure increases up to 1.2 nPa and the cone angle varies about 25°~30°. The THEMIS probes approach to apogee of 14.7 R_E and return to the magnetosheath and/or bow shock region.

[39] Thus, during this prolonged expansion event (about 40 min to 1 h), we reveal significant differences between the observed MP location and the Sh98 model: ~3.5 R_E in the dayside and ~7 R_E in the tail region. The observed magnetosheath pressure near the magnetopause was ~0.16 nPa and the ratio K ~0.2, both are extremely small. The dayside MP undulates with a period of ~10 min near a new equilibrium position, which we find at ~13.5 to 14.5 R_E (i.e., somewhere between the innermost THA and outermost THB probes). In the beginning of the interval considered, that equilibrium MP location is substantially affected by the enhanced substorm activity.

5. Long-Lasting Event on 4 August 2007

[40] A 14 h interval of quasi-radial IMF occurred at 0100 to 1500 UT on 4 August 2007. As one can see in Figure 3, the event is characterized by steady and quiet SW and geomagnetic conditions: the SW velocity is ~400 km/s, the SW total pressure is low and decreases from 0.7 nPa to 0.5 nPa, and IMF Bz, AE, and Dst are small. The models predict the MP and bow shock location at ~12.5 and 17~18 R_E, respectively (see Figure 10).

[41] In Figures 3 and 10, we find the expanded MP observed by the outer THEMIS probes continuously during ~4 h from ~0300 to ~0700 UT. Then, until ~0800 UT, they observe magnetosheath intervals of a few minutes duration. After that time, when THEMIS approaches to apogee of ~14.7 R_E, the probes enter deep into the magnetosheath and sometimes encounter with the magnetosphere.

[42] Figure 10 demonstrates a part of that at 0400–1200 UT, when the THEMIS probes are located at the distances from ~12 to 14.7 R_E (see Figure 4c). During 0400–0700 UT, all the probes observe the magnetosphere. However, the magnetopause model predicts magnetosheath for the outer probes THB, THC, THD, and THE. That is not the case. Since THB magnetic field on average is 2.5 times stronger than the dipole, we infer that THB located at ~14.4 R_E observes the shielding effect of the Chapman-Ferraro current and, hence, it is close to the magnetopause. That inference is supported by multiple MP crossings observed by THB at 0700–0800 UT.

[43] In the magnetosphere, THEMIS probes observe quasi-periodic variations of the geomagnetic field with average period of ~10 min that indicates MP undulations.

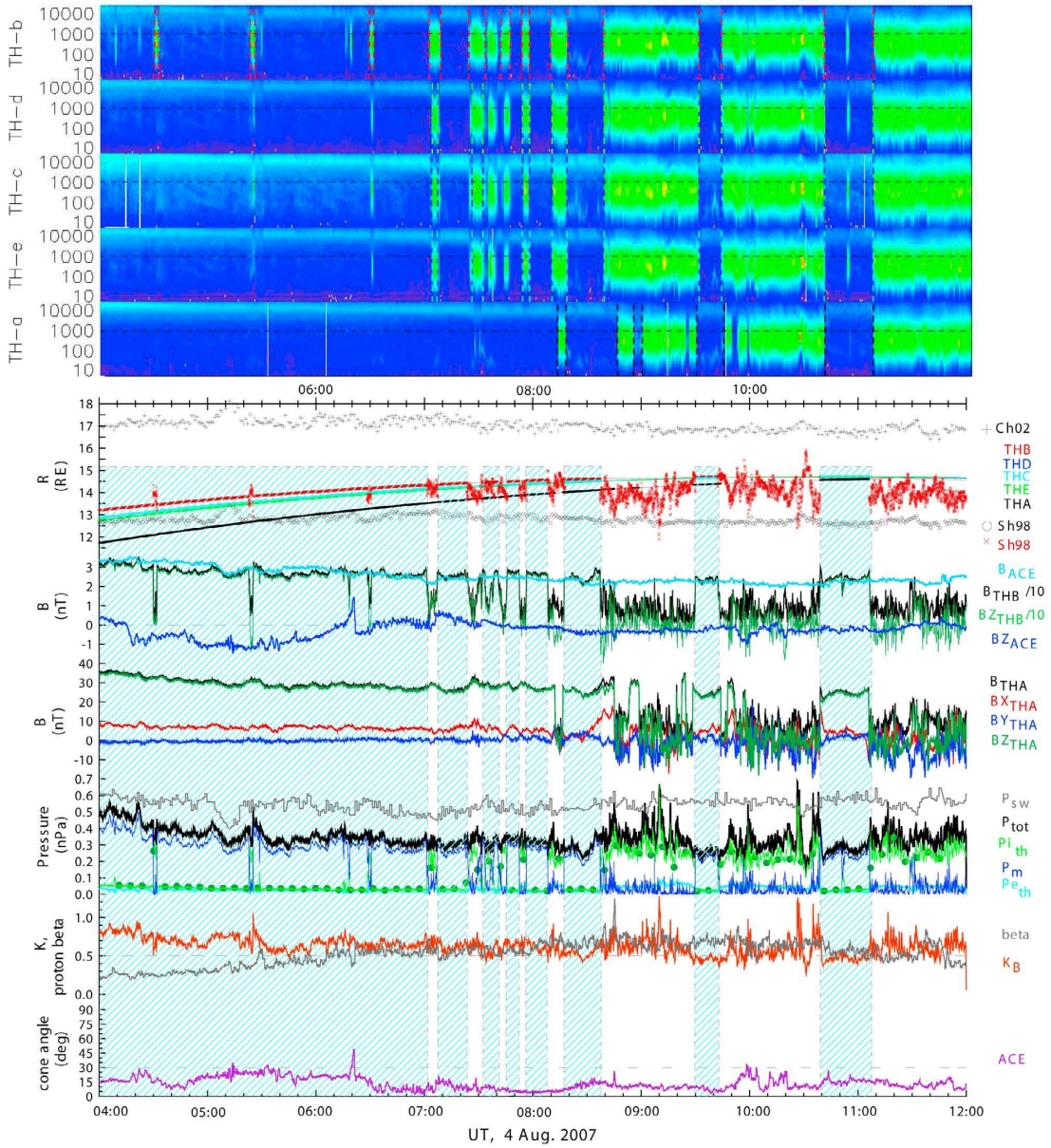

Figure 10. The same as Figure 6 but for 0400–1200 UT on 4 August 2007. A panel with THA magnetic field (magnitude and components) is shown instead of a panel with THB velocity components.

Sometimes, about one time per hour, the fluctuations of MP location are so large that the THB crosses the magnetopause. Transient magnetosheath rebounds of ~1 min duration are observed by THB at ~0430 UT, ~0525 UT, and ~0630 UT. Note, that during this 3 h interval, we find no obvious correlation of the magnetospheric field variations with the SW pressure, although a prominent change of the SW pressure at ~0500–0520 UT produces a geomagnetic field decrease.

[44] After 0700 UT, the outer probes approach to the magnetopause and observe multiple magnetosheath encounters. The innermost THA probe does not leave the magnetosphere until ~0810 UT and observes geomagnetic field variations correlating well with the inward and outward magnetopause motion. We have to point out that those MP fluctuations as well as others occurred later (see, for example, THA at 0900–1000 UT) do not relate to variations of solar wind parameters. A similar situation is revealed for

three magnetosphere rebounds observed by all the probes at 0820–0840, 0930–0945, and 1040–1110 UT. Moreover, the MP crossings of THA do not correlate with the magnetosheath pressure variations observed by the outer THEMIS probes.

[45] From ~0810 UT, all the THEMIS probes successively enter the magnetosheath. The innermost probe THA crosses the magnetopause at distance of ~14.0 R_E and enters the magnetosheath for 5 min. The average velocity of the inward MP motion is estimated at ~16 km/s, which is not typical for transient events. From 0820 UT, all satellites are located inside the magnetosphere and observe decreasing geomagnetic field with minimum at ~0830 UT. This means that the MP moves far from the outermost THB probe located at 14.6 R_E; i.e., the magnetopause is at distances that are at least ~2.1 R_E larger than the Sh98 model prediction of ~12.5 R_E. The model prediction becomes much more accurate when we use the magnetosheath total pressure *Ptot* measured by THB instead solar wind pressure *Psw*.

[46] From 0840 UT, all probes enter to the magnetosheath. Comparing THE and THA locations and magnetospheric field profiles from 0830 to 0900 UT we determine the MP velocity of 5 km/s and average MP position between 14.2 and 14.5 R_E. The magnetosheath intervals at 0840–0930, 0945–1040, and after 1110 UT are highly turbulent and populated by sporadic structures of high plasma pressure, which are similar to magnetosheath transient plasma jets [*Němeček et al.*, 1998; *Savin et al.*, 2004, 2008]. Such transient jets are characterized by intense localized ion fluxes, whose kinetic energy density can be even higher than those in the upstream solar wind.

[47] In the present case, the magnetosheath total pressure measured by THB fluctuates from 0.3 to 0.7 nPa, and the ratio K varies quickly between 0.3 and 1.3. The LPM is characterized by quasi-static flow balance with the base line of *Psw* ~0.3 nPa and K ~0.4 to 0.5. That balance is disturbed by inherent transient dynamics manifested in the plasma jets. There is no obvious correlation of the magnetosheath pressure variations with the dynamics of cone angle and/or SW pressure.

6. Discussion

[48] We have analyzed three cases of quasi-radial IMF and revealed substantial magnetopause expansions accompanied by nearly constant solar wind total pressure. With in situ THEMIS and Geotail observations, we have found that during quasi-radial IMF, the whole magnetosphere is expanded significantly, far beyond the expected position. Dramatic decreases in the magnetosheath total pressure in each case were observed by the THEMIS probes.

[49] At ~0525 UT on 8 August, THEMIS observed the subsolar magnetopause at distance of ~14.5 R_E, which is >3 R_E from the model prediction. At the same time, Geotail observed the MP in the tail region at distances of ~7 R_E from the model prediction of ~21 R_E for *Psw* ~1.1 nPa. That is different from the assumption of bullet-like magnetopause proposed by *Merka et al.* [2003]. The maximum magnetopause distance of 14.7 R_E, observed by THEMIS in apogee at ~1100 UT on 4 August for *Psw* ~0.6 nPa, is restricted by the orbital bias. We estimate that the subsolar magnetopause might expand up to 16 R_E.

[50] Such a distant position is proper to the bow shock rather than to the magnetopause. Because of the orbital bias, the distant bow shock could not be observed for those cases. On the basis of average velocities of the magnetopause and bow shock observed at 0533–0535 UT on 8 August, we estimate a bow shock distance of ~16.4 R_E and magnetosheath thickness of ~1.9 R_E, which is substantially different from their nominal values of ~15 R_E and ~4 R_E, respectively. This discrepancy is a subject of further investigations based on THEMIS data in 2008 to 2009 when the outer probes move to larger distances from the Earth.

[51] For quasi-radial IMF, we have found an ambiguous dependence of the subsolar magnetopause distance on the solar wind pressure. Namely, the average location of the expanded subsolar magnetopause is estimated at ~12.5 to 12.7 R_E for the SW pressure *Psw* ~1.3–1.5 nPa at ~2000–2030 UT on 16 July, ~14.5 R_E for the *Psw* ~1.1–1.3 nPa at ~0500–0530 UT on 8 August, and ~14.4 R_E for the *Psw* ~0.5–0.6 nPa at ~0600–0800 UT on 4 August. The difference in the magnetopause locations cannot be explained by the effect of southward IMF because the magnitude of IMF *Bz* was very small. These cases were not accompanied by geomagnetic storms. Therefore, the magnetopause location in these cases is controlled by other driving parameters.

[52] A significance of these driving parameters is demonstrated in the following example. Comparing Figures 6 and 8, we reveal that for the same SW pressure of ~1.3 nPa and northward IMF, the subsolar MP is located between THA and THE (i.e., between 10.5 and 11.7 R_E) at ~1955 UT on 16 July, whereas it is beyond 14.5 R_E at ~0530 UT on 8 August. From the presented examples, we can determine the maximal observed displacement of the subsolar MP is at least >3 R_E and possibly as large as ~5 R_E, which corresponds to ~30% uncertainty in the MP location.

[53] It is well known that the magnetopause is driven directly by the plasma and magnetic pressure of adjacent magnetosheath. According to classical hydrodynamic theory (see *Spreiter et al.* [1966] for reference), a ratio K of the stagnation pressure at the subsolar magnetopause to the upstream SW pressure should approach to 0.881 when the Mach number is much greater than unity. However, after the late 1980s, scientists found indications that MP location under quiet conditions (northward IMF) is controlled not only by the SW pressure but also by the IMF orientation [e.g., *Fairfield et al.*, 1990; *Sibeck*, 1995]. It was proposed that during radial (transverse) IMF, the pressure applied to the magnetopause is smaller (higher). This idea was used for interpretation of unusually distant MP [*Laakso et al.*, 1998; *Merka et al.*, 2003; *Zhang et al.*, 2009].

[54] THEMIS observations of the low-pressure magnetosheath support the idea proposed by *Fairfield et al.* [1990] that the fraction of the SW pressure applied to the magnetopause depends on the orientation of IMF, and for radial IMF the ratio K is considerably smaller than theoretical prediction of 0.881. In the case of pronounced LPM, we discover very low thermal pressure P_{th} and extremely low magnetic pressure P_m in the magnetosheath, such that only a small portion of solar wind kinetic energy is applied to the subsolar magnetopause and the ratio K is ~0.5 and even less. Under such conditions, the magnetosheath plasma β is very large. The high-β magnetosheath for quasi-radial IMF was reported by *Le and Russell* [1994]. They showed that during

quasi-radial IMF the high value of plasma β in the magnetosheath does not depend on the IMF strength and value of the solar wind plasma β.

[55] We have to note that the accuracy of ratio K calculation can be greatly affected by the quality of upstream solar wind data and THEMIS calibration errors. It is known that the characteristics of SW plasma and IMF affecting the magnetosphere might be different from those observed far upstream of the Earth [*Zastenker et al.*, 1998; *Richardson and Paularena*, 2001; *Riazantseva et al.*, 2002]. The difference increases with a spacecraft separation perpendicular to the Sun-Earth line (P-separation), as one can see in Figures 1–3. To minimize this effect, upstream data provided by the ACE monitor is used, which has the smallest P-separation. In addition, the solar wind with small IMF cone angles is more structured than that for the perpendicular IMF, such that even for small P-separation, solar wind structures observed far upstream correlate weakly with those observed near the Earth. Without a near-Earth satellite, this effect is difficult to rule out.

[56] However, a major parameter controlling that correlation is the variability of the SW density. In Figures 1–3, one can see relatively weak density variations as observed by ACE. Under such conditions, the SW dynamic pressure detected by ACE is close to that detected by Wind at very large P-separation. Hence, it is unlikely that the solar wind plasma conditions affecting the Earth's magnetosphere appear substantially different than that observed in a wide spatial range by ACE and Wind. At the same time, we can point out a pure correlation for the IMF such that the quasi-radial IMF is observed by Wind occasionally. It is reasonable to suggest that Wind observes different IMF due to the large P-separation. Therefore, the ACE plasma and magnetic data are more reliable for the present study.

[57] Absolute calibration of the THEMIS plasma instruments was done through cross calibration with the Wind-SWE instrument [*McFadden et al.*, 2008]. As for the considered period of summer 2007, the authors also executed a final test of the absolute calibration when magnetopause crossings were evaluated to check for pressure balance (i.e., the same way used in our study). The total pressure was found to be nearly constant during the MP crossings, which proves the accurate absolute calibrations of the plasma instruments. Here we have to point out that the THEMIS/ESA instrument operates in various modes. The high-resolution measurements of plasma parameters, including velocity, are provided in the fast and slow survey full modes with 1.5 and 6 min resolution. Very often in the magnetosheath the instrument operates in the fast survey reduced mode with a low angular/energy resolution and high time resolution (3 s). As a result, that mode provides reliable data only for low-speed plasma. In the first case event on 16 July, the THEMIS/ESA operated in the fast reduced mode. Figure 7 shows that the transversal components of the magnetosheath plasma velocity are not very large in close vicinity of the magnetopause. Therefore, the most reliable plasma data and total magnetosheath pressure can be obtained only near the magnetopause. The second and third case events, when plasma velocity was unavailable (slow reduced mode with omni-directional spectra), were analyzed on the base of that rule. This way, we obtain reliable estimations of the ratio K derived from the ACE and THEMIS data.

[58] The problem of solar wind energy transformation in the LPM mode is an important but still poorly understood issue. It is quite possible that the origin of LPM is related to particular formation of the bow shock and magnetosheath under quasi-radial IMF conditions that result in redistribution of the solar wind energy and decreasing the portion of energy affecting the magnetopause. First of all, the transverse component of quasi-radial IMF is so small that magnetic field is weakly amplified at the bow shock and in the magnetosheath [*Le and Russell*, 1994].

[59] In the literature, we have found a few mechanisms that might cause a low ratio K. *Wilkinson* [2003] presents the high-Mach-number $Q_{||}$ bow shock as a thick ($\geq$2–2.5 R_E, radially) magnetic pulsation region, characterized by ion reflection at bow shock front and leakage from the magnetosheath with propagation far into the upstream region and by a rich variety of interacting wave modes and particle distributions. In that region, the SW is heated and deflected, often by 20°–40° or more. *Schwartz and Burgess* [1991] propose a general description of that transition zone as a quite filamentary 3-D structure. Deceleration of the solar wind upstream of the $Q_{||}$ bow shock is also essential due to the interaction with short large-amplitude magnetic structures [*Schwartz et al.*, 1992] and with ion foreshocks [*Zhang et al.*, 1995].

[60] *Savin et al.* [2008] suggested another mechanism of the solar energy redistribution inside the magnetosheath. They found that the magnetosheath kinetic energy density during more than 1 h can exhibit an average level and a series of jets (i.e., peaks far exceeding the kinetic energy density in the undisturbed solar wind). It was suggested that dynamic interaction in the magnetosheath plasma is nonuniform and intrinsically transient, as the plasma is still evolving from the shocked to a statistically equilibrium turbulent state. In the course of this evolution, it seems that processes may occur that concentrate the free energy in the still underdeveloped turbulence and focus the plasma into jets. It was noted that the jets could weakly interact with the magnetopause and thus provide the super-diffusive plasma transport inside the magnetosphere. Apparently, in the presence of jets, the background magnetosheath energy should be decreased.

[61] SW structures with quasi-radial IMF are observed quite often at declining speed profiles within the trailing portions of ICME [*Neugebauer et al.*, 1997] or within corotating rarefaction regions [*Jones et al.*, 1998; *Gosling and Skoug*, 2002]. Those structures, expanding from the Sun, can last from hours to several days. They are characterized by relatively weak IMF and relatively low plasma density/pressure in the upstream solar wind [e.g., *Riley and Gosling*, 2007].

[62] In order to estimate numerically the characteristic properties of solar wind for quasi-radial IMF in the 23rd solar cycle, we have performed a statistical analysis of 16 s ACE magnetic and 1 min plasma data for 11 years from 1998 to 2008. In Figure 11, a statistical distribution of the solar wind dynamic pressure measured by ACE during intervals of quasi-radial IMF is compared with common distribution for 11 years. A deficiency of medium and high pressures is revealed for the intervals of quasi-radial IMF. The mean pressure for those intervals is ~1.4 nPa, which is smaller than the mean of 1.7 nPa for the common distri-

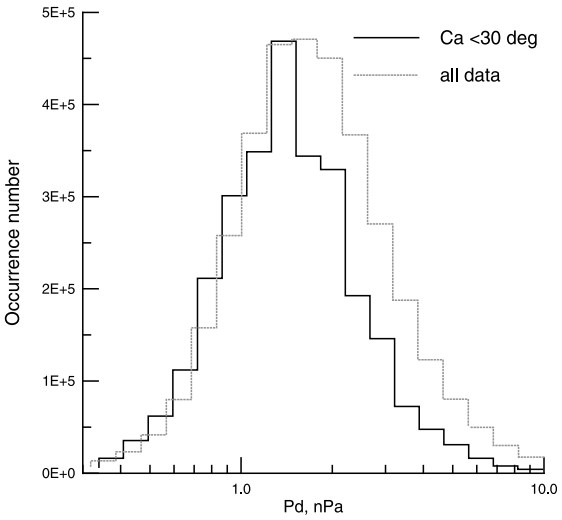

Figure 11. Statistical distributions of the solar wind dynamic pressure *Pd* observed by ACE for quasi-radial IMF with cone angle <30° (black solid histogram) and for whole time (gray dotted histogram) in 1998 to 2008. The mean, median, and most probable values of *Pd* for those two distributions are about 1.4 and 1.7 nPa, respectively. A deficiency of medium and high pressures is revealed for the statistics of quasi-radial IMF.

bution. Note that the mean pressure of 1.7 nPa is smaller than the average SW dynamic pressure of 2 nPa obtained for four solar cycles. That relatively small mean pressure results from relatively low solar wind density of ~2 to 4 cm^{-3} owing to an abnormal behavior of the 23rd solar cycle [*Dmitriev et al.*, 2009]. Therefore, the MP expansion related to quasi-radial IMF can be masked by the effect of low solar wind pressures, which makes statistical finding of the quasi-radial IMF effect difficult.

[63] From the statistical analysis we also find that cone angles of <30° are observed ~16% of the time. Figure 12 shows statistical distributions of integral occurrence probability of duration of intervals with cone angles below 30° for whole 11 year period and for 1 year in solar minimum. One can see that the intervals with a duration of more than 10 min contribute to ~30% of statistics. Therefore, they can be observed ~5% of time. Five minutes intervals occur ~8% of the time. The number of long-lasting intervals is higher in the solar minimum. Thus, the quasi-radial IMF occurs quite often. In this sense, the phenomenon of LPM-associated MP expansion might be rather typical than unusual and thus the effect of small cone angle should be taken into account in future magnetopause modeling.

[64] Figure 13 illustrates the effect of magnetopause expansion for the LPM mode. The MP crossings observed by THEMIS on 16 July 2007 and by THEMIS and Geotail on 8 August 2007 can be predicted by the reference model applied for the magnetosheath pressure of 0.5 nPa ($K = 0.3$) and 0.1 nPa ($K = 0.07$), respectively. Note that the SW pressure for those cases was ~1.1–1.5 nPa. The MP crossings observed by THEMIS on 4 August 2007 are well described by the model calculated for the magnetosheath pressure of 0.3 nPa, while the SW pressure is 0.6 nPa.

[65] The expanded outer magnetosphere has a lower magnetic field and thus becomes more sensitive to variations of both major and minor driving parameters. As a result, a small change in the SW pressure and/or IMF orientation can lead to a substantial transient motion of the boundary. We have also found MP displacements in response to variations of substorm activity, represented by the *AE* index. Therefore, during LPM the effect of cone angle can strongly interfere with effects produced by other driving parameters.

[66] We observed several cases of prominent MP inward/outward motion when the cone angle exceeds/falls down a certain threshold of 20° to 25°. However, we also have found a number of cases when the MP motion is not related to both variations of the upstream parameters, including the cone angle and the magnetosheath pressure. Such motion probably can be attributed to the MP undulations with a wide range of periods. Thus, a feature of the MP dynamics for long-lasting quasi-radial IMF is characterized by a superposition of the steady state expansion and wavy MP motion. New equilibrium position of the MP can be remote by several R_E from the nominal. That position is mainly controlled by the ratio *K*, which is much smaller than the theoretical prediction of 0.881. The magnetopause undulates near the new equilibrium location. The velocity of undulating magnetopause is found to be highly variable from several kilometers per second to >200 km/s (see Table 1). A

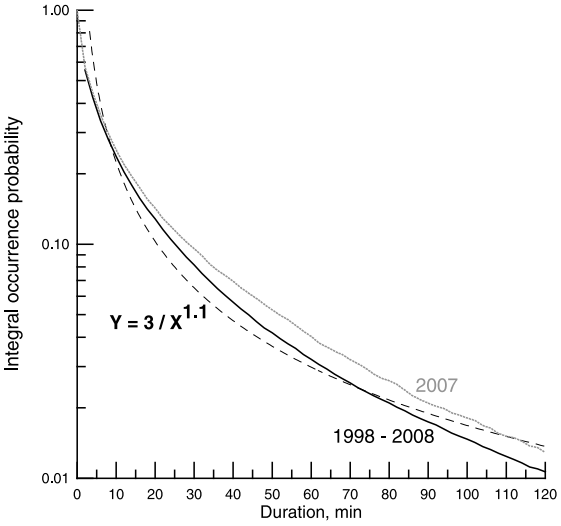

Figure 12. Integral occurrence probability of intervals with quasi-radial IMF (cone angle <30°) constructed on the base of 16 s resolution ACE magnetic data for 11 years from 1998 to 2008 (black solid line) and for the year 2007 (gray dotted line). The 11 year distribution can be fit by a power function (dashed line) with the exponent of ~1.1. The solar minimum in 2007 is enriched by long-lasting intervals of quasi-parallel IMF.

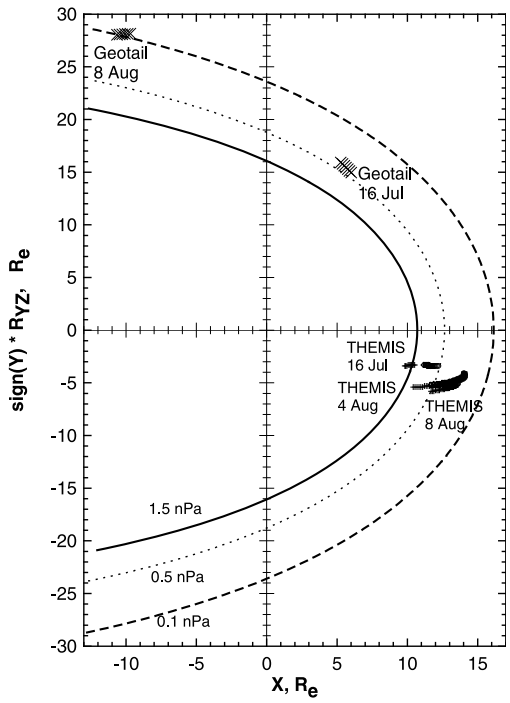

Figure 13. GSM locations of the THEMIS probes and Geotail at 1950–2037 UT on 16 July 2007, 0400–0600 UT on 8 August 2007, and 0400–1200 UT on 4 August 2007. The magnetopause profiles are predicted by a reference model [*Shue et al.*, 1998] for various pressures: 0.1 (dashed line), 0.5 (dotted line), and 1.5 nPa (solid line).

similar range of the MP velocities for quasi-radial IMF was reported by *Le and Russell* [1994].

[67] We have to point out that the ratio K has no direct linear relationship with the cone angle. We observe that for the large cone angles of >25°, the ratio increases and approaches to its theoretical value. However, the small cone angles (<20°) are accompanied by the K varying in a wide range from 0.16 to 0.6. We can assume that the value of K for quasi-radial IMF depends on the upstream SW plasma β. On 16 July and 4 August, when the proton β was much smaller than 1, the value of K was about 0.5. During the interval of very low K on 8 August, the SW plasma β was close to 1 and even larger.

[68] Our assumption is based on results of magnetosheath modeling. *De Sterck and Poedts* [1999, 2001] investigated the bow shock and magnetosheath topology for quasi-radial IMF, a Mach number less than 6, and low proton β (<0.6). The 3-D MHD simulation was performed for the idealized setting of flow around a rigid paraboloid magnetopause. The authors reveal very complex topology of the bow shock and magnetosheath, which is controlled by three SW parameters: β, the Mach number, and IMF cone angle. It is hard to apply those results directly to our cases, which are accompanied by high Mach numbers and relatively high proton β (>0.6). However, it is possible that the same driving parameters might control the LPM mode.

[69] In the present study, we demonstrate three cases characterized by different durations, upstream solar wind and magnetosheath plasma properties, and magnetospheric conditions. But they have one common feature: LPM. It is quite possible that the LPM might result from different mechanisms. Thus, we believe that further comprehensive statistical study of the magnetosheath plasma and magnetic field properties is an important key to a clear insight into the mechanisms of the LPM formation.

7. Conclusions

[70] With THEMIS data, we reveal that the magnetopause expansions are caused by a significant decrease of total pressure in high-β magnetosheath (LPM mode). Prominent LPM mode is observed when the IMF cone angles are less than 20° ~ 25°.

[71] From simultaneous observations of Geotail and THEMIS, we infer a global expansion of the magnetopause. The magnetopause is found more than 3 and ~7 R_E away from the nominal location in the dayside and tail region, respectively.

[72] The MP expansion can persist for a few hours, as long as quasi-radial IMF conditions, which indicates a steady state process driving the magnetopause. The equilibrium MP position was determined at 12.5 to 12.7 R_E for the upstream SW pressure *Psw* ~1.3–1.5 nPa and the adjacent magnetosheath total pressure *Ptot* ~0.5 nPa, ~14.5 R_E for *Psw* ~1.1–1.3 nPa and *Ptot* ~0.16–0.3 nPa, and ~14.4 R_E for *Psw* ~0.5–0.6 nPa and *Ptot* ~0.25–0.35 nPa. The equilibrium MP position is affected by geomagnetic activity.

[73] Minimal value of the total pressure observed by THEMIS in the adjacent magnetosheath is 0.16 nPa and thus the fraction K of the SW pressure applied to the MP can be as extremely small as 0.2. The ratio K decreases with increasing upstream SW plasma β.

[74] Statistical study of 11 years of ACE data reveals that the quasi-radial IMF conditions are not very rare and occur for ~16% of time. Those conditions frequently interfere with the small solar wind pressure, which makes it difficult to distinguish the cone angle effect statistically.

[75] **Acknowledgments.** We acknowledge NASA contract NAS5-02099 and V. Angelopoulos for use of data from the THEMIS mission. We thank K.H. Glassmeier and U. Auster for the use of FGM data provided under contract 50 OC 0302. We thank N. Ness and D.J. McComas for the use of ACE solar wind data made available via the CDAWeb. The Geotail magnetic field and plasma data were provided by T. Nagai and Y. Saito, respectively. This work was supported by grants NSC 98-2811-M-008-043, NSC-98-2111-M-008-019, and NSC 98-2111-M-008-004. The work at Charles University was supported by the Czech Grant Agency under contract 205/09/0112 and by the Research Plan MSM 0021620860.

[76] Philippa Browning thanks Nick Omidi and another reviewer for their assistance in evaluating this paper.

References

Angelopoulos, V. (2008), The THEMIS mission, *Space Sci. Rev.*, *141*(1–4), 5–34, doi:10.1007/s11214-008-9336-1.

Auster, H. U., et al. (2008), The THEMIS fluxgate magnetometer, *Space Sci. Rev.*, *141*, 235– 264, doi:10.1007/s11214-008-9365-9.

Chao, J. K., D. J. Wu, C.-H. Lin, Y.-H. Yang, X. Y. Wang, M. Kessel, S. H. Chen, and R. P. Lepping (2002), Models for the size and shape of the Earth's magnetopause and bow shock, in *Space Weather Study Using Multipoint Techniques*, edited by L.-H. Lyu, pp. 127–136, Elsevier Sci., Netherlands.

De Sterck, H., and S. Poedts (1999), Stationary slow shocks in the magnetosheath for solar wind conditions with $\beta < 2/\gamma$: Three-dimensional MHD simulations, *J. Geophys. Res.*, *104*(A10), 22,401–22,406.

De Sterck, H., and S. Poedts (2001), Disintegration and reformation of intermediate-shock segments in three-dimensional MHD bow shock flows, *J. Geophys. Res.*, *106*(A12), 30,023–30,037, doi:10.1029/2000JA000205.

Dmitriev, A. V., J.-K. Chao, and D. J. Wu (2003), Comparative study of bow shock models using Wind and Geotail observations, *J. Geophys. Res.*, *108*(A12), 1464, doi:10.1029/2003JA010027.

Dmitriev, A. V., A. V. Suvorova, and I. S. Veselovsky (2009), Statistical characteristics of the heliospheric plasma and magnetic field at the Earth's orbit during four solar cycles 20–23, in *Handbook on Solar Wind: Effects, Dynamics and Interactions*, edited by H. E. Johannson, pp. 81–144, NOVA Sci., Inc., New York.

Fairfield, D. H., W. Baumjohann, G. Paschmann, H. Lühr, and D. G. Sibeck (1990), Upstream pressure variations associated with the bow shock and their effects on the magnetosphere, *J. Geophys. Res.*, *95*(A4), 3773–3786.

Gosling, J. T., and R. M. Skoug (2002), On the origin of radial magnetic fields in the heliosphere, *J. Geophys. Res.*, *107*(A10), 1327, doi:10.1029/2002JA009434.

Jelinek, K., Z. Nemecek, J. Safrankova, J.-H. Shue, A. V. Suvorova, and D. G. Sibeck (2010), Thin magnetosheath as a consequence of the magnetopause deformation: THEMIS observations, *J. Geophys. Res.*, doi:10.1029/2010JA015345, in press.

Jones, G. H., A. Balogh, and R. J. Forsyth (1998), Radial heliospheric magnetic fields detected by Ulysses, *Geophys. Res. Lett.*, *25*(16), 3109–3112.

Laakso, H., et al. (1998), Oscillations of magnetospheric boundaries driven by IMF rotations, *Geophys. Res. Lett.*, *25*(15), 3007–3010.

Le, G., and C. T. Russell (1994), The thickness and structure of high beta magnetopause current layer, *Geophys. Res. Lett.*, *21*(23), 2451–2454.

Lockwood, M. (2001), The day the solar wind nearly died, *Nature*, *409*, 677–679, doi:10.1038/35055654

McFadden, J. P., C. W. Carlson, D. Larson, M. Ludlam, R. Abiad, B. Elliott, P. Turin, M. Marckwordt, and V. Angelopoulos (2008), The THEMIS ESA plasma instrument and in-flight calibration, *Space Sci. Rev.*, *141*, 277–302, doi:10.1007/s11214-008-9440-2.

Merka, J., A. Szabo, J. Šafránková, and Z. Němeček (2003), Earth's bow shock and magnetopause in the case of a field-aligned upstream flow: Observation and model comparison, *J. Geophys. Res.*, *108*(A7), 1269, doi:10.1029/2002JA009697.

Němeček, Z., J. Šafránková, L. Přech, D. G. Sibeck, S. Kokubun, and T. Mukai (1998), Transient flux enhancements in the magnetosheath, *Geophys. Res. Lett.*, *25*(8), 1273–1276.

Neugebauer, M., R. Goldstein, and B. E. Goldstein (1997), Features observed in the trailing regions of interplanetary clouds from coronal mass ejections, *J. Geophys. Res.*, *102*(A9), 19,743–19,752.

Petrinec, S. M., and C. T. Russell (1993), External and internal influences on the size of the dayside terrestrial magnetosphere, *Geophys. Res. Lett.*, *20*(5), 339–342.

Riazantseva, M. O., P. A. Dalin, A. V. Dmitriev, Y. V. Orlov, K. I. Paularena, J. D. Richardson, and G. N. Zastenker (2002), A multifactor analysis of parameters controlling solar wind ion flux correlations using an artificial neural network technique, *J. Atmos. Sol. Terr. Phys.*, *64*(5–6), 657–660.

Richardson, I. G., D. Berdichevsky, M. D. Desch, and C. J. Farrugia (2000), Solar-cycle variation of low density solar wind during more than three solar cycles, *Geophys. Res. Lett.*, *27*(23), 3761–3764, doi:10.1029/2000GL000077.

Richardson, J., and K. Paularena (2001), Plasma and magnetic field correlations in the solar wind, *J. Geophys. Res.*, *106*(A1), 239–251.

Riley, P., and J. T. Gosling (2007), On the origin of near-radial magnetic fields in the heliosphere: Numerical simulations, *J. Geophys. Res.*, *112*, A06115, doi:10.1029/2006JA012210.

Russell, C. T., S. M. Petrinec, T. L. Zhang, P. Song, and H. Kawano (1997), The effect of foreshock on the motion of the dayside magnetopause, *Geophys. Res. Lett.*, *24*(12), 1439–1441.

Savin, S. P., et al. (2004), Dynamic interaction of plasma flow with the hot boundary layer of a geomagnetic trap, *JETP Lett.*, Engl. Transl., *79*(8), 452–456.

Savin, S. P., et al. (2008), High energy jets in the Earth's magnetosheath: Implications for plasma dynamics and anomalous transport, *Sov. Phys. JETP*, Engl. Transl., *87*(11), 593–599.

Schwartz, S. J., and D. Burgess (1991), Quasi-parallel shocks: A patchwork of three-dimensional structures, *Geophys. Res. Lett.*, *18*, 373–376.

Schwartz, S. J., D. Burgess, W. P. Wilkinson, R. L. Kessel, M. Dunlop, and H. Lühr (1992), Observations of short large-amplitude magnetic structures at a quasi-parallel shock, *J. Geophys. Res.*, *97*(A4), 4209–4227.

Shevyrev, N. N., and G. N. Zastenker (2005), Some features of the plasma flow in the magnetosheath behind quasiparallel and quasiperpendicular bow shocks, *Planet. Space Sci.*, *53*, 95–102.

Shevyrev, N. N., G. N. Zastenker, and J. Du (2007), Statistics of low-frequency variations in solar wind, foreshock and magnetosheath: INTERBALL-1 and CLUSTER data, *Planet. Space Sci.*, *55*(15), 2330–2335.

Shue, J.-H., et al. (1998), Magnetopause location under extreme solar wind conditions, *J. Geophys. Res.*, *103*(A8), 17,691–17,700.

Sibeck, D. G. (1992), Transient events in the outer magnetosphere: Boundary waves or flux transfer events?, *J. Geophys. Res.*, *97*(A4), 4009–4026.

Sibeck, D. G. (1994), Signatures of flux erosion from the dayside magnetosphere, *J. Geophys. Res.*, *99*(A5), 8513–8529.

Sibeck, D. G. (1995), The magnetospheric response to foreshock pressure pulses, in *Physics of the Magnetopause*, edited by P. Song, B. U. O. Sonnerup, and M. Thomsen, pp. 293–302, AGU, Washington, D. C.

Sibeck, D. G., and J. T. Gosling (1996), Magnetosheath density fluctuations and magnetopause motion, *J. Geophys. Res.*, *101*(A1), 31–40.

Sibeck, D. G., et al. (1989), The magnetospheric response to 8-minute-period strong-amplitude upstream pressure variations, *J. Geophys. Res.*, *94*(A3), 2505–2519.

Spreiter, J. R., A. L. Summers, and A. Y. Alksne (1966), Hydromagnetic flow around the magnetoshere, *Planet. Space Sci.*, *14*, 223–253.

Terasawa, T., et al. (2000), GEOTAIL observations of anomalously low density plasma in the magnetosheath, *Geophys. Res. Lett.*, *27*(23), 3781–3784, doi:10.1029/2000GL000087.

Wilkinson, W. P. (2003), The Earth's quasi-parallel bow shock: Review of observations and perspectives for Cluster, *Planet. Space Sci.*, *51*, 629–647.

Zastenker, G. N., P. A. Dalin, A. J. Lazarus, K. I. Paularena (1998), Comparison of the solar wind parameters measured simultaneously aboard several spacecraft (in Russian), *Kosmich. Issled.*, *36*(3), 228–240.

Zastenker, G. N., M. N. Nozdrachev, Z. Němeček, J. Šafránková, L. Přech, K. I. Paularena, A. J. Lazarus, R. P. Lepping, and T. Mukai (1999), Plasma and magnetic field variations in the magnetosheath: Interball–1 and ISTP spacecraft observations, in *Interball in the ISTP Program: Studies of the Solar Wind-Magnetosphere-Ionosphere Interaction*, vol. 537, *NATO Science Series*, edited by D. G. Sibeck and K. Kudela, pp. 277–294, Kluwer Acad., Netherlands.

Zastenker, G. N., M. N. Nozdrachev, Z. Němeček, J. Šafránková, K. L. Paularena, J. D. Richardson, R. P. Lepping, and T. Mukai (2002), Multispacecraft measurements of plasma and magnetic field variations in the magnetosheath: Comparison with Spreiter models and motion of the structures, *Planet. Space Sci.*, *50*, 601–612.

Zhang, T.-L., K. Schwingenschuh, and C. T. Russell (1995), A study of the solar wind deceleration in the Earth's foreshock region, *Adv. Space Res.*, *15*(8–9),137–140.

Zhang, H., Q.-G. Zong, D. G. Sibeck, T. A. Fritz, J. P. McFadden, K.-H. Glassmeier, and D. Larson (2009), Dynamic motion of the bow shock and the magnetopause observed by THEMIS spacecraft, *J. Geophys. Res.*, *114*, A00C12, doi:10.1029/2008JA013488.

K. Ackerson, Department of Physics and Astronomy, Van Allen Hall, University of Iowa, Iowa City, IA 52242, USA.

A. V. Dmitriev, J.-H. Shue, and A. V. Suvorova, Institute of Space Science, National Central University, Jhongli City 32001, Taiwan. (suvorova_alla@yahoo.com)

H. Hasegawa, ISAS/JAXA, 3-1-1 Yoshinodai, Sagamihara, Kanagawa 229-8510, Japan.

K. Jelínek, Z. Němeček, and J. Šafránková, Faculty of Mathematics and Physics, Charles University, V Holesovickach 2, 18000 Praha 8, Czech Republic.

J. P. McFadden, Space Science Laboratory, University of California, Berkeley, CA 94720, USA.

D. G. Sibeck, NASA Goddard Space Flight Center, Code 674, Greenbelt, MD 20771, USA.

C.3 Thin magnetosheath as a consequence of the magnetopause deformation: THEMIS observations

JOURNAL OF GEOPHYSICAL RESEARCH, VOL. 115, A10203, doi:10.1029/2010JA015345, 2010

Thin magnetosheath as a consequence of the magnetopause deformation: THEMIS observations

K. Jelínek,[1] Z. Němeček,[1] J. Šafránková,[1] J.-H. Shue,[2] A. V. Suvorova,[2,3] and D. G. Sibeck[4]

Received 8 February 2010; revised 14 May 2010; accepted 24 May 2010; published 2 October 2010.

[1] This paper presents a simultaneous observation of the bow shock and magnetopause by THEMIS probes that allows determination of the actual magnetosheath thickness at the subsolar point. Moreover, Geotail located at the dusk dayside magnetosheath registered a brief excursion to the magnetosphere in this time. The spacecraft configuration reveals a significant deformation of the magnetopause surface that locally decreases its curvature radius. The highly curved magnetopause results in the decrease of the magnetosheath thickness to about half of its standard value in a particular observation point. The observed phenomenon is attributed to a rotation of the interplanetary magnetic field (IMF). Although it is generally expected that the bow shock and magnetopause move in accord, being driven mainly by the solar wind dynamic pressure, we suggest that the local and transient thinning of the magnetosheath can result from different responses of its boundaries to a sudden change of the pressure and/or IMF orientation.

Citation: Jelínek, K., Z. Němeček, J. Šafránková, J.-H. Shue, A. V. Suvorova, and D. G. Sibeck (2010), Thin magnetosheath as a consequence of the magnetopause deformation: THEMIS observations, *J. Geophys. Res.*, *115*, A10203, doi:10.1029/2010JA015345.

1. Introduction

[2] The bow shock and magnetopause are formed by interaction of the solar wind and interplanetary magnetic field (IMF) with the Earth's magnetic field, and the magnetosheath is a region separating these boundaries. Using aerodynamics, *Seiff and Whiting* [1962] empirically showed that the standoff distance of the bow shock normalized by the radius of the obstacle (magnetopause) is nearly linearly proportional to the inverse density ratio across the bow shock. The relationship is as follows:

$$\frac{\Delta_{msh}}{a_{mp}} = 1.1\,\frac{\rho_{sw}}{\rho_{msh}} \tag{1}$$

where ρ is the density, Δ_{msh} is the standoff distance of the bow shock from the obstacle (equivalently, the magnetosheath thickness), a_{mp} is the distance from the center to the nose of the obstacle, and the subscripts indicate the upstream (*sw*) and the downstream (*msh*) states. The bow shock distance from the Earth, a_s is estimated as follows:

$$a_s = a_{mp} + \Delta_{msh}. \tag{2}$$

[3] *Spreiter et al.* [1966] applied this knowledge to gasdynamic flow around a magnetosphere and showed that the density ratio is related to the compressibility of the medium and the asymptotic free-stream Mach number, M, thus the relationship between these quantities is as follows:

$$\frac{\Delta_{msh}}{a_{mp}} = 1.1\,\frac{(\gamma-1)M^2+2}{(\gamma+1)M^2} \tag{3}$$

where γ is the polytropic index. This expression was later included into the bow shock model by *Formisano et al.* [1973]. The coefficient of 1.1 is supposed to be valid for explanation of the bow shock position in front of a blunt obstacle [*Seiff and Whiting*, 1962]. However, *Spreiter et al.* [1966] did not change the shape of the obstacle to test whether this value is valid for other blunt obstacles.

[4] *Farris and Russell* [1994] discussed the magnetosheath thickness and argued that it should be a function of the curvature radius, R_C of the obstacle. The authors modified the relation (3) to take into account this radius. Moreover, they pointed out that this relation provides a finite magnetosheath thickness for $M = 1$ and suggested a new expression that becomes the following:

$$a_s = R_C\left(\frac{a_{mp}}{R_C} + 0.8\,\frac{(\gamma-1)M^2+2}{(\gamma+1)(M^2-1)}\right). \tag{4}$$

[1]Faculty of Mathematics and Physics, Charles University, Prague, Czech Republic.
[2]Institute of Space Science, National Central University, Jhongli, Taiwan.
[3]Skobeltsyn Institute of Nuclear Physics, Moscow State University, Moscow, Russia.
[4]NASA Goddard Flight Center, Greenbelt, Maryland, USA.

0148-0227/10/2010JA015345

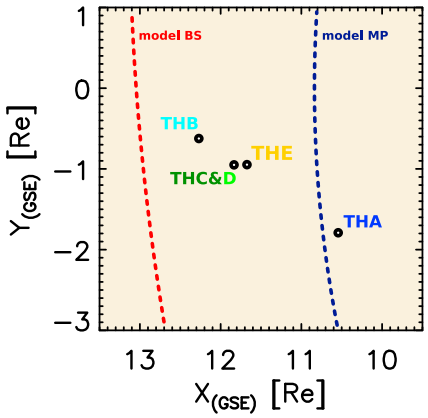

Figure 1. Locations of the THEMIS probes in the *X*-*Y* plane (in the GSE system) at 20 UT. The *Z* coordinates were between −3.3 R_E (THB) and −2.8 R_E (THA). Model magnetopause [*Shue et al.*, 1998] and bow shock [*Jeřáb et al.*, 2005] are showed by the blue and red dotted curves, respectively.

The correction puts the bow shock to infinity for $M = 1$ as one would intuitively expect. It would be noted that the discussed equations were derived using a gas dynamic approach where the Mach number has a clear meaning. A variety of wave modes propagating through the magnetized plasma with different speeds leads to definitions of their own Mach numbers; e.g., sonic, Alfvén, or magnetosonic Mach numbers.

[5] On the other hand, *Němeček and Šafránková* [1991] replaced the factor of 1.1 in (3) with a term that includes the IMF strength and used explicitly the Alfvénic Mach number. This approach was later precised by *Jeřáb et al.* [2005]. Further, *Cairns and Grabbe* [1994] developed an MHD theory for the bow shock standoff distance, a_s and thickness Δ_{msh} of the magnetosheath predicting that the ratio of Δ_{msh}/a_{mp} should depend strongly on θ, M_A and M_S, the angle between the magnetic field and flow, Alfvénic and sonic Mach numbers, respectively, for $M_A \leq 6$.

[6] We can conclude that the magnetosheath thickness is given by the difference between the locations of the bow shock and magnetopause, thus their motion in response to varying upstream conditions changes its thickness. However, the statistical models of these boundaries have different sets of driving parameters; only the solar wind dynamic pressure is common. For example, a dependence of the magnetopause location on the IMF B_Z sign is well established in magnetopause models [e.g., *Fairfield*, 1971; *Sibeck et al.*, 1991; *Roelof and Sibeck*, 1993; *Petrinec and Russell*, 1996; *Shue et al.*, 1997; *Boardsen et al.*, 2000] but the analysis in both *Jeřáb et al.* [2005] and *Merka et al.* [2005] shows that the bow shock does not respond to IMF B_Z changes.

[7] Furthermore, an influence of other parameters on locations of both boundaries was examined in different papers; for example, a rotation of the direction of the magnetic field across the magnetosheath [*Pudovkin et al.*, 1982], both IMF polar and azimuthal angles, and the angle between the IMF and the bow shock normal [*Laakso et al.*, 1998; *Šafránková et al.*, 2003], IMF B_Y component [*Sibeck et al.*, 2000], or Alfvénic fluctuations dominating the solar wind [*Tsubouchi et al.*, 2000]. Moreover, larger displacements of boundaries as a result of their interaction with different solar wind discontinuities (e.g., HFAs, strong interplanetary shocks, pressure pulses) were widely discussed by many authors [e.g., *Sibeck et al.*, 1999; *Farrugia et al.*, 2008; *Zhang et al.*, 2009; *Jacobsen et al.*, 2009].

[8] We went through THEMIS observations of the subsolar bow shock and magnetopause at the 2007–2009 years and found more than 10 cases when the whole magnetosheath was swept along the probes in 2–5 minutes. Since the typical values of speeds of the magnetopause [*Haaland et al.*, 2004] and bow shock [e.g., *Lepidi et al.*, 1996; *Šafránková et al.*, 2003] displacements are about 30–60 km/s, these observations suggest that the magnetosheath can be very thin (or the speeds of boundary displacements are very large) under some circumstances.

[9] The present paper discusses one case when the bow shock and magnetopause were observed simultaneously by two THEMIS probes and the magnetosheath thickness can be unambiguously estimated. We show that the thin magnetosheath is a consequence of a transient deformation of the magnetopause surface resulting in a locally decreased curvature radius. The magnetopause deformation is probably connected with the change of the IMF orientation.

2. Observations

[10] As shown in Figure 1, all THEMIS probes scanned the subsolar bow shock and magnetopause on the late afternoon of 16 July 2007. The locations of probes in GSE coordinates, times, and normals of the boundary crossings are listed in Table 1. The magnetopause normals are determined from magnetic field measurements [*Auster et al.*, 2008] by a minimum variance method, and the bow shock normals are calculated using magnetic coplanarity theorem. Table 1 also contains the parameters of crossings observed nearly simultaneously by Geotail at the dayside dusk magnetosheath.

[11] IMF and solar wind parameters propagated from the ACE (+225; −2; +23 R_E in GSE) and Wind (+253; −67; +17 R_E in GSE) locations toward THEMIS B (THB) together with Geotail observations in the magnetosheath are shown in Figure 2. We applied a standard two-step propagation method. In the first step, an auxiliary time lag between both spacecraft is computed under an assumption that the solar wind speed is 450 km/s. The real velocity measured by an upstream monitor at the time given by this auxiliary lag is then used for a determination of the final lag. Such procedure was applied to each point of the THB measurements for both solar wind monitors.

[12] The upstream density (first image) and velocity (second and third images) were very similar and stable on both monitors throughout the depicted interval. The same is true for the magnetic field magnitudes (fourth and fifth images). Consequently, typical driving parameters: the upstream dynamic pressure ($p_{SW} \sim 1.3$ nPa) and Mach number ($M_A \sim 11$) were about constant, and they cannot be responsible for observed displacements of boundaries. On the other hand, the IMF direction changed several times

Table 1. Survey of Magnetopause and Bow Shock Crossings Observed by THEMIS and Geotail[a]

Spacecraft	Time (UT)	Boundary	GSE Position [R_E]			n_{MP}/n_{BS}			Event
TH-B	2020:43.7	MP	12.11	−0.74	−3.33	−0.997	0.028	0.066	1
	2024:43.7	MP	12.16	−0.71	−3.34	−0.884	0.305	0.355	2
	*2032:43.7	MP	12.24	−0.65	−3.37	−0.794	0.321	0.516	3
	†2037:23.1	BS	12.28	−0.61	−3.38	−0.961	0.167	0.219	9
	2039:10.0	BS	12.30	−0.60	−3.39	−0.701	0.263	−0.663	11
TH-D	*2033:30.6	MP	11.83	−0.99	−3.23	−0.823	0.306	0.479	4
TH-C	*2033:32.5	MP	11.82	−0.95	−3.24	−0.859	0.186	0.477	5
TH-E	*2034:34.3	MP	11.68	−0.95	−3.22	−0.830	0.176	0.529	6
TH-A	*2036:13.7	MP	10.54	−1.80	−2.82	−0.899	0.107	0.424	7
	2036:30.6	MP	10.55	−1.80	−2.82	−0.422	−0.472	0.774	8
	†2037:41.8	MP	10.56	−1.79	−2.83	−0.338	−0.851	−0.402	10
	2042:04.3	MP	10.63	−1.76	−2.85	−0.959	0.271	0.088	14
Geotail	2039:45.0	MP	5.48	15.64	1.09	−0.635	−0.762	0.128	12
	2042:00.0	MP	5.45	15.67	1.08	−0.054	−0.734	−0.677	13

[a]The columns indicate the spacecraft name, times of boundary crossings of a particular spacecraft, the boundary crossed, coordinates of the crossing in GSE, estimated normals, and event numbers that are used in the figures. The asterisks denote the times used for calculation of a mean magnetopause normal and speed by the triangulation method, and the daggers stand for the bow shock and magnetopause crossings used for a determination of the instantaneous magnetosheath thickness.

and differs at ACE and Wind locations as it can be seen from IMF components and cone angles (sixth image). The cone angle was computed as the angle between the X_{GSE} axis and the IMF direction. Since the IMF orientation is principal for an interpretation of results, we add to the IMF images the THB magnetic field (as diamonds) for an interval around ≈2038 UT when it was located in the solar wind just upstream of the quasi-perpendicular bow shock. One can note that B_Y (green points) is the only nonzero component (≈4 nT) in THB observations.

[13] The last three images show the Geotail magnetic field, electron spectra, and five channels of the EPIC energetic ions. The energy of electrons, together with a moderate and fluctuating magnetic field, indicate that Geotail was in the magnetosheath for the whole interval except a short excursion into the magnetosphere at ≈2040 UT (see Table 1 for timing). A strongly spin-modulated flux of energetic particles suggests that Geotail was behind the quasi-parallel shock from 1920 to 2045 UT.

[14] The subject of a deeper analysis is the time interval from 2015 to 2045 UT that is distinguished by the shadowed area in Figure 2. Figure 3 presents observations of the THEMIS spacecraft ordered according to the distance of a particular spacecraft from the Earth. The first two images show ion energy spectra and magnetic field vector as measured by the outermost THB [*Auster et al.*, 2008; *McFadden et al.*, 2008]. One can note three magnetopause and two bow shock crossings. The last THB magnetopause crossing is followed by the crossings observed by THC, THD, and THE; they are indicated by the vertical lines in the next three images. The last two images present ion energy spectra and magnetic field from THA, and one can identify four magnetopause crossings there.

[15] We would like to stress some features in the ion energy spectrogram of THB. At ≈2036 UT, there is a dropout of energetic particles (first image in Figure 3) suggesting that the upstream bow shock changed from quasi-parallel to quasi-perpendicular. This change is complemented by the increase of the magnetosheath density and temperature.

[16] Analyzing multipoint observations of the magnetopause crossings, their sequence yields the magnetopause speed of ≈44.9 km/s along the normal (−0.936; +0.138; +0.324). These parameters were determined by the timing method [*Russell et al.*, 1983] that uses locations and times of crossings observed by THB-THE (events 3, 4, 5, and 6 in Table 1). We would like to point out that this fast and large (more than 1.6 R_E) magnetopause displacement was connected with significant distortion of the magnetopause surface. The normal to the *Shue et al.* [1998] model surface at the point of the THB magnetopause crossing is (+0.988; −0.093; −0.123), whereas we found an enlarged Z component of the normal in all magnetopause crossings (events 3–6). The other indication of this deformation is the direction of the magnetic field just inbound the magnetopause. In accord with the THEMIS location and a large positive tilt angle (+25°), one would expect that B_Z would be a principal component. Indeed, all THEMIS spacecraft observed the B_Z dominated magnetic field prior to 2020 UT, but the B_X component gradually increases afterward and becomes comparable with B_Z at the magnetopause crossings. Observations of THA reveal that the rotation back to the B_Z dominated orientation occurred between the second and third THA magnetopause crossings. Another check of a presence of the magnetopause deformation provides a comparison of the model magnetic field with observations. The *Tsyganenko and Stern* [1996] model predicts $\vec{B}$ = (7;3;42) nT just prior to the last THB magnetopause crossing, whereas THB observes $\vec{B}$ = (25;0;30) nT. A large B_X component suggests a deformation of the magnetopause surface in the XZ plane, but the fact that B_Y is comparable in both the model and observations does not imply that the magnetopause conserved its shape in the XY plane.

3. Discussion

[17] Since an interpretation of observations is rather difficult, we divide this section into two parts. It is generally expected that the magnetopause and bow shock locations are determined by upstream state, thus the first part deals with the upstream observations, whereas the discussion of the magnetosheath thickness is a subject of the second part.

3.1. Upstream Observations

[18] Upstream observations do not reveal any cause for the observed magnetopause displacement because the solar

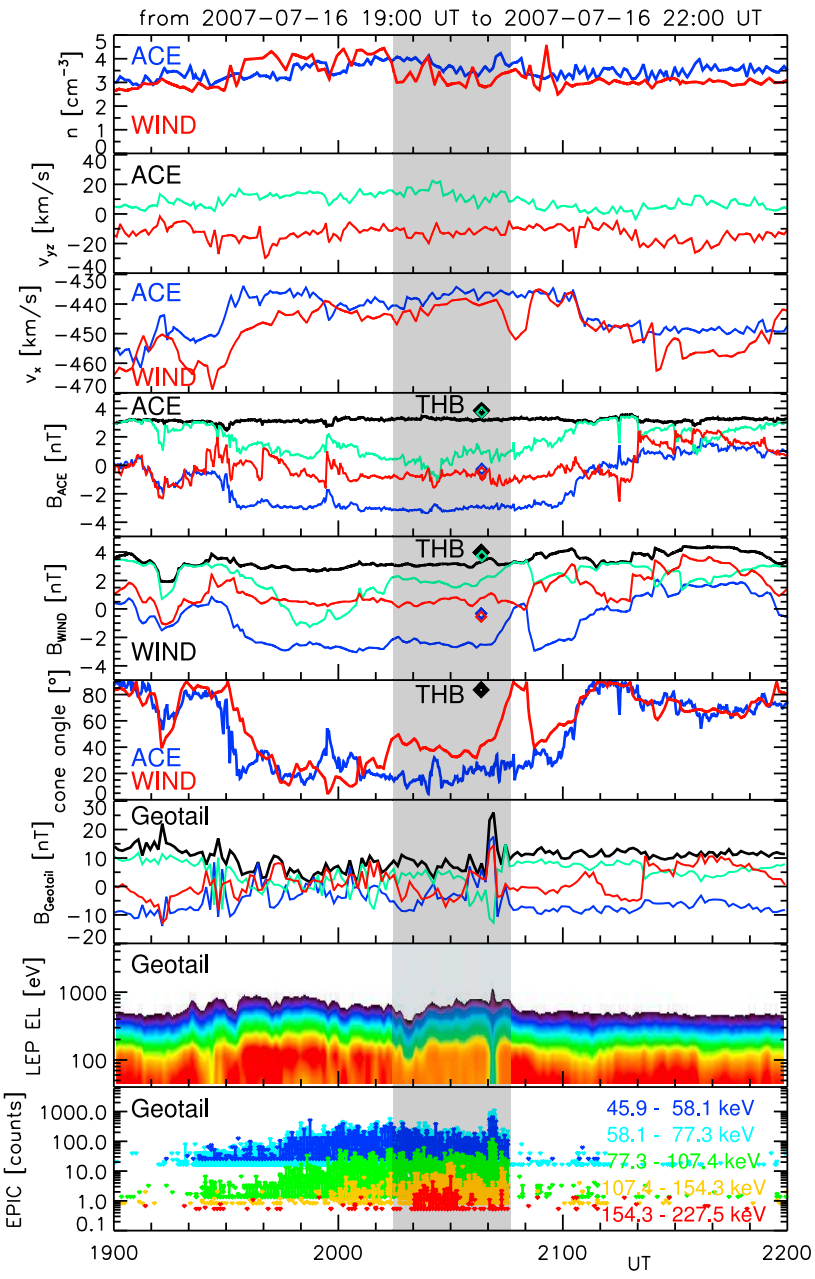

Figure 2. Solar wind data from ACE and Wind, and Geotail magnetosheath observations on July 16, 2007 from 1900 to 2200 UT. From top to bottom: ACE and Wind densities; ACE v_Y (green) and v_Z (red) velocity components; details of ACE and Wind v_X components; three components and strength of ACE IMF; the same data from Wind; cone angles computed from ACE and Wind; three components and strength of the Geotail magnetic field; and Geotail electrons and energetic particles measured by LEP and EPIC. In the magnetic field images, the X component is marked by blue, Y component by green, and Z component by red colors, respectively. The values obtained from THB in the solar wind are indicated by diamonds. The shadowed area indicates the time interval that will be discussed further. Time resolutions of a particular spacecraft were: Wind - 3-s magnetic field and 1-minute plasma data; ACE - 20-s magnetic field and 1-minute plasma data; Geotail - 1-minute magnetic field and plasma data; and THEMIS - 3-s magnetic field and plasma data.

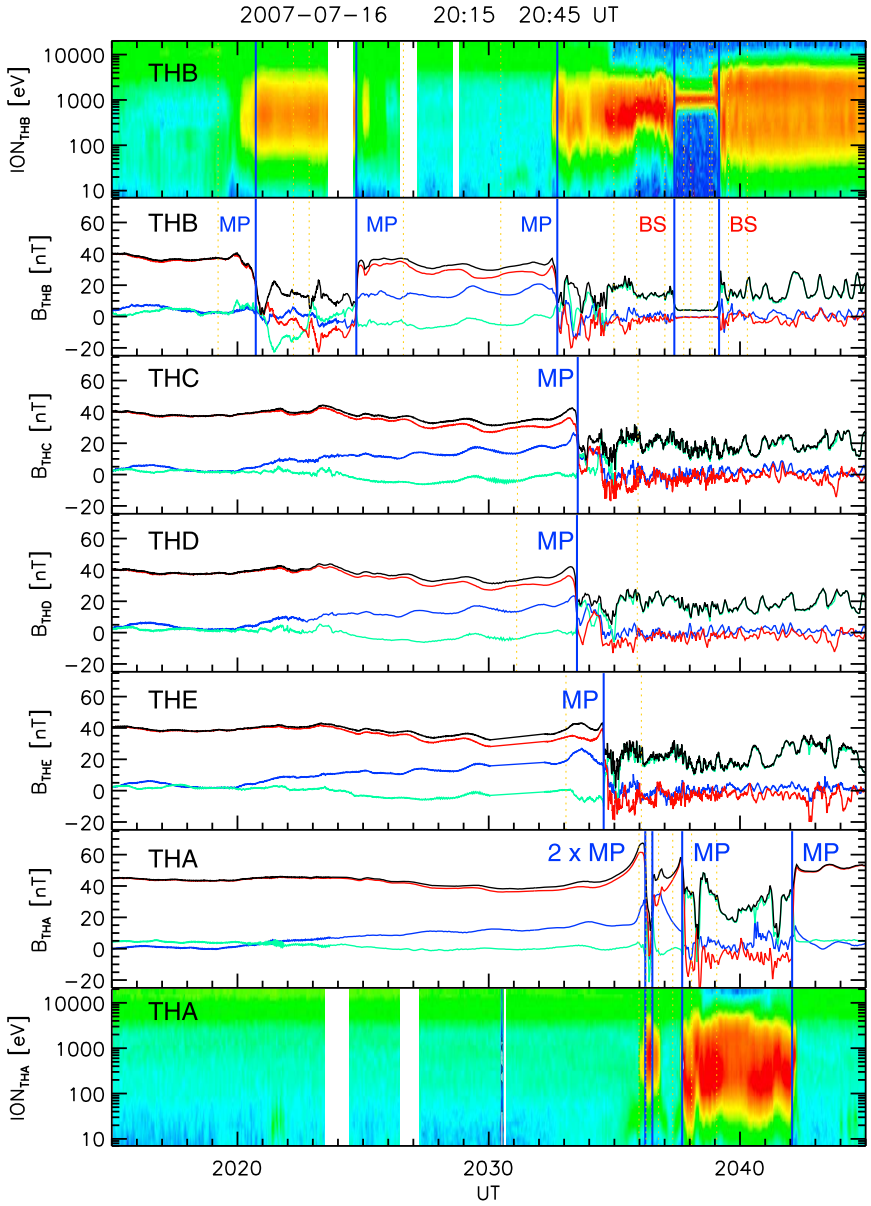

Figure 3. Measurements of THEMIS probes through the interval from 2015 to 2045 UT. From top to bottom: ion spectra from THB, five images of magnetic field observations ordered by the distance of probes from the Earth (THB, THC, THD, THE, THA), and ion spectra from THA. The vertical lines indicate the magnetopause and bow shock crossings. In magnetic field images, B_X, B_Y, B_Z components are marked by blue, green, and red colors, respectively.

wind density and velocity are nearly stable, and the same is true for the IMF magnitude and B_Z component. Small variations of these parameters result in changes of the ram pressure between 1 and 1.4 nPa but the magnetopause beyond THB and/or Geotail locations requires the pressure as low as 0.3 nT (computed according to the *Shue et al.* [1998] model), whereas the magnetopause downstream of THA requires the pressure in excess of 1.5 nPa. However, the B_X and B_Y components change their proportions in the discussed subinterval. We can use three monitors, but their measurements substantially differ. Whereas the ACE cone angle is nearly constant and below 30° during the whole subinterval, Wind shows its sharp increase from ≈30° to ≈50° at 2013 UT and a following new increase to ≈90° at

2045 UT. The best solar wind monitor would be THB that observed the ≈90° cone angle at 2039 UT, but it was in the solar wind only for ≈2 minutes.

[19] We have applied the minimum variance analysis method on observed IMF rotations and found that all of them can be classified as tangential discontinuities (nearly zero normal magnetic field component, negligible changes of the magnetic field magnitude, and plasma parameters across the discontinuity) and that the normals are highly declined (50°–80°) from the solar wind direction. Such discontinuities are hard to propagate.

[20] It has been shown that the IMF fluctuations may be oriented in approximately planar structures that are tilted with respect to the solar wind direction and this causes the IMF propagating from a point of measurement to arrive at other locations with a timing that may be significantly different from what would be expected [*Horbury et al.*, 2001a, 2001b; *Weimer et al.*, 2003; *Weimer and King*, 2008]. One can rely on the typical IMF orientation that is aligned along the Parker spiral, around 45° to the solar wind flow direction, but more sophisticated methods estimate the normal from multispacecraft timing or from gradient methods [e.g., *Russell et al.*, 1983, 2000; *Haaland et al.*, 2004], or use the local field or plasma measurements from a single spacecraft [e.g., *Sonnerup et al.* 2006], or apply different variants of the minimum variance analysis technique [e.g., *Sonnerup and Cahill*, 1967; *Sonnerup and Scheible*, 1998; *Mailyan et al.*, 2008; *Pulkkinen and Rastatter*, 2009]. These propagation methods find minimum variance planes (approximately) perpendicular to the mean magnetic field direction; however, they are based on an assumption of planarity of discontinuity. In our case, this assumption is broken because the discontinuities observed, for example, by Wind would be earlier or later observed by ACE that is not the case. It means that a part of upstream structures is smaller than the ACE-Wind separation or/and that they significantly evolve between the L1 and Earth. We assume that the Earth was affected by a turbulent stream that is missing the ACE location.

[21] For this reason, we are forced to use magnetosheath measurements for an estimation of the IMF direction in front of the bow shock. All monitors register the IMF strength of ≈4 nT. The Geotail magnetic field is about 12 nT until 1920 UT and after 2045 UT, while it is about 5 nT in between. The low compression factor is consistent with the quasi-parallel bow shock in front of Geotail. This conclusion is supported with the presence of energetic particles observed by Geotail (Figure 2, last image) and with the low cone angle measured by ACE. The abrupt decrease of the flux of energetic particles occurred at Geotail at 2045 UT. Moreover, the same effect was observed by THB at ≈2035 UT (first image in Figure 3). We suggest that these changes are caused by an IMF discontinuity arriving at 2035 UT to THB, slowly skimming the bow shock and reaching Geotail approximately 10 minutes later. This discontinuity is denoted as *D*1 hereafter.

[22] As an example of such discontinuity, that observed by Wind at ≈2012 UT can serve (discontinuity *D*2 hereafter). The normal of this discontinuity is (−0.356; −0.933; −0.057) and such discontinuity would skim the bow shock surface with a speed of ≈160 km/s that corresponds to the travel time from Geotail to THEMIS of about 10 minutes. We can point out that similar discontinuities often create HFAs [e.g., *Sibeck et al.*, 1999]; however, in our case, the motional electric field points away from the discontinuity. We should note that the discontinuity *D*2 cannot be a proper cause of the changes observed by THEMIS and Geotail because such discontinuity would propagate from Geotail to THEMIS. We have taken this discontinuity only as evidence that such discontinuities are observed in the solar wind.

[23] Consequently, we cannot rely on the upstream observations, and we should limit ourselves to the indirect evidences that are: (1) The quasi-parallel bow shock in front of THEMIS until 2035 UT; (2) The quasi-parallel bow shock in front of Geotail until 2045 UT; and (3) The B_Y dominated IMF just outbound the subsolar bow shock at ≈2038 UT.

[24] As noted above, these observational facts are consistent with an oblique IMF discontinuity already identified as *D*1. Its normal derived from timing of THB (2035 UT) and Geotail (2045 UT) observations and solar wind speed is about (0.35; −0.93; 0). It should convert a nearly radial IMF that corresponds to the quasi-parallel dayside bow shock to the B_Y dominated IMF observed by THB. Note that this discontinuity is shown by the green dashed-dotted line in Figure 5, and it is discussed in the next section.

[25] The slow motion of the discontinuity along the bow shock leads to situation when the IMF orientation in front of Geotail differs from that at THB for about 10 minutes. This can explain the fact that IMF observed by THB at 2038 UT would lead to the quasi-perpendicular bow shock at Geotail, but it is behind the quasi-parallel one until 2045 UT.

3.2. Magnetosheath Thickness

[26] A geometry of the bow shock (THB) and magnetopause (THA) crossings shown in Figure 3 is illustrated in two images of Figure 4. The red and blue dotted curves stand for the model bow shock [*Formisano et al.*, 1973] and magnetopause [*Shue et al.*, 1998], respectively. Since the spacecraft motion during the analyzed intervals is negligible, only locations at 2036 UT are shown. The straight blue lines depict the estimated magnetopause fronts, while the full red line presents the estimated bow shock front (the numbers correspond to Table 1). Until 2020 UT, the magnetopause is upstream of THB, far away of its model location.

[27] It should be noted that the THEMIS observations on the same day until 2030 UT were analyzed by *Suvorova et al.* [2010] and the authors argued that this effect is caused by a nearly radial IMF orientation (see also [*Merka et al.*, 2003]).

[28] Our attempt to find this effect in the set of ≈6000 magnetopause crossings failed, in spite of its amplitude that follows from the mentioned study. We think that the dependence of the magnetopause position on the IMF cone angle is strongly nonlinear and can be observed only for very small cone angles.

[29] In our case, the small cone angle lasts until ≈2020 UT when the discontinuity arrived to THEMIS and led to the cone angle rise. The discontinuity plane is shown by a green dashed-dotted line in Figure 5. This discontinuity evoked a magnetopause inward motion that resulted in the first magnetopause crossing of THB. Note that the discontinuity is connected with the increase of IMF B_Y and a similar change is seen in the THB magnetosheath observation after the crossing. A new IMF orientation gradually pushes the deformed

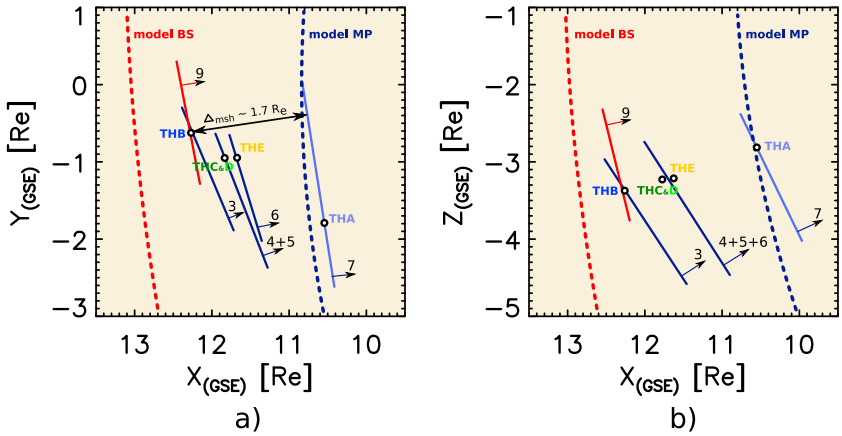

Figure 4. Projections of the THEMIS trajectories onto (a) the *X*-*Y* and (b) *X*-*Z* planes (in the GSE system). Model magnetopause [*Shue et al.*, 1998] and bow shock [*Jeřáb et al.*, 2005] are shown by the blue and red dotted curves, respectively. The straight lines show the estimated orientation of the bow shock (red) and magnetopause (blue and black) surfaces. The black arrows display the directions of normals, and the numbers correspond to the events in Table 1.

magnetopause inward and the bow shock follows it and crosses the THB location.

[30] Figure 4a reveals that the magnetosheath is very thin; the projection of the THA–THB separation vector onto the magnetopause normal (we used an average normal of crossings denoted by asterisks in Table 1) yields the value of $\Delta_{msh} = 1.7\ R_E$ that is equal to the thickness determined from the timing of crossings, whereas equation (3) provides a value of 2.3 R_E. Using the magnetopause curvature radius from the *Shue et al.* [1998] model ($a_{mp} = R_C = 10.9\ R_E$) and assuming $\gamma = 5/3$, $M_A = 11$, then equation (4) leads again to the magnetosheath thickness of 2.3 R_E. To receive the observed thickness, the magnetopause curvature radius would be as small as $R_C = 7.8\ R_E$ according to equation (4). The projection onto the XZ plane (Figure 4b) reveals a significant magnetopause deformation that was discussed in the previous section.

[31] We argue that the bow shock and magnetopause normals were determined very reliably because we have received the same results for various time intervals used for their computation. Moreover, the MP normals estimated from the data of the different spacecraft are very similar (Figure 4, Table 1). The bow shock and magnetopause planes (the red and blue lines in Figure 4b) determined at THB and THA locations, respectively, clearly tend to converge to a very small separation at $Z = 0$. Since these two crossings occurred nearly simultaneously, it means that the subsolar magnetosheath is even thinner than we determined from the THB–THA observations.

[32] A possible explanation of the low magnetosheath thickness through its dependence on the IMF cone angle [*Cairns and Lyon*, 1996] can be ruled out for two reasons: (1) This dependence is notable for $M_A \leq 6$ [*Cairns and Grabbe*, 1994], however, $M_A \approx 11$ in our case; and (2) The magnetosheath thinning appears for the cone angles below 20° [*Cairns and Lyon*, 1996] but THB observed the cone angle ≈90° just outbound of the bow shock.

[33] We suggest that the thin magnetosheath is a consequence of a local decrease of the curvature radius results from the magnetopause deformation. The inward magnetopause motion discussed above was observed at the subsolar region, whereas simultaneous outward displacement of the dusk dayside magnetopause was recorded by Geotail. Figure 5 depicts a possible shape of boundaries at ≈2040 UT consistent with the observed crossings. The magnetopause is at (or even downstream of) the THA location and at (or

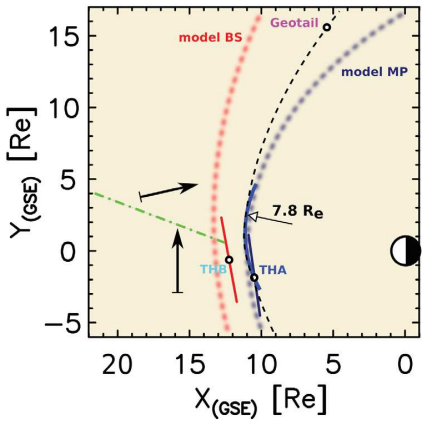

Figure 5. Projections of the observed situation onto the *X*-*Y* plane. The red and blue dotted curves show the model bow shock and magnetopause, respectively. The thin dashed curve presents estimated magnetopause shape at ≈2042 UT. The green dashed–dotted line stands for the IMF discontinuity estimated from THEMIS and Geotail observations, and IMF orientations shown by the black arrows correspond to those observed by ACE prior to (2015 UT) and by THB after (2038 UT) the discontinuity arrival.

upstream of) the Geotail location. We assume that this very distorted magnetopause shape is caused by the IMF discontinuity discussed above. This discontinuity shown in Figure 5 as the green dashed–dotted line causes the different IMF orientations (black arrows) upstream of THA and Geotail. The exact orientation and position of the discontinuity is unknown, but we know the IMF orientation (purely duskward) at the THB location. However, Geotail was behind the quasi-parallel shock until 2045 UT and it implies a small cone angle. The low cone angle displaces the magnetopause outward at the Geotail position [*Suvorova et al.*, 2010], whereas the large cone angle at THB results in the magnetopause return to a nominal position. This temporal decrease proceeds along the bow shock and leads to a local decrease of the magnetopause curvature radius and thus to corresponding magnetosheath thinning. We would like to stress that the IMF orientation was probably the main factor driving the observed displacements of the boundaries and that this orientation is not necessarily identical along the bow shock surface.

[34] Finally, we can propose the most probable scenario of the event as follows:

[35] 1. The subsolar magnetopause was expanded until 2020 UT due to a radial IMF that causes the decreased magnetosheath pressure [*Suvorova et al.*, 2010].

[36] 2. A tangential discontinuity shaped like that shown in Figure 5 approaches the dawn bow shock flank at 2020 UT and brings the duskward pointing IMF to the parts of the bow shock dawnward of the discontinuity.

[37] 3. The magnetosheath pressure behind the discontinuity increases and pushes the affected parts of the magnetopause inward. This process is responsible for the decreasing curvature radius of the subsolar magnetopause inferred from THEMIS and Geotail observations.

[38] 4. The discontinuity proceeds along the bow shock surface duskward and approaches THB at 2032 UT. Its arrival causes a fast inward motion of both the magnetopause and bow shock.

[39] 5. At 2045 UT, the discontinuity crosses the Geotail location, the expanded magnetopause moves inward and the bow shock becomes quasiperpendicular at this point.

4. Conclusions

[40] We have analyzed a case of simultaneous observations of the dayside magnetopause and bow shock by THEMIS and Geotail. The analysis is supported by ACE and Wind upstream observations propagated to the bow shock. We can conclude that:

[41] (1) Although the precise orientation of the IMF just upstream from Earth's bow shock may differ from that seen far upstream, we showed that oblique IMF discontinuities with large normals transverse to the Sun-Earth line were present in both locations.

[42] (2) Oblique IMF discontinuities result in prolonged intervals of differing IMF orientation upstream from the pre- and post-noon bow shock.

[43] (3) Although not included in any of empirical models, our study suggests that the IMF orientation controls the magnetopause and bow shock positions. However, the effect can be limited to a relatively narrow range of the cone and/or clock angles.

[44] (4) The position of a particular point on the magnetopause is governed by the pressure balance across the magnetopause at this point. At any given time, inward and outward motions at different points of the magnetopause can take place simultaneously according to the difference of corresponding IMF orientations.

[45] (5) IMF directional variations result in large transient deformations of the magnetopause shape.

[46] (6) The deformation of the magnetopause surface exhibiting suppressed curvature radius leads to a transient magnetosheath thinning (to about 70% of its standard value in the reported case).

[47] These conclusions are based on a favorable configuration of the spacecraft and we think that the probability to find a similarly documented case is very low. However, a statistical processing of the data collected by THEMIS, Geotail, and Cluster at the dayside magnetopause can answer the question how frequent are observed phenomena.

[48] **Acknowledgments.** We acknowledge the Geotail team for the magnetic field and plasma data and NASA contract NAS5-02099 and V. Angelopoulos for use of data from the THEMIS mission. Specifically, C. W. Carlson and J. P. McFadden for use of ESA data and K. H. Glassmeier, U. Auster and W. Baumjohann for the use of FGM data provided under the lead of the Technical University of Braunschweig and with financial support through the German Ministry for Economy and Technology and the German Center for Aviation and Space (DLR) under contract 50 OC 0302. The present work was partly supported by the Czech Grant Agency under Contracts 205/09/0170 and 205/09/0112, and partly by the Research Plan MSM 0021620860 that is financed by the Ministry of Education of the Czech Republic. The work at NCU was supported by the grant NSC 98-2811-M-008-043. K. Jelínek thanks the Charles University Grant Agency (GAUK 102508) for support.

[49] Masaki Fujimoto thanks Ken Tsubouchi and another reviewer for their assistance in evaluating this paper.

References

Auster, H. U., et al. (2008), The THEMIS Fluxgate Magnetometer, *Space Sci. Rev.*, *141*, 235, doi:10.1007/s11214-008-9365-9.

Boardsen, S. A., T. E. Eastman, T. Sotirelis, and J. L. Green (2000), An empirical model of the high-latitude magnetopause, *J. Geophys. Res.*, *105*(A10), 23,193–23,219, doi:10.1029/1998JA000143.

Cairns, I. H., and C. L. Grabbe (1994), Towards an MHD theory for the standoff distance of Earth's bow shock, *Geophys. Res. Lett.*, *21*(25), 2781–2784.

Cairns, I. H., and J. G. Lyon (1996), Magnetic field orientation effects on the standoff distance of Earth's bow shock, *Geophys. Res. Lett.*, *23*(21), 2883–2886.

Fairfield, D. H. (1971), Average and unusual locations of the Earth's magnetopause and bow shock, *J. Geophys. Res.*, *76*(28), 6700–6716, doi:10.1029/JA076i028p06700.

Farris, M. H., and C. T. Russell (1994), Determining the standoff distance of the bow shock: Mach number dependence and use of models, *J. Geophys. Res.*, *99*(A9), 17,681–17,689.

Farrugia, C. J., et al. (2008), Two-stage oscillatory response of the magnetopause to a tangential discontinuity/vortex sheet followed by northward IMF: Cluster observations, *J. Geophys. Res.*, *113*, A03208, doi:10.1029/2007JA012800.

Formisano, V., P. C. Hedgecock, G. Moreno, F. Palmiotto, and J. K. Chao (1973), Solar Wind Interaction with the Earth's Magnetic Field, 2. Magnetohydrodynamic Bow Shock, *J. Geophys. Res.*, *78*(19), 3731–3744.

Haaland, S. E., et al. (2004), Four-spacecraft determination of magnetopause orientation, motion and thickness: comparison with results from single-spacecraft methods, *Ann. Geophys.*, *22*, 4, 1347–1365.

Horbury, T. S., D. Burgess, M. Fränz, and C. J. Owen (2001a), Prediction of Earth arrival times of interplanetary southward magnetic field turnings, *J. Geophys. Res.*, *106*, 30,001–30,009.

Horbury, T. S., D. Burgess, M. Fränz, and C. J. Owen (2001b), Three spacecraft observations of solar wind discontinuities, *Geophys. Res. Lett.*, *28*, 677–680, doi:10.1029/2000GL000121.

Jacobsen, K. S., et al. (2009), Themis observations of extreme magnetopause motion caused by a hot flow anomaly, *J. Geophys. Res.*, *114*, A08210, doi:10.1029/2008JA013873.

Jeřáb, M., Z. Němeček, J. Šafránková, K. Jelínek, and J. Merka (2005), A study of bow shock locations, *Planet. Space Sci.*, *53*, 85–94.

Laakso, H., et al. (1998), Oscillations of magnetospheric boundaries driven by IMF rotations, *Geophys. Res. Lett.*, *25*(15), 3007–3010, doi:10.1029/98GL50916.

Lepidi, S., U. Villante, A. J. Lazarus, A. Szabo, and K. Paularena (1996), Observations of bow shock motion during times of variable solar wind conditions, *J. Geophys. Res.*, *101*, 11,107–11,123.

Mailyan, B., C. Munteanu, and S. Haaland (2008), What is the best method to calculate the solar wind propagation delay?, *Ann. Geophys.*, *26*, 2383–2394.

McFadden, J. P., C. W. Carlson, D. Larson, M. Ludlam, R. Abiad, B. Elliott, P. Turin, M. Marckwordt, and V. Angelopoulos (2008), The THEMIS ESA plasma instrument and in-flight calibration, *Space Sci. Rev.*, *141*, 277, doi:10.1007/s11214-008-9440-2.

Merka, J., A. Szabo, J. Šafránková, and Z. Němeček (2003), Earth's bow shock and magnetopause in the case of a field-aligned upstream flow: Observation and model comparison, *J. Geophys. Res.*, *108*(A7), 1269, doi:10.1029/2002JA009697.

Merka, J., A. Szabo, J. A. Slavin, and M. Peredo (2005), Three-dimensional position and shape of the bow shock and their variation with upstream Mach numbers and interplanetary magnetic field orientation, *J. Geophys. Res.*, *110*, A04202, doi:10.1029/2004JA010944.

Němeček, Z., and J. Šafránková (1991), The Earth's bow shock and magnetopause position as a result of the solar wind-magnetosphere interaction, *J. Atmos. Terr. Phys.*, *53*, 1049–1054.

Petrinec, S. M., and C. T. Russell (1996), Near-Earth magnetopause shape and size as determined from the magnetopause flaring angle, *J. Geophys. Res.*, *101*(A1), 137–152, doi:10.1029/95JA02834.

Pudovkin, M. I., M. F. Heyn, and V. V. Lebedeva (1982), Magnetosheath's parameters and their dependence on intensity and direction of the solar wind magnetic field, *J. Geophys. Res.*, *87*(A10), 8131–8138, doi:10.1029/JA087iA10p08131.

Pulkkinen, A., and L. Rastätter (2009), Minimum variance analysis-based propagation of the solar wind observations: Application to real-time global magnetohydrodynamic simulations, *Space Weather*, *7*, S12001, doi:10.1029/2009SW000468.

Russell, C. T., M. M. Mellott, E. J. Smith, and J. H. King (1983), Multiple spacecraft observations of interplanetary shocks: Four spacecraft determination of shock normals, *J. Geophys. Res.*, *88*, 4739–4748.

Roelof, E. C., and D. G. Sibeck (1993), Magnetopause shape as a bivariate function of interplanetary magnetic field Bz and solar wind dynamic pressure, *J. Geophys. Res.*, *98*(A12), 21,421–21,450, doi:10.1029/93JA02362.

Russell, C. T., et al. (2000), The interplanetary shock of September 24, 1998: Arrival at Earth, *J. Geophys. Res.*, *105*, 25,143–25,154.

Šafránková, J., K. Jelínek, and Z. Němeček (2003), The bow shock velocity from two-point measurements in frame of the INTERBALL project, *Adv. Space Res.*, *31*, 5, 1377–1382, doi:10.1016/S0273-1177(02)00951-1.

Seiff, A., and E. E. Whiting (1962), Correlation study of bow-wave profiles on blunt bodies, 62N10002, Report Number: NASA-TN-D-1148.

Shue, J.-H., J. K. Chao, H. C. Fu, K. K. Khurana, C. T. Russell, H. J. Singer, and P. Song (1997), A new functional form to study the solar wind control of the magnetopause size and shape, *J. Geophys. Res.*, *102*(A5), 9497–9511, doi:10.1029/97JA00196.

Shue, J.-H., et al. (1998), Magnetopause location under extreme solar wind conditions, *J. Geophys. Res.*, *103*(A8), 17,691–17,700.

Sibeck, D. G., R. E. Lopez, and E. C. Roelof (1991), Solar wind control of the magnetopause shape, location, and motion, *J. Geophys. Res.*, *96*(A4), 5489–5495, doi:10.1029/90JA02464.

Sibeck, D. G., et al. (1999), Comprehensive study of the magnetospheric response to a hot flow anomaly, *J. Geophys. Res.*, *104*(A3), 4577–4593, doi:10.1029/1998JA900021.

Sibeck, D. G., et al. (2000), Magnetopause motion driven by interplanetary magnetic field variations, *J. Geophys. Res.*, *105*, A11, 25155–25169, doi:10.1029/2000JA900109.

Sonnerup, B. U. Ö., and L. J. Cahill Jr. (1967), Magnetopause structure and altitude from Explorer-12 observations, *J. Geophys. Res.*, *72*, 171–183.

Sonnerup, B. U. Ö., and M. Scheible (1998), Minimum and maximum variance analysis, in *Analysis Methods for Multi-spacecraft Data*, edited by G. Paschmann and P. W. Daly, ISSI SR-001, pp. 185–220, ESA Publ. Div., Noordwijk, Netherlands.

Sonnerup, B. U. Ö., S. Haaland, G. Paschmann, M. W. Dunlop, H. Rème, and A. Balogh (2006), Orientation and motion of a plasma discontinuity from single-spacecraft measurements: Generic residue analysis of Cluster data, *J. Geophys. Res.*, *111*, A05203, doi:10.1029/2005JA011538.

Spreiter, J. R., A. L. Summers, and A. Y. Alksne (1966), Hydromagnetic flow around the magnetosphere, *Planet. Space Sci.*, *14*, 223–253.

Suvorova, A. V., J.-H. Shue, A. V. Dmitriev, D. G. Sibeck, J. P. McFadden, H. Hasegawa, K. Ackerson, K. Jelínek, J. Šafránková, and Z. Němeček (2010), Magnetopause expansions for quasi-radial interplanetary magnetic field: THEMIS and Geotail observations, *J. Geophys. Res.*, doi:10.1029/2010JA015404, in press.

Tsubouchi, K., T. Terasawa, T. Mukai, Y. Saito, T. Yamamoto, S. Kokubun, H. Kojima, and H. Matsumoto (2000), Motion of the Earth's bow shock in the deep-tail flank, *J. Geophys. Res.*, *105*(A11), 25,097–25,112, doi:10.1029/1999JA000454.

Tsyganenko, N. A., and D. P. Stern (1996), A new-generation global magnetosphere field model based on spacecraft magnetometer data, *ISTP Newsl. 6/1* 21.

Weimer, D. R., and J. H. King (2008), Improved calculations of interplanetary magnetic field phase front angles and propagation time delays, *J. Geophys. Res.*, *113*, A01105, doi:10.1029/2007JA012452.

Weimer, D. R., D. M. Ober, N. C. Maynard, M. R. Collier, D. J. McComas, N. F. Ness, C. W. Smith, and J. Watermann (2003), Predicting interplanetary magnetic field (IMF) propagation delay times using the minimum variance technique, *J. Geophys. Res.*, *108*(A1), 1026, doi:10.1029/2002JA009405. (Correction, *J. Geophys. Res.*, *109*, A12104, doi:10.1029/2004JA010691, 2004.)

Zhang, H., Q. G. Zong, D. G. Sibeck, T. A. Fritz, J. P. McFadden, K.-H. Glassmeier, and D. Larson (2009), Dynamic motion of the bow shock and the magnetopause observed by THEMIS spacecraft, *J. Geophys. Res.*, *114*, A00C12, doi:10.1029/2008JA013488.

K. Jelínek, Z. Němeček, and J. Šafránková, Faculty of Mathematics and Physics, Charles University, V Holešovičkách 2, 180 00 Prague 8, Czech Republic.

J.-H. Shue and A. V. Suvorova, Institute of Space Science, National Central University, Jhongli, Taiwan.

D. G. Sibeck, NASA Goddard Flight Center, Greenbelt, MD 20771, USA.

C.4 Themis: location of dayside bow shock and magnetopause

WDS'09 Proceedings of Contributed Papers, Part II, 15–21, 2009. ISBN 978-80-7378-102-6 © MATFYZPRESS

Themis: Locations of Dayside Bow Shock and Magnetopause

K. Jelínek, Z. Němeček, J. Šafránková

Charles University, Faculty of Mathematics and Physics, Prague, Czech Republic

Abstract. The paper presents a statistical study of bow shock and magnetopause positions in the subsolar region during the years 2007 and 2008 based on observation of five Themis spacecraft. The main attention is paid to a bias caused by a low apogee of the spacecraft which limits distances where bow shock crossings could be recorded. To overcome these problems, we developed a method eliminating this bias and an automatic technique to recognise bow shock and magnetopause positions. A comparison of results obtained by these methods shows a good agreement for low values of the upstream dynamic pressure. Our results suggest that the generally used scaling of the magnetopause and bow shock with the sixth root of the upstream dynamic pressure is a good approximation for a low pressure but that there is a systematic deviation for pressures above 3–4 nPa.

Introduction

The magnetopause is a boundary which originates by an interaction between the solar wind and Earth's magnetic field and its standoff position results from compensation of the solar wind dynamic pressure and Earth's magnetic field strength. Propagation of the solar wind plasma is supersonic and therefore ahead the magnetopause forms a shock wave which we call the bow shock. Predictions of the bow shock and magnetopause locations is a proof of our understanding of processes governing the solar wind–magnetosphere interaction. Models describing locations of these boundaries as a function of upstream parameters are based on a statistical processing of crossings observed by a single spacecraft and (usually distant) solar wind monitor.

In early published papers, it was found that the magnetopause position is mainly influenced by the upstream dynamic pressure and various model based on this assumtion have been discussed in *Fairfield* [1971], *Fairfield* [1976], *Formisano et al.* [1979], *Sibeck et al.* [1991], *Petrinec and Russell* [1996], and *Sotirelis and Meng* [1999]. The generally used scaling with sixth root of the solar dynamic pressure is based on assumption of the dipole Earth magnetic field. In the paper of *Shue et al.* [1997], different scaling is used and is explained by a change of a magnetosphere cavity that leads to increase of the magnetosphere's magnetic pressure near the magnetopause. Further, it was also found that the B_Z-component of the interplanetary magnetic field (IMF) changes the position and shape of the magnetopause *Sibeck et al.* [1991], *Petrinec et al* [1991], *Petrinec and Russell* [1996] and *Shue et al.* [1997], because the IMF B_Z affects reconnection at the magnetopause. Other parameters causing displacement of the magnetopause position are discussed in the papers of *Šafránková et al.* [2002], *Jeřáb et al.* [2005], *Šafránková et al.* [2005], *Měrka et al.* [2003], etc.

The bow shock (BS) is the most studied example of collisionless shocks (e.g., *Fairfield* [1971]; *Formisano et al.* [1973]; *Tsurutani and Stone* [1985]; *Němeček et al.* [1989]; *Burgess* [1995]; *Russell* [1995], and references therein). According to these and many other papers, the bow shock position depends on the magnetopause position and on the magnetosheath thickness which is a function of the magnetosonic Mach number. In the paper of *Russell and Mulligan* [2002], it was shown that also a curvature of the obstacle (ICME) influences the thickness of the magnetosheath.

In spite of prolonged research of the bow shock and magnetopause locations, current em-

pirical models still exhibit a high scatter to experimental data. Large uncertainty is connected with the dynamic response of both boundaries to abrupt changes of upstream and downstream parameters which are usually neglected for simplicity.

In the present study, we deal with a problem how to unify individual data sets from several spacecraft together with elimination of unfavorable conditions as multiple crossings or orbit limitations. We have developed two methods to find the bow shock and magnetopause positions only from the magnetic field magnitude measured by a particular spacecraft and the IMF from the OMNI database.

Determination of bow shock and magnetopause locations from crossings of the boundaries

Data set

We collected magnetopause (MP) and bow shock (BS) crossings observed through period of the 2007 and 2008 years when the Themis spacecraft traversed upstream of the subsolar magnetosphere. Recorded crossings are shown as projections onto the XY plane (in the GSE coordinate system) in Fig. 1 (grey diamonds and black triangles represent bow shock and magnetopause positions, respectively). Although we have identified crossings in a broad range of local times (LT), only those in the range of $1030 - 1330$ LT are considered in the present study. The region under study is distinguished by two black dashed lines in Fig. 1. We expect that shapes of both boundaries can be well approximated by spheres in this limited range and thus the location of a particular crossing can be described by a single parameter – the distance from the Earth's center, R.

During the 2007 year, in the first phase of the mission, Themis spacecraft were very close each other with the apogee of 14.6 Re. This is enough to register properly magnetopause crossings but positions of bow shock crossings are biased by such a low apogee. In the second stage of the mission, after alternation of the spacecraft apogee, only two of them (Themis B and C with apogee of 20 and 30 Re) could record the bow shock and magnetopause under standard

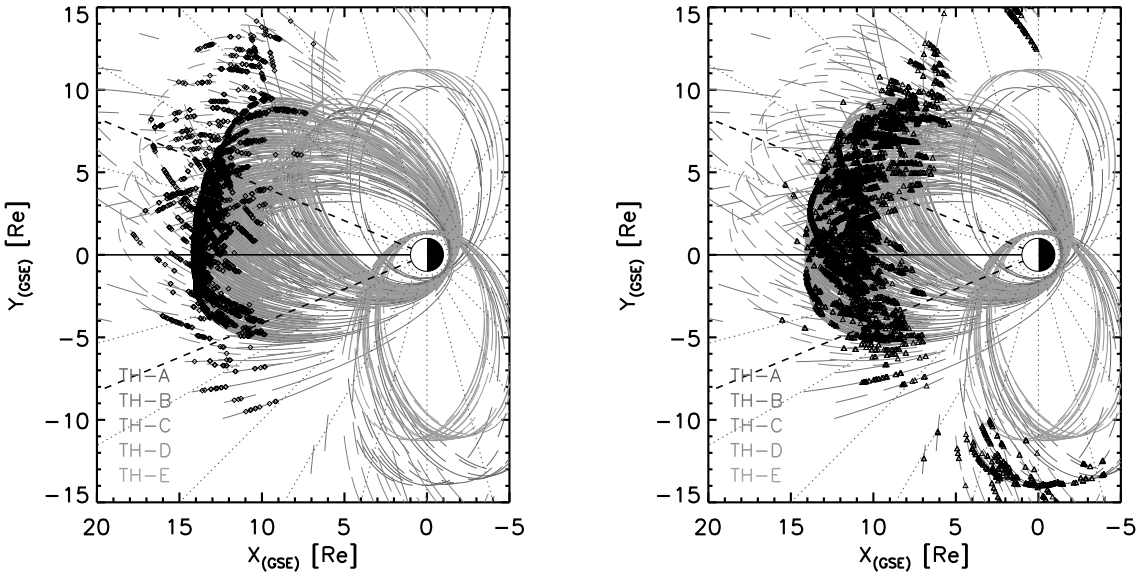

Figure 1. A projection of locations of bow shock (left panel) and magnetopause (right panel) crossings observed by five Themis spacecraft onto the XY plane. The light gray lines represent their trajectories around the time when one spacecraft recorded a particular crossing. The dotted lines show local time. In our study, we focused on the region from 10:30 to 13:30 LT (subsolar region) that is bounded by the thick dashed lines.

upstream conditions. We have identified about 6,660 BS and 5,330 MP crossings as described in the following section.

Bias elimination

We note that the analyzed data were collected during a solar minimum (2007 and 2008) and thus the solar wind dynamic pressure was often well below its average value with the most probable value ≈ 1 nPa. In combination with a low Themis apogee (2007), it represents a bias for bow shock observations. To avoid a misinterpretation of our data, we developed a method which allows us to combine crossings from the 2007 and 2008 years and to suppress bias caused by orbital limitations. Since it is generally accepted that the main parameter controlling the magnetopause (and therefore the bow shock) position is the upstream dynamic pressure, we created $p_{dyn} - R$ histograms of crossings as presented in Fig. 2. We use the OMNI database (http://omniweb.gsfc.nasa.gov/ow_min.html) as a solar wind monitor. In Fig. 2, the gray scale shows the number of observations of bow shock (left) and magnetopause (right) crossings in bins of 0.1 nPa width and 0.1 Re height. Since a majority of crossings was recorded in 2007, one can clearly see a cut-off caused by the Themis apogee, thus this cut-off requires an application of an appropriate data normalization prior to a further analysis. Our normalization is based on following assumptions: (1) All parts of Themis orbits above 8 Re were inspected and all crossings of boundaries were identified, and (2) we used those crossings for which the solar wind data were available. Using solar wind observations according to (2), we construct normalization $p_{dyn} - R$ table from all inspected Themis data. This table is shown in Fig. 3 in the same format as in Fig. 2. The gray scale shows how many minutes the spacecraft spent in a particular bin. The ratio of the number of crossings identified in a particular bin (Fig. 2) and the number of minutes that the spacecraft spent in the same bin (Fig. 3) provides a probability of appearance of the boundary crossings in each bin. The result of this procedure is plotted in two panels of Fig. 4. It can be seen that the bias is almost suppressed (bias cannot be completely suppressed by the presented method because of the bins without any THEMIS data) and it is possible to find mean positions of both boundaries which are shown as the solid lines.

We have to point out that such procedure could be applied on the data used for development of the empirical model of boundaries because a similar bias would exhibit crossings of the spacecraft like Cluster, Prognoz series, IMP 8, Hawkey, and others that are often used for this purpose.

This method of normalization is robust and can combine data from the spacecraft with considerable different trajectories, however, it is quite time consuming to identify all crossings by a visual inspection of plots.

Automatic identification of mean locations of boundaries

There were a lot of attempts to develop automated procedures for an identification of bow shock and/or magnetopause crossings. However, the results are not satisfactory because the procedures often produce false crossings and, on the other hand, real crossings are missed. For this reason, we based our procedure on identifications of whole visited regions. This means that we use some parameter (see below) measured by the Themis spacecraft to identify in which region (solar wind, magnetosheath or magnetosphere) the spacecraft is located. Then, it is plotted normalized 2D-histogram (in our case, we use distance from Earth, R and solar wind dynamic pressure p_{dyn}, as coordinates) of occurrence of each region and a border between them represents the bow shock and magnetopause.

Since we are dealing with the subsolar region, we use the magnetic field for an identification of regions. We compute one minute mean value of the ratio between the IMF magnitude from OMNI and the magnetic field measured by the Themis spacecraft ($r_B = |B|_{THEMIS}/|B|_{OMNI}$). Histogram of these ratios (Fig. 5, left panel) exhibits two peeks and a plateau. The first peak with maximum of r_B around 1 can be attributed to the solar wind (r_B is choosen from 0 to

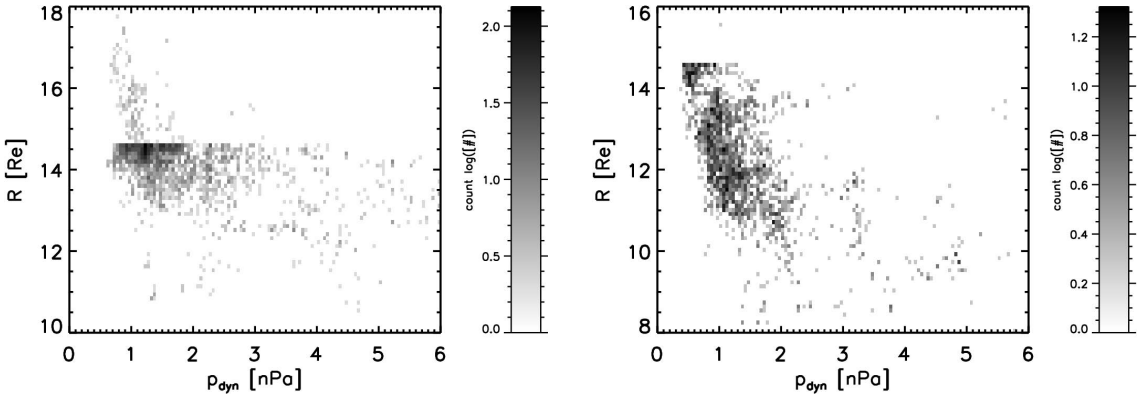

Figure 2. Color coded distribution of bow shock (left panel) and magnetopause (right panel) crossings in the $p_{dyn} - R$ histogram (in all presented histograms, pure white color represents no crossing or no meassured data insite intervals).

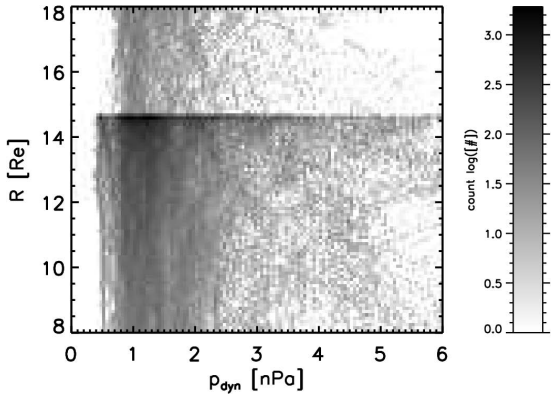

Figure 3. Distribution of one minute intervals in which the Themis spacecraft were located in a particular distance from the Earth and the magnetosphere was under influence of a particular dynamic pressure. Only local times from 10:30 to 13:30 are considered.

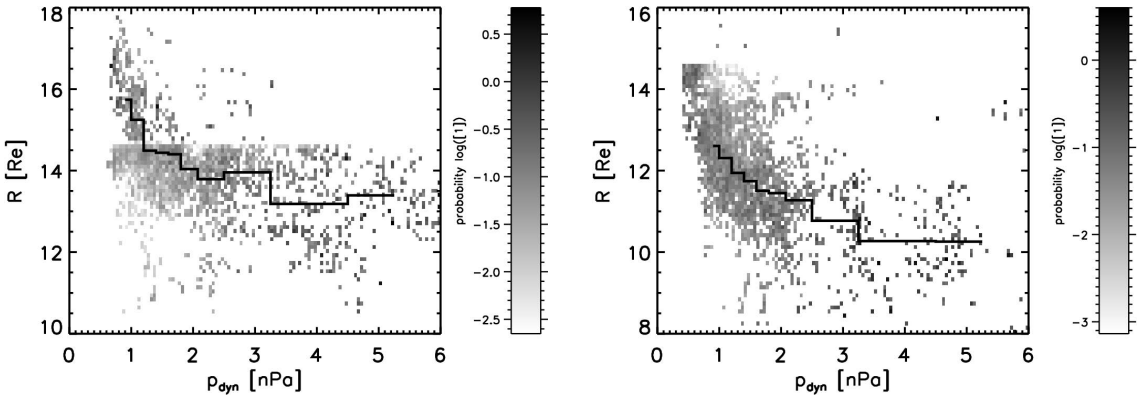

Figure 4. Normalized distribution of bow shock (left) and magnetopause (right) crossings. The solid lines represent mean position of particular boundaries as a function of the dynamic pressure.

1.7), the second peak around 3.8 is recognized as the magnetosheath ($2.3 \leq r_B \leq 6$). The transition between the magnetosheath and magnetopause is not so distinct but it still can be identified (r_B is between 6-8). Furthermore, we eliminated shadowed regions in Fig. 5 that can contain a mixture of two regions. Our procedure provides three tables of times where the satellite was in the solar wind (SW), in the magnetosheath (MSH), in the magnetosphere (MS) and we again build three $p_{dyn} - R$ histograms from each table. These histograms were divided by the normalization $p_{dyn} - R$ table (Fig. 5, right panel). The results for the magnetosheath are shown in Fig. 6. The plot shows a probability that the spacecraft is located in MSH for a particular distance R and dynamic pressure p_{dyn}. Note that the figures for SW and PS are similar and do not provide additional insight to the BS/MP position.

Finally, we can determine bow shock and the magnetopause positions from the MSH observation probability. For this purpose, we applied two methods. First of them uses a threshold of 50% of the probability (shown as solid black lines in Fig. 6) and the second uses a maximum gradient of the probability (dotted lines). As it can be seen from the figure, both methods provide very similar locations of both boundaries.

Comparison of boundary identification methods

In Fig. 6, the gray scale shows a probability of the magnetosheath distribution binned by p_{dyn} and R. The panel is complemented with the bow shock and magnetopause positions as a function of the upstream dynamic pressure. Stepwise functions are from experimental data and smooth functions are two fits with scaling of the dynamic pressure used in magnetopause models (*Petrinec and Russell* [1996] and *Shue et al.* [1997]). It can be seen that all methods provide very similar trends for the dynamic pressure up to 2–3 nPa. As the dynamic pressure increases, the method based on the identification of particular crossings places the boundaries farther from the Earth than the automated method. The reason can be connected with the fact that there is a decreasing number of BS and MP crossings which probably results in a greater error and thus the method based on an identification of crossings starts to be unreliable due to few data points. It is evident that the second automatic method has an advantage in more data points for the enhanced dynamic pressure. We believe that the mean locations of boundaries identified by the automated procedure is more reliable. Nevertheless, this explanation should be confirmed by a analysis of intervals with the enhanced pressure (not during solar minimum).

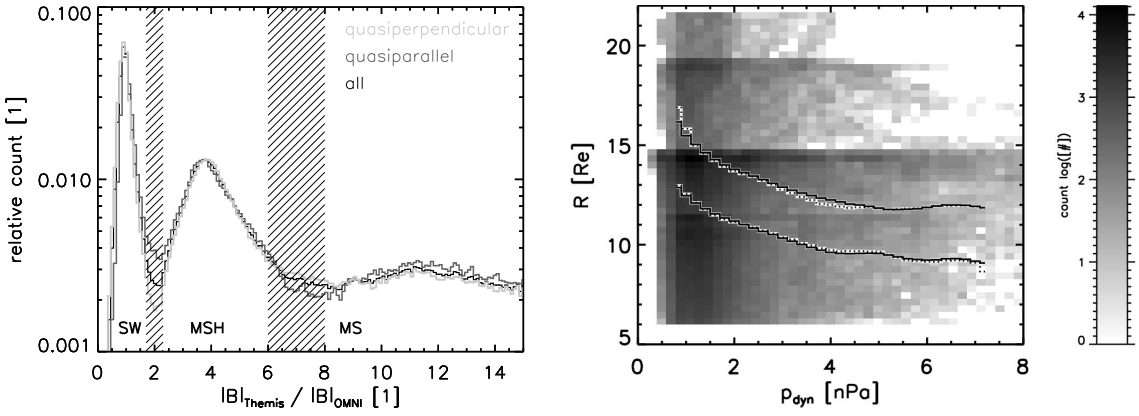

Figure 5. The left panel shows histogram of the $|B|_{Themis}/|B|_{OMNI}$ ratio which was used to distinguish different regions where the Themis spacecraft during orbits were located. The right panel is similar to Fig. 3 , however, it represents covering of $p_{dyn} - R$ by all avaiable Themis data during the years of 2007 and 2008 and we do not need information about the bow shock or magnetopause crossings.

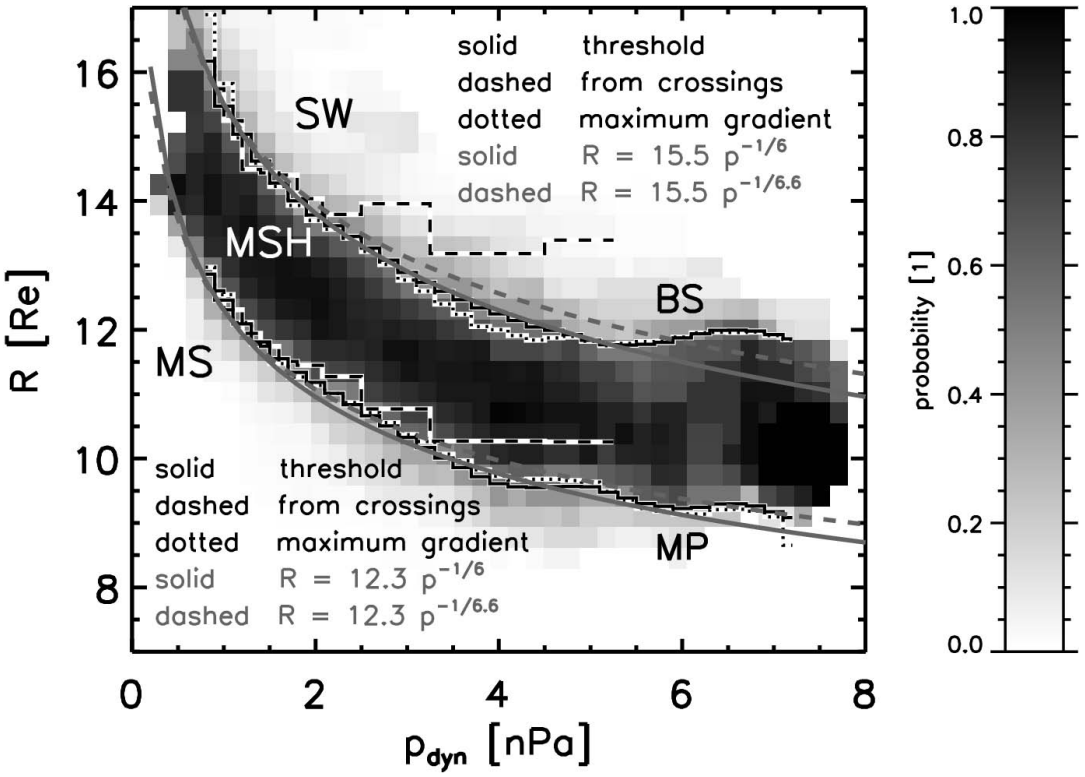

Figure 6. Overwiev of results obtained from both methods – crossing identification and authomated identification of boundaries. See text for detailed descriptions.

Conclusion

We have developed two methods which allow us to combine data from the different spacecraft and which can eliminate bias caused by orbital limitations. We tested both of them in the subsolar region where both boundaries, the bow shock and the magnetopause, can be approximated by spheres. Both techniques use parameters of the solar wind and IMF; we utilize 1-minute data from the OMNI database. We found the automatic method to be more reliable for higher dynamic pressures because more data points were involved in the statistics. Ad absurdum, a whole functional dependence of the bow shock and magnetopause position on the dynamic pressure can be created by spacecraft measurements with only one bow shock and one magnetopause crossing.

A next step of our study will be an analysis of BS and MP positions as a function of other upstream parameters like IMF B_Z, magnetosonic Mach number, and inner parameters of the magnetosphere (tilt of the magnetic field, Dst, Kp, and AE indexes). Since the response of the location of boundaries can be non-linear and the investigated parameters are (probably) mutually correlated in a degree, we should perform multidimensional analysis.

Acknowledgments. The present work was supported by the Czech Grant Agency under Contracts 202/08/H057, and 205/09/0170, by the Charles University Grant Agency under Contract 147307 and partly by Research project MSM0021620860 financed by the Ministry of Education of Czech Republic.

References

Burgess, D., Collisionless Shocks, In: *Introduction to Space Physics, M.G. Kivelson and C.T.Russell (eds)*, Cambridge: *Cambridge University Press*, Chapt. 5, pp. 129-163, 1995.

Fairfield, D.H., Average and unusual location of the Earth's magnetopause and bow shock, *J. Geophys. Res.*, **76**, 6700, 1971.

Fairfield, D.H., A summary of observations of the Earth's bow shock, In: *Physics of Solar Planetary Environments*, pp. 514-527, 1976.

Formisano, V., G. Hedgecock, G. Moreno, F. Palmiotto, and J.K. Chao, Solar wind interaction with the Earth's magnetic field, 2, Magnetohydrodynamics bow shock, *J. Geophys. Res.*, **87**, 3731, 1973.

Formisano, V., V. Domingo, K.-P. Wenzel, The tree-dimensional shape of the magnetopause, *Planet. Space Sci.*, **27**, 1137-1149, 1979.

Jeřáb, M., Z. Němeček, J. Šafránková, K. Jelínek, J. Měrka, Improved bow shock model with dependence on the IMF strength, *Planet. Space Sci.*, **53**, 85-93, 2005.

Měrka, J., A. Szabo, T.W. Narock, J.H. King, K.I. Paularena, J.D. Richardson, A comparison of IMP 8 observed bow shock position with model predictions, *J. Geophys. Res.*, **108**, 1269 doi: 10.1029/2002JA009697, 2003.

Němeček, Z., J. Šafránková and G. Zastenker, Dynamics of the bow shock position, *Adv. Space Res.*, **8**, No. 9-10, (9)167-(9)170, 1989.

Petrinec, S.M., P. Song, and C.T. Russell, Solar cycle variation in the size and shape of the magnetopause, *J. Geophys. Res.*, **96**, 7893, 1991.

Petrinec, S.M., C.T. Russell, Near-Earth magnetotail shape and size as determined from the magnetopause flaring angle, *J. Geophys. Res.*, **101**, 137, 1996.

Russell, C.T. (ed.), Physics of collisionless shocks: Proceedings of the Symposium of COSPAR Scientific Commission D, Vol. D2.1, *Pergamon Press*, 1995.

Russell, C.T and T. Mulligan, On the magnetosheath thicknesses of interplanetary coronal mass ejections, *Planet. Space Sci.*, **50**(5/6), 527-534, 2002.

Šafránková, J., Z. Němeček, Š. Dušík, L. Přech, D. G. Sibeck, and N. N. Borodkova, The magnetopause shape and location: a comparison of the Interball and Geotail observations with models, *Ann. Geophys.* **20**, 301, 2002.

Šafránková, J., Š. Dušík, Z. Němeček, The shape and location of the high-latitude magnetopause, *Adv. Space Res.*, **36** (10), 1934, 2005.

Shue, J.-H., J.K Chao, H.C. Fu, C.T. Russell, P.Song, K.K. Khurana, and H.J. Singer, A new functional form to study the solar wind control of the magnetopause size and shape, *J. Geophys. Res.*, **102**, 9497-9511, 1997.

Sibeck, D.G., R.E. Lopez, E.C. Roelof, Solar wind control of the magnetopause shape, location, and motion, *J. Geophys. Res.*, **96**, 5489-5495, 1991.

Sotirelis, T. and C. T. Meng, Magnetopause from pressure balance, *J. Geophys. Res.* **104**, 6889, 1999.

Tsurutani, B.T. and R.G. Stone, Collisionless shock in the heliosphere: Reviews of current research, *Washington DC, American Geophysical Union, Geophysical Monograph Series* **35**, AGU, Washington, D.C., 1985.

C.5 A new approach to magnetopause and bow shock modeling based on authomated region identification

JOURNAL OF GEOPHYSICAL RESEARCH, VOL. 117, A05208, doi:10.1029/2011JA017252, 2012

A new approach to magnetopause and bow shock modeling based on automated region identification

K. Jelínek,[1] Z. Němeček,[1] and J. Šafránková[1]

Received 10 October 2011; revised 12 March 2012; accepted 20 March 2012; published 3 May 2012.

[1] The present empirical models describing a location and shape of the magnetopause and bow shock are based on a statistical evaluation of magnetopause and bow shock crossings. The crossings are usually identified by a visual inspection of the plots or by automatic methods which are less reliable. We present a new method of determination of the most probable boundary locations. The method is based on continuous plasma and magnetic field measurements in the regions visited by a sounding spacecraft (the solar wind, magnetosheath, and magnetosphere) and on the determination of ratios of these parameters to simultaneously monitored upstream parameters. The regions identified by this method are then used for development of simple models of the magnetopause and bow shock locations parameterized by the upstream pressure. The performance of the models is tested with corresponding boundary crossings based mainly on the THEMIS observations. Both developed models are in a good agreement with the results obtained from identification of crossings.

Citation: Jelínek, K., Z. Němeček, and J. Šafránková (2012), A new approach to magnetopause and bow shock modeling based on automated region identification, *J. Geophys. Res.*, *117*, A05208, doi:10.1029/2011JA017252.

1. Introduction

[2] The magnetopause is the obstacle varying in a size and shape in a flow of the solar wind plasma. In early published papers [e.g., *Fairfield*, 1971; *Formisano et al.*, 1973, 1979; *Sibeck et al.*, 1991; *Roelof and Sibeck*, 1993; *Petrinec and Russell*, 1996; *Shue et al.*, 1997, 1998; *Boardsen et al.*, 2000], it was found that the upstream dynamic pressure strongly influences the Earth's magnetopause position. In some of these models, a stand-off position, R is scaled with the solar wind dynamic pressure, p as $R \approx \sqrt[6]{p}$ that is based on an assumption of the dipole Earth magnetic field. On the other hand, the pressure scaling factor was included as a free fitting parameter for other models. The authors found it to be larger than 6 (e.g., 6.16 in *Boardsen et al.* [2000] or 6.6 in *Shue et al.* [1997, 1998]). By contrast, the recent papers of *Dušík et al.* [2010] and *Lin et al.* [2010] proposed the lower scaling factor of 4.8 and 5.2, respectively. The same factor (5.2) follows from an analysis of the global MHD model made by *Lu et al.* [2011].

[3] Furthermore, it was found that the second parameter driving the position and shape of the magnetopause is the B_Z component of the interplanetary magnetic field (IMF). The IMF B_Z dependence is a subject of the papers by *Sibeck et al.* [1991], *Roelof and Sibeck* [1993], *Petrinec and Russell* [1996], *Shue et al.* [1997, 1998] and many others. On the other hand, *Verigin et al.* [2009] argued that no dependence of the subsolar magnetopause position on the IMF B_Z component has been revealed in a large set of the Interball data. *Boardsen et al.* [2000] developed an empirical model of the shape of the near-Earth high-latitude magnetopause that is parameterized by the solar wind dynamic pressure, IMF B_Z component and dipole tilt angle. The authors argued that the dipole tilt angle and solar wind pressure are the most significant factors influencing the shape of the high-latitude magnetopause and that the IMF B_Z dependence can be found only if the pressure and tilt angle effects are removed by a proper scaling. Similar results were reported by *Tsyganenko* [1998] and by *Eastman et al.* [2000]. *Šafránková et al.* [2005] have analyzed high-latitude magnetopause crossings and suggested a simple correction of the *Petrinec and Russell* [1996] model that reflects the magnetopause indentation in the cusp region. This indentation was later explicitly included into the *Lin et al.* [2010] model and confirmed by statistical analysis of magnetopause and bow shock positions [e.g., *Jelínek et al.*, 2008].

[4] The solar wind plasma flow is supersonic, therefore the bow shock rises ahead of the magnetopause. The Earth's bow shock is the most studied collisionless shock [see, e.g., *Burgess*, 1995]. According to many papers, the bow shock position depends on the size and geometry of the obstacle, i.e., the magnetopause location and on the magnetosheath thickness that is a function of the Mach number. The thickness of the magnetosheath is influenced by the curvature radius, R_C of the obstacle, as it was discussed in the papers of *Farris and Russell* [1994] for the Earth's magnetosheath and *Russell and Mulligan* [2002] for the magnetosheath

[1]Faculty of Mathematics and Physics, Charles University, Prague, Czech Republic.

Corresponding Author: Z. Němeček, Faculty of Mathematics and Physics, Charles University, V Holešovičkách 2, CZ-180 00 Prague 8, Czech Republic. (zdenek.nemecek@mff.cuni.cz)

0148-0227/12/2011JA017252

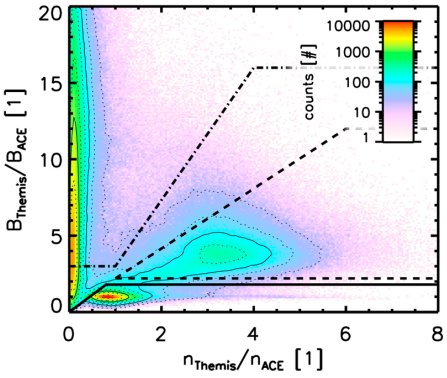

Figure 1. A 2D histogram of the ratios of r_B vs r_n which were used to distinguish three regions: the solar wind (SW) is at the bottom and it is bounded with the full line; the magnetosphere (MS) is located at the left part of the figure and bounded with the dotted-dashed line; and the magnetosheath (MSH) is a triangle distinguished with the dashed line in the middle of the panel. The values in the histogram are numbers of one-minute intervals in logarithmic scale.

of ICMEs (Interplanetary Coronal Mass Ejections). On the other hand, *Němeček and Šafránková* [1991] and *Jerab et al.* [2005] suggested that the magnetosheath thickness is a rising function of the IMF strength.

[5] The models describing actual locations and shapes of the magnetopause and bow shock as a function of upstream parameters are based on a statistical processing of crossings observed by a single spacecraft and (usually distant) solar wind monitor. This approach implicitly assumes that the downstream parameters are proportional to their upstream values. Such assumption introduces many inaccuracies when, for example, a strong sudden change of solar wind conditions results in unusual boundary crossings, or multiple crossings follow in a short time and these effects could negatively affect statistical results. Moreover, a visual inspection of data plots is time consuming and subjective because the criteria for a boundary identification could vary.

[6] Another problem is the orbital bias of particular data sets. The spacecraft on a nearly circular orbit can observe the boundary at a distance given by the orbit only, whereas the spacecraft on an elongated orbit spends a majority of time near the apogee and thus the resulting set of crossings is biased toward this apogee. This problem is important namely for the data set used in the present paper because we use the THEMIS spacecraft in the time period of 2007–2008. *Fairfield* [1971] give 14.6 R_E as the average bow shock stand-off distance and the apogee of THEMIS was 14.7 R_E in 2007. Consequently, THEMIS spent about 25% of time in distances between 13.7 and 14.7 R_E from the Earth. For this reason, *Jelínek et al.* [2009] proposed a method that partly eliminates such orbital bias. The suggested procedure weights a number of crossings observed in a particular spatial bin by a time that the spacecraft spent in this bin. However, the method cannot reflect the fact that none of crossings can be observed beyond the spacecraft apogee.

[7] For above mentioned reasons, we developed a new method of an automatic identification of both boundaries from observations of the magnetic field and plasma density. One-minute averages of these parameters measured by a sounding spacecraft are normalized to corresponding values measured at the L1 point and propagated to the sounding spacecraft location. The normalized values are then used for an identification of three regions: the solar wind, magnetosheath, and inner magnetosphere. We explain the method of data processing and apply it for the development of a simple model of the bow shock and magnetopause.

2. Data Processing

[8] For our method, we take advantage of orbits of five THEMIS spacecraft that move through all investigated regions: the solar wind (SW), the magnetosheath (MSH), and the inner magnetosphere (MS), and computed one-minute medians of the magnetic field magnitude, $|B_{Themis}|$ and density, n_{Themis}. As a solar wind monitor, we used ACE one-minute medians of the IMF magnitude, $|B_{ACE}|$, density, n_{ACE}, solar wind dynamic pressure, p, and plasma velocity, v_{ACE} shifted to THEMIS positions by convection along the X_{GSE} axis. We use two-step propagation algorithm that is described in *Šafránková et al.* [2002].

[9] For all measurements of the THEMIS spacecraft at altitudes larger than 5 R_E in the period from March 2007 to September 2009, we computed the ratio of the magnetic fields, r_B

$$r_B = \frac{|B_{Themis}|}{|B_{ACE}|}. \quad (1)$$

Because the compression ratio of the magnetic field in the magnetosheath decreases toward the flanks, we added the density compression factor, r_n

$$r_n = \frac{n_{Themis}}{n_{ACE}}. \quad (2)$$

These two ratios allowed us to identify SW, MSH, and MS regions on whole dayside parts of orbits and even toward the flanks in the range of ± 7 hours of local time around the local noon.

[10] Figure 1 shows 2D histogram of r_B and r_n occurrence rates. One can clearly distinguish three regions: solar wind measurements are spread around $r_B = 1$ and $r_n = 1$ (it is not exactly the point for two reasons: shifting and comparison of distant data sources and foreshock fluctuations); the magnetosheath is specified by compression ratios of about $r_B \approx 4$ and $r_n \approx 3$ (the magnetosheath has a large spread of points around these ratios because its parameters depend on a particular position inside the magnetosheath and magnetosheath plasma and magnetic field are highly fluctuating). In many regions of the inner magnetosphere, the plasma density is small and the magnetic field does not depend on IMF and r_B can reach high values. It can be seen as a long ridge for $r_n < 1$. However, we processed all available THEMIS data regardless the spacecraft location and thus a part of magnetospheric observations was taken from the plasmasphere where the density can be higher than that in the solar wind. In Figure 1, we show the chosen boundaries

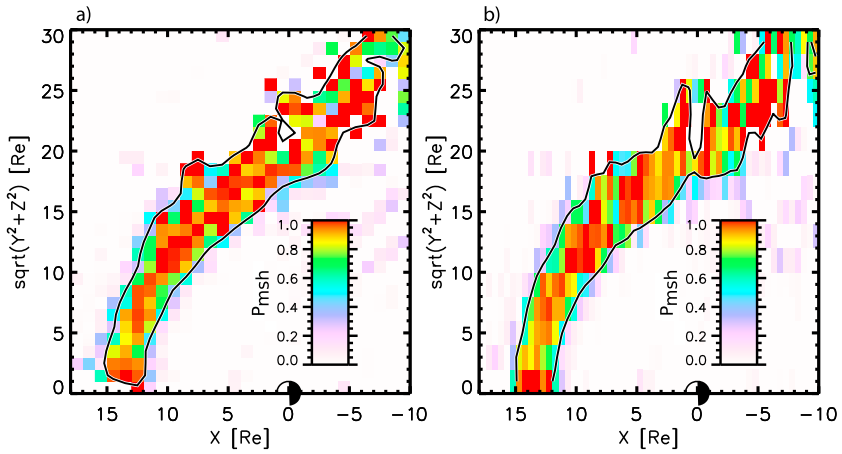

Figure 2. An example of a possible data binning in aberrated *GSE* coordinates. The color scale shows the values of the probability P_{MSH} in rectangular bins for the interval of upstream dynamic pressures from 1 to 1.1 nPa. The black line stands for an approximate location of bins with $P_{MSH} = 0.5$. (a) The 1 by 1 R_E bins. (b) The 0.5 by 2 R_E bins.

between particular regions. The points which lie outside these boundaries are not used in the further processing.

3. Coordinate System and Data Binning

[11] Since this is a first attempt to apply the above described identification of regions for a description of mean positions of the bow shock and magnetopause, we expect that their locations are controlled exclusively by the solar wind dynamic pressure. The method is based on a probability that the spacecraft at a given spatial point and under a given solar wind dynamic pressure, p visited one of regions specified in Figure 1. We assume that both the magnetopause and bow shock are rotationally symmetric around the aberrated X_{GSE} axis. The aberration takes into account the Earth orbital motion; the perpendicular components of the solar wind velocity are omitted in accord with the study of *Šafránková et al.* [2002].

[12] All data were sorted into bins described by two spatial co-ordinates X and Y and the upstream pressure, p and we computed the probability, P that we can find the solar wind (SW), magnetosheath (MSH) or magnetosphere (MS) in a particular bin.

$$P_{SW}(p,X,Y) = \frac{N_{SW}(p,X,Y)}{N_{ALL}(p,X,Y)} \tag{3}$$

$$P_{MSH}(p,X,Y) = \frac{N_{MSH}(p,X,Y)}{N_{ALL}(p,X,Y)} \tag{4}$$

$$P_{MS}(p,X,Y) = \frac{N_{MS}(p,X,Y)}{N_{ALL}(p,X,Y)}, \tag{5}$$

where N_{SW}, N_{MSH}, and N_{MS} are numbers of one-minute intervals spent in particular regions and N_{ALL} is their sum.

[13] Equations (3)–(5) do not expect any particular coordinate system. In principle, it is possible to use aberrated *GSE* coordinates and equidistant binning in space and pressure. Examples of possible binnings are shown in Figures 2a (square 1 by 1 R_E bins) and 2b (rectangular 0.5 by 2 R_E bins). The color scale shows the values of the probability P_{MSH} in aberrated *GSE* coordinates for the interval of upstream dynamic pressures from 1 to 1.1 nPa. The black line stands for an approximate location of bins with $P_{MSH} = 0.5$. We can note that the line indicates possible magnetopause and bow shock locations but the binning 1 by 1 R_E shown in Figure 2a is too coarse. On the other hand, a volume of the bin is at a lowest applicable limit because there are already several bins without measurements. The different bin shapes can improve the spatial resolution in a particular region as it is shown in Figure 2b. The bins 0.5 by 2 R_E are appropriate for the subsolar region but different shapes or orientations of the bins would be used for earlier or later local times.

[14] A possible solution is an application of non-Cartesian coordinates reflecting expected shapes of both boundaries. Since the bow shock and magnetopause surfaces are often described by second order surfaces, we expect the parabolic shapes of both boundaries. Consequently, we transform aberrated $GSE(x, y, z)$ coordinates into generalized parabolic coordinates (σ, τ, ϕ) by following expressions

$$\tau = \sqrt{\sqrt{x^2 + (\lambda_y y)^2 + (\lambda_z z)^2} - x} \tag{6}$$

$$\sigma = \sqrt{\sqrt{x^2 + (\lambda_y y)^2 + (\lambda_z z)^2} + x} \tag{7}$$

$$\phi = \arctan\frac{\lambda_y y}{\lambda_z z} \tag{8}$$

where λ_y and λ_z are scaling factors.

[15] The standard parabolic coordinates can be obtained from our generalized coordinates given by equations (6)–(8) putting $\lambda_y = \lambda_z = 1$. An example of the data binning in the

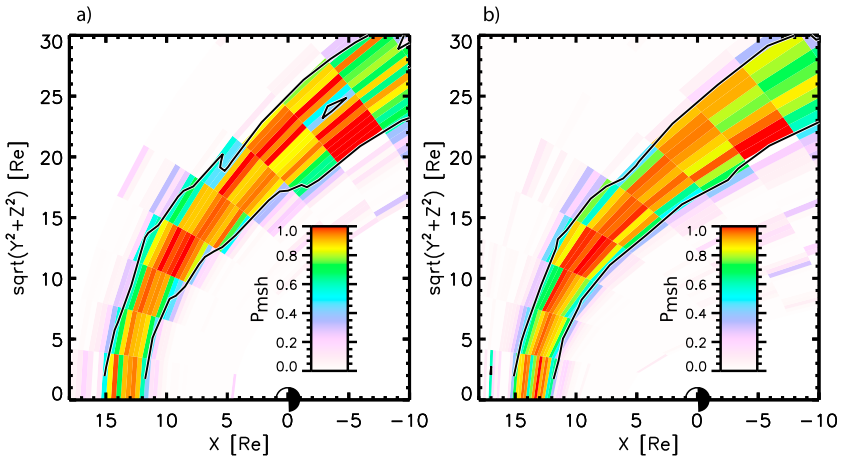

Figure 3. An example of data binning in (a) parabolic coordinates and (b) so-called magnetosheath coordinates. The definition of magnetosheath coordinates is given in the text.

standard parabolic coordinates is shown in Figure 3a and one can note that the results are better than that obtained by a binning in *GSE* coordinates shown in Figure 2. However, the matching of bins with the boundaries is not as perfect as one would expect and it is the reason why we introduced generalized coordinates that use scaling factors λ_y and λ_z. These scaling factors describe a "flaring" of parabolas in the direction of a particular axis. The bow shock or magnetopause would lie on surfaces $\sigma = constant$ if these factors are chosen properly. Since we expect the rotational symmetry, locations of both boundaries do not depend on the angular coordinate, ϕ and we can write $\lambda_y = \lambda_z = \lambda$. However, the flaring angles of the bow shock and magnetopause surfaces are different, thus the optimum scaling factors for both boundaries would differ. Nevertheless, their values λ_{MP} and λ_{BS} can be determined by optimization procedures that are described in the next section. Expecting that the values λ_{MP} and λ_{BS} are already determined, we can make a further generalization and suppose that λ is a linear function of the distance from the Earth. The value of λ can be determined for each point A by finding the inter-sections of its radius vector, r_A with the bow shock (r_{BS}) and magnetopause (r_{MP}) surfaces from:

$$\lambda_A = \lambda_{MP} + \frac{\lambda_{BS} - \lambda_{MP}}{r_{BS} - r_{MP}}(r_A - r_{MP}) \tag{9}$$

[16] We will call these coordinates as a magnetosheath coordinate system in the further text. An example of the data binning in this coordinate system is shown in Figure 3b and we can see that it provides the best possible results for a given upstream dynamic pressure.

[17] A majority of previous studies used equidistant binning according to the solar wind dynamic pressure. However, it is well known that a response of the magnetopause or bow shock locations to the upstream pressure is non-linear. It is usually described as

$$R \approx p^{-\frac{1}{\epsilon}}. \tag{10}$$

where the suggested values of ϵ range from 4.79 [*Dušík et al.*, 2010], over 5.15 [*Lin et al.*, 2010] to 6.667 [*Shue et al.*, 1997]. To account for this non-linearity, we used the binning of the dynamic pressure as:

$$\Delta p \approx p^{+\frac{1+\epsilon}{\epsilon}}. \tag{11}$$

The value of ϵ will be specified later by the fitting to the data set.

4. The Bow Shock and Magnetopause Model

[18] There are several possibilities how to identify the bow shock and magnetopause locations from the probabilities $P(\sigma, \tau, p)$. One of them is to find locations where the probability of observations of neighboring regions (SW and MSH or MSH and MS) is equal to 0.5. Examples of this determination are shown in Figures 2 and 3. However, this way is very sensitive to missing data. For this reason, we defined an analytical expression for the bow shock and magnetopause and determined the free parameters of the model by fitting to the full data set. As already noted, we expect a parabolic shape of both boundaries that responds to the upstream pressure as $p^{-\frac{1}{\epsilon}}$. It implies that we can find the scaling factors λ_{MP} and λ_{BS} such that the bow shock or magnetopause would lie on surfaces $\sigma = const$ in the whole range of the dynamic pressure. Using the least squares method, we have found following scaling factors: $\lambda_{BS} = 1.17$ and $\lambda_{MP} = 1.54$. In such a case, model bow shock and magnetopause positions can be expressed as

$$\sigma = \sqrt{2Rp^{-\frac{1}{\epsilon}}} \tag{12}$$

where R is the stand-off distance for $p = 1$ nPa and a given pressure factor, ϵ. Note that the fitting procedure uses the magnetosheath parabolic coordinates introduced above and the data are redistributed to new bins at each iteration step because our binning depends on values of λ_{MP}, λ_{BS}, and ϵ. The iteration procedure is complicated because it searches for a combination of R_{MP}, R_{BS}, ϵ_{MP}, ϵ_{BS}, λ_{MP}, and λ_{BS} such

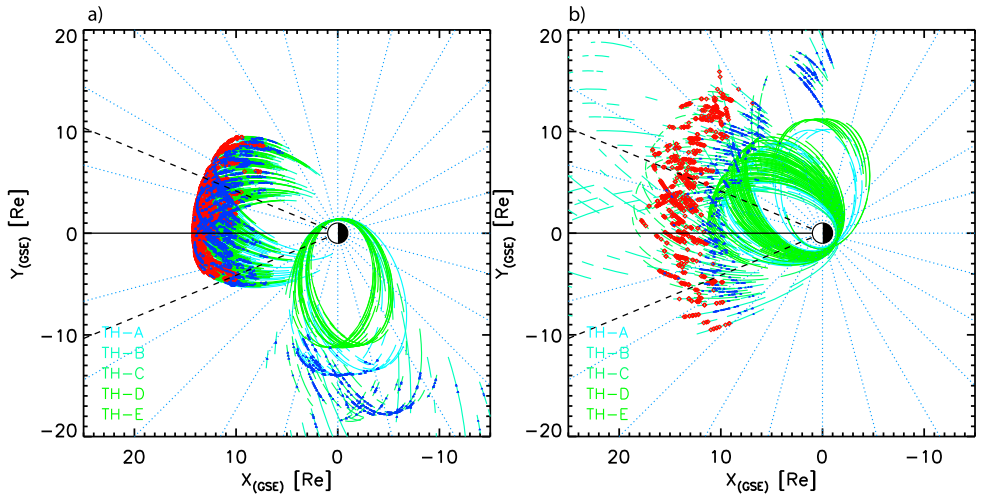

Figure 4. Distributions of bow shock (red points) and magnetopause (blue points) crossings during (a) 2007 and (b) 2008 in the X-Y plane.

that a sum of squares of distances of the bins from both boundaries given by equation (12) in the 3D space with coordinates τ, σ, p is minimized.

[19] Application of the least squares method leads to following expressions:

$$R_{MP} = 12.82\, p^{-\frac{1}{5.26}} \tag{13}$$

$$R_{BS} = 15.02\, p^{-\frac{1}{6.55}} \tag{14}$$

where R_{MP} and R_{BS}, respectively are stand-off distances of the magnetopause and bow shock, respectively. The bow shock and magnetopause surfaces in aberrated GSE coordinates can be thus written in the parametric form as

$$x = R_0\, p^{-\frac{1}{\epsilon}} - \frac{1}{2}\tau^2 \tag{15}$$

$$R_{yz} = \frac{\sqrt{2R_0\, p^{-\frac{1}{\epsilon}}\tau}}{\lambda} \tag{16}$$

where R_0 = 12.82 or 15.02 and ϵ = 5.26 or 6.55 for the magnetopause or bow shock, respectively.

5. Verification of Models

5.1. Data Preparation

[20] The described models were developed using probabilities of observations of particular regions and their performance can be tested by a comparison with real observed crossings of both boundaries. We have visually identified more than 6000 bow shock and 5500 magnetopause crossings in the THEMIS plasma and magnetic field data [*Angelopoulos*, 2008; *Auster et al.*, 2008; *McFadden et al.*, 2008] in course of the 2007 and 2008 years. These sets were biased by a low apogee of the THEMIS spacecraft, mainly during the first stage of the THEMIS project, as it can be seen in Figure 4a. Figure 4b shows distributions of magnetopause and bow shock crossings through the second stage of the THEMIS mission when the apogee reached 20 R_E. The influence of the orbital limitations is seen also in Figure 5a that shows the distribution of subsolar bow shock crossings (11–13 hours of local time) in $R - p_{dyn}$ coordinates (R stands for the distance of the bow shock from the Earth center). One can clearly see the red spot and horizontal line caused by the low apogee of THEMIS in 2007. We used the procedure of *Jelínek et al.* [2009] that weights the number of crossings by a time that the spacecraft spent in a particular bin. This method suppresses the bias only partly as Figure 5b presents because none of crossings can be observed beyond the spacecraft apogee. Nevertheless, we applied this method with a slight modification; we used parabolic coordinates and nonlinear binning of the solar wind dynamic pressure in the present paper.

5.2. Comparison of the Model and Experimental Data

[21] Figure 6 presents an example of a comparison between bow shock and magnetopause models and positions of observed bow shock (a) and magnetopause (b) crossings. The color scale shows the probability that the bow shock (magnetopause) crossing is observed in a particular spatial bin and under a given p (p is ranging from 1.0 to 1.1 nPa in the figure). One can note a good matching of crossings and model results. Histograms in Figure 7 represent the differences between average positions of the bow shock (a) and the magnetopause (b) determined from boundary crossings and from the proposed models. Both distributions are almost centered.

[22] Since the empirical models of boundaries are usually developed by fitting to observed crossings, we can follow this approach and test our model by this way. We divided the probability of crossing observations (see Figure 5b) into bins in parabolic coordinates and applied the above described fitting procedure to these sets of probabilities. The resulting

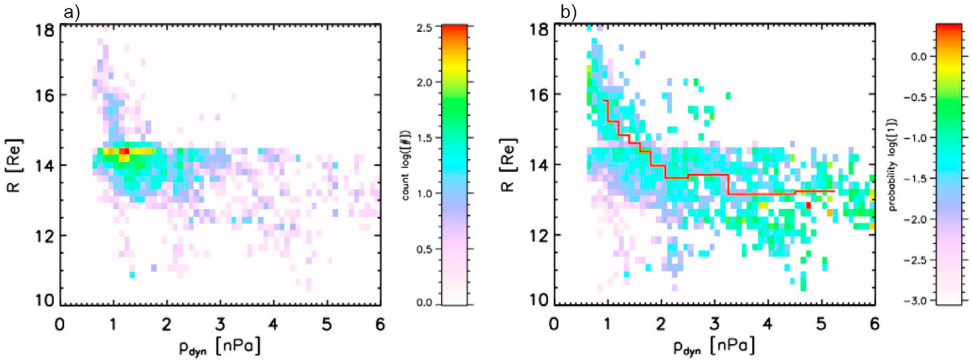

Figure 5. (a) The distribution of subsolar bow shock crossings (11–13 hours of local time) in $R - p_{dyn}$ coordinates when R stands for the distance of the bow shock from the Earth center and p_{dyn} is the dynamic pressure. (b) The same histogram weighed by a time that the spacecraft spent in a particular bin. The red line represents average bow shock location.

stand-off positions of the magnetopause, R_{MP} and bow shock, R_{BS} can be written in a similar form to equations (13) and (14)

$$R_{MP} = 12.90\, p^{-\frac{1}{4.92}} \tag{17}$$

$$R_{BS} = 14.94\, p^{-\frac{1}{6.62}}. \tag{18}$$

Comparing both sets of the equations (13)–(14) and (17)–(18), we can conclude that values R_0 and ϵ are close to the suggested models. This result validates our method but, as mentioned above, the sets of crossings suffer with the orbital bias and it is not clear if the method of *Jelínek et al.* [2009] can remove this bias completely. On the other hand, the method used for the model development in the present paper does not depend on the spacecraft orbits because it searches for a place where the probability of observations of two neighboring regions is equal to 0.5. If the spacecraft apogee is too low, such place simply would not be found.

6. Discussion

[23] The described method relies on the identification of the regions and we use the magnetic field and ion density for this purpose. The identification could be more reliable if the number of used parameters would be extended. We tried to add the ratio of velocities, however, it reduced the data set to approximately one quarter due to missing data and did not bring any significant improvement of the region identification. Nevertheless, we believe that it is the right way for a further enhancement of our method.

[24] A surprisingly low value of ϵ in the case of the magnetopause can be probably explained by a pressure of plasma

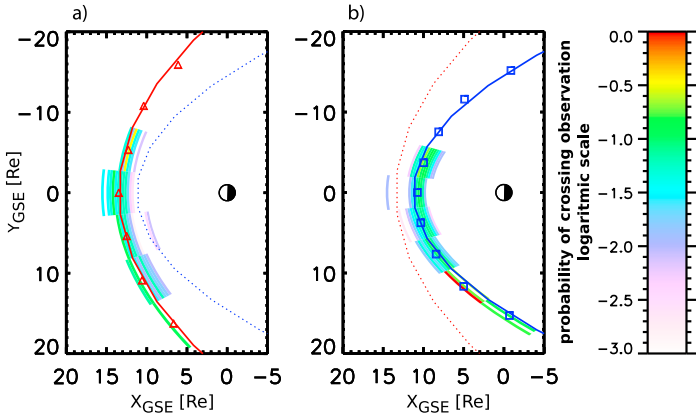

Figure 6. A comparison of the presented (a) bow shock and (b) magnetopause models with the observed bow shock and magnetopause crossings. The color scale shows the probability of observation of the particular boundary crossing in a given bin. The crossings from the pressure range of 1.0–1.1 nPa are shown and the full line stands for the model boundary location under 1.05 nPa of the dynamic pressure (Figure 6a – red line, Figure 6b – blue line). The second boundary (Figure 6a – the magnetopause, Figure 6b – the bow shock) is given by the dotted line for the sake of reference.

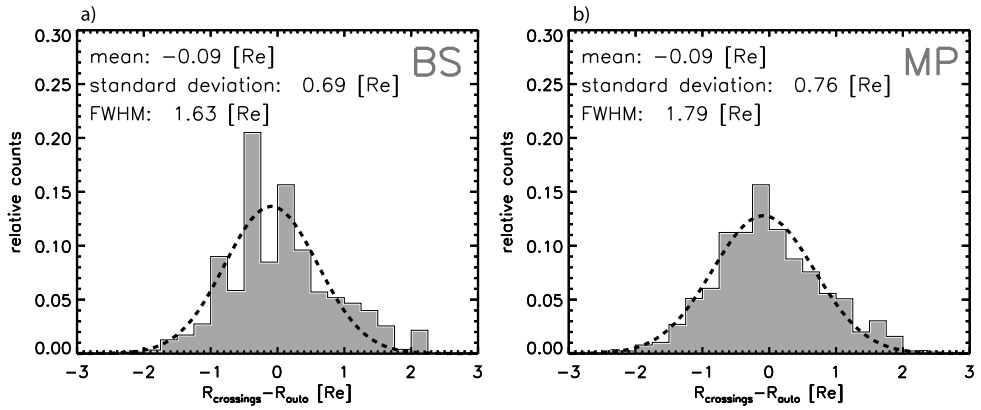

Figure 7. (a) Distributions of differences between positions of observed bow shock crossings and model positions. (b) The same plot for the magnetopause. The parameters of the Gaussian fit are given at the top of each panel.

inside the magnetosphere. However, we should note that the recent papers of *Lin et al.* [2010] and *Dušík et al.* [2010] report even lower exponents, ≈5.15 and 4.79, respectively. We have tested the dependence of the magnetopause location on the IMF B_Z sign but we did not find any statistically significant difference between sets for large positive or negative IMF B_Z. We will return to this point after collection of a significantly larger data set.

[25] The expression for the bow shock does not take into account the Mach number, however, the dependence of the bow shock location on the Mach number is expected to be rather weak for $M > 4$ and this condition is fulfilled for a majority of the observations. On the other hand, different values of ϵ for the bow shock and magnetopause suggest that the magnetosheath thickness would be a slightly rising function of the solar wind dynamic pressure. Since both the Mach number and solar wind dynamic pressure depend on the upstream density and speed, the change of the magnetosheath thickness with solar wind dynamic pressure following from equations (13)–(14) would be apparent and connected with well established dependence of this thickness on the upstream Mach number.

[26] The width of the distribution in Figure 7 seems to be large (FWHM ≈ 1.7 R_E) but we can compare this width with other models. The analysis of *Šafránková et al.* [2002] provides FWHM varying from ≈1.2 to ≈1.9 R_E for different magnetopause models and the value 1.7 R_E lies in this interval. Moreover, we applied our model on the set ≈1700 of dayside magnetopause crossings described in *Šafránková et al.* [2002] and found that FWHM = 1.3. Figure 8 presents the histogram of relative deviations of modeled and observed crossings, R_{MOD}/R_{OBS} in the same form as the histograms in the *Šafránková et al.* [2002] paper for an easier comparison. This result is fully comparable with another empirical models [*Petrinec and Russell*, 1996; *Shue et al.*, 1997, 1998] in the subsolar region at low latitudes.

[27] *Lin et al.* [2010] developed a very complex magnetopause model parameterized with the dynamic pressure, IMF B_Z, and tilt angle. They tested their model as well as several older models using a set of 62 observed low-latitude crossings and found that the values of standard deviations are in the range 0.65–1 R_E and only their model provided standard deviations of 0.54 R_E. From this comparison it follows that our result (0.76 R_E) is relatively good if we take into account that we incorporate only the dependence on the solar wind dynamic pressure.

[28] However, our model is based on THEMIS observations that cover only very limited ranges of latitudes and tilt angles. In spite of its relatively good performance, the model cannot describe the dependence of the magnetopause location on the tilt angle [*Boardsen et al.*, 2000; *Šafránková et al.*, 2005; *Jelínek et al.*, 2008; *Lin et al.*, 2010] or elliptical magnetopause cross-section suggested by, e.g., *Roelof and Sibeck* [1993], *Boardsen et al.* [2000], and *Lin et al.* [2010]. Such effects could be included after enlargement of the original data set with observations of other spacecraft like Cluster or earlier Prognoz type satellites that map the high-latitude regions. With such data set, we could account for different curvature radii of the magnetopause nose in the X-Y and X-Z planes simply assuming that λ_y and λ_z in equations (6)–(8) are not equal and determining their values

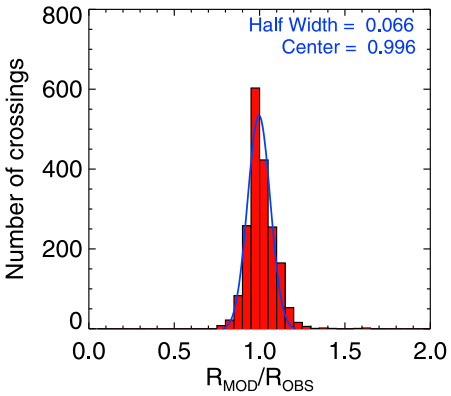

Figure 8. Histogram of R_{MOD}/R_{OBS} ratios for the present magnetopause model and the set of crossings in *Šafránková et al.* [2002].

by the fitting procedure. Moreover, since Cluster and THEMIS operate in the dayside regions in different parts of year, the combined data set can cover the full range of tilt angles, thus the dependence of model parameters on the tilt angle could be resolved.

[29] Nevertheless, our model(s) can serve as a very useful tool for an analysis of any data from the region covered by the measurements used for its(their) development. An example of their application can be found in the study of pressure profiles in the magnetosheath by *Samsonov et al.* [2012].

7. Conclusion

[30] We have developed a new automated method for identifications of bow shock and magnetopause positions and shapes. We successfully validated this method using ≈6000 BS and ≈5500 magnetopause dayside crossings that we have identified by a visual inspection of THEMIS data plots. Taking into account the limitations of the used data set, we can recommend the application of our models for the dayside low-latitude region in the range of solar wind dynamic pressures from 0.6 to 11 nPa.

[31] The main advantage of the suggested method is that it can be used for development of the magnetopause and bow shock models without necessity to identify boundary crossings. We have applied the method on THEMIS observations but it can be used for any spacecraft (or ensemble of the spacecraft including those on a geostationary orbit) orbiting in the near-Earth space and providing the plasma density and magnetic field strength if the simultaneous solar wind and IMF monitoring is available.

[32] Both models are in a good agreement with results obtained from observed boundary crossings and they are comparable with the previous more complex models. We plan to significantly enlarge the input data set and to extend the number of control parameters, especially to add IMF B_Z and the tilt angle for the magnetopause, and the Mach number for the bow shock.

[33] Another direction that can enhance the results of the bow shock and magnetopause modeling is an application of different non-Cartesian coordinate systems for the magnetopause and bow shock. A simple comparison of models with observed crossings in different local times (not shown) revealed that whereas the generalized parabolic coordinates provide good results for the bow shock, a modification of elliptical coordinates would be more appropriate for the description of the magnetopause location.

[34] **Acknowledgments.** The authors acknowledge the NASA contract NAS5-02099 and V. Angelopoulos for use of data from the THEMIS mission. Specifically, C. W. Carlson and J. P. McFadden for use of ESA data and K. H. Glassmeier, U. Auster and W. Baumjohann for the use of FGM data provided under the lead of the Technical University of Braunschweig and with financial support through the German Ministry for Economy and Technology and the German Center for Aviation and Space (DLR) under contract 50 OC 0302. The present work was partly supported by the Czech Grant Agency under contracts 205/09/0112 and 205/09/0170, and partly by the Research Plan MSM 0021620860 that is financed by the Ministry of Education of the Czech Republic.

[35] Philippa Browning thanks the reviewers for their assistance in evaluating this paper.

References

Angelopoulos, V. (2008), The THEMIS mission, *Space Sci. Rev.*, *141*, 5, doi:10.1007/s11214-008-9336-1.

Auster, H. U., et al. (2008), The THEMIS fluxgate magnetometer, *Space Sci. Rev.*, *141*, 235, doi:10.1007/s11214-008-9365-9.

Boardsen, S. A., T. E. Eastman, T. Sotirelis, and J. L. Green (2000), An empirical model of the high-latitude magnetopause, *J. Geophys. Res.*, *105*, 23,193.

Burgess, D. (1995), Collisionless shocks, in *Introduction to Space Physics*, edited by M. G. Kivelson and C. T. Russell, chap. 5, p. 129, Cambridge Univ. Press, Cambridge, U. K.

Dušík, Š., G. Granko, J. Šafránková, Z. Němeček, and K. Jelínek (2010), IMF cone angle control of the magnetopause location: Statistical study, *Geophys. Res. Lett.*, *19*, L19103, doi:10.1029/2010GL044965.

Eastman, T. E., S. A. Boardsen, S.-H. Chen, S. F. Fling, and R. L. Kessel (2000), Configuration of high-latitude and high-altitude boundary layers, *J. Geophys. Res.*, *105*, 23,221.

Fairfield, D. H. (1971), Average and unusual locations of the Earth's magnetopause and bow shock, *J. Geophys. Res.*, *76*, 6700.

Farris, M. H., and C. T. Russell (1994), Determining the standoff distance of the bow shock: Mach number dependence and use of models, *J. Geophys. Res.*, *99*, 17,681.

Formisano, V., P. C. Hedgecock, G. Moreno, F. Palmiotto, and J. K. Chao (1973), Solar wind interaction with the Earths magnetic field: 2. Magnetohydrodynamic bow shock, *J. Geophys. Res.*, *78*, 3731.

Formisano, V., V. Domingo, and K.-P. Wenzel (1979), The three-dimensional shape of the magnetopause, *Planet. Space Sci.*, *27*, 1137.

Jelínek, K., Z. Němeček, J. Šafránková, and J. Merka (2008), Influence of the tilt angle on the bow shock shape and location, *J. Geophys. Res.*, *113*, A05220, doi:10.1029/2007JA012813.

Jelínek, K., Z. Němeček, and J. Šafránková (2009), Themis: Locations of dayside bow shock and magnetopause, in *WDS'09 Proceedings of Contributed Papers: Part II–Physics of Plasmas and Ionized Media*, edited by J. Safrankova and J. Pavlu, p. 15, Matfyzpress, Prague.

Jeřáb, M., Z. Němeček, J. Šafránková, K. Jelínek, and J. Merka (2005), A study of bow shock locations, *Planet. Space Sci.*, *53*, 85.

Lin, R. L., X. X. Zhang, S. Q. Liu, Y. L. Wang, and J. C. Gong (2010), A three-dimensional asymmetric magnetopause model, *J. Geophys. Res.*, *115*, A04207, doi:10.1029/2009JA014235.

Lu, J. Y., Z.-Q. Liu, K. Kabin, M. X. Zhao, D. D. Liu, Q. Yhou, and Y. Xiao (2011), Three dimensional shape of the magnetopause: Global MHD results, *J. Geophys. Res.*, *116*, A09237, doi:10.1029/2010JA016418.

McFadden, J. P., C. W. Carlson, D. Larson, M. Ludlam, R. Abiad, B. Elliott, P. Turin, M. Marckwordt, and V. Angelopoulos (2008), The THEMIS ESA plasma instrument and in-flight calibration, *Space Sci. Rev.*, *141*, 277, doi:10.1007/s11214-008-9440-2.

Němeček, Z., and J. Šafránková (1991), The Earth's bow shock and magnetopause position as a result of the solar wind-magnetosphere interaction, *J. Atmos. Terr. Phys.*, *53*, 1049.

Petrinec, S. M., and C. T. Russell (1996), Near-Earth magnetopause shape and size as determined from the magnetopause flaring angle, *J. Geophys. Res.*, *101*, 137.

Roelof, E. C., and D. G. Sibeck (1993), Magnetopause shape as a bivariate function of interplanetary magnetic field Bz and solar wind dynamic pressure, *J. Geophys. Res.*, *98*, 21421.

Russell, C. T., and T. Mulligan (2002), On the magnetosheath thicknesses of interplanetary coronal mass ejections, *Planet. Space Sci.*, *50*(5/6), 527.

Šafránková, J., Z. Němeček, Š. Dušík, L. Přech, D. G. Sibeck, and N. N. Borodkova (2002), The magnetopause shape and location: a comparison of the Interball and Geotail observations with models, *Ann. Geophys.*, *20*, 301.

Šafránková, J., Š. Dušík, and Z. Němeček (2005), The shape and location of the high-latitude magnetopause, *Adv. Space Res.*, *36*, (10), 1934.

Samsonov, A. A., Z. Němeček, and J. Šafránková, and K. Jelínek (2012), Why does the subsolar magnetopause move sunward for radial interplanetary magnetic field?, *J. Geophys. Res.*, doi:10.1029/2011JA017429, in press.

Shue, J.-H., J. K. Chao, H. C. Fu, K. K. Khurana, C. T. Russell, H. J. Singer, and P. Song (1997), A new functional form to study the solar wind control of the magnetopause size and shape, *J. Geophys. Res.*, *102*, 9497.

Shue, J.-H., et al. (1998), Magnetopause location under extreme solar wind conditions, *J. Geophys. Res.*, *103*, 17,691.

Sibeck, D. G., R. E. Lopez, and E. C. Roelof (1991), Solar wind control of the magnetopause shape, location, and motion, *J. Geophys. Res.*, *96*, 5489.

Tsyganenko, N. A. (1998), Modeling of twisted/warped magnetospheric configurations using the general deformation method, *J. Geophys. Res.*, *103*, 23,551.

Verigin, M. I., G. A. Kotova, V. V. Bezrukikh, G. N. Zastenker, and N. Nikolaeva (2009), Analytical Model of the near-Earth magnetopause according to the data of the Prognoz and Interball satellite data, *Geomagn. Aeron.*, *49*, 8, 1176.

C.6 Why does the subsolar magnetopause moves sunward for radial interplanetary magnetic field?

JOURNAL OF GEOPHYSICAL RESEARCH, VOL. 117, A05221, doi:10.1029/2011JA017429, 2012

Why does the subsolar magnetopause move sunward for radial interplanetary magnetic field?

A. A. Samsonov,[1,2] Z. Němeček,[3] J. Šafránková,[3] and K. Jelínek[3]

Received 2 December 2011; revised 21 March 2012; accepted 21 March 2012; published 11 May 2012.

[1] This paper analyzes the distribution of different pressure components (dynamic, thermal, magnetic) in the magnetosheath along the Sun-Earth line for northward and radial interplanetary magnetic field (IMF) orientations with motivation to explain an unusual location and shape of the magnetopause often observed during the intervals of the radial IMF. The analysis employs isotropic and anisotropic MHD models, and their results are compared with the statistical processing of THEMIS observations. We have found that (1) the temperature anisotropy in the magnetosheath controls the pressure distribution near the magnetopause, and (2) the total pressure exerted on the subsolar magnetopause depends on the IMF orientation being significantly lower than the solar wind dynamic pressure for the radial IMF. The results of both MHD simulations and statistical investigations are quantitatively consistent with already published observations of the average magnetopause location as a function of the IMF orientation.

Citation: Samsonov, A. A., Z. Němeček, J. Šafránková, and K. Jelínek (2012), Why does the subsolar magnetopause move sunward for radial interplanetary magnetic field?, *J. Geophys. Res.*, *117*, A05221, doi:10.1029/2011JA017429.

1. Introduction

[2] Magnetic activity of the Earth's magnetosphere depends on the solar wind conditions. The interplanetary magnetic field (IMF) is one of the solar wind parameters, which strongly affects the solar wind–magnetosphere interaction. Due to its significant variability, its small fluctuations are hardly predictable and this effect makes difficult to accurately predict some magnetospheric changes. Moreover, even stable solar wind conditions with some non-typical IMF (whether because of an unusual orientation or strength) may result in a surprising magnetospheric configuration. One of such examples is the case with a nearly radial IMF, which can be observed in the solar wind very occasionally, but causes a very specific magnetopause shape. Recent observational results show that the subsolar magnetopause moves sunward in events with a nearly radial IMF, and in our paper we give a theoretical explanation of these observations.

[3] Using Wind and IMP 8 bow shock crossings, *Slavin et al.* [1996] found that the bow shock position shifts on ∼10% toward the Earth with respect to an average position when the cone angle θ between the IMF and Sun-Earth line is smaller than 20°. *Verigin et al.* [2001] constructed a three-dimensional bow shock shape based on the Wind data and noted that the subsolar bow shock is closer to the Earth for small θ and Alfvén Mach number (M_A). *Merka et al.* [2003] presented a study of multiple bow shock crossings encountered by Interball and IMP 8, when the IMF was nearly aligned with the solar wind velocity for a long interval of ∼9 hours. They found that both bow shock and magnetopause positions differ from the model predictions and that the subsolar magnetopause is more distant (∼2 R_E from the *Shue et al.* [1998] model prediction), while the bow shock is observed either closer [*Formisano*, 1979] or farther [*Cairns and Lyon*, 1995] from the Earth than the corresponding bow shock models predict. The observations suggest a magnetosheath thickness <10% of a_{mp} for these events where a_{mp} is the magnetopause standoff distance. Note that the typical magnetosheath thickness is nearly 0.3 a_{mp}. *Merka et al.* [2003] proposed that the magnetopause has a bullet-like shape, and the bow shock flares significantly less than MHD models predict. *Dmitriev et al.* [2003] found that all considered bow shock models overestimate the bow shock distance in the dayside region if $\theta < 30°$.

[4] Using THEMIS observations, recent studies [*Suvorova et al.*, 2010; *Dušík et al.*, 2010; *Jelínek et al.*, 2010] give a new evidence that the subsolar magnetopause lies significantly farther from the Earth for radial IMF orientations than it is expected. *Suvorova et al.* [2010] studied three events with relatively stable solar wind conditions and $\theta < 25°$ and found that the magnetosheath total pressure decreases 2–5 times in comparison with the solar wind pressure for these events and the magnetopause is 3 and 7 R_E outbound the mean location in the dayside and flank regions, respectively.

[1]Department of Earth Physics, Physical Faculty, St. Petersburg State University, St. Petersburg, Russia.
[2]Also at Space Research Institute, Austrian Academy of Sciences, Graz, Austria.
[3]Department of Surface and Plasma Science, Faculty of Mathematics and Physics, Charles University, Prague, Czech Republic.

Corresponding author: A. A. Samsonov, Department of Earth Physics, Physical Faculty, St. Petersburg State University, St. Petersburg 198504, Russia. (andre.samsonov@gmail.com)

0148-0227/12/2011JA017429

Dušík et al. [2010] presented a statistical study which demonstrates the dependence of the subsolar and flank magnetopause on θ, and they confirmed an increase of the stand-off distance for small θ. The difference of the magnetopause positions between the IMF aligned with and IMF perpendicular to the solar wind flow was found to be statistically about 1.4 R_E.

[5] *Jelínek et al.* [2010] analyzed the event when the IMF discontinuity dividing regions of nearly radial and standard IMF orientations was swept along the bow shock. The authors have shown that a part of the magnetopause affected by a radial IMF is expanded, whereas the part affected by the standard IMF orientation remained at a nominal location corresponding to the upstream dynamic pressure. It led to a significant (several R_E) magnetopause distortion that propagated along the magnetopause together with the IMF discontinuity.

[6] The observations are partly confirmed by magnetohydrodynamic (MHD) simulations. As it was shown by *Spreiter and Rizzi* [1974], the MHD equations can be transformed into the hydrodynamic equations with a peculiar equation of state in a purely radial IMF case (when directions of the solar wind velocity and IMF coincide). Simulating a flow around a fixed-shape obstacle, *Spreiter and Rizzi* [1974] predicted that the subsolar bow shock shifts closer to the Earth and the tailward bow shock moves farther in response to an decrease of the Alfvén Mach number in the radial case. There is a stagnation point at the nose of the magnetopause where $B = 0$ and ρ and T reach maximum values in the magnetosheath. An analysis of the three-dimensional global MHD simulations for different θ performed by *Cairns and Lyon* [1996] confirmed the Spreiter and Rizzi's finding that the thickness of the subsolar magnetosheath decreases with the decrease of the Alfvén Mach number for $\theta < 20°$. The magnetosheath thickness was found to be $<0.1\ a_{mp}$ for $M_A < 2$ and $\theta = 0°$. *Farrugia et al.* [2010] applied the *Spreiter and Rizzi* [1974] approach and solved analytical formulae for MHD parameters in the magnetosheath in the field-aligned case. They demonstrated that their model well predicts the magnetic field in the nightside magnetosheath observed by Wind. However, in the MHD simulations, the magnetopause shape has been determined from the pressure balance using the Newtonian relation as *Spreiter et al.* [1966] described. Thus, the shape of the obstacle was supposed to depend only on the solar wind dynamic pressure but not on the IMF orientation. Using a 3-D MHD model, *Samsonov* [2006] studied influence of the IMF orientation on magnetosheath parameters in quasi-stationary solutions and found that the magnetic barrier almost disappears for $\theta = 20°$. However, this work did not investigate variations of the magnetopause pressure or changes of the magnetopause shape.

[7] For very specific solar wind parameters (certain combinations of low M_A and β in the range $M_A < 2$ and $\beta < 1$), *De Sterck and Poedts* [1999]; *Chapman et al.* [2004] and *Cable et al.* [2007] showed that a dimple forms at the bow shock nose in the field-aligned flow, and the MHD solution in the subsolar region contains not only a reversed fast shock (bow shock), but also intermediate shocks, a switch-on shock and a tangential discontinuity [*De Sterck et al.*, 1998]. To our knowledge, no observation confirms directly this theoretical prediction at the Earth's bow shock, but similar structures possibly form upstream of magnetic clouds [*Feng et al.*, 2009].

[8] If the angle between the IMF and the bow shock normal is small, the foreshock magnetically connected to the bow shock arises in the upstream region. Many papers emphasize that the waves originated in the foreshock sufficiently disturb the magnetosheath flow and can penetrate into the magnetosphere [e.g., *Engebretson et al.*, 1991; *Lin et al.*, 1991; *Fairfield et al.*, 1990; *Russell et al.*, 1983; *Sibeck*, 1995; *Sibeck et al.*, 2003; *Shevyrev et al.*, 2007]. The global hybrid simulations [*Blanco-Cano et al.*, 2009; *Lin and Wang*, 2005] predict a generation of diamagnetic cavities or cavitons which are characterized by a decrease of the magnetic field and density in the center and an increase of the magnetic field and density at the edges of the structure. These structures propagate through the magnetosheath and result in magnetopause surface waves [*Lin and Wang*, 2005]. They may cause large but localized distortions of the magnetopause shape, e.g., as it observed by *Shue et al.* [2009] for a radial IMF. However, it cannot explain a large-scale deformation of the whole magnetopause, like the bullet-like magnetopause proposed by *Merka et al.* [2003].

[9] The MHD approach is also fault if the ion Larmor radius becomes comparable with the size of system. The Larmor radius is really larger in the magnetosheath for radial IMF than for other IMF orientations because of a weaker magnetic field. However, even in the radial case, the Larmor radius in the magnetosheath is not very different from the solar wind Larmor radius. For example, if the magnetic field magnitude is equal to 5 nT and the temperature is 100 eV, it gives the proton Larmor radius ~300 km what is sufficiently less than a characteristic length in the magnetosheath. Note that the MHD theory successfully describes the solar wind flow even with a weaker magnetic field farther from the Sun, in the heliosheath. Despite a little skepticism, we believe that predictions of the MHD theory should be thoroughly studied, even if some radial IMF events might be properly explained only by the kinetic approach.

[10] Observations in the magnetosheath [e.g., *Anderson and Fuselier*, 1993; *Crooker et al.*, 1976; *Gary et al.*, 1993; *Samsonov et al.*, 2007] reveal that the ion distribution function is anisotropic and the perpendicular thermal pressure, $p_\perp$ is usually higher than the parallel thermal pressure, $p_\parallel$ (both perpendicular and parallel directions with respect to the magnetic field). *Denton and Lyon* [1996], *Erkaev et al.* [1999], *Farrugia et al.* [2000], *Samsonov and Pudovkin* [1998, 2000], and *Samsonov et al.* [2001] have developed numerical anisotropic MHD models for the Earth's magnetosheath which predict variations of the temperature anisotropy, $p_\perp/p_\parallel$, in a good agreement with the magnetosheath observations [*Farrugia et al.*, 2001; *Samsonov et al.*, 2007]; however, it has not been previously realized that the use of the anisotropic models may change the total pressure at the outer side of the magnetopause boundary. The magnetopause is usually assumed to be a tangential discontinuity for which the total pressure, $p_\perp + B^2/8\pi$ is balanced on both sides in a stationary case. Under some conditions, the perpendicular pressure predicted by an anisotropic MHD model may sufficiently differ from the thermal pressure predicted by an isotropic MHD model, therefore the magnetopause position would change.

[11] In this paper, we inspect MHD predictions at the vicinity of the Sun-Earth line for the radial and northward IMF orientations. We show that (1) at the subsolar magnetopause, the total pressure differs from the solar wind dynamic pressure, and that this difference depends on the IMF orientation; and (2) the predictions of the anisotropic MHD model differ from the predictions of the isotropic model and the temperature anisotropy would help to explain the observations of unusual magnetopause shapes for a radial IMF.

2. Analysis of Isotropic MHD Equations

[12] Let us consider variations of the total pressure at the Sun-Earth line between the bow shock and magnetopause. We use such coordinate system where the magnetic field vector lays in the XZ plane. The X axis coincides with the Sun–Earth line and points toward the Sun. The assumption of a symmetry leads to $V_z = 0$.

[13] Using the stationary equation of motion, we get

$$\frac{\partial(\rho V_x^2)}{\partial x} = V_x\frac{\partial(\rho V_x)}{\partial x} + \rho V_x\frac{\partial V_x}{\partial x} = V_x\frac{\partial(\rho V_x)}{\partial x} - \frac{\partial(p + (B_x^2 + B_z^2)/8\pi)}{\partial x} + \frac{1}{4\pi}\left(B_x\frac{\partial B_x}{\partial x} + B_z\frac{\partial B_x}{\partial z}\right). \quad (1)$$

[14] From (1), we obtain variations of the total pressure at the Sun-Earth line

$$\frac{\partial}{\partial x}\left(\rho V_x^2 + p + B_z^2/8\pi\right) = V_x\frac{\partial(\rho V_x)}{\partial x} + \frac{1}{4\pi}B_z\frac{\partial B_x}{\partial z}. \quad (2)$$

[15] We integrate (2) through the magnetosheath profile

$$P_{tot}(BS) - P_{tot}(MP) = \int_{MP}^{BS}\left(V_x\frac{\partial(\rho V_x)}{\partial x} + \frac{1}{4\pi}B_z\frac{\partial B_x}{\partial z}\right)dx, \quad (3)$$

where $P_{tot} = \rho V_x^2 + p + B_z^2/8\pi$.

[16] The right part of (3) contains two terms. As it will be shown below, the first term causes a decrease of the total pressure due to the flow diversion along the magnetopause and the second term gives an increase of the pressure connected with the magnetic field draping against the magnetopause. We will discuss each term under some assumptions.

[17] Estimating the first term, we assume that the earthward velocity at the Sun-Earth line ($-V_x$) linearly decreases from the value just downstream of the bow shock, V_{BS} to zero at the magnetopause. This assumption is well confirmed by previous MHD simulations [e.g., *Wu*, 1992; *Samsonov and Pudovkin*, 2000]. We obtain

$$\int_{MP}^{BS} V_x\frac{\partial(\rho V_x)}{\partial x}dx = \rho V_x^2(BS) - \int_{MP}^{BS}\rho V_x\frac{\partial(V_x)}{\partial x}dx = \rho V_x^2(BS) + V_{BS}\int_{MP}^{BS}\rho V_x dx. \quad (4)$$

[18] The spatial coordinate is normalized to ($x_{BS} - x_{MP}$). In the next step, we assume that ρ is nearly constant through the magnetosheath, except the plasma depletion layer (PDL), i.e., a relatively narrow region adjacent to the magnetopause. Because V_x is small in the PDL, such assumption gives only a small error. Thus, finally, we get

$$\int_{MP}^{BS} V_x\frac{\partial(\rho V_x)}{\partial x}dx \simeq \rho V_{BS}^2 + \rho V_{BS}\int_{MP}^{BS} V_x dx = \rho V_{BS}^2/2. \quad (5)$$

[19] Considering a high Mach number solar wind, the density and velocity immediately downstream of the bow shock are simply estimated from the solar wind values:

$$V_{BS} = \frac{1}{4}V_{SW}, \rho_{BS} = 4\rho_{SW}.$$

[20] As a result, we obtain

$$P_{tot}(BS) - P_{tot}(MP) = \frac{1}{2}\rho_{BS}V_{BS}^2 = \frac{1}{8}\rho_{SW}V_{SW}^2. \quad (6)$$

[21] Since the total pressure varies continuously, $P_{tot}(BS) = P_{tot}(SW) \simeq \rho_{SW}V_{SW}^2$, we get $P_{tot}(MP) \simeq 0.875\rho_{SW}V_{SW}^2$.

[22] This simple estimation is very close to the expression for the stagnation pressure at the nose of a blunt obstacle in a supersonic hydrodynamic stream found by *Spreiter et al.* [1966], $P_{tot}(MP) \simeq 0.881\rho_{SW}V_{SW}^2$ (for the polytropic index $\gamma = 5/3$). The small difference against the Spreiter et al.'s result may be caused by our assumption about a constant density. In a hydrodynamic solution, the density increases near the subsolar magnetopause, thus the mean magnetosheath density is higher than the density just downstream of the bow shock ρ_{BS}. The term $\int_{MP}^{BS}\rho V_x dx$ in (4) is negative, so a larger density results in a decrease of ($P_{tot}(BS) - P_{tot}(MP)$), thus approaching Spreiter et al.'s result. A strictly radial IMF case coincides with the hydrodynamic case. In such a case, the density also increases near the magnetopause and the second right term in (3) vanishes because $B_z = 0$.

[23] If the magnetic field is straight and perpendicular to the X axis, as it may occur in the solar wind upstream of the bow shock, then $\frac{\partial B_x}{\partial z} = 0$. When the magnetic field becomes tangential to the magnetopause, we would estimate $\frac{\partial B_x}{\partial z} \simeq -B_{MP}/R_{MP}$. We assume that the second term on the right side of (3) is sufficient only in a layer near the magnetopause with a plasma beta less than unity, i.e., in the magnetic barrier. When we determine Δ_{MB} as a width of this layer at the Sun–Earth line, then

$$\int_{MP}^{BS}\frac{1}{4\pi}B_z\frac{\partial B_x}{\partial z}dx \simeq -\frac{B_{MP}^2}{4\pi R_{MP}}\Delta_{MB}. \quad (7)$$

In order to continue, we estimate $\Delta_{MB}/R_{MP} \simeq 0.1$ (ignoring the dependence of the Δ_{MB} on the solar wind Alfvén Mach number for simplicity) and assume

$$\frac{B_{MP}^2}{8\pi} \simeq \frac{2}{3}P_{tot}(SW)$$

(note that it corresponds to a mean β in the magnetic barrier $\sim$0.5).

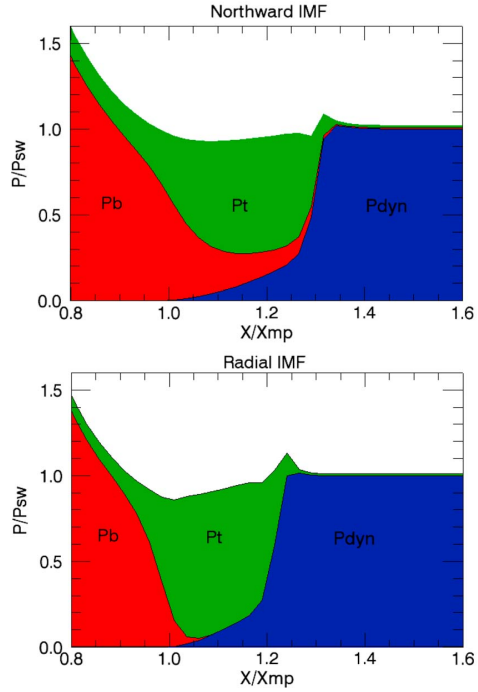

Figure 1. Dynamic (blue), thermal (green), and magnetic (red) pressures at the Sun-Earth line obtained by the global BATS-R-US code for the northward and radial interplanetary magnetic field (IMF) cases. The normalization unit X_{mp} is the position of the subsolar magnetopause.

[24] Finally, in this simple estimation, we obtain

$$P_{tot}(BS) - P_{tot}(MP) \simeq \frac{1}{8}\rho_{SW}V_{SW}^2 - \frac{4}{30}\rho_{SW}V_{SW}^2 \simeq 0. \quad (8)$$

Although the estimations above are rough, we can conclude that the total pressure at the subsolar magnetopause depends on the IMF orientation. In particular, it appears to be smaller in a radial IMF case than in the northward IMF case for the same solar wind dynamic pressure. A larger total pressure in the northward case results from the magnetic field draping and magnetic barrier formation. The obtained difference of the total pressure in two cases estimated from the isotropic MHD equations at the Sun–Earth line is small and gives only about 10–15%, but this effect can be stronger if the anisotropic MHD equations would be applied.

3. Analysis of Anisotropic MHD Equations

[25] In a collisionless plasma, the ion and electron distribution functions are anisotropic. In the double adiabatic one-fluid MHD approach, variations of the perpendicular and parallel (with respect to the magnetic field) thermal pressures are described by the CGL equations [*Chew et al.*, 1956]

$$\frac{d}{dt}\left(\frac{p_\perp}{\rho B}\right) = 0, \quad \frac{d}{dt}\left(\frac{p_\parallel B^2}{\rho^3}\right) = 0. \quad (9)$$

[26] It is easy to estimate variations of these two pressure components through the perpendicular and parallel bow shocks with a high Mach number. For a strong perpendicular shock, it gives us the jumps of the density and magnetic field through the bow shock, $\rho_{BS}/\rho_{SW} \simeq B_{BS}/B_{SW} \simeq 4$;, while for a strong parallel shock, we get $\rho_{BS}/\rho_{SW} \simeq 4$ but $B_{BS}/B_{SW} \simeq 1$. Correspondingly, $p_{\perp BS}/p_{\perp SW} \simeq 16$ and $p_{\parallel BS}/p_{\parallel SW} \simeq 4$ for the perpendicular shock; and $p_{\perp BS}/p_{\perp SW} \simeq 4$ and $p_{\parallel BS}/p_{\parallel SW} \simeq 64$ for the parallel shock. Thus, the solar wind kinetic energy redistributes into the perpendicular thermal energy in the perpendicular shock, and into the parallel thermal energy in the parallel case. The mirror and ion cyclotron instabilities develop in the magnetosheath downstream of the perpendicular bow shock (where $p_\perp/p_\parallel$ is larger than the corresponding thresholds [see, e.g., *Samsonov et al.*, 2001], resulting in the isotropization of the ion distribution. Similarly, the firehose instability may develop under condition $p_\parallel > p_\perp + B^2/4\pi$.

[27] Using the anisotropic MHD equations, we get an expression similar to (2) but with two pressure components. The anisotropic equation of motion is given as follows [*Samsonov et al.*, 2001]:

$$\frac{\partial}{\partial t}(\rho\mathbf{V}) = -\nabla\cdot[\rho\mathbf{VV} + I(p_\perp + \frac{B^2}{8\pi}) + \frac{\mathbf{BB}}{4\pi}(4\pi\frac{p_\parallel - p_\perp}{B^2} - 1)]. \quad (10)$$

[28] Taking the x component of (10) in a stationary case, we obtain

$$\frac{\partial}{\partial x}(\rho V_x^2 + p_\perp + B_z^2/8\pi) + \frac{\partial}{\partial x}\left(\frac{p_\parallel - p_\perp}{B^2}B_x^2\right) + \frac{\partial}{\partial z}\left(\frac{p_\parallel - p_\perp}{B^2}B_xB_z\right) = V_x\frac{\partial(\rho V_x)}{\partial x} + \frac{1}{4\pi}B_z\frac{\partial B_x}{\partial z}. \quad (11)$$

Expression (11) differs from (2) only by two anisotropic terms which include the dimensionless parameter $(p_\parallel - p_\perp)/B^2$. In this case, an accurate self-consistent MHD solution can be found only using numerical simulations.

4. Results of Global Isotropic MHD Simulations

[29] Figure 1 shows results of the global MHD BATS-R-US code at the Sun-Earth line which illustrates pressure changes in two runs for northward and radial IMF orientations conserving all other upstream conditions. In these runs, the solar wind sound and Alfvén Mach numbers equal 6.95 and 8.13, respectively. In the northward case, the IMF is strictly perpendicular to the Sun-Earth line. On the other hand, in the radial case, the angle between the IMF and Sun-Earth line equals 3.6° ($B_x = -4.99$ nT and $B_x = 0.316$ nT at the solar wind boundary) and the solar wind velocity directs along the Sun-Earth line. We use the blue, green, and red colors in order to distinguish portions of the dynamic, thermal, and magnetic pressures constituting the total pressure. Note that we consider here only the pressure pushing the

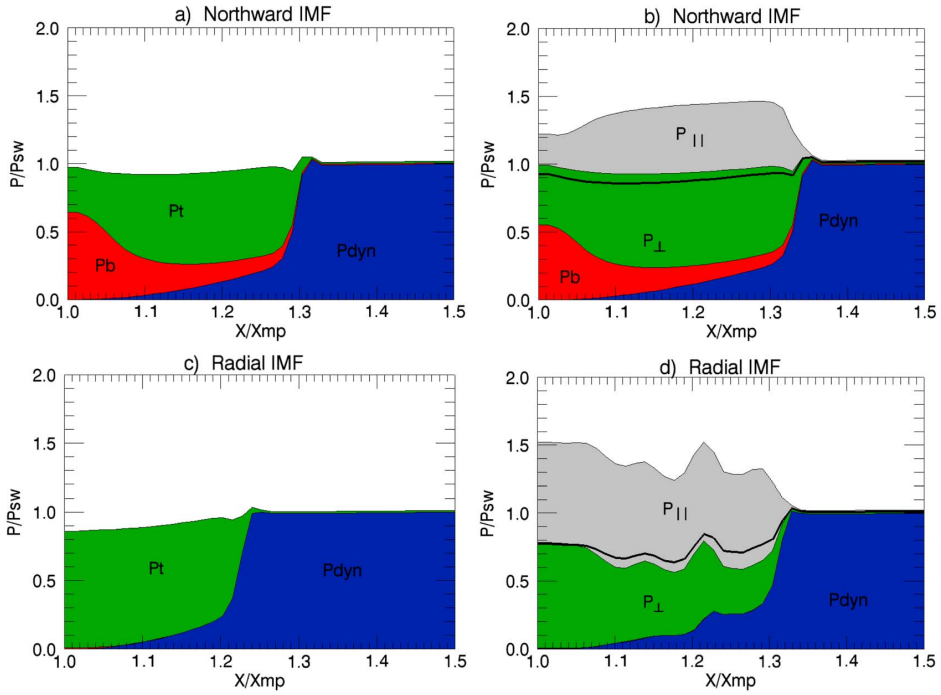

Figure 2. Results of the (a and c) isotropic and (b and d) anisotropic magnetosheath models at the Sun-Earth line in the northward and radial IMF cases. Black lines on Figures 2b and 2 d show estimations of the total pressure in the isotropic approximation, $2/3p_{\perp} + 1/3p_{\|}$.

magnetopause, i.e., the radial dynamic and tangential magnetic pressures.

[30] The region with a dominant dynamic pressure in Figure 1 is apparently the supersonic solar wind upstream of the bow shock. At the bow shock, the dynamic pressure converts mainly into the thermal pressure. For the northward IMF case, the thermal pressure gradually transforms into the magnetic pressure when reaching the magnetopause. Near the subsolar magnetopause, the magnetic pressure is usually larger than the thermal pressure with the plasma $\beta = 8\pi p/B^2$ varying between 0.1 and 1 [*Anderson and Fuselier*, 1993; *Phan et al.*, 1994]. The dynamic pressure decreases from the bow shock to magnetopause and becomes negligible at the subsolar point. For the radial IMF case, the thermal pressure is dominant through the whole subsolar magnetosheath, and the magnetic pressure grows only at the magnetopause.

[31] In the global simulations, the total pressure near the magnetopause becomes smaller than that in the supersonic solar wind both in the northward and radial runs. Our estimations for the two runs give 97% and 86%, respectively of the solar wind dynamic pressure. In the radial case, this estimation agrees with the approximate estimation in section 2. For the purely northward IMF, the accuracy may be worse since it is difficult to determine precisely the magnetopause position.

[32] The use of the anisotropic MHD equations instead of the isotropic equations in the magnetosheath modeling appears to be more suitable. The ion thermal pressure tensor consists of the perpendicular and parallel components which can sufficiently differ in both the inner and outer magnetosheaths. Note that only the perpendicular pressure compresses the magnetopause. We find variations of the perpendicular and parallel pressures through the magnetosheath (not shown) from the same numerical results as above getting the $p_{\perp}/p_{\|}$ ratio from (9) and taking $2p_{\perp} + p_{\|} = 3p$, where p is the isotropic thermal pressure calculated by the global MHD code. The parallel thermal pressure for the radial IMF in this approach is several times greater than the perpendicular thermal pressure through the magnetosheath, except the region close to the magnetopause. We conclude that this simple method clearly overestimates the $p_{\|}/p_{\perp}$, and we need to solve a full system of anisotropic MHD equations.

5. Results of the Anisotropic Magnetosheath Model

[33] We use a modification of the anisotropic three-dimensional (3-D) magnetosheath model developed by *Samsonov et al.* [2001, 2007]. The model calculates the double-adiabatic MHD equations (like equation (9)), but growth of the temperature anisotropy, i.e., the ratio of perpendicular to parallel temperatures, is limited by the thresholds of the mirror and proton-cyclotron instabilities as described by *Samsonov et al.* [2007]. The TVD Lax-Friedrichs II-order scheme [e.g., *Toth and Odstrčil*, 1996] has been used for the numerical simulation.

[34] Unlike *Samsonov et al.* [2007], we solve the problem in spherical coordinates. The grid size is ~900 km in radial

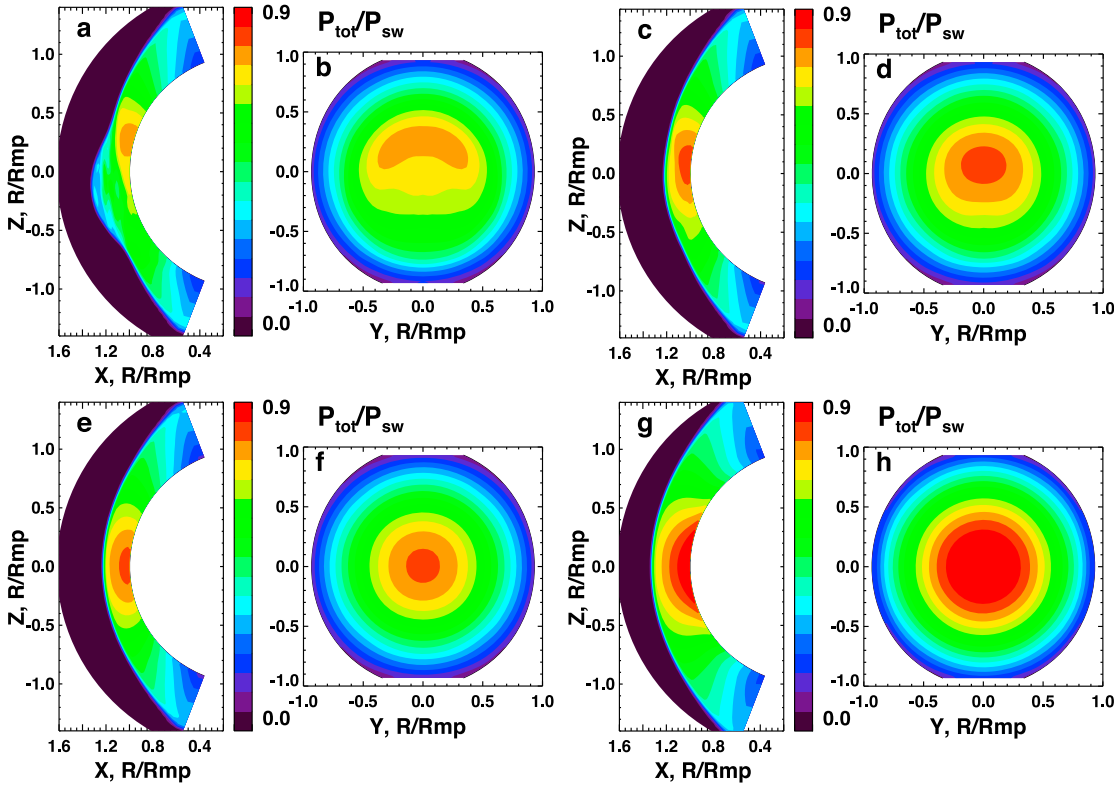

Figure 3. Sum of the magnetic and perpendicular thermal pressures in the noon meridional plane and projected on the magnetopause obtained by the anisotropic MHD model in the radial IMF case (a and b) without and (c and d) with the firehose instability threshold, (e and f) by the isotropic MHD model and (g and h) by the anisotropic MHD model in the northward IMF case.

direction and 2–3 times larger in two other directions. We have made a control run with a double spatial resolution what corresponds to a smaller numerical viscosity. We find that the difference between usual and high-resolution runs is limited mainly to the bow shock and plasma depletion layer near the inner boundary. In particular, jumps of all parameters through the bow shock are sharper and growth of the magnetic field near the magnetopause is stronger in the high-resolution run. However, changes of the total pressure exerted on the magnetopause are negligible and thus the main conclusions of the paper do not depend on the grid spacing.

[35] The inner boundary of the model corresponds to the magnetopause with conditions $B_n = 0$ and $V_n = 0$, and the outer boundary is situated in the supersonic solar wind. We make runs with the same solar wind conditions as in the previous global MHD simulations. At the beginning, we obtain two isotropic MHD solutions (for northward and radial IMFs) and then, using these solutions as initial conditions, we get two anisotropic solutions. We have checked that the obtained solutions are quasi-stationary (except one anisotropic solution for the radial IMF discussed below), i.e., the time evolution of all parameters is negligible after ~15 min of the model runs.

[36] Variations of the dynamic, thermal, and magnetic pressures at the Sun-Earth line upstream of the magnetopause for the isotropic and anisotropic models are shown in Figure 2.

[37] First, let us consider results of the isotropic model. As it was shown above in the global MHD simulation, the thermal pressure is largest in the outer magnetosheath, and the magnetic pressure prevails in the inner magnetosheath in the northward IMF case. When the IMF becomes radial, the magnetosheath model predicts a dominant thermal pressure in the most part of the subsolar magnetosheath with a typical plasma β near or above 100. Thus, the external total pressure at the subsolar magnetopause consists mainly of the thermal pressure in this case.

[38] Using results of the anisotropic MHD model (Figures 2b and 2d), we see that the perpendicular thermal pressure exceeds the parallel pressure in the northward case, but the perpendicular and parallel pressures are nearly equal near the magnetopause in the radial case. However, comparing the isotropic and anisotropic results for the radial case, we find that the total pressure which compresses the magnetopause, i.e., the sum of $P_\perp$ and $B^2/8\pi$ decreases by 8% in the anisotropic case with respect to the isotropic one. The total pressure near the magnetopause in the anisotropic modeling is equal to 99% and 78% of the solar wind dynamic pressure in the northward and radial cases, respectively. In other words, the external magnetopause pressure is more than

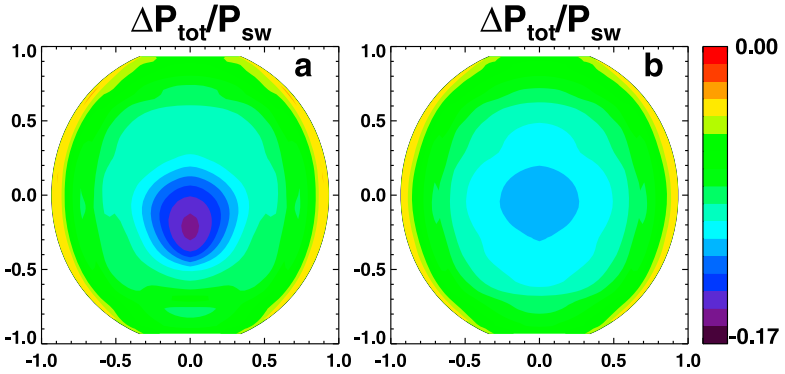

Figure 4. Difference between the magnetopause total pressures in the radial and northward cases using the (a) anisotropic and (b) isotropic MHD simulations.

20% weaker in the radial case than in the northward case keeping the same other solar wind parameters.

[39] If the IMF orientation is close to radial in the solar wind, the magnetospheric compression becomes peculiar not only at the subsolar point, but in a large part of the dayside magnetopause. Figures 3a and 3b show the distribution of $P_{tot} = p_\perp + B_\tau^2/8\pi$ on the noon-meridional plane and at the magnetopause boundary for the anisotropic MHD model. A very small northward IMF component in the radial case results in the large north-south asymmetry of the magnetospheric compression. However, we find that the numerical solution is unstable because of the growth of the firehose instability.

[40] The firehose instability has been obtained in the CGL-MHD [*Kowal et al.*, 2011] and kinetic [*Gary et al.*, 1998] simulations for $p_\parallel > p_\perp$. *Kasper et al.* [2002] derived the instability threshold $p_\perp/p_\parallel = 1 - 1.21\beta_\parallel^{-0.76}$ using the proton temperatures measured in the solar wind by the Wind spacecraft. This empirical relation is in a good agreement with the linear theory of the resonant firehose instability and the 1-D simulations results of *Gary et al.* [1998]. We apply the *Kasper et al.* [2002] threshold to impose a lower limit of the $p_\perp/p_\parallel$ in our model in addition to the ion cyclotron $(p_\perp/p_\parallel)_{ic} = 1 + 0.64\beta_\parallel^{-0.41}$ and mirror $(p_\perp/p_\parallel)_{mir} = 1 + 0.99\beta_\parallel^{-0.63}$ thresholds which determine the upper limits. Numerical results of this modified anisotropic model with the three thresholds are shown in Figures 3c and 3d. For comparison, we draw also the results of the isotropic MHD model in the radial case (Figures 3e and 3f) and the results of the anisotropic model with the thresholds in the northward case (Figures 3g and 3h).

[41] The sharp boundary between a low P_{tot} in the supersonic solar wind and a high P_{tot} in the magnetosheath (in the noon meridional plane in Figure 3) indicates the bow shock position that forms self-consistently in the numerical simulation. In Figure 3a, the large deformation of the bow shock shape in the part where the IMF direction and shock normal nearly coincide, i.e., at the parallel bow shock region, is caused possibly by the instability of the solution. Such feature is obtained only in the anisotropic MHD modeling in the radial case when the variations of $p_\perp/p_\parallel$ are unlimited by the firehose threshold and it disappears for other IMF orientations.

[42] Using the firehose instability threshold, it keeps the $p_\perp/p_\parallel$ close to unity in a high β region downstream of the parallel bow shock and thus the solution becomes stable. The results in Figures 3c and 3d better match the results of the isotropic modeling (Figures 3e and 3f) than the results of the anisotropic modeling without the firehose threshold. By contrast to the isotropic results, there is a small asymmetry in Figure 3d with the highest magnetopause pressure being in the north hemisphere. The total pressure at the subsolar magnetopause in the stable radial case does not exceed 86% of the solar wind dynamic pressure, and it is 14% less than in the anisotropic results for the northward IMF. In agreement with previous studies, the bow shock is closer to the magnetopause for the radial IMF than for the northward IMF. Comparing Figures 3c and 3g, we see that the difference of the bow shock position in the subsolar region is about 35%. The differences among the three runs with the radial IMF decrease moving from the subsolar region toward the flank where $p_\perp/p_\parallel$ is near or slightly above unity and the firehose instability does not grow.

[43] In this paper, we emphasize the fact that the magnetopause pressure in radial and northward IMF cases sufficiently differs, therefore we plot the differences between the both total pressures at the magnetopause, i.e., $(P_{tot}(\theta = 3.6°) - P_{tot}(\theta = 90°))/\rho_{SW}V_{SW}^2$ in Figure 4. Figures 4a and 4b correspond to the anisotropic (with the firehose threshold) and isotropic models, respectively. Although the both models predict a decrease of the total pressure at the subsolar magnetopause, this effect is stronger in the anisotropic model. The maximum difference of P_{tot} in the stable anisotropic simulation shifts southward from the subsolar point (because of the small northward component in the radial case) and reaches $\sim 0.16\ \rho_{SW}V_{SW}^2$, while the difference is nearly symmetric around the subsolar point in the isotropic simulations. At the flanks, the models predict a slightly lower magnetospheric compression in the radial case and the difference between the anisotropic and isotropic models is almost absent.

[44] *Cable et al.* [2007] studied a radial case with a low solar wind β and found that magnetopause magnetic reconnection occurs in the hemisphere where the magnetospheric and magnetosheath fields are antiparallel. We inspect a possibility of reconnection in our radial case using the results of

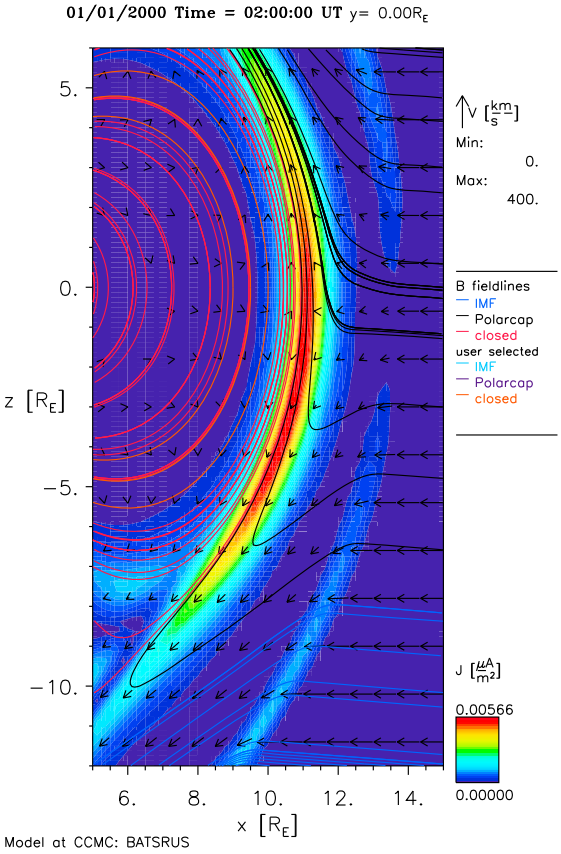

Figure 5. Magnetic field configuration in the radial case simulated by the global MHD BATS-R-US code. The colors show the electric current magnitude which intensifies at the dayside magnetopause. The red, blue, and black lines correspond to the magnetic field lines which are closed, open, and connected to the north polar cap, respectively. The arrows show velocity vectors.

the global isotropic MHD BATS-R-US simulation. Figure 5 shows a configuration of the magnetic field in a region with the X_{GSM} between 5 and 15 R_E. The figure demonstrates that in the most part of the dayside magnetopause (at least, for $X > 6R_E$), the magnetosheath and magnetospheric magnetic fields are parallel, therefore magnetopause reconnection in the present case does not play any role in the subsolar region.

6. Experimental Confirmation of MHD Results

[45] MHD models provided the pressure profiles through the magnetosheath along the Sun-Earth line under northward and radial IMF. However, the periods of such clear IMF orientations are not too frequent and they are often short. For this reason, we did not succeed in finding a satellite path through the whole magnetosheath near the Sun-Earth line under required IMF orientations and we were forced to confirm the MHD results applying a statistical processing of a large volume of the data.

6.1. Data Set and Processing

[46] We have used observations of all THEMIS spacecraft from the launch in 2007 till the middle of 2009. The initial set contained the 1 min averages of the measured density, parallel and perpendicular temperatures, velocity, and magnetic field. We used all available measurements made outbound of a 6 R_E sphere without any other constrain. These data were complemented with the upstream parameters (IMF and dynamic pressure) measured in the L1 point by ACE and propagated into a particular place of the THEMIS spacecraft. As a next step, the coordinates of the THEMIS spacecraft were scaled in order to account for changes of the magnetopause and bow shock locations with upstream conditions. The scaling uses the magnetopause and bow shock models of *Jelínek et al.* [2012] and generalized parabolic magnetosheath coordinates τ and σ introduced therein by following expressions:

$$\tau = \sqrt{\sqrt{x^2 + (\lambda y)^2 + (\lambda z)^2} - x} \tag{12}$$

$$\sigma = \sqrt{\sqrt{x^2 + (\lambda y)^2 + (\lambda z)^2} + x} \tag{13}$$

where λ is a scaling factor.

[47] For each data point we calculated expected locations of the bow shock and magnetopause and the coordinate τ that corresponds to the distance from the Earth and that was scaled to put a particular spacecraft to the appropriate position with respect to the boundaries.

[48] The resulting coverage of the region under question is shown in Figure 6. This figure shows a total number of minutes that the spacecraft spent in a particular spatial bin (Figure 6a), the number of minutes when the upstream IMF was nearly radial (i.e., the IMF cone angle was lower than 15° or greater than 165°, Figure 6b), and the number of minutes for IMF $B_z \geq 2$ (Figure 6c). Although the calculations shown in the previous section were done exactly along the Sun-Earth line, we applied a combination of the data from three bins adjacent to this line because the number of data points in the first bins is too small, especially for the radial IMF case. The investigated region is bounded by the horizontal axis and by the dashed line in the figure. The sorting of the data was based on the ACE magnetic field propagated to the bow shock nose. The propagation algorithm expects the solar wind speed being equal to 400 km/s in the first step, and finds the measured velocity at the time given by this assumption and ACE separation from the bow shock nose. The second step uses this new velocity for determination of the proper time delay [*Šafránková et al.*, 2002].

6.2. Comparison of Experimental Results With the Anisotropic MHD Model

[49] Since the magnetosheath plasma is highly anisotropic and only the perpendicular component of pressure can influence the magnetopause location, we started with an analysis of this anisotropy. Figure 7 shows the results in the same format as used in the study of the solar wind temperature anisotropy by *Bale et al.* [2009]. The ratio of parallel and perpendicular temperatures is plotted as a function of the parallel proton beta. The lines show theoretical thresholds

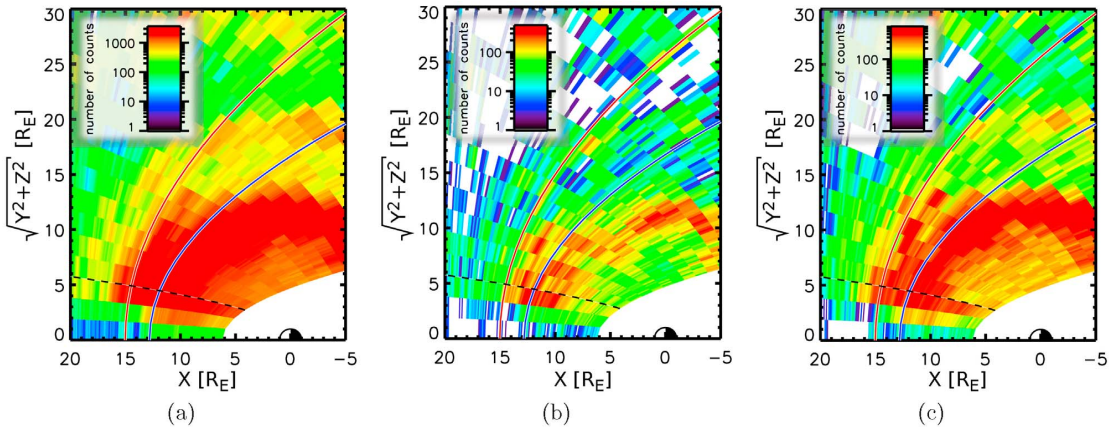

Figure 6. A data coverage of the magnetosheath and adjacent regions. The color scales represent (a) a total number of 1 min observations of the spacecraft in a particular bin; (b) the number of 1 min intervals under a nearly radial IMF (i.e., in a cone of $\pm 15^\circ$ from the Sun-Earth line); and (c) the number of minutes for IMF $B_z \geq 2$ nT.

imposed by an excitation of different wave modes (dotted, mirror instability; full, proton cyclotron waves; dashed, firehose instability). We use the functional forms given in the previous sections but we should note that the expressions from *Hellinger et al.* [2006] lead to a little higher thresholds for the parallel and oblique firehose instabilities and slightly lower thresholds for the mirror and proton cyclotron instabilities. Although it was shown that the firehose threshold limits the proton anisotropy in the solar wind [*Kasper et al.*, 2002], it has not been demonstrated yet in the magnetosheath. All our magnetosheath measurements show the anisotropy near and even above the predicted thresholds. A comparison of Figures 7a and 7b reveals a larger anisotropy for the cases with a large positive B_z ($\geq$2 nT) component (Figure 7a). Moreover, we can see the formation of a magnetic barrier (PDL) in front of the magnetopause for the cases with a large positive B_z that is not present in the cases of a nearly radial IMF. This barrier is a low-β region seen in Figure 7a, whereas the measurements for plasma β lower than unity are absent in Figure 7b.

[50] Enhanced anisotropy for the cases with a large positive B_z is consistent with the pressure distributions along the Sun-Earth line shown in Figure 8. The plots are in a similar format as those in Figure 2. The ratio of the different pressure components is plotted on the vertical axis and the distance on the horizontal axis is in the units of the subsolar magnetosheath thickness. The plots in Figure 2 starts at the magnetopause because it is the boundary of the simulation box, whereas Figure 8 shows the evolution of pressure components down to the magnetosphere. Figure 8a shows the distribution of pressures for the IMF $B_z \geq 2$ nT. Although the pressure was scaled to the propagated ACE pressure, the measured pressure in the solar wind (right edge of the plot) slightly differs from unity. This difference can be caused by intercalibration between of ACE and THEMIS measurements or, more probably, by foreshock effects (the solar wind deceleration [e.g., *Zhang et al.*, 1995; *Cao et al.*, 2009]). When the IMF cone angle is small the whole dayside bow shock is quasiparallel, but the reflected particles quickly escape from the foreshock region, thus their influence on the dynamic pressure can be smaller than in the case of the IMF $B_z \geq 2$ nT. This constraint does not exclude the foreshock in the subsolar region and the accelerated particles spend a longer time in this region. Since subjects of our study are relative changes of the different pressure components within the magnetosheath, the results cannot be influenced by these effects and they will be a subject of a consecutive investigation.

[51] In Figure 8, where the horizontal axis is calibrated in units of the magnetosheath thickness, D_{MSH}, an expected magnetopause is at 0 and bow shock at 1. The mean bow shock location can be easily found as a sharp decrease of the dynamic pressure (blue area) that is partly replaced by the increase of the magnetic pressure (red area) but mainly by the increase of the perpendicular component of the plasma pressure. The gray area shows the parallel pressure component and the full line stands for the total pressure computed in an isotropic approximation. For completeness, the difference between the dotted line and upper edge of the blue area displays the component of the dynamic pressure tangential to the magnetopause that does not influence its location.

[52] One can note that the bow shock is at about 1.1 in units of the horizontal scale (in Figure 8a). The identification of the magnetopause is rather difficult in this case. If we expect that the magnetopause is at the point where the perpendicular component of the dynamic pressure vanishes, it is at about -0.1. Although it is usually expected that the magnetic pressure is dominant inbound the magnetopause, the plot reveals that the plasma pressure prevails on the magnetospheric side of the magnetopause and that a sharp drop of this pressure component occurs at about -0.15. This region is probably the low-latitude boundary layer that can be rather thick for the northward IMF [e.g., *Šafránková et al.*, 2007]. The ratio of the pressures just upstream of the bow shock,

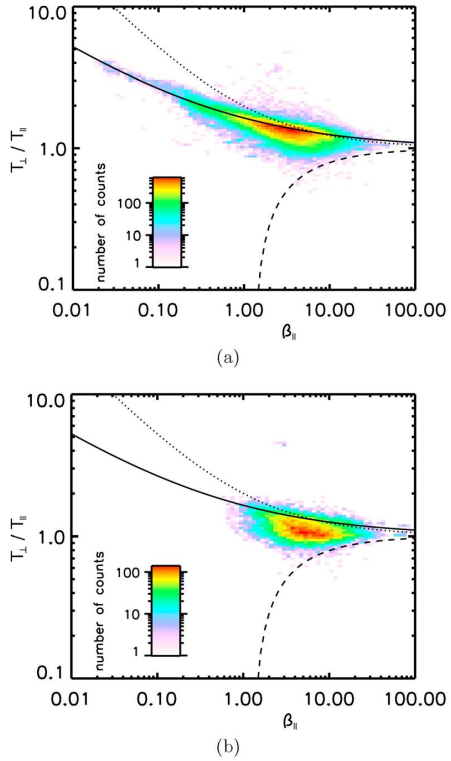

Figure 7. The distributions of proton temperature anisotropy ($T_\perp/T_\parallel$) measurements with respect to the parallel plasma beta $\beta_\parallel$. The lines display thresholds imposed by excitation of different wave modes (dashed line, firehose instability; dotted line, mirror wave; full line, ion cyclotron instability) for (a) the IMF $B_z \geq 2$ nT and (b) an IMF in a cone of $\pm 15°$ from the Sun-Earth line.

$(X - X_{MP})/D_{MSH} = 1.15$ and upstream of the magnetopause, $(X - X_{MP})/D_{MSH} = 0.05$ is 0.95, it means that the pressure exerted onto the magnetopause is about 95% in this case.

[53] Figure 8b presents an analogous plot for a radial IMF. The basic features are very similar but there are several differences that should be stressed out. First, the bow shock is located at approximately 0.9 on the scale of the figure, whereas it was at ~1.1 in Figure 8a. It means that the bow shock is closer to the Earth for the radial IMF than for the large positive IMF B_z. The difference is about 20% of the average magnetosheath thickness. The identification of the magnetopause in the plot is even more confusing than that in the case of the positive IMF B_z. Using the same definition (vanishing of the dynamic pressure) would put the magnetopause to 0.0, whereas the sharp increase of the magnetic pressure occurs at ~−0.1. Since the analysis of *Dušík et al.* [2010] revealed the expanded magnetopause for a radial IMF, we believe that the identification that is based on the dynamic pressure is better. However, it again shows a layer of a dominant plasma pressure inside the magnetopause. In spite of this uncertainty, we can conclude that the pressure exerted on the magnetopause is about 76% of the upstream pressure.

7. Discussion

[54] The present study is motivated by the experimental finding of case studies of *Suvorova et al.* [2010] and *Jelínek et al.* [2010] and a statistical study of *Dušík et al.* [2010] that the magnetopause is expanded from its average position during the intervals of a radial IMF. This expansion is as

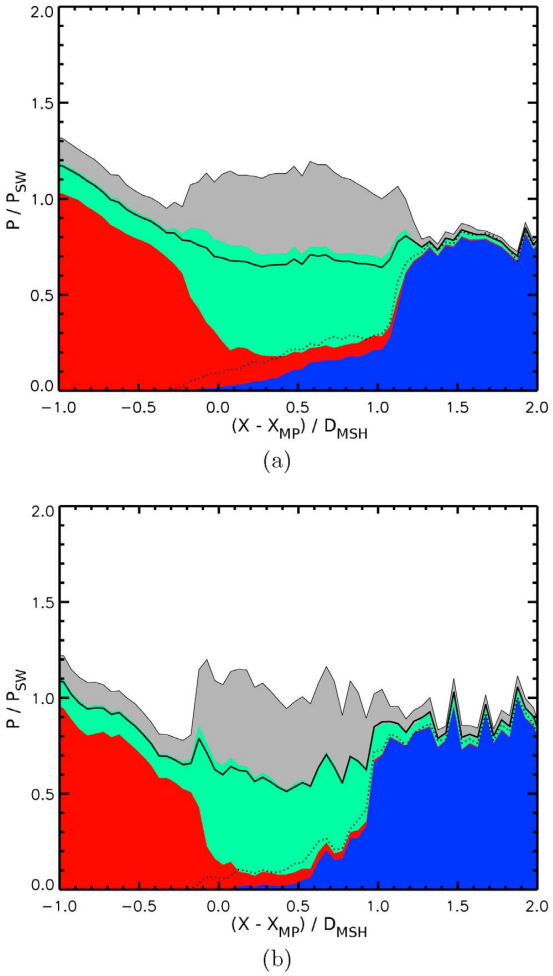

Figure 8. Pressure profiles from the experimental data for two cases: (a) $B_z \geq 2$ nT; and (b) IMF in a cone of $\pm 15°$ from the Sun-Earth line. The colored areas indicate dynamic (blue), magnetic (red), thermal perpendicular (green), and parallel (gray) pressures at the Sun–Earth line. Solid line shows total pressure in the isotropic approximation, and the dotted line shows total dynamic pressure including the velocity component parallel to the magnetopause. The horizontal axes are calibrated in units of the magnetosheath thickness, D_{MSH}, and thus the model magnetopause is at $(X - X_{MP})/D_{MSH} = 0$ and the bow shock lies at 1.

large as 1 R_E for the purely radial IMF. This fact requires a reduction of the pressure exerted on the magnetopause to about 60% in comparison with the case of IMF perpendicular to the Sun–Earth line. The statistical analysis of the data as well as anisotropic MHD calculations performed in this paper provides a little lower reduction, but it should be taken into account that the statistics is based on a broad range of cone angles ($\pm 15°$), and *Dušík et al.* [2010, Figure 4] suggests that the effect is non-linear.

[55] Moreover, both calculations and statistics present the pressure profiles in a stationary state, whereas the crossings of the boundaries are often observed far away from their equilibrium locations. For example, *Jelínek et al.* [2010] reported a magnetopause expansion due to an abrupt IMF rotation toward a radial orientation. This expansion was as large as ≈ 5 R_E but it lasted only ≈ 1 min in spite of the IMF remaining oriented radially. Such events are registered as magnetopause crossings and they enlarge the mean magnetopause displacement. We suggest that this effect is similar to a temporary overcompression of the magnetopause after the abrupt increase of the upstream pressure [see *Samsonov et al.*, 2007, Figure 5].

[56] Another uncertainty of this study is connected with a possible influence of the foreshock that can modify the solar wind pressure even in front of the bow shock. This effect is clearly seen in Figure 8. We can conclude that the modification of the solar wind parameters starts in the foreshock and that these processes are a part of the chain that defines the magnetopause location. However, the main reduction of the total pressure in the radial case in both the statistical analysis and anisotropic MHD simulation occurs at the bow shock crossing (compare Figures 2d and 8b). Note that the general jump conditions for a discontinuity in an anisotropic magnetized plasma [e.g., *Hudson*, 1970] include a term $(P_{\|} - P_{\perp})$ B_n^2/B^2 which is positive on the magnetosheath side in the radial case. It results in a decrease of the total pressure $(\rho V_n^2 + P_{\perp} + B_t^2/8\pi)$ through the bow shock. The total pressure in the outer magnetosheath (downstream of the quasi-parallel bow shock) mostly consists of the dynamic and perpendicular thermal pressures. In both observations and simulations, the total pressure reaches its minimum in the middle of the subsolar magnetosheath and then slightly increases toward the magnetopause because even in the nearly radial IMF cases magnetic field lines drape the magnetopause surface and the $p_{\perp}/p_{\|}$ ratio increases. On the other hand, the perpendicular thermal pressure in the northward case is usually larger than the thermal pressure obtained in the isotropic MHD simulation or in the statistical analysis using the relation $(2p_{\perp} + p_{\|})/3$.

[57] Considering the equation of motion, we find that changes of the total pressure along the Sun–Earth line between the magnetopause and bow shock have two main reasons. The total pressure decreases toward the magnetopause due to a flow diversion along the magnetopause surface, and it increases because of magnetic field draping against the magnetopause. In a purely hydrodynamic solution or in the case of a radial IMF, the total pressure at the subsolar magnetopause is always smaller than that in the upstream solar wind. On the other hand, if the IMF points northward and the magnetic barrier forms near the magnetopause, the total pressure at the subsolar point is only slightly below the solar wind dynamic pressure.

[58] A comparison of isotropic and anisotropic MHD models shows the importance of the temperature anisotropy in the magnetosheath formation. Using the isotropic MHD model, the difference of the subsolar magnetopause pressure in the northward and radial cases is found to be 12% (for the given solar wind conditions). However, the ratio $p_{\perp}/p_{\|}$ differs downstream of the quasi-perpendicular and quasi-parallel bow shocks. Since the magnetopause is supposed to be a tangential discontinuity, the total pressure exerted onto the magnetopause contains only the perpendicular thermal pressure component. For this reason we observe that the difference of the magnetopause pressure in the northward and radial cases increases up to 15–20% in the anisotropic MHD simulation.

[59] The anisotropic MHD equations should include thresholds of the anisotropic instabilities (i.e., mirror, ion cyclotron and firehose). In our previous works, we have added special diffusion terms in the double-adiabatic equations whether with a finite diffusion time [*Samsonov and Pudovkin*, 2000; *Samsonov et al.*, 2001] or with a diffusion time equal to zero [*Samsonov et al.*, 2007]. In the last case, the growth of the temperature anisotropy is strictly limited by a threshold, so it seems to be implicitly assumed that the instability may grow even below this threshold. The last approach is usually applied in data analysis, i.e., there are several empirical thresholds for anisotropic instabilities obtained in the solar wind and magnetosheath. We use the same approach in this work. Furthermore, we make another run for radial IMF in which the ratio $T_{\perp}/T_{\|}$ is unlimited by the firehose threshold and obtain a non-stationary numerical solution with the firehose instability in it. In the runs without the instability threshold (this can correspond to a case when the instability is not saturated), we receive even larger differences between the radial and northward IMF cases.

[60] The analysis of the THEMIS observations confirms the anisotropic MHD simulations. Analyzing results in Figure 8, we obtain that the total pressure on the subsolar magnetopause decreases to 76% and 95% of the solar wind total pressure just upstream of the bow shock in the radial and northward cases, respectively. Thus, the variations of the magnetopause pressure in the statistical results quantitatively agree with the simulations.

[61] However, the upper and lower values of the $p_{\perp}/p_{\|}$ ratio should be limited by the thresholds of anisotropic instabilities. The upper limit is given by a competition between the mirror and ion cyclotron instabilities, while the lower limit is determined by the firehose instability. The extreme values of the $p_{\perp}/p_{\|}$ ratio obtained from the THEMIS observations lies above the firehose threshold and at or in some cases slightly above the ion cyclotron and mirror thresholds determined for stationary conditions. However, the plasma in the subsolar magnetosheath is far away of an equilibrium state due to permanent changes of upstream conditions because conditions for the wave excitation vary with IMF changes. The travel time of the plasma from the bow shock to the subsolar magnetopause (2–3 R_E) is about 1–2 min, i.e., only several periods of low–frequency waves carrying maximum power.

[62] Since the growth of the anisotropic instabilities changes components of the thermal pressure tensor in the magnetosheath, it influences the total magnetopause pressure. For example, if we do not limit the temperature anisotropy by the

firehose threshold in our simulation, the pressure exerting on the magnetopause becomes even weaker.

8. Conclusion

[63] The MHD models as well as the analysis of the THEMIS observations revealed the following:

[64] 1. The total pressure exerted onto the subsolar magnetopause is lower than the upstream dynamic pressure.

[65] 2. The pressure reduction depends on the IMF orientation being ≈5% for a purely northward IMF and ≈24% for the IMF aligned with the solar wind velocity.

[66] 3. The anisotropic MHD model should be employed for a realistic description of the pressure transformation inside the magnetosheath. The isotropic MHD solution underestimates the influence of the IMF orientation on the pressure transformation in the magnetosheath.

[67] 4. The temperature anisotropy in the magnetosheath only slightly exceeds the limits imposed by the plasma instabilities that were estimated in the solar wind.

[68] The obtained values of the pressure reduction in the subsolar region are in a good agreement with the magnetopause expansion reported by *Dušík et al.* [2010].

[69] **Acknowledgments.** The work at Charles University was partly supported by the Czech Grant Agency under contract 205/09/0112 and partly by the Research Plan MSM 0021620860 that is financed by the Ministry of Education of the Czech Republic. A.A.S.'s work was supported by grants of St. Petersburg State University. The authors acknowledge NASA contract NAS5-02099 and V. Angelopoulos for use of data from the THEMIS mission. Specifically, the authors thank C. W. Carlson and J. P. McFadden for use of ESA data and K. H. Glassmeier, U. Auster, and W. Baumjohann for the use of FGM data provided under the lead of the Technical University of Braunschweig and with financial support through the German Ministry for Economy and Technology and the German Center for Aviation and Space (DLR) under contract 50 OC 0302. Global MHD simulation results have been provided by the Community Coordinated Modeling Center at NASA Goddard Space Flight Center through their public Runs on Request system (http://ccmc.gsfc.nasa.gov). The CCMC is a multiagency partnership between NASA, AFMC, AFOSR, AFRL, AFWA, NOAA, NSF, and ONR. The BATS-R-US model was developed by the Computational Magnetohydrodynamics (MHD) Group at the University of Michigan, now the Center for Space Environment Modeling (CSEM).

[70] Masaki Fujimoto thanks the reviewers for their assistance in evaluating this paper.

References

Anderson, B. J., and S. A. Fuselier (1993), Magnetic pulsations from 0.1 to 4.0 Hz and associated plasma properties in the Earth's subsolar magnetosheath and plasma depletion layer, *J. Geophys. Res.*, *98*, 1461–1479, doi:10.1029/92JA02197.

Bale, S. D., J. C. Kasper, G. G. Howes, E. Quataert, C. Salem, and D. Sundkvist (2009), Magnetic fluctuation power near proton temperature anisotropy instability thresholds in the solar wind, *Phys. Rev. Lett.*, *103*, 211101, doi:10.1103/PhysRevLett.103.211101.

Blanco-Cano, X., N. Omidi, and C. T. Russell (2009), Global hybrid simulations: Foreshock waves and cavitons under radial interplanetary magnetic field geometry, *J. Geophys. Res.*, *114*, A01216, doi:10.1029/2008JA013406.

Cable, S., Y. Lin, and J. L. Holloway (2007), Intermediate shocks in three-dimensional magnetohydrodynamic bow-shock flows with multiple interacting shock fronts, *J. Geophys. Res.*, *112*, A09202, doi:10.1029/2007JA012419.

Cairns, I. H., and J. G. Lyon (1995), MHD simulations of Earth's bow shock at low Mach numbers: Standoff distances, *J. Geophys. Res.*, *101*, 17,173–17,180, doi:10.1029/95JA00993.

Cairns, I. H., and J. G. Lyon (1996), Magnetic field orientation effects on the standoff distance of Earth's bow shock, *Geophys. Res. Lett.*, *23*, 2883–2886, doi:10.1029/96GL02755.

Cao, J. B., H. S. Fu, T. L. Zhang, H. Reme, I. Dandouras, and E. Lucek (2009), Direct evidence of solar wind deceleration in the foreshock of the Earth, *J. Geophys. Res.*, *114*, A02207, doi:10.1029/2008JA013524.

Chapman, J. F., I. H. Cairns, J. G. Lyon, and C. R. Boshuizen (2004), MHD simulations of Earth's bow shock: Interplanetary magnetic field orientation effects on shape and position, *J. Geophys. Res.*, *109*, A04215, doi:10.1029/2003JA010235.

Chew, G. F., M. L. Goldberger, and F. E. Low (1956), The Boltzmann equation and the one-fluid hydromagnetic equations in the absence of particle collisions, *Proc. R. Soc. London, Ser. A*, *236*, 112–118, doi:10.1098/rspa.1956.0116.

Crooker, N. U., G. L. Siscoe, and R. B. Geller (1976), Persistent pressure anisotropy in the subsonic magnetosheath region, *Geophys. Res. Lett.*, *3*, 65–68, doi:10.1029/GL003i002p00065.

Denton, R. E., and J. G. Lyon (1996), Density depletion in an anisotropic magnetosheath, *Geophys. Res. Lett.*, *23*, 2891–2894.

De Sterck, H., and S. Poedts (1999), Field-aligned magnetohydrodynamic bow shock flows in the switch-on regime: Parameter study of the flow around a cylinder and results for the axi-symmetrical flow over a sphere, *Astron. Astrophys.*, *343*, 641–649.

De Sterck, H., B. C. Low, and S. Poedts (1998), Complex magnetohydrodynamic bow shock topology in field-aligned low-β flow around a perfectly conducting cylinder, *Phys. Plasmas*, *5*, 4015–4027, doi:10.1063/1.873124.

Dmitriev, A. V., J. K. Chao, and D. J. Wu (2003), Comparative study of bow shock models using Wind and Geotail observations, *J. Geophys. Res.*, *108*(A12), 1464, doi:10.1029/2003JA010027.

Dušík, Š., G. Granko, J. Šafránková, Z. Němeček, and K. Jelínek (2010), IMF cone angle control of the magnetopause location: Statistical study, *Geophys. Res. Lett.*, *37*, L19103, doi:10.1029/2010GL044965.

Engebretson, M. J., N. Lin, W. Baumjohann, H. Luehr, B. J. Anderson, L. J. Zanetti, T. A. Potemra, R. L. McPherron, and M. G. Kivelson (1991), A comparison of ULF fluctuations in the solar wind, magnetosheath, and dayside magnetosphere: 1. Magnetosheath morphology, *J. Geophys. Res.*, *96*, 3441–3454, doi:10.1029/90JA02101.

Erkaev, N. V., C. J. Farrugia, and H. K. Biernat (1999), Three-dimensional, one-fluid, ideal MHD model of magnetosheath flow with anisotropic pressure, *J. Geophys. Res.*, *104*, 6877–6887.

Fairfield, D. H., W. Baumjohann, G. Paschmann, H. Luehr, and D. G. Sibeck (1990), Upstream pressure variations associated with the bow shock and their effects on the magnetosphere, *J. Geophys. Res.*, *95*, 3773–3786, doi:10.1029/JA095iA04p03773.

Farrugia, C. J., N. V. Erkaev, and H. K. Biernat (2000), On the effects of solar wind dynamic pressure on the anisotropic terrestrial magnetosheath, *J. Geophys. Res.*, *105*, 115–128, doi:10.1029/1999JA900350.

Farrugia, C. J., N. V. Erkaev, D. F. Vogl, H. K. Biernat, M. Oieroset, R. P. Lin, and R. P. Lepping (2001), Anisotropic magnetosheath: Comparison of theory with Wind observations near the stagnation streamline, *J. Geophys. Res.*, *106*, 29,373–29,386, doi:10.1029/2001JA000034.

Farrugia, C. J., et al. (2010), Magnetosheath for almost-aligned solar wind magnetic field and flow vectors: Wind observations across the dawnside magnetosheath at X = −12 Re, *J. Geophys. Res.*, *115*, A08227, doi:10.1029/2009JA015128.

Feng, H. Q., C. C. Lin, J. K. Chao, D. J. Wu, L. H. Lyu, and L. C. Lee (2009), Observations of an interplanetary switch-on shock driven by a magnetic cloud, *Geophys. Res. Lett.*, *36*, L07106, doi:10.1029/2009GL037354.

Formisano, V. (1979), Orientation and shape of the Earth's bow shock in three dimensions, *Planet. Space Sci.*, *27*, 1151–1161, doi:10.1016/0032-0633(79)90135-1.

Gary, S. P., S. A. Fuselier, and B. J. Anderson (1993), Ion anisotropy instabilities in the magnetosheath, *J. Geophys. Res.*, *98*, 1481–1488, doi:10.1029/92JA01844.

Gary, S. P., H. Li, S. O'Rourke, and D. Winske (1998), Proton resonant firehose instability: Temperature anisotropy and fluctuating field constraints, *J. Geophys. Res.*, *103*, 14,567–14,574, doi:10.1029/98JA01174.

Hellinger, P., P. Travnicek, J. C. Kasper, and A. J. Lazarus (2006), Solar wind proton temperature anisotropy: Linear theory and WIND/SWE observations, *Geophys. Res. Lett.*, *33*, L09101, doi:10.1029/2006GL025925.

Hudson, P. D. (1970), Discontinuities in an anisotropic plasma and their identification in solar wind, *Planet. Space Sci.*, *18*(11), 1611–1622, doi:10.1016/0032-0633(70)90036-X.

Jelínek, K., Z. Němeček, J. Šafránková, J.-H. Shue, A. V. Suvorova, and D. G. Sibeck (2010), Thin magnetosheath as a consequence of the magnetopause deformation: THEMIS observations, *J. Geophys. Res.*, *115*, A10203, doi:10.1029/2010JA015345.

Jelínek, K., Z. Němeček, and J. Šafránková (2012), A new approach to magnetopause and bow shock modeling based on automated region identification, *J. Geophys. Res.*, doi:10.1029/2011JA017252, in press.

Kasper, J. C., A. J. Lazarus, and S. P. Gary (2002), Wind/SWE observations of firehose constraint on solar wind proton temperature anisotropy, *Geophys. Res. Lett.*, *29*(17), 1839, doi:10.1029/2002GL015128.

Kowal, G., D. A. Falceta-Gonçalves, and A. Lazarian (2011), Turbulence in collisionless plasmas: Statistical analysis from numerical simulations with pressure anisotropy, *New J. Phys.*, *13*(5), 053001, doi:10.1088/1367-2630/13/5/053001.

Lin, N., M. J. Engebretson, R. L. McPherron, M. G. Kivelson, W. Baumjohann, H. Luehr, T. A. Potemra, B. J. Anderson, and L. J. Zanetti (1991), A comparison of ULF fluctuations in the solar wind, magnetosheath, and dayside magnetosphere: 2. Field and plasma conditions in the magnetosheath, *J. Geophys. Res.*, *96*, 3455–3464, doi:10.1029/90JA02098.

Lin, Y., and X. Y. Wang (2005), Three-dimensional global hybrid simulation of dayside dynamics associated with the quasi-parallel bow shock, *J. Geophys. Res.*, *110*, A12216, doi:10.1029/2005JA011243.

Merka, J., A. Szabo, J. Šafránková, and Z. Němeček (2003), Earth's bow shock and magnetopause in the case of a field-aligned upstream flow: Observation and model comparison, *J. Geophys. Res.*, *108*(A7), 1269, doi:10.1029/2002JA009697.

Phan, T.-D., G. Paschmann, W. Baumjohann, N. Sckopke, and H. Lühr (1994), The magnetosheath region adjacent to the dayside magnetopause: AMPTE/IRM observations, *J. Geophys. Res.*, *99*(A1), 121–141, doi:10.1029/93JA02444.

Russell, C. T., J. G. Luhmann, T. J. Odera, and W. F. Stuart (1983), The rate of occurrence of dayside Pc 3,4 pulsations: The L-value dependence of the IMF cone angle effect, *Geophys. Res. Lett.*, *10*, 663–666, doi:10.1029/GL010i008p00663.

Šafránková, J., Z. Němeček, Š. Dušík, L. Přech, D. G. Sibeck, and N. N. Borodkova (2002), The magnetopause shape and location: A comparison of the Interball and Geotail observations with models, *Ann. Geophys.*, *20*, 301–309.

Šafránková, J., Z. Němeček, L. Přech, J. Šimůnek, D. G. Sibeck, and J.-A. Sauvaud (2007), Variations of the flank LLBL thickness as response to the solar wind dynamic pressure and IMF orientation, *J. Geophys. Res.*, *112*, A07201, doi:10.1029/2006JA011889.

Samsonov, A. A. (2006), Numerical modelling of the Earth's magnetosheath for different IMF orientations, *Adv. Space Res.*, *38*(8), 1652–1656, doi:10.1016/j.asr.2005.06.009.

Samsonov, A. A., and M. I. Pudovkin (1998), Ideal anisotropic plasma flow around a sphere in the CGL approach (in Russian), *Geomagn. Aeron.*, *38*, 50–57.

Samsonov, A. A., and M. I. Pudovkin (2000), Application of the bounded anisotropy model for the dayside magnetosheath, *J. Geophys. Res.*, *105*, 12,859–12,868, doi:10.1029/2000JA900009.

Samsonov, A. A., M. I. Pudovkin, S. P. Gary, and D. Hubert (2001), Anisotropic MHD model of the dayside magnetosheath downstream of the oblique bow shock, *J. Geophys. Res.*, *106*, 21,689–21,700, doi:10.1029/2000JA900150.

Samsonov, A. A., O. Alexandrova, C. Lacombe, M. Maksimovic, and S. P. Gary (2007), Proton temperature anisotropy in the magnetosheath: Comparison of 3-D MHD modelling with Cluster data, *Ann. Geophys.*, *25*, 1157–1173, doi:10.5194/angeo-25-1157-2007.

Shevyrev, N. N., G. N. Zastenker, and J. Du (2007), Statistics of low-frequency variations in solar wind, foreshock and magnetosheath: INTERBALL-1 and CLUSTER data, *Planet. Space Sci.*, *55*, 2330–2335, doi:10.1016/j.pss.2007.05.014.

Shue, J.-H., et al. (1998), Magnetopause location under extreme solar wind conditions, *J. Geophys. Res.*, *103*, 17,691–17,700, doi:10.1029/98JA01103.

Shue, J.-H., J.-K. Chao, P. Song, J. P. McFadden, A. Suvorova, V. Angelopoulos, K. H. Glassmeier, and F. Plaschke (2009), Anomalous magnetosheath flows and distorted subsolar magnetopause for radial interplanetary magnetic fields, *Geophys. Res. Lett.*, *36*, L18112, doi:10.1029/2009GL039842.

Sibeck, D. G. (1995), The magnetospheric response to foreshock pressure pulses, in *Physics of the Magnetopause*, *Geophys. Monogr. Ser.*, vol. 90, edited by P. Song, B. U. Ö. Sonnerup, and M. F. Thomsen, pp. 293–302, AGU, Washington, D. C.

Sibeck, D. G., N. B. Trivedi, E. Zesta, R. B. Decker, H. J. Singer, A. Szabo, H. Tachihara, and J. Watermann (2003), Pressure-pulse interaction with the magnetosphere and ionosphere, *J. Geophys. Res.*, *108*(A2), 1095, doi:10.1029/2002JA009675.

Slavin, J. A., A. Szabo, M. Peredo, R. P. Lepping, R. J. Fitzenreiter, K. W. Ogilvie, C. J. Owen, and J. T. Steinberg (1996), Near-simultaneous bow shock crossings by WIND and IMP 8 on December 1, 1994, *Geophys. Res. Lett.*, *23*, 1207–1210, doi:10.1029/96GL01351.

Spreiter, J. R., and A. W. Rizzi (1974), Aligned magnetohydrodynamic solution for solar wind flow past the Earth's magnetosphere, *Acta Astronaut.*, *1*, 15–35.

Spreiter, J. R., A. L. Summers, and A. Y. Alksne (1966), Hydromagnetic flow around the magnetosphere, *Planet. Space Sci.*, *14*, 223–250, doi:10.1016/0032-0633(66)90124-3.

Suvorova, A. V., et al. (2010), Magnetopause expansions for quasi-radial interplanetary magnetic field: THEMIS and Geotail observations, *J. Geophys. Res.*, *115*, A10216, doi:10.1029/2010JA015404.

Toth, G., and D. Odstrčil (1996), Comparison of some flux corrected transport and total variation diminishing numerical schemes for hydrodynamic and magnetohydrodynamic problems, *J. Comput. Phys.*, *128*(1), 82–100.

Verigin, M., G. Kotova, A. Szabo, J. Slavin, T. Gombosi, K. Kabin, F. Shugaev, and A. Kalinchenko (2001), Wind observations of the terrestrial bow shock: 3-D shape and motion, *Earth Planets Space*, *53*, 1001–1009.

Wu, C. C. (1992), MHD flow past an obstacle: Large-scale flow in the magnetosheath, *Geophys. Res. Lett.*, *19*, 87–90, doi:10.1029/91GL03007.

Zhang, T. L., K. Schwingenschuh, and C. T. Russell (1995), A study of the solar wind deceleration in the Earth's foreshock region, *Adv. Space Res.*, *15*(8/9), 137–140.

C.7 Improved bow shock model with dependence on the IMF strength

Available online at www.sciencedirect.com
SCIENCE DIRECT®
Planetary and Space Science 53 (2005) 85–93
Planetary and Space Science
www.elsevier.com/locate/pss

Improved bow shock model with dependence on the IMF strength

M. Jeřáb[a], Z. Němeček[a,*], J. Šafránková[a], K. Jelínek[a], J. Měrka[b]

[a]Charles University, Faculty of Mathematics and Physics, V Holesovickach 2, 180 00 Praha 8, Czech Republic
[b]NASA Goddard Space Flight Center, Greenbelt, Maryland, USA

Accepted 12 September 2004

Abstract

The presence of the bow shock in front of an obstacle immersed into a supersonic flow of collisionless plasma has been theoretically predicted and experimentally confirmed more than 40 years ago. However, in spite of a great effort of theoreticians and experimenters, we are still not able to predict the bow shock location under varying upstream conditions with a sufficient accuracy. Gasdynamic and MHD models cannot account for kinetics effects, whereas the kinetic models can be used only to study particular phenomena due to limited computer capacity. Models based on fits of experimental data usually expect that the bow shock location is a simple function of several upstream parameters as the solar wind dynamic pressure, upstream Mach number, and direction or magnitude of the interplanetary magnetic field. Since the bow shock location would be determined by the downstream parameters, these models implicitly assume that these parameters are unambiguously determined by the upstream conditions. The uncertainty of the bow shock prediction is usually attributed to the uncertainty in determination of the upstream state or to an irregular bow shock motion.

We have accumulated a large set of bow shock crossings observed by INTERBALL-1, MAGION-4, GEOTAIL, IMP 8, and CLUSTER-2 spacecraft and complemented this set with upstream measurements of WIND with motivation to improve the accuracy of a prediction of the bow shock location provided by the Němeček and Šafránková (J. Atmos. Terr. Phys. 53 (1991) 1049) model. Although proposed corrections conserve a simplicity of the original model, they decrease significantly the most probable error of the prediction.

PACS: 94.30 Va; 94.30 Oi

Keywords: Solar wind interaction; Upstream conditions; Magnetopause; Bow shock; Bow shock models

1. Introduction

The determination of the actual magnetopause and bow shock positions tests our knowledge about the interaction between the solar wind and Earth's magnetic field. The shape, position, and motion of the Earth's bow shock (BS) have been a subject of experimental and theoretical research for the last four decades. In course of these years, many BS models (predominantly empirical) have been developed (e.g., Měrka et al. (2003) for survey). In these models, BS has been approximated using ellipsoidal, paraboloidal or hyperboloidal surfaces with varying standoff distances under assumption that both position and shape can be expressed as a function of upstream plasma parameters (usually by the dynamic pressure of the incoming solar wind and by upstream Mach numbers).

The most known model of the BS was published by Fairfield (1971). This model is based only on observations made near the ecliptic plane and thus the model is two-dimensional second-order fit to BS positions. It assumes axial symmetry along the solar wind flow direction and does not include any corrections to

*Corresponding author.
E-mail address: zdenek.nemecek@mff.cuni.cz (Z. Němeček).

0032-0633/$ - see front matter © 2004 Elsevier Ltd. All rights reserved.
doi:10.1016/j.pss.2004.09.032

compensate effects of the solar wind dynamic pressure except an aberration due to the orbital motion of Earth.

Formisano et al. (1971) found that the BS location can be predicted with a higher accuracy when the upstream magnetosonic Mach number is taken into account. Slavin and Holzer (1981) examined Mach number effects on the shock position and compared results with the gasdynamic theory. This topic was treated by many authors in the past, especially in connection with studies focused on unusual positions of the BS crossings (e.g., Fairfield and Feldman, 1975; Farris et al., 1991; Cairns et al., 1995). Formisano (1979) developed a BS model parametrized by both upstream dynamic pressure and magnetosonic Mach number. Further, Němeček and Šafránková (1991) used the Formisano approach and suggested a new model including explicitly the solar wind dynamic pressure, magnetosonic Mach number and interplanetary magnetic field strength.

Peredo et al. (1995) developed a three-dimensional empirical model predicting the statistical BS position and shape for arbitrary values of the solar wind pressure, IMF, and Alfvén Mach number. They investigated the influence of variations in the sonic (M_S), Alfvénic (M_A), and magnetosonic (M_{MS}) Mach numbers as well as the orientation of IMF. The authors removed the effects associated with Earth's orbital motion by rotating the crossings into aberrated GSE coordinates. Changes due to solar wind dynamic pressure variations have been taken into consideration by normalizing the observed crossings to the average value of 3.1 nPa and variations due to different IMF orientations were taken into account by rotating all crossings into geocentric interplanetary medium coordinates (Bieber and Stone, 1979), where the B_Z component of the IMF vanishes.

Other point of view was presented in the paper of Farris and Russell (1994) where the authors investigated analytical hydrodynamic and MHD formulas across the BS and along the boundary of an obstacle to the solar wind flow. They found that the BS position can be better described by downstream Mach number and upstream plasma parameters. The main difference of this approach from those used in previous estimations is that the BS moves toward infinity for very low upstream Mach numbers, which is what the authors expected physically (e.g., Russell and Zhang, 1992). On the other hand, the suggested correction of the BS position is negligible for the Mach numbers which are frequently observed ($M>4$). Moreover, the authors suggest to use the radius of curvature of the magnetopause for the determination of the magnetosheath thickness rather than a distance of the subsolar point from the Earth center. We would like to note that the application of this suggestion would lead to a more stable BS position because the distance of the subsolar magnetopause from the Earth decreases, whereas the radius of curvature and, consequently, the magnetosheath thickness increases when IMF B_Z becomes more negative. A similar approach to the prediction of the BS location was used by many other authors (e.g., Russell and Zhang, 1992; Grabbe, 1997).

Cairns and Grabbe (1994) developed an MHD theory for the BS standoff distance and the thickness of the magnetosheath. The global three-dimensional MHD simulations of Cairns and Lyon (1995) further improved the theory and obtained the expression for both parameters. The magnetosheath thickness strongly depended on the Alfvénic and sonic Mach numbers and on the angle between the solar wind velocity and direction of IMF. Their BS predictions agreed with gasdynamic predictions in the high M_A limit (Spreiter et al., 1966).

Měrka et al. (2003) compared model predictions with a large collection of individual BS crossings observed by the IMP 8 spacecraft over 12 years. They obtained 2293 normalized unambiguous crossings for which they found IMP 8 upstream IMF and solar wind parameters. In this study, they chosen the Formisano (F79), Němeček and Šafránková (NS91) models, two Farris and Russell models (with sonic and magnetosonic Mach numbers) (FR94, FR94c), Cairns and Lyon (CL95), and Peredo (P95) models (Formisano et al., 1973; Němeček and Šafránková, 1991; Farris and Russell, 1994; Cairns and Lyon, 1995; Peredo et al., 1995). To test the FR94, FR94c, and CL95 models, a paraboloid was used for the BS shape. The accuracy of models was estimated based on the radii of predicted-to-observed radial distances R_{mod}/R_{obs} to the actual BS. From comparison, the authors concluded that the predictions of F79, FR94, FR94c, CL95 are the most accurate with F79 giving a slightly better result. The widely used P95 model seems to be biased by $\sim 20\%$, consistently with note in Šafránková et al. (1999a,b) and the original paper by Peredo et al. (1995). For large values of the IMF and its components and for the low upstream Mach numbers, all models except NS91 underestimate the BS distance. The same effect was found for changes in the relative orientation of the IMF and solar wind velocity vector (see Figs. 4–6 in Měrka et al. (2003)). According to a discussion to these figures, a simple dependence on the IMF magnitude in NS91 is sufficient to explain the shifts for B_Y and B_Z.

The short survey of previous results shows that a further study is desirable because discrepancies between model predictions and observations are still rather large. From Figs. 4–6 in Měrka et al. (2003), it follows that the NS91 model is nearly independent on the variations of IMF and its components as well as on extreme values of solar wind parameters. We think that this fact is very important and opens a space for further development of BS models. We collected a new set of BS crossings from

many spacecraft with motivation to find major sources of model uncertainties and to find a way to their correction.

2. Data set

We accumulated BS crossings from many ISTP and other spacecraft. We used the BS database of IMP 8 crossings which is available at http://nssdc.gsfc.nasa.gov/ftphelper/bowshock1.html and the similar database of BS crossings of GEOTAIL and CLUSTER available on the same NASA server. We have completed this set with INTERBALL-1 and MAGION-4 crossings which have been collected by the authors. Together, we identified ~ 5400 unambiguous BS crossings for which we have WIND upstream solar wind parameters (1017 BS crossings from INTERBALL-1; 1007 from MAGION-4, 2193 from IMP 8, 812 from GEOTAIL, and 326 from CLUSTER II). The set includes both outbound and inbound crossings, many of them being multiple. The effect of multiple crossings is most pronounced on the flanks. The distribution of investigated BS crossings is illustrated in Fig. 1. The distances from the X_{GSE} axis given on the vertical axis are plotted as positive or negative values for the dawn and dusk flanks, respectively. This arrangement allows us to see the influence of the solar wind aberration on observed positions of crossings.

The observed crossings are located from $X_{GSE} \sim 15R_E$ to $X_{GSE} \sim -22R_E$ and within $\pm 25R_E$ in Z. The crossings occurred under various upstream conditions: the solar wind velocity varied from 270 to 770 km/s, density from ~ 1 to 35 cm^{-3}, and computed Alfvénic Mach number from ~ 2 to 60.

The solar wind and IMF data were taken from the WIND observations (Ogilvie et al., 1995; Lepping et al., 1995). The time of propagation of solar wind features from the WIND position to the BS registered on a particular spacecraft was computed as a two-step

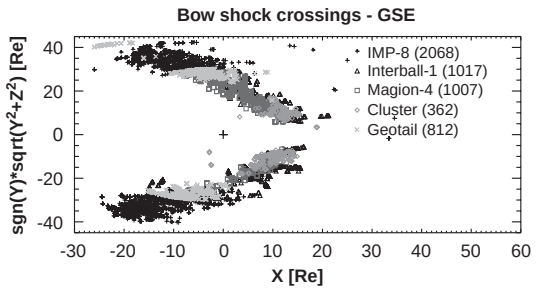

Fig. 1. Cylindrical projection of all studied BS crossings (in the GSE coordinate system) non-normalized to standard solar wind parameters. Observations of BS crossings of the different spacecraft are denoted by various steps of the gray scale.

approximation from WIND solar wind velocity measurements. The values of the solar wind dynamic pressure and IMF used for the study were computed as 5-min averages centered around the time determined as given above.

We have decided to use the data from one solar wind monitor because the data of different spacecraft are often hardly comparable. The problem of timing connected with a large distance of WIND from the Earth is compensated by the fact that such monitor is always in the undisturbed solar wind, whereas the satellite in the BS vicinity appears frequently in the foreshock.

3. Method of the analysis

Since Měrka et al. (2003) have shown that the Němeček and Šafránková (1991) model provides the best results in a broad range of upstream parameters, our analysis will be based on this model. However, the NS91 model is closely connected with the Formisano (1979) model and thus we start with a short description of these models.

Formisano (1979) derived a set of fully three-dimensional BS models because their data set included a large number of crossings from the high-latitude region. These authors normalized the observed shock radial distance, $R(\theta)$, to an average upstream solar wind dynamic pressure according to the following equation:

$$R(\theta) = \frac{R_{av}(\theta)}{R_0} \cdot \frac{C}{(NV^2)^{1/6}} \cdot \left(1 + 1.1\frac{(\gamma-1)M^2+2}{(\gamma+1)M^2}\right), \quad (1)$$

where $R(\theta)$ is the geocentric distance of the BS at the Sun–Earth–satellite angle, θ (this angle stands for both angular coordinates because the model is three-dimensional); $R_{av}(\theta)$ is the geocentric distance (in the θ direction) of a surface taken as a reference giving the shape of the shock surface (Binsack and Vasyliunas, 1968); R_0 is the geocentric distance of the subsolar point of the reference surface; C is a constant related to the equatorial magnetic field at ground level; N, V are the proton number density and bulk velocity in the solar wind, respectively; and M is the upstream magnetosonic Mach number. γ is the effective ratio of specific heats in the solar wind usually taken as 5/3 but note that Zhuang and Russell (1981) suggested a value of 2.15 instead of 5/3 in order to find a better description of the BS position. The numerical value of C depends on the units; for the most frequently used units ($R(\theta)$ in Earth radii (R_E), N in cm^{-3}, and V in km^{-1}), a value of $C \approx 95$ was found in Formisano et al. (1973). In their model, the second-order three-dimensional surface derived from the data normalized to the average solar wind

conditions ($N = 9.4\,\mathrm{cm}^{-3}$, $V = 450\,\mathrm{km}^{-1}$) had the form

$$a_{11}X^2 + a_{22}Y^2 + a_{33}Z^2 + a_{12}XY + a_{14}X + a_{24}Y + a_{44} = 0, \quad (2)$$

where X, Y and Z are GSE coordinates (in R_E) of the surface and the coefficients of the best single-surface fit were

$$a_{11} = 0.45;\ a_{22} = 1;\ a_{33} = 1.11;$$
$$a_{12} = 0.18;\ a_{14} = 46.6;\ a_{24} = -4.16;\ a_{44} = -618. \quad (3)$$

The model fit describes the observations rather well but the uncertainty of the order of $\sim 20\%$ remains.

Němeček and Šafránková (1991) analyzed a different set of BS crossings and found that as the strength of IMF increased, the BS location tended to move further away from the Earth than it follows from the Mach number relationship used in Formisano (1979). The authors used the Formisano approach and developed the equation

$$R(\theta,\phi) = \frac{R_{\mathrm{av}}(\theta,\phi)}{R_0}\cdot\frac{C}{(NV^2)^{1/6}} \times \left(1 + D\frac{(\gamma-1)M_{\mathrm{MS}}^2 + 2}{(\gamma+1)M_{\mathrm{MS}}^2}\right), \quad (4)$$

where $R(\theta,\phi)$ is the geocentric BS distance in a direction described by θ and ϕ angles; $R_{\mathrm{av}}(\theta,\phi)$ is the distance of the normalized Formisano surface given by Eq. (2); M_{MS} is the solar wind magnetosonic Mach number, and $C = 100$ is a constant (this constant is such that the term $C/(NV^2)^{1/6}$ gives the magnetopause standoff distance in R_E). The dependence of D on the interplanetary magnetic field was approximated by a linear function and the best fit was

$$D = 1 + 0.5\frac{B}{B_0}, \quad (5)$$

where B is the upstream magnetic field strength and $B_0 = 5.5\,\mathrm{nT}$ is the mean IMF strength.

However, as Měrka et al. (2003) commented, this result should not be interpreted as showing a dependence of standoff distance on magnetic field strength itself. The higher values of the magnetic field increase the Alfvén and magnetosonic speeds. The empirical parameter D in NS91, defined by (5), can be restated as

$$D = 1 + \frac{1}{2}\cdot\frac{M_0}{\sqrt{P_0}}\cdot\frac{\sqrt{P_{\mathrm{SW}}}}{M_{\mathrm{A}}}, \quad (6)$$

where the index 0 denotes average values of the ram pressure and Alfvén Mach number. Using average values $N = 9.4\,\mathrm{cm}^{-3}$, $V = 450\,\mathrm{km}^{-1}$ and $B_0 = 5.5\,\mathrm{nT}$, we obtain

$$D = 1 + 3.2\frac{\sqrt{P_{\mathrm{SW}}}}{M_{\mathrm{A}}}, \quad (7)$$

where P_{SW} is measured in nP.

These equations could be interpreted as showing an increase of the magnetosheath thickness either for greater values of solar wind dynamic pressure, P_{SW}, or for smaller values of the upstream Alfvén Mach number, M_{A}. However, the empirical parameter D should rather be viewed as a correction to both magnetopause and BS positions and/or shapes. Měrka et al. (2003) concluded that the parameter D is necessary since the magnetopause subsolar distance determined by the first term of Eq. (2) does not account for the dependence of the magnetopause position on IMF B_Z (e.g., Petrinec et al., 1991; Sibeck et al., 1991; Shue et al., 1997).

Our analysis of sources of prediction uncertainties is based on Eq. (4) for the BS location. This equation uses the magnetosonic Mach number but we decided, in accord with the discussion in Peredo et al. (1995), the replace the magnetosonic Mach number, M_{MS} with Alfvénic Mach number, M_{A}. Then we adjusted the parameter D for each crossing to achieve a matching of observed and predicted BS locations. The plots of D as a function of coordinates, upstream parameters, etc. allow us to estimate an influence of the particular parameter on the BS location and to find a way for its correction.

4. Corrections to the NS91 model

In order to establish an initial state, we present results of the NS91 model in Fig. 2. The histogram shows the distribution of relative errors expressed as a ratio of predicted (R_{model}) to observed (R_{observed}) radial distances of BS from the Earth center. In order to quantify the accuracy of prediction, we have fitted the histogram with a Gaussian function. The fit shown as a heavy line is centered around 1.15 and its half-width is 0.108. It means that in average the NS91 model predicts the BS on about 15% farther from the Earth than observed.

A fact that the distribution perfectly fits the Gaussian function suggests that the underlying processes responsible for this spread are random. Of course, it does not mean that the model cannot be improved because the

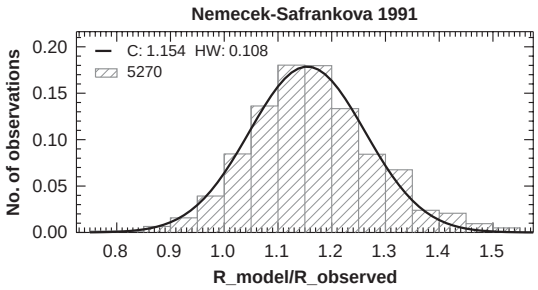

Fig. 2. Histogram of relative deviations of observed BS positions from predictions of the NS91 model. The full line illustrates a Gaussian fit and its center and half-width was used to judge model validity.

principal random input is represented by the solar wind itself.

The development of the NS91 model was based on a relatively small number of BS crossings observed by Prognoz 10 in the subsolar region; on the other hand, the complex analysis of Měrka et al. (2003) was based on IMP 8 observations covering predominantly the night part of bow shocks. However, the presented set of BS crossings covers a broad range of the X coordinate. Fig. 3 shows the D parameter as a function of the X coordinate computed for all crossings from Fig. 1. The figure displays all values of D as dots. The median values of D, in 2.5 R_E bins, are represented by thick broken lines and the most probable errors of D are displayed by thinner lines. One can note that medians of D fluctuate around a mean value of 1.1 originally suggested by Formisano et al. (1973) for $X<8\,R_E$, whereas they rise to the value of ~ 2 for larger X. This rise cannot be interpreted in terms of the increasing magnetosheath thickness. We suppose that it is probably connected with the fact that the model surface given by Eq. (2) does not describe the shape of a subsolar BS with sufficient accuracy. Since the number of crossings in this region is rather small in our data set, we will limit a further investigation to the region $X<8R_E$.

Fig. 4 shows the D parameter as a function of the GSE latitude. We have used only the crossings with $X<8\,R_E$ and the figure reveals that, in spite of using the high-latitude spacecraft as INTERBALL or CLUSTER, all crossings are located in low and middle latitudes and a number of crossings out of the $\pm 45^\circ$ range is negligible. On the other hand, the D parameter seems to rise with the latitude within this range. This dependence can be corrected by a change of a_{33} coefficient in formula (3). Crossings outside of $\pm 45^\circ$ of latitude seem to exhibit an opposite trend but their number is too small to make a reliable conclusion.

The NS91 model does not include explicitly an effect of the Earth's orbital motion. This influence (or its average result) is implicitly involved in formula (2) for the reference surface (terms a_{12} and a_{24}). However, the solar wind velocity is changing and the Earth velocity is constant and thus one can expect a dawn–dusk

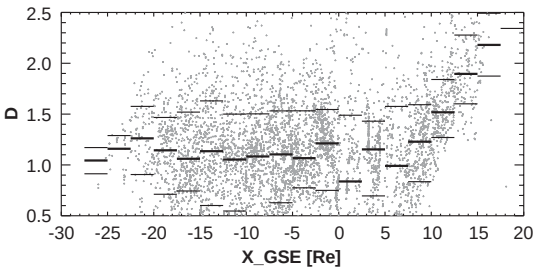

Fig. 3. The distribution of the D parameter along the X_{GSE} axis.

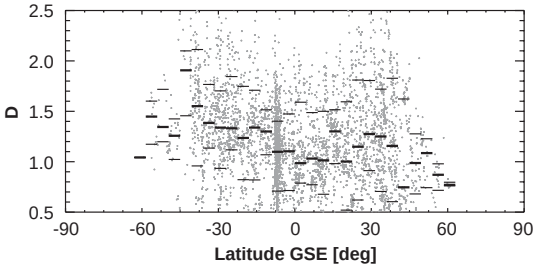

Fig. 4. The dependence of the D parameter on the geographic latitude.

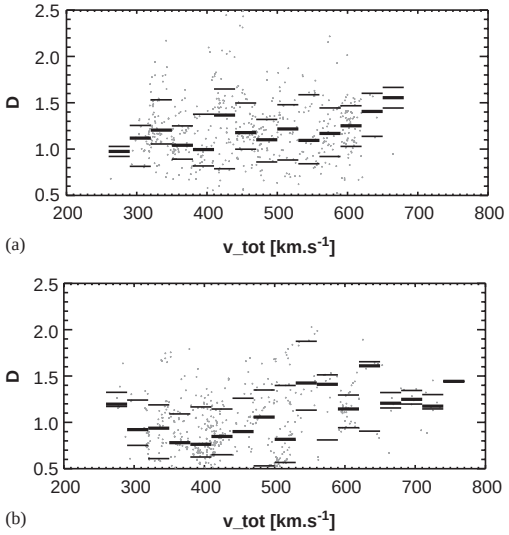

Fig. 5. The dependence of D as a function of the solar wind velocity for dawn (a) and dusk (b) sides.

asymmetry in prediction accuracy changing with the solar wind velocity. Since the aberration effect would act on dayside and nightside (dawn and dusk) in opposite directions, we have plotted the parameter D as a function of the solar wind velocity, V_{tot}, for dawn and dusk sides of the night part separately in Fig. 5. We have expected to receive complementary functions but, as a comparison of left and right parts of the figure shows, the D parameter slightly rises with the solar wind velocity on both flanks. It means that the aberration is a minor cause of prediction uncertainties and its description in formula (2) is sufficient.

The plot of the D parameter as a function of the Alfvénic Mach number, M_A, is shown in Fig. 6. This plot reveals a systematic decrease of D with M_A in a range $3<M_A<8$. The number of crossings in this range of M_A is very large and thus this dependence is probably real, whereas the decrease of D for crossings with

$M_A < 3$ is probably connected with a small number of crossings observed under such unusual conditions.

An important feature distinguishing the NS91 model is explicitly expressed dependence of the BS location on the IMF strength, whereas other authors suggested that the BS shape and locations would be rather controlled by the IMF direction. To check these ideas, we have used several different ways of analysis but we cannot confirm any clear influence of IMF directions on the BS shape or locations. On the other hand, the magnitude of IMF (or a particular component) can play a very important role, as we see from the following figures. A less important component in this respect is B_X as can be seen from Fig. 7a. The averaged D does not depend on the B_X value and fluctuates around 1.1. This is rather surprising because Cairns and Lyon (1996) predicted a significant BS shift during intervals of a radial IMF. However, the set of crossings used in Fig. 7a was limited to $X < 8$ and thus it cannot reflect the subsolar region where Cairns and Lyon (1996) predict the largest BS displacement. On the other hand, Fig. 7b shows a clear increase of D with the magnitude of the IMF B_Y component. D has a clear minimum around $B_Y \sim 0$. The increase seems to break at $\sim | B_Y | > 15$ but such magnetic fields are often connected with very unusual events like magnetic clouds or CMEs and thus the BS behavior can be connected with other phenomena.

The plot of D versus IMF B_Z in Fig. 7c exhibits a very similar trend because D rises with $| B_Z |$ in a "normal" range of values and falls down for extreme positive or negative values of this component. This trend is interesting because the magnetopause changes its shape with the sign of IMF B_Z but such trend is not observed for BS. We think that the result in Fig. 7c has a deeper physical meaning and we will discuss it later.

Since the NS91 model corrects the BS location using the IMF magnitude, we have plotted D as a function of this magnitude in Fig. 7d. One can see that this plot exhibits a better ordering of crossings than any of previous plots. It means that the original idea of the NS91 model is confirmed, whatever is its physical meaning. The dotted line shows a linear function that will be later used in our modification of the NS91 model.

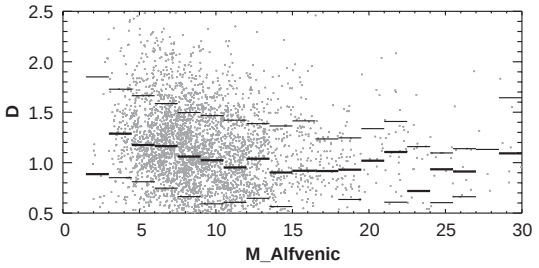

Fig. 6. The dependence of the D parameter on the Alfvénic Mach number.

5. Discussion

An important point of a statistical analysis is to exclude possible biases in the original data set. Such bias is often connected with orbital limitations of the particular spacecraft. For example, INTERBALL-1 can observe the nightside BS only if it is compressed, whereas IMP 8 crosses the dayside BS during intervals of extremely low solar wind dynamic pressure. Nevertheless, we are using data from four spacecraft with very different orbits (MAGION-4 and INTERBALL-1 can

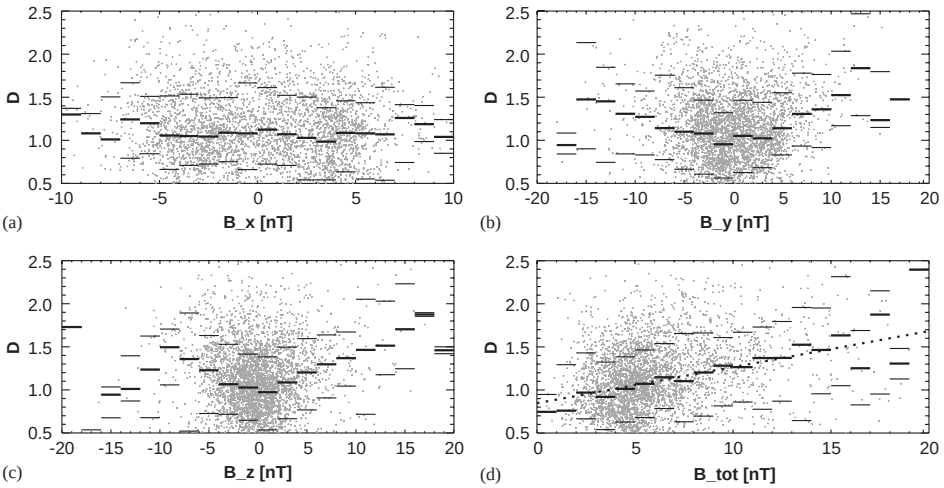

Fig. 7. The dependence of D on IMF components and magnitude ((a) B_X component, (b) B_Y, (c) B_Z, (d) IMF magnitude).

be considered as one spacecraft for this purpose) and thus we can believe that these biases compensate each other. Another source of bias in the data can be a distribution of upstream parameters because the solar wind is not stationary on short time scales. Our set includes all crossings observed by the mentioned spacecraft in course of 1995–2002 years when the data from the WIND were available. This period starts at a solar minimum and ends at a solar maximum and thus it covers both important intervals. However, a majority of dayside crossings were registered by CLUSTER-2 (see Fig. 1) during the solar maximum. We cannot exclude that the rise of the D parameter in Fig. 3 in a subsolar region is connected with this bias and thus we excluded the crossings with $X > 8\,R_E$ from our analysis.

An analysis of Měrka et al. (2003) and Šafránková et al. (1999a,b) have shown that NS91 is most successful in prediction of the BS location in a wide range of upstream parameters. The only problem of the original model is that the model predicts the BS on 15% farther from the Earth than observed (Fig. 2). However, Eq. (4) describing the BS location can be simply re-normalized changing the value of the empirical constant, C. Fig. 3 suggests that a shape of the BS is well described by Eq. (2) with coefficients according to (3). However, as Fig. 4 shows, the BS cross-section seems to be elongated in the vertical (Z) direction. This can be simply reflected by an appropriate change of the coefficient a_{33} in Eq. (3). We will do it but our crossings are distributed predominantly in low latitudes and thus this correction can be used only for latitudes lower than 45°.

Eq. (4) consists of two terms. These terms are often interpreted as a location of the magnetopause and magnetosheath thickness. We would like to point out that this interpretation is misleading. Formisano et al. (1973) analyzed magnetopause and BS locations and found that although the shape of both boundaries can be expressed by Eq. (2), the values of coefficients (Eq. (3)) are different for them. Moreover, it is well known that the magnetopause shape and location depend on the sign of the IMF B_Z component, whereas we did not find such behavior of BS (Fig. 7c). We assume that this apparent discrepancy can be explained taking into account the results of Farris and Russell (1994). They suggest that the magnetosheath thickness is determined by the curvature radius of the obstacle. The negative IMF B_Z shifts a subsolar magnetopause inward but it increases the curvature radius and thus increases a magnetosheath thickness. The result of these two effects is that the BS location does not depend on the IMF B_Z sign. For these reasons, we suggest to consider the first term in Eq. (4) as an auxiliary term reflecting a change of the BS location with the upstream dynamic pressure. It is probably possible to build up the BS model based on a good magnetopause model but above discussion shows that it would be rather complicated. Moreover, MHD magnetosheath models predict a strong dependence of the magnetosheath thickness on the IMF B_Y direction and we did not find such effect for the BS location.

The NS91 model uses the magnetosonic Mach number for the BS description but we replace M_{MS} in (4) with M_A in this study. Fig. 6 shows that in such case, the BS location (parameter D) depends slightly on M_A. Since this dependence is notable for low M_A only, it can be simply corrected using suggestion of Farris and Russell (1994) and writing the second term in (4) in a form

$$D.\frac{(\gamma-1)M_A^2+2}{(\gamma+1)(M_A^2-1)}. \tag{8}$$

The most clear dependence of the D parameter is its rise with the magnetic field strength (Fig. 7d). Since the magnetic field is connected with the Mach number, both dependencies should be considered together. The resulting best fit of D which takes into account a correction to M_A according to (8) can be written in a form

$$D = D'.(\alpha + \beta.\mid B \mid), \tag{9}$$

where D', α, β are constants and $\mid B \mid$ stands for the IMF strength.

We would like to point out that the analysis is limited to $X < 8R_E$. We cannot exclude that the subsolar BS location is sensitive to the IMF orientation because changes of the magnetopause position with IMF B_Z are most pronounced in this region. As we noted, we suppose to re-analyze subsolar BS positions after accumulation of a larger number of BS crossings covering a longer time interval.

6. Corrected bow shock model

The suggested model after all corrections can be written in the form

$$R(\theta,\phi) = \frac{R_{av}(\theta,\phi)}{R_0}.\frac{C}{(NV^2)^{1/6}} .\left(1 + D\frac{(\gamma-1)M_A^2+2}{(\gamma+1)(M_A^2-1)}\right), \tag{10}$$

where $R_{av}(\theta,\phi)$ is given by equation

$$a_{11}X^2 + a_{22}Y^2 + a_{33}Z^2 + a_{12}XY + a_{14}X + a_{24}Y + a_{34}Z + a_{44} = 0, \tag{11}$$

where X, Y and Z are GSE coordinates (in R_E) of the surface. The coefficients of the best single-surface fit are

$$a_{11} = 0.45;\ a_{22} = 1;\ a_{33} = 0.8;\ a_{12} = 0.18;$$
$$a_{14} = 46.6;\ a_{24} = -2.2;\ a_{34} = -0.6;\ a_{44} = -618 \tag{12}$$

and the D parameter and constant C are

$$D = 0.937 \times (0.846 + 0.042 \mid B \mid); \quad C = 91.55. \qquad (13)$$

The resulting histograms of relative errors are shown in Figs. 8 and 9. Fig. 8 presents the crossings for which the analysis was done (i.e., crossings with $X < 8\,R_E$). Consequently, it is not surprising that a distribution of relative errors is centered around unity. However, the half-width is more than 2% lower than the distribution of errors of the original NS91 model. We assume that this improvement is significant because it was achieved by very simple means and the suggested corrections conserve a simplicity of the original model.

The histogram in Fig. 9 includes all crossings of our set. In spite of the significant enlargement of a number of crossings (5270 instead of 4038), the distribution of relative errors is nearly the same as that in Fig. 8. It means that the model can be used for the subsolar BS but one should take into account the effect analyzed in Fig. 3. This figure shows that crossings in the subsolar region ($X > 8\,R_E$) would be probably observed farther from the Earth than our model predicts.

A very important feature of the NS91 model following from the Měrka et al. (2003) analysis was its applicability to a wide range of upstream parameters. Since our suggestions on a model modification change notably only its dealing with IMF, we present the plot

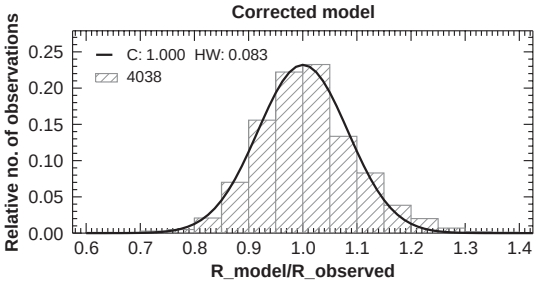

Fig. 8. Histogram of relative deviations of observed BS crossings and model predictions for the region of $8 > X > -17 > R_E$.

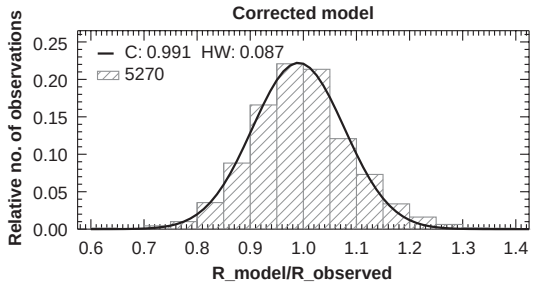

Fig. 9. Histogram of relative deviations of observed BS crossings and model predictions for a full data set.

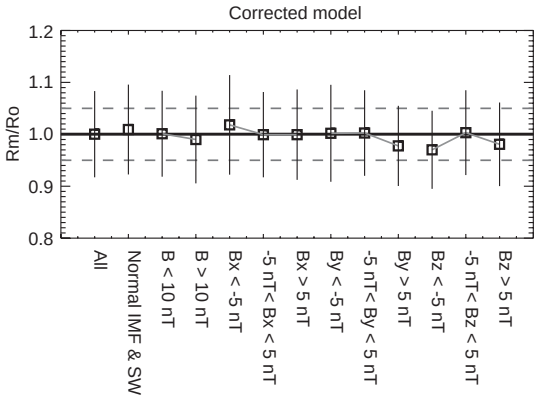

Fig. 10. The corrected BS model and its prediction with respect to the IMF variations. Note that we use the distant (WIND) solar wind monitor, whereas Měrka et al. (2003) used the "local" (IMP 8) monitor for similar plots.

analyzing the applicability of the model for extreme IMF values in Fig. 10. It can be seen that predictions of the corrected model do not depend significantly on values of upstream IMF or its components. The model slightly underestimates the BS distance from the Earth's for large values of IMF perpendicular (B_Y and B_Z) components but the shift is less than 2%. We suppose that this effect is connected with the magnetosheath thickness being a function of the IMF cone angle. This error could be probably depressed, if a correction on the IMF magnitude in the model would be replaced by a correction to the perpendicular components but such correction is out of the scope of the present paper.

7. Conclusion

We have collected a set of BS crossings from several spacecraft and used 5270 events to an analysis of the NS91 model. As a result, we suggested some corrections of the mentioned model. The analysis has shown that:

- The NS91 model BS surface does not adequately describe the elliptical cross-section of the BS. This problem was solved by a change of the surface (Eqs. (11) and (12), coefficients a_{24}, a_{33} and a_{34}).
- The NS91 model underestimates the BS distance in a low M_A range. The suggested correction is based on the Farris and Russell (1994) idea and has a form given by Eq. (8).
- Although the NS91 model uses a very rough correction for the Earth orbital motion, we did not find any statistically significant dependence of the BS location on the upstream speed.
- The NS91 model and, consequently, our corrected model probably underestimates the distance of the

subsolar BS from the Earth. This effect is not too significant (compare Figs. 8 and 9) but we recommend to use the corrected model for $X<8R_E$.

- The BS location is not a function of the IMF direction and/or IMF components but it depends linearly on the IMF magnitude. This linear dependence is given by Eq. (13).

We suppose that the corrected model can be broadly applied in physics of solar wind–magnetosphere interactions and that it represents a good base for a further development of empirical BS models.

Acknowledgements

This work was supported by the Czech Grant Agency under Contract 205/03/0953 and by the Research Project MSM 113200004. Their financial support is greatly acknowledged.

References

Bieber, J.W., Stone, E.C., 1979. In: Proceedings of Magnetospheric Boundary Layers Conference, Alpbach. Eur. Space Agency, Spec. Publ. ESA SP-148.

Binsack, J.H., Vasyliunas, V.M., 1968. Simultaneous IMP-2 and OGO 1 observations of bow shock compression. J. Geophys. Res. 73, 429.

Cairns, I.H., Grabbe, C.L., 1994. Towards an MHD theory for the standoff distance of Earth's bow shock. Geophys. Res. Lett. 21, 2781–2784.

Cairns, I.H., Lyon, J.G., 1995. MHD simulations of Earth's bow shock at low Mach numbers: standoff distances. J. Geophys. Res. 100, 17173–17180.

Cairns, I.H., Lyon, J.G., 1996. Magnetic field orientation effects on the standoff distance of Earth's bow shock. Geophys. Res. Lett. 23, 2883–2886.

Cairns, I.H., Fairfield, D.H., Anderson, R.R., Carlton, E.H., Paularena, K.I., Lazarus, A.J., 1995. Unusual locations of Earth's bow shock on September 24–25, 1987: Mach number effects. J. Geophys. Res. 100, 47.

Fairfield, D.H., 1971. Average and unusual locations of the Earth's magnetopause and bow shock. J. Geophys. Res. 76, 6700.

Fairfield, D.H., Feldman, W.C., 1975. Standing waves at low Mach number laminar bow shocks. J. Geophys. Res. 80, 515.

Farris, M.H., Russell, C.T., 1994. Determining the standoff distance of the bow shock: Mach number dependence and use of models. J. Geophys. Res. 99, 17681.

Farris, M.H., Petrinec, S., Russell, C.T., 1991. The thickness of the magnetosheath: constraints on the polytropic index. Geophys. Res. Lett. 18, 1821.

Formisano, V., 1979. Orientation and shape of the Earth's bow shock in three dimensions. Planet. Space Sci. 27, 1151.

Formisano, V., Hedgecock, P.C., Moreno, G., Sear, J., Bollea, D., 1971. Observations of Earth's bow shock for low Mach numbers. Planet. Space Sci. 19, 1519.

Formisano, V., Hedgecock, P.C., Moreno, G., Palmiotto, F., Chao, J.K., 1973. Solar wind interaction with the Earth's magnetic field, 2. Magnetohydrodynamic bow shock. J. Geophys. Res. 78, 3731.

Grabbe, C.L., 1997. Low Mach number predictions in an extended axially symmetric MHD theory of the magnetosheath. Geophys. Res. Lett. 24, 2495–2498.

Lepping, R.P., Acuna, M.H., Burlaga, L.F., Farrell, W.M., Slavin, J.A., Schatten, K.H., Mariani, F., Ness, N.F., Neubauer, F.M., Whang, Y.C., 1995. The WIND magnetic field investigation. Space Sci. Rev. 71, 207.

Měrka, J., Szabo, A., Narock, T.W., King, J.H., Paularena, K.I., Richardson, J.D., 2003. A comparison of IMP 8 observed bow shock positions with model predictions. J. Geophys. Res. 108, 1269 doi: 10.1029/2002JA009697.

Němeček, Z., Šafránková, J., 1991. The Earth's bow shock and magnetopause position as a result of solar wind—magnetosphere interaction. J. Atmos. Terr. Phys. 53, 1049.

Ogilvie, K.W., et al., 1995. SWE, a comprehensive plasma instrument for the Wind spacecraft. Space Sci. Rev. 71, 41–54.

Peredo, M., Slavin, J.A., Mazur, E., Curtis, S.A., 1995. Three-dimensional position and shape of the bow shock and their variation with Alfvénic sonic and magnetosonic Mach numbers and interplanetary magnetic field orientation. J. Geophys. Res. 100, 7907.

Petrinec, S.P., Song, P., Russell, C.T., 1991. Solar cycle variations in the size and shape of the magnetopause. J. Geophys. Res. 96, 7893–7896.

Russell, C.T., Zhang, T.L., 1992. Usually distant bow shock encounters at Venus. Geophys. Res. Lett. 19, 833.

Šafránková, J., Němeček, Z., Borák, M., 1999a. MAGION-4 observations of the bow shock crossings. Czech. J. Phys. 49, 563–578.

Šafránková, J., Němeček, Z., Borák, M., 1999b. Bow shock position: observations and models. In: Sibeck, D.G., Kudela, K. (Eds.), Interball in the ISTP Program, Studies of the Solar Wind–Magnetosphere–Ionosphere Interaction, NATO Science Series C, vol. 537, pp. 187–202.

Shue, J.-A., Chao, J.K., Fu, H.C., Russell, C.T., Song, P., Khurana, K.K., Singer, H.J., 1997. A new functional form to study the solar wind control of the magnetopause size and shape. J. Geophys. Res. 102, 9497.

Sibeck, D., Lopez, R., Roelof, E., 1991. Solar wind control of the magnetopause shape, location and motion. J. Geophys. Res. 96, 489.

Slavin, J.A., Holzer, R.E., 1981. Solar wind flow about the terrestrial planets, 1. Modeling bow shock position and shape. J. Geophys. Res. 86, 401.

Spreiter, J.R., Summers, A.L., Alksne, A.Y., 1966. Hydromagnetic flow around the magnetosphere. Planet. Space Sci. 14, 223.

Zhuang, H.C., Russell, C.T., 1981. An analytic treatment of the structure the bow shock and magnetosheath. J. Geophys. Res. 86, 2191.

C.8 Influence of the tilt angle on the bow shock shape and location

JOURNAL OF GEOPHYSICAL RESEARCH, VOL. 113, A05220, doi:10.1029/2007JA012813, 2008

Influence of the tilt angle on the bow shock shape and location

K. Jelínek,[1] Z. Němeček,[1] J. Šafránková,[1] and J. Merka[2,3]

Received 13 September 2007; revised 20 December 2007; accepted 8 February 2008; published 30 May 2008.

[1] The bow shock is created in front of an obstacle immersed into a supersonic flow and its location depends on the size and shape of the obstacle. It was found that the obstacle (magnetopause) is scaled with the solar wind dynamic pressure and changes its dimensions and shape with the dipole tilt angle and interplanetary magnetic field orientation. Similar functional dependencies would be expected for the bow shock position, however, none of the bow shock models considers the parametrization of bow shock properties with the tilt angle. The present study employs a set of bow shock crossings registered during 1994–2002 by different spacecraft and demonstrates the tilt angle influence on the bow shock location. The study is based on a comparison of a recent bow shock model with observations and shows that the night–side bow shock moves in the direction of the positive Z_{GSM} axis for positive tilt angles. The magnitude of the displacement can reach $\approx 3\ R_E$. The analysis reveals that the high–latitude bow shock surface is significantly distorted near the dawn–dusk meridian. This effect was identified as a counterpart of the magnetopause indentation in the cusp region.

Citation: Jelínek, K., Z. Němeček, J. Šafránková, and J. Merka (2008), Influence of the tilt angle on the bow shock shape and location, *J. Geophys. Res.*, *113*, A05220, doi:10.1029/2007JA012813.

1. Introduction

[2] Many studies were devoted to the influence of the tilt angle (the angle between the Earth's dipole axis and the Z_{GSM} coordinate) on formation of the magnetosphere as a whole and a location of the magnetopause in particular [e.g., *Spreiter and Briggs*, 1962; *Choe et al.*, 1973; *Petrinec and Russell*, 1995; *Zhou and Russell*, 1997; *Zhou et al.*, 1999; *Sotirelis and Meng*, 1999]. Observations as well as MHD models reveal that the magnetotail is shifted vertically for non–zero dipole tilt (λ) and the vertical offset of the subsolar point from the Sun–Earth line varies nearly linearly with this angle reaching approximately 3 R_E (Earth's radii) for maximum tilt and having only a weak dependence on solar wind dynamic pressure [e.g., *Sotirelis and Meng*, 1999]. *Petrinec and Russell* [1995] examined empirically the cusp effects and found that during periods of northward IMF, the magnetopause crossings close to cusp regions are observed at distances closer to the Earth than those in the equatorial plane. Their study resulted in a complicated numerical approximation of the high–latitude magnetopause.

[3] *Boardsen et al.* [2000] discussed an empirical model for the shape of the near–Earth high–latitude magnetopause which was parametrized by solar wind dynamic pressure, interplanetary magnetic field (IMF) B_Z component and dipole tilt angle and found that the dipole tilt angle and solar wind pressure are the most significant factors influencing the shape of the high–latitude magnetopause, whereas the IMF B_Z dependence is separable only after the effects of the pressure and tilt are removed. Similar shifts were reported by *Tsyganenko* [1998] who modeled the effects of the planetary dipole tilt and the IMF related twisting of the cross–tail current sheet and found that its deformation affects not only the shape of the tail current sheet but an entire magnetosphere. Using the data from Hawkeye 1 high–latitude, high–apogee spacecraft, similar results were reported by *Eastman et al.* [2000].

[4] *Zhou and Russell* [1997] and *Zhou et al.* [1999] used magnetopause crossings to demonstrate that, in the neighborhood of the magnetopause, the polar cusp location is controlled by a tilt of the Earth dipole, so that it moves increasingly toward the Sun as the dipole tilts sunward. Results of the Interball–1 project presented by *Nemeček et al.* [2000] suggested an even more pronounced shift in latitude. Moreover, the cusp magnetopause indentation was identified [e.g., *Petrinec and Russell*, 1995; *Eastman et al.*, 2000] and its deepness and location were connected with the dipole tilt [e.g., *Šafránková et al.*, 2002, 2005]. Furthermore, based on the Cluster measurements, *Zhang et al.* [2007] have shown that the boundary between the magnetosheath and cusp exhibits a clear indentation on the dawn and dusk sides of the cusp.

[5] The bow shock position and shape are controlled by the obstacle size and shape, upstream Mach numbers, and the IMF orientation. Moreover, *Merka and Szabo* [2004] discussed the size and stability of the bow shock shape/position with respect to IMF and solar wind flow directions. The size and geometry of the obstacle – the magnetopause –

[1]Charles University, Faculty of Mathematics and Physics, Prague, Czech Republic.
[2]Goddard Earth Sciences and Technology Center, University of Maryland, Baltimore, Maryland, USA.
[3]Also at Heliospheric Physics Laboratory, NASA/GSFC, Greenbelt, Maryland, USA.

0148-0227/08/2007JA012813$09.00

are a result of combined solar wind ram pressure, IMF orientation, and dipole tilt angle effects as we already mentioned. The ram pressure effect scales the magnetopause size, while the IMF orientation and dipole tilt affect the geometry of the boundary. Interaction of the supersonic solar wind with Earth's magnetosphere (magnetopause) creates fast mode magnetosonic waves that travel back upstream to form the bow shock. Thus the distance to the bow shock is the sum of the magnetopause distance and the magnetosheath thickness and it is reasonable to expect that the bow shock shape and position depend on the same parameters as the obstacle. However, the changes of the bow shock shape and location with tilt angle variations were not reported, although *Merka and Szabo* [2004] noted that the tilt angle effect is likely to be also important for the estimation of the bow shock position. Their analysis of bow shock crossings observed at X_{GSM} from the interval -15 and -10 R_E demonstrated that the shock's cross–section shifts by 3.8 R_E when the dipole tilt changes from sunward (tilt angle $\lambda > 15°$) to antisunward (tilt angle $\lambda < 15°$) orientations during average solar wind conditions. *Merka and Szabo* [2004] also confirmed these experimental results with 3D MHD numerical simulations in the selected range of the X coordinate.

[6] We present a short statistical study of bow shock locations for varying tilt angles. The study is based on a comparison of the bow shock model predictions with observations of several spacecraft.

2. Data Sets, Methodology, and Used Models

[7] Our set covers bow shock crossings observed between the 1995 and 2002 years by following spacecraft – IMP 8, Interball–1, Magion–4, Geotail and CLUSTER. Together, we identified ≈5.400 unambiguous BS crossings for which we have found Wind upstream solar wind parameters (1018 bow shock crossings from Interball–1; 1008 from Magion–4, 2069 from IMP 8, 813 from Geotail, and 312 from Cluster II). The set includes both outbound and inbound crossings, many of them being multiple. The effect of multiple crossings is most pronounced on the flanks.

[8] The observed crossings are located from $X_{GSE} \approx 15$ R_E to $X_{GSE} \approx -25$ R_E and within ±32 R_E in Z_{GSM} as it is demonstrated in Figure 1 where the projection of all observed bow shock crossings onto the $Y - Z_{GSM}$ plane is shown. Note that different parts of the bow shock surface were preferentially visited by a particular spacecraft and none of them is able to cover a whole investigated range of X_{GSM} coordinates.

[9] The crossings occurred under various upstream conditions: the solar wind velocity varied from 270 to 770 km/s, density from ∼1 to 35 cm^{-3}, and Alfvénic Mach number from ∼2 to 60.

[10] The solar wind and IMF data were taken from the Wind observations [*Ogilvie et al.*, 1995; *Lepping et al.*, 1995]. The time of propagation of solar wind features from the Wind position to the BS registered on a particular spacecraft was computed as a two–step approximation from Wind solar wind velocity measurements. As the first step, we expect a solar wind speed equal to 400 km/s and find the temporary time lag δt_1. The Wind solar wind speed at the time $t_1 = t - \delta t_1$ (where t_1 is the time of the bow shock observation) is then used for a determination of the lag that is applied to the Wind data. The values of the solar wind dynamic pressure and IMF used for the study were computed as five–minute averages centered around the time determined as given above.

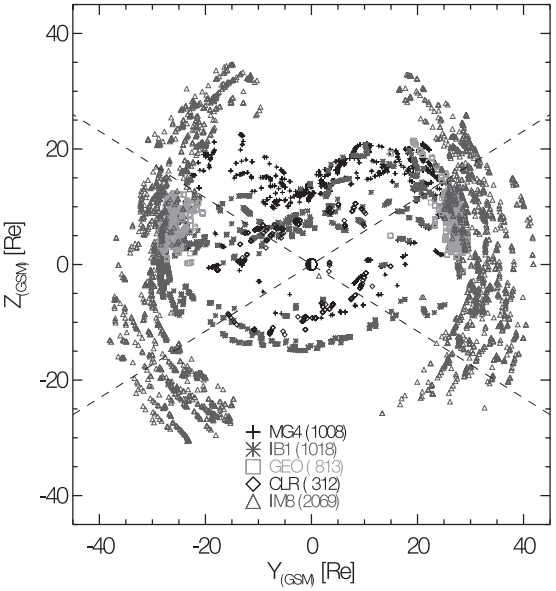

Figure 1. Projections of all used bow shock crossings observed on different spacecraft onto the $Y - Z_{GSM}$ plane. Abbreviations of the spacecraft: Magion–4 (MG4), Interball–1 (IB1), Geotail (GEO), Cluster II (CLR), IMP 8 (IM8). The dashed lines show the boundary between high and low latitudes used throughout the paper.

[11] The analysis is based on differences between observed and predicted locations of a particular bow shock crossing. To prediction, we have applied the *Jerab et al.* [2005] model for calculation of predicted distances. The model is based on *Formisano* [1979] and *Nemeček and Šafránková* [1991] models and consists of a second order surface that can be considered as an obstacle:

$$0.45X^2 + Y^2 + 0.8Z^2 + 0.18XY + 46.6X - 2.2Y - 0.6Z - 618 = 0 \quad (1)$$

where X, Y and Z are *GSE* coordinates (in R_E) of the obstacle surface. This equation implicitly involves a mean aberration caused by the Earth orbital motion. The main idea behind the model is that the distance of any bow shock point from the Earth center, $R(\theta, \phi)$, responds to the upstream changes by the same way:

$$R(\theta,\phi) = R_{av}(\theta,\phi).\frac{5.55}{(NV^2)^{1/6}}.\left(1 + D\frac{(\gamma-1)M_A^2+2}{(\gamma+1)(M_A^2-1)}\right) \quad (2)$$

where $R_{av}(\theta, \phi)$ is the geocentric distance (in the θ, ϕ directions) of an obstacle and it is given by the equation (1); N, V are the proton number density and bulk velocity of the

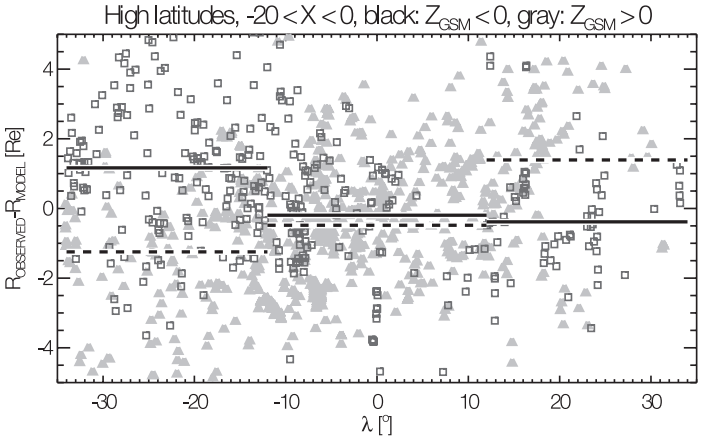

Figure 2. Differences between observed, R_{OBSERVED} and predicted, R_{MODEL} high−latitude ($\alpha > 30°$) bow shock locations in both northern ($Z_{GSM} > 0$, dashed lines and gray triangles) and southern ($Z_{GSM} < 0$, heavy lines and black open squares) hemispheres in the range of $-20\ R_E < X < 0\ R_E$ as a function of the tilt angle, λ. The lines represent medians.

solar wind, respectively; M_A is the upstream Alfvénic Mach number, γ is the effective ratio of specific heats in the solar wind taken as 5/3, and the D parameter is $D = 0.937 \times (0.846 + 0.042\ |B|)$. B stands for the IMF strength.

[12] The formula (2) consists of two terms. The first of them scales the obstacle in response to the solar wind dynamic pressure and generally behaves as the magnetopause. The second term is a function of the upstream Mach number and IMF strength and can be considered as a relative magnetosheath thickness measured along the radius vector. However, the above interpretation of the model should be considered with care because both terms were adjusted to receive the best fit of observed bow shock crossings (see *Jerab et al.* [2005] for details). Moreover, the authors limited the validity of their model to $X_{GSE} < 8\ R_E$ because it slightly underestimates the subsolar bow shock distance from the Earth.

[13] The equation (2) provides the bow shock distance from the Earth in the spherical coordinates. These coordinates are appropriate in the subsolar region because the angle between the shock normal and the radius vector is small in this region. On the other hand, these two vectors are nearly perpendicular at the nightside region. For this reason, we have measured the difference between observed and model bow shock locations, $R_{\mathrm{OBSERVED}} - R_{\mathrm{MODEL}}$, along the radius vector for $X < 0$, whereas this difference is measured from the X_{GSE} axis for $X > 0$. Since these two differences are equal for $X = 0$, there is no discontinuity in our definition. This procedure removes known effects of solar wind ram pressure and the influence of the IMF and the expected effect of the tilt angle can be determined more reliably.

3. Bow Shock Location Versus Tilt Angle

[14] *Šafránková et al.* [2005] have shown that the tilt angle influences predominantly the location of the high−latitude night−side magnetopause. For this reason, we have divided the set of bow shock crossings into high− and low−latitude parts. The breakpoint $\alpha = \arctan(Z_{GSM}/Y_{GSM}) = 30°$ was chosen in accord with the aforementioned paper and it is distinguished by dashed lines in Figure 1. The following set of figures presents the difference between observed, R_{OBSERVED} and predicted, R_{MODEL} bow shock locations as a function of either the tilt angle, λ or X_{GSM} coordinate.

[15] Figure 2 shows the difference of $R_{\mathrm{OBSERVED}} - R_{\mathrm{MODEL}}$ for high−latitude ($\alpha > 30°$) night−side bow shock crossings as a function of the tilt angle for both northern ($Z_{GSM} > 0$, black points) and southern ($Z_{GSM} < 0$, grey points) hemispheres. The heavy lines show median bow shock locations in three ranges of the tilt angles. Although the spread of experimental points is rather large, medians clearly indicate that the bow shock crossings are located farther from the Earth in that hemisphere in which the Earth dipole is substantially tilted toward the Sun, whereas the differences are the same and close to zero regardless of the hemisphere for small tilt angles. The difference of the medians from a zero−tilt bow shock location is of the order of $\approx 1\ R_E$ (i.e., about 5% of the mean bow shock distance from the Earth) but the medians are computed from all high−latitude observations regardless of the X coordinate and one would expect a larger effect in a distant tail than at the dawn−dusk meridian.

[16] Since the northern hemisphere exhibits a better observational coverage in our data set, we will concentrate on this hemisphere at the beginning of the study. Figure 3 shows how the tilt angle effects are distributed along the X_{GSM} axis. The differences between observed and model bow shock locations are plotted as a function of the tilt angle in the four panels. Each of them covers a slice of 10 R_E in length along the X_{GSM} axis. The dependencies are fitted with straight lines. One can note that the slopes are very similar in top two panels covering the night−side sector. It suggests that the bow shock displacement due to the increase of the tilt angle can be described as a simple translation in the direction of the positive Z_{GSM} axis. Such approximation cannot be used on the dayside because the bow shock location depends on the tilt angle stronger near

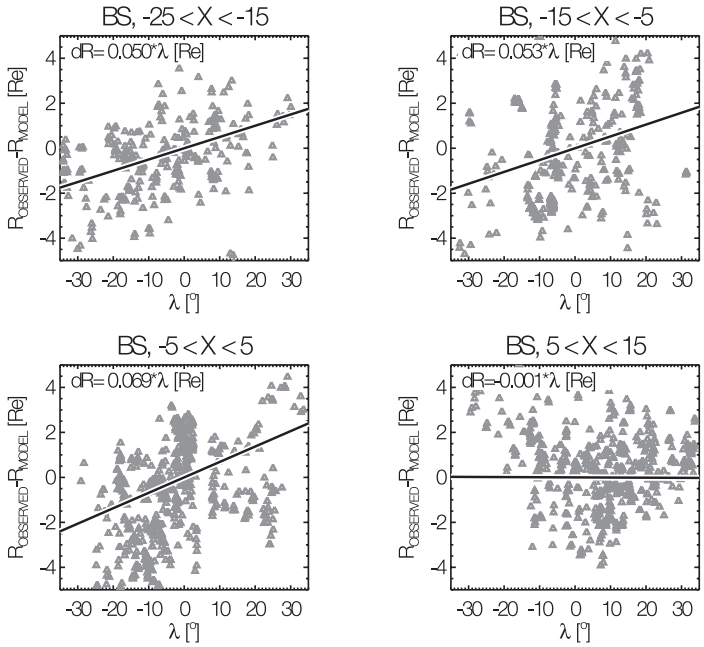

Figure 3. Differences between observed and predicted bow shock (BS) locations in the northern hemisphere at high latitudes as a function of the tilt angle; the panels represent four bins along the X_{GSM} coordinate. The heavy lines show the slope of the tilt–angle dependence in a particular range of X_{GSM}. The equation of the fit is given at the top of each panel.

the dawn–dust meridian (lower left panel), whereas this dependence nearly vanishes and changes its sign on the dayside (lower right panel). This observation is in agreement with numerical simulations by *Merka and Szabo* [2004] and suggests that the bow shock changes its shape due to tilt angle variations. We will discuss this feature later in this paper.

[17] A different view on the tilt angle effects on the bow shock location provides Figure 4. The same points as in previous figures are divided into two groups according to the tilt angle sign and plotted as a function of the X_{GSM} coordinate. We are using the same sign convention as *Merka and Szabo* [2004], i.e., λ is positive when the dipole is tilted toward the Sun in the northern hemisphere. The

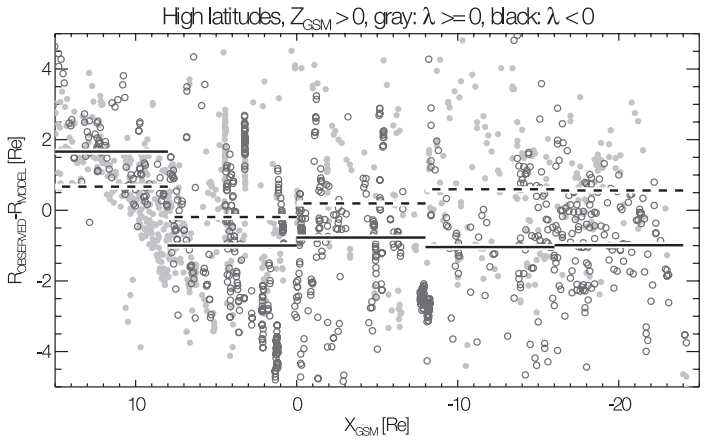

Figure 4. Differences between observed and predicted bow shock locations in the northern hemisphere at high latitudes as a function of the X_{GSM} coordinate. The crossings are divided into two groups according to the tilt–angle sign (gray full circles and dashed lines represent positive tilts; open black circles and full black lines represent negative tilts).

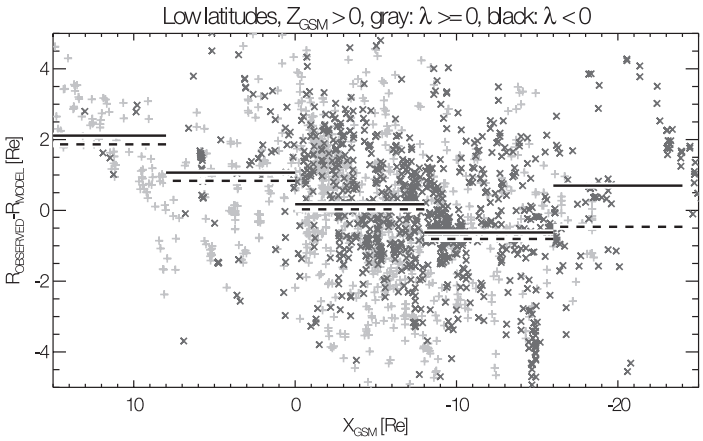

Figure 5. The same as Figure 4 but for a subset of low-latitude ($\alpha < 30°$) bow shock crossings (positive tilts: light crosses and dashed lines; negative tilts: dark crosses and full black lines).

night–side part exhibits an almost constant displacement of median bow shock locations. This displacement is about $\pm 0.7\ R_E$ and its sign corresponds to the sign of the tilt. The trend continues to $X < 8\ R_E$ and reverses at the subsolar region ($X > 8\ R_E$). However, this division is arbitrary and depends on the X_{GSM} binning. We will discuss the bow shock shape in a vicinity of the dusk–dawn meridian later in this paper.

[18] In order to check the latitudinal extend of the tilt–angle influence, we have plotted low–latitude crossings in Figure 5. The way of data presentation is the same as that in Figure 4. We can note that these data do not exhibit any systematic dependence on the tilt angle in the whole range of the X coordinates where the number of crossings is sufficient for a reliable determination of medians.

[19] As a next step, we have fitted the tilt–angle dependence and adjusted model predictions as

$$R'_{\mathrm{MODEL}} = R_{\mathrm{MODEL}} + 0.08\lambda \sin\alpha \qquad (3)$$

where λ stands for the tilt angle in degrees and α is the geomagnetic latitude defined above. The adjusted model captures the tilt angle effect on the night–side magnetosheath rather well as it can be seen in Figure 6. This figure repeats Figure 4 but the model bow shock locations are corrected. The medians are nearly identical and close to zero for positive and negative tilts. Since *Jerab et al.* [2005] limited the validity of their bow shock model to $X < 8\ R_E$, the data for $X > 8\ R_E$ were not corrected. Figure 4 shows that the subsolar bow shock is observed farther from the Earth than the model predicts for both positive and negative

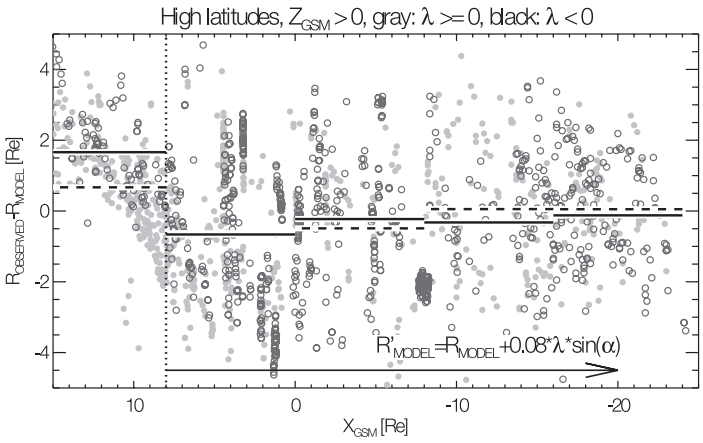

Figure 6. Differences between observed and predicted bow shock locations in the northern hemisphere at high latitudes as a function of the XGSM coordinate for two tilt-angle signs. The predicted bow shock locations are corrected according to the equation (3); positive tilts: gray full circles and dashed lines; negative tilts: open black circles and full black lines.

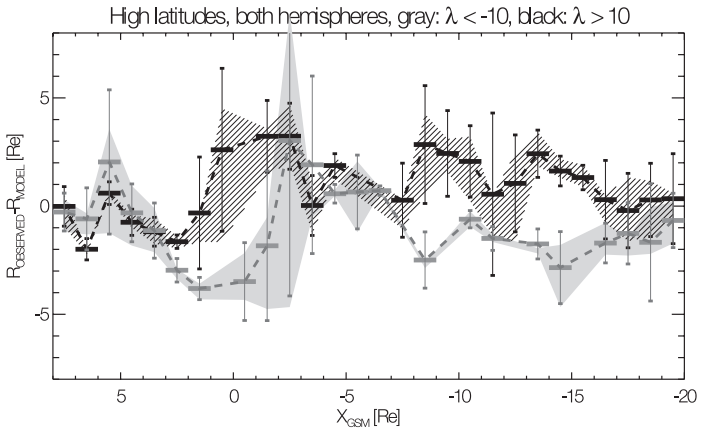

Figure 7. Differences between observed and predicted bow shock locations in both hemispheres at high latitudes along the X_{GSM} coordinate for two groups of tilt angles. Shadowing distinguishes the areas between 25% and 75% percentiles for both groups of tilt angles; positive tilts ($\lambda > 10°$): heavy lines and heavy shadowing; negative tilts ($\lambda < -10°$): gray lines and light shadowing.

tilt angles. Thus predictions for $X > 8\ R_E$ would require a different correction because the shock displacement in this region due to the tilt orientation is in an opposite direction in comparison to the region downstream (Figure 6). Moreover, our correction expects the opposite bow shock displacement for different signs of λ but *Sotirelis and Meng* [1999] and *Boardsen et al.* [2000] have shown that the magnetopause nose moves inward for a large $|\lambda|$ regardless of its sign and one would expect that the bow shock would follow the magnetopause motion.

[20] The magnitude of the bow shock displacement seen in Figure 4 is roughly the same as that reported by *Šafránková et al.* [2005] for the night–side magnetopause. It means that the average magnetosheath thickness is not significantly affected by the dipole tilt. On the other hand, *Šafránková et al.* [2005] have found a magnetopause indentation in the cusp region but the analysis in Figures 4 and 6 is too coarse to reveal such tiny features on the bow shock surface. The medians are computed over broad ranges of the X coordinate ($\approx 8\ R_E$) because the main purpose of this analysis is to show that equation (3) can be used for correction of the bow shock model. Nevertheless, even this rough analysis suggests that a further improvement of the model of the bow shock surface is possible because the standard deviations of observations from the medians shown in Figure 6 are $\sim 2.2\ R_E$ for the region $-8 < X < 8$, whereas they are about $1.3\ R_E$ in other two regions.

[21] A precise study of the bow shock shape requires shorter binning along the X axis because a possible bow shock indentation could be narrow. On the other hand, the number of bow shock crossings in Figures 2–6 is rather small because we have used the data from the northern hemisphere only and it does not allow narrowing the intervals for the median computation substantially. Figure 2 suggests that the tilt angle effects in the southern hemisphere would be the same as those in the northern hemisphere if the sign of the tilt is reversed. This is consistent with statement of *Mead and Fairfield* [1975] that the field line topology in one hemisphere for a given positive tilt angle is very similar to the topology in the opposite hemisphere for the same negative tilt. It allows us to nearly double the number of crossings for our study.

[22] The analysis of the combined data set including the data from both hemispheres is shown in Figure 7 where the differences between observed and predicted bow shock locations are shown for two groups of tilt angles: $\lambda > 10°$, $\lambda < -10°$. The medians are computed over intervals of $1\ R_E$ in length, thus the depicted error bars (standard deviations) are rather wide. To distinguish the changes of the bow shock shape with the tilt angle, we have shadowed the areas between 25% and 75% percentiles for both groups of tilt angles. The figure reveals that the high–latitude bow shock shape is heavily distorted near the dawn–dusk meridian. This distortion starts with an indentation that is followed by an overshoot. The shape of this distortion is similar for positive and negative tilts but it is shifted toward the Sun when the Earth's dipole points sunward (positive tilts in the northern hemisphere and vice versa). The deepness of the indentation is $\approx 1–2\ R_E$, the overshoot height is about $2–3\ R_E$ and the width of both features is about $4\ R_E$. The difference between locations of the distortion for positive and negative tilts is $\approx 3\ R_E$ along the X axis. Moreover, the figure suggests that the bow shock surface is undulated at high latitudes. The overshoot of the indentation is followed by surface waves with the wavelength $\approx 6–7\ R_E$ and amplitude $\approx 1–2\ R_E$. However, although the shadowed areas in Figure 7 are clearly separated, we think that a precise determination of the bow shock shape requires a significantly larger data set of bow shock crossings.

4. Discussion

[23] We have found the shift of the night–side bow shock location in a north–south direction. Such shift was demonstrated by *Merka and Szabo* [2004] using IMP 8 data and the BATS-R-US global MHD model. However, *Merka and Szabo* [2004] used the IMP 8 data and this spacecraft was orbiting near the equatorial plane and it could reach $\sim 45°$ of

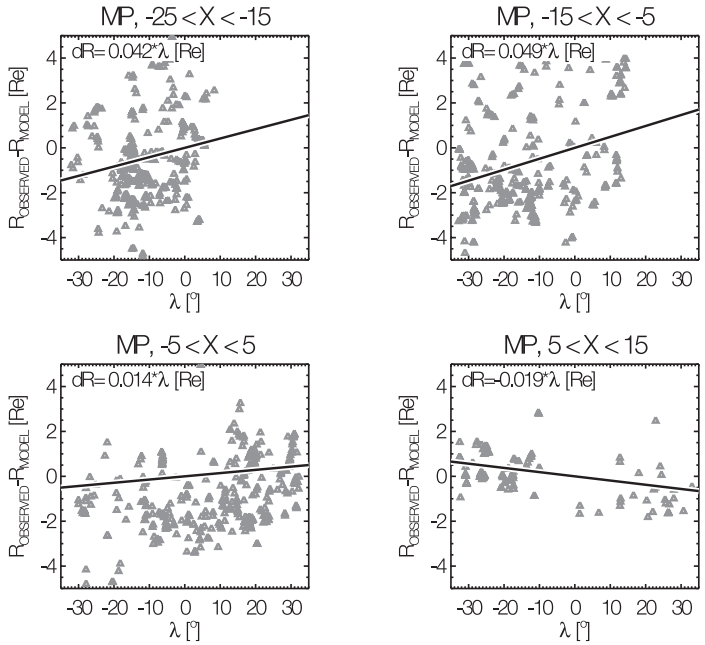

Figure 8. Differences between observed and modeled magnetopause (MP) locations in the northern hemisphere at high latitudes as a function of the tilt angle.

geomagnetic latitude only (Figure 1). Our data set is complemented with the data of Interball−1 and Magion−4 that were moving along the orbit with inclination ∼63° and provide an excellent coverage of high−latitude bow shock on the dayside and near tail (up to $\approx X > -15\ R_E$). Later, Cluster II observations further extend the dayside high−latitude bow shock crossings as it is demonstrated in Figure 1.

[24] The bow shock distance from the Earth can be considered as a sum of the magnetopause distance and magnetosheath thickness. *Šafránková et al.* [2005] have determined the magnitude of the north−south displacement of the night−side magnetopause to be about 1.5 R_E when the tilt changes from negative to positive values. According to Figure 4, the magnitude of the bow shock displacement is very similar and thus we can conclude that the dipole tilt does not affect the magnetosheath thickness. Figure 4 suggests that the magnitude of the bow shock displacement slightly increases tailward. However, we have applied the correction that does not depend on the X coordinate to the data shown in Figure 6, thus we can note that this effect is probably only apparent and it is likely caused by a nonuniform distribution of bow shock crossings with large tilt angles along the X axis.

[25] The mentioned values of bow shock and magnetopause displacements are differences between averaged locations of the boundaries for all positive and negative tilts, the differences between actual locations for maximum positive and negative tilts would be significantly larger. Top panels in Figure 3 show that the bow shock displacement can reach $\approx 3\ R_E$. Since comparable magnetopause data are not available, we have revisited the set of magnetopause crossings used by *Šafránková et al.* [2005] and plotted them by the same way in Figure 8. The plot uses the *Petrinec and Russell* [1996] magnetopause model. This model is written in spherical coordinates for $X > 0$ and cylindrical coordinates are applied for $X < 0$. Consequently, the definition of R_{MODEL} for the magnetopause is analogous with our definition of R_{MODEL} for the bow shock surface.

[26] A comparison of Figure 8 with Figure 3 leads to the conclusion that the night−side bow shock and magnetopause displacements due to tilt changes are very similar for all tilt angles. Moreover, when we compare the dayside portions of these crossings (lower right panels in Figures 3 and 8) we can identify very similar inward shifts with the increasing tilt and thus, the bow shock displacement simply follows the displacement of the magnetopause in this region. We should point out that the last sentence refers to the northern hemisphere because we have a smaller number of high-latitude bow shock crossings in the southern hemisphere. However, magnetospheric hemispheres would respond to dipole tilt orientation and upstream orientations in the same way, so we expect the same bow shock behavior in the southern hemisphere.

[27] In order to discuss the bow shock distortion that follows from Figure 7, a schematics of bow shock and magnetopause locations in the $X - Z$ plane is shown in Figure 9. The *Petrinec and Russell* [1996] magnetopause and *Jerab et al.* [2005] bow shock models are shown for the sake of reference by the thin dotted lines. The magnetopause locations for positive and negative tilts are given by heavy dashed lines and follow the corrections of the magnetopause shape suggested by *Šafránková et al.* [2005]. The construction of the bow shock shape is based

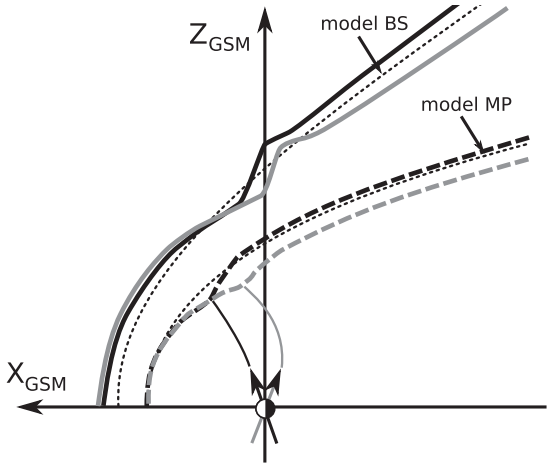

Figure 9. A sketch of the magnetopause and bow shock shapes for positive (black) and negative (gray) tilts. The *Petrinec and Russell* [1996] magnetopause and *Jerab et al.* [2005] bow shock models are shown for the sake of reference by the thin dotted lines.

on differences from the *Jerab et al.* [2005] model that are given in Figure 7. We can note that the magnitudes of the distortions of both bow shock and magnetopause surfaces are very similar and that these distortions move sunward on similar angles when the tilt increases. The distortion of the bow shock is located more tailward but it is consistent with the fact that the bow shock is built by waves generated at the magnetopause. These waves propagate radially in the magnetosheath plasma frame but they are blown downstream with the magnetosheath flow.

5. Conclusion

[28] Figure 9 schematically depicts the main conclusions of this short study that the tilt angle effect on the bow shock displacement in the northern hemisphere can be roughly separated into three parts:

[29] (1) The dayside ($X_{GSM} > 4\ R_E$) bow shock moves slightly inward ($\approx 0.5\ R_E$) when the tilt angle changes from negative to positive values.

[30] (2) The night–side ($X_{GSM} < -4$) bow shock moves outward when the tilt angle increases. This displacement was quantified as $\Delta R = 0.08\lambda \sin \alpha$.

[31] (3) The bow shock near the dawn–dusk meridian ($-4 < X_{GSM} < 4$) exhibits a distortion that is caused by the presence of the magnetopause indentation in the cusp region. This distortion can reach $-2 \div +3\ R_E$ in the Z direction and moves sunward with increasing tilt angle.

[32] These conclusions are based on the statistical processing of the bow shock crossings and their confirmation by MHD modeling is desirable.

[33] **Acknowledgments.** The authors thank the Wind team for the magnetic field and plasma data. The present work was partly supported by the Czech Grant Agency under Contracts 205/06/0875 and 205/07/0694, and partly by the Research Plan MSM 0021620860 that is financed by the Ministry of Education of the Czech Republic. K. Jelinek would like to thank the Grant Agency of Charles University (GAUK 147307).

[34] Zuyin Pu thanks Mona Kessel and Scott Boardsen for their assistance in evaluating this paper.

References

Boardsen, S. A., T. E. Eastman, T. Sotirelis, and J. L. Green (2000), An empirical model of the high-latitude magnetopause, *J. Geophys. Res.*, *105*, 23,193–23,219.

Choe, J. Y., D. B. Beard, and E. C. Sullivan (1973), Precise calculation of the magnetopause surface for a tilt dipole, *Planet. Space Sci.*, *21*, 485–498.

Eastman, T. E., S. A. Boardsen, S.-H. Chen, S. F. Fling, and R. L. Kessel (2000), Configuration of high-latitude and high-altitude boundary layers, *J. Geophys. Res.*, *105*, 23,221–23,238.

Formisano, V. (1979), Orientation and shape of the Earth's bow shock in three dimensions, *Planet. Space Sci.*, *27*, 1151.

Jerab, M., Z. Nemecek, J. Safrankova, K. Jelinek, and J. Merka (2005), A study of bow shock locations, *Planet. Space Sci.*, *53*, 85–94.

Lepping, R. P., M. H. Acuna, L. F. Burlaga, W. M. Farrell, J. A. Slavin, K. H. Schatten, F. Mariani, N. F. Ness, F. M. Neubauer, and Y. C. Whang (1995), The wind magnetic field investigation, *Space Sci. Rev.*, *71*, 207.

Mead, G. D., and D. H. Fairfield (1975), Quantitative magnetospheric model derived from spacecraft magnetometer data, *J. Geophys. Res. 80*, *4*, 523–534.

Merka, J., and A. Szabo (2004), Bow shock's geometry at the magnetospheric flanks, *J. Geophys. Res.*, *109*, A12224, doi:10.1029/2004JA010567.

Nemeček, Z., and J. Šafránková (1991), The Earth's bow shock and magnetopause position as a result of solar wind–magnetosphere interaction, *J. Atmos. Terr. Phys.*, *53*, 1049.

Nemeček, Z., J. Měrka, and J. Šafránková (2000), The tilt angle control of the outer cusp position, *Geophys. Res. Lett.*, *27*, 77–80.

Ogilvie, K. W., et al. (1995), SWE, a comprehensive plasma instrument for the Wind spacecraft, *Space Sci. Rev.*, *71*, 41–54.

Petrinec, S. M., and C. T. Russell (1995), An examination of the effect of dipole tilt angle and cusp regions on the shape of the dayside magnetopause, *J. Geophys. Res.*, *100*, 9559–9566.

Petrinec, S. M., and C. T. Russell (1996), Near-Earth magnetopause shape and size as determined from the magnetopause flaring angle, *J. Geophys. Res.*, *101*, 137–152.

Šafránková, J., Z. Nemeček, Š. Dušík, L. Přech, D. G. Sibeck, and N. N. Borodkova (2002), The magnetopause shape and location: A comparison of the Interball and Geotail observations with models, *Ann. Geophys.*, *20*, 301.

Šafránková, J., Š. Dušík, and Z. Nemeček (2005), The shape and location of the high-latitude magnetopause, *Adv. Space Res.*, *36*(10), 1934.

Sotirelis, T., and C.-I. Meng (1999), Magnetopause from pressure balance, *J. Geophys. Res.*, *104*, 6889–6898.

Spreiter, J. R., and B. R. Briggs (1962), Theoretical determination of the form of the boundary of the solar corpuscular stream produced by interaction with the magnetic dipole field of the Earth, *J. Geophys. Res.*, *67*, 37–51.

Tsyganenko, N. A. (1998), Modeling of twisted/warped magnetospheric configurations using the general deformation method, *J. Geophys. Res.*, *103*, 23,551–23,563.

Zhang, H., M. W. Dunlop, Q.-G. Zong, T. A. Fritz, A. Balogh, and Y. Wang (2007), Geometry of the high-latitude magnetopause as observed by Cluster, *J. Geophys. Res.*, *112*, A02204, doi:10.1029/2006JA011774.

Zhou, X. W., and C. T. Russell (1997), The location of the high-latitude polar cusp and the shape of the surrounding magnetopause, *J. Geophys. Res.*, *102*, 105–110.

Zhou, X. W., C. T. Russell, G. Le, S. A. Fuselier, and J. D. Scudder (1999), The polar cusp location and its dependence on dipole tilt, *Geophys. Res. Lett.*, *26*, 429–432.

K. Jelínek, Z. Němeček, and J. Šafránková, Charles University, Faculty of Mathematics and Physics, V Holešovičkách 2, 180 00 Prague 8, Czech Republic. (zdenek.nemecek@mff.cuni.cz)

J. Merka, Goddard Earth Sciences and Technology Center, University of Maryland, College Perk, Baltimore, MD 20742, USA.

C.9 Small-scale deformation of the bow shock

Available online at www.sciencedirect.com
ScienceDirect
Advances in Space Research 41 (2008) 1519–1527
ADVANCES IN SPACE RESEARCH (a COSPAR publication)
www.elsevier.com/locate/asr

Small-scale deformation of the bow shock

K. Jelínek, Z. Němeček, J. Šafránková *

Charles University, Faculty of Mathematics and Physics, V Holesovickach 2, 180 00 Prague, Czech Republic

Received 1 November 2006; received in revised form 5 April 2007; accepted 17 April 2007

Abstract

The prediction of the bow shock location is a proof of our understanding of the processes governing the solar wind – magnetosphere interaction. However, the models describing the bow shock location as a function of upstream parameters are based on a statistical processing of bow shock crossings observed by a single spacecraft. Such crossings locate the bow shock in motion, i.e., in a non-equilibrium state and this fact can be a source of significant errors. We have carefully analyzed a long interval of simultaneous observations of the bow shock and magnetopause and another interval of bow shock observations at two well-separated points. Our results suggest that often a small-scale deformation of the bow shock front due to magnetosheath fluctuations is the most appropriate interpretation of observations. Since the low-frequency magnetosheath variations exhibit largest amplitudes, a simultaneous bow shock displacement over a distance of 10–15 R_E can be observed. We suggest that bow shock models can be probably improved if the tilt angle would be implemented as a parameter influencing the bow shock location in high latitudes.

Keywords: Solar wind; Bow shock; Magnetopause; Bow shock models

1. Introduction

The terrestrial bow shock is formed in the solar wind when the supersonic plasma emitted from the Sun encounters the Earth's magnetic field. The dipole magnetic field acts, in the first approximation, as an impenetrable barrier to the solar wind which flows around this obstacle. In this process, the magnetopause is formed, separating the magnetic field inside from the solar wind that flows around it. Ahead of the magnetopause, the bow shock forms a surface across which the solar wind plasma is heated and slowed down from supersonic to subsonic speeds. The Earth's bow shock has been the subject of extensive observational and theoretical investigations (e.g., Fairfield, 1976; Burgess, 1995). Typically, a distance from the Earth to the subsolar point of the bow shock is ~14 R_E but the location of the bow shock is highly variable, depending on the speed and density of the solar wind. In general terms, the large-scale geometry of the bow shock depends on the solar wind dynamic pressure (Fairfield, 1971). As for all collisionless plasmas, the nature of the shock transition from supersonic to subsonic flow depends, primarily, on two parameters: one is the Mach number of the shock wave, i.e., the ratio of upstream velocity to the characteristic wave speed (e.g., Alfvén or magnetosonic); and the second is the θ_{Bn} angle between the upstream magnetic field direction and the normal direction to the shock surface. The physics within the transition is also influenced by the upstream plasma β (the ratio of the thermal pressure to magnetic pressure).

A number of models have been developed that relate the bow shock positions, bow shock shape and motion to upstream conditions. Most of the commonly used models are derived from Spreiter et al. (1966) gas-dynamic simulations. Fairfield (1971) introduced the scaling of the bow shock nose with the solar wind dynamic pressure and Formisano (1979) developed a 3D model that includes the dependence of the magnetosheath thickness on an

* Corresponding author.
E-mail addresses: karel.jelinek@matfyz.cz (K. Jelínek), jana.safrankova@mff.cuni.cz (J. Šafránková).

0273-1177/$34.00 © 2008 Published by Elsevier Ltd on behalf of COSPAR.
doi:10.1016/j.asr.2007.04.050

upstream Mach number. The dependence of the bow shock position on the Mach number in a reasonable agreement with the gas-dynamic theory that was then demonstrated by Slavin and Holzer (1981), Slavin et al. (1984). Němeček and Šafránková (1991) followed approach of Formisano (1979) and complemented his model with an dependence of the bow shock position on the IMF strength. Since this dependence was a subject of debate (Farris and Russell, 1994; Měrka et al., 2003b), Jeřáb et al. (2005) carried out a comprehensive analysis of about 2000 bow shock crossings and confirmed this suggestion. Farris and Russell (1994) slightly modified the Mach number dependence of the bow shock location used in aforementioned models and suggested a new model based on the importance of the magnetopause curvature on the bow shock location. Rather complicated implementation of the Mach number dependence is used in the Peredo et al. (1995) model.

The Mach number effect is connected with compressibility of the gas and thus with the ratio of specific heats. Models use generally that of an ideal gas but some author argue that the presence of the magnetic fields leads to increase of this ratio up to 2 and Zhuang and Russell (1981) even suggested a value of 2.15 for a better description of the bow shock location.

Since we are using the Jeřáb et al. (2005) model in our investigation, we briefly summarize their approach. The model consists of a second order surface that represents a magnetopause. Its shape is scaled with the solar wind dynamic pressure. The second term expresses the relative magnetosheath thickness that is an explicit function of the upstream Mach number and the IMF strength. Here, we could note that the authors carefully analyzed their data set but they did not find any clear dependence of the bow shock location on the IMF direction.

Multiple bow shock crossings occurring over intervals from minutes to several hours are usually interpreted in terms of bow shock motions with respect to the observing spacecraft (e.g., Němeček et al., 1988; Zastenker et al., 1988). Determinations of the bow shock velocity typically ranges between a few km/s up to ~100 km/s (e.g., Volk and Auer, 1974; Newbury et al., 1998; Šafranková et al., 2003). Volk and Auer (1974) considered that bow shock velocities in the subsolar region of the order of 100 km/s can be induced by a bow shock interaction with solar wind discontinuities, while smaller velocities may be determined by smooth interplanetary disturbances such as Alfvén waves. Lepidi et al. (1996) examined a few periods of multiple bow shock crossings on IMP 8 and confirmed previous findings interpreting multiple crossings as response to changes in external solar wind conditions. They also found that an inward motion of the shock is accompanied by large magnetosheath densities just before shock sweeps across the spacecraft.

Maksimovic et al. (2003) used a combination of the Farris and Russell (1994) bow shock and Sibeck et al. (1991) magnetopause models and applied them to eleven quasi-perpendicular bow shocks observed by Cluster on March 31, 2001 to measure the speed and location of the shock, and to estimate its large-scale motion over more than two hours. They used the ACE data to compute the temporal variations of the ram pressure and of the Alfvén Mach number in the solar wind and used simple four spacecraft timings, assuming planarity and constant bow shock motion during each crossing. The authors concluded that temporal variations of bow shock standoff distance deduced from the Cluster observations are consistent with model predictions not only in a statistical sense, i.e., over a lot of crossings during long-time periods but the assumptions of the models are valid also on shorter time-scales as the shock responds to changing upstream conditions.

Slavin et al. (1996) studied near-simultaneous bow shock crossings by Wind and IMP 8 when the magnetic field made an angle <20° to the Sun–Earth line. They found that the radial distance of the shock at both spacecraft was

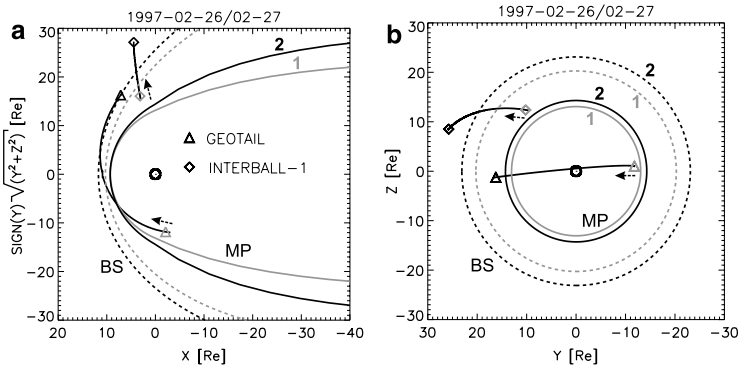

Fig. 1. (a) Positions of the Interball-1/Magion-4 and Geotail spacecraft during observations of multiple bow shock and magnetopause crossings (from 26 Feb. 1997; 2000 UT to 27 Feb. 1997; 2000 UT). For a sketch, the Petrinec and Russell (1996) model magnetopause and Jeřáb et al. (2005) bow shock models were used. (b) Projections of spacecraft trajectories onto the Y–Z plane. The numbers (1) and (2) denote the magnetopause or bow shock model locations at the beginning (1) and end (2) of the interval under study.

only ~80–85% of that predicted by models. Cairns and Grabbe (1994) developed an MHD theory for the bow shock standoff distance and the thickness of the magnetosheath predicting that they should depend strongly on θ (the angle between the incident solar wind velocity and magnetic field), M_A, and M_S for $M_A < 6$. On the other hand, MHD simulations of Cairns and Lyon (1995) showed a weak dependence of the bow shock position on the interplanetary magnetic field (IMF) orientation for $\theta = 45°$ and 90°. Měrka et al. (2003a) presented a study of multiple bow shock crossings when IMF was nearly aligned with the incident solar wind flow ($\theta = 10°$) and the upstream conditions were very stable for ~9 h. Observations by the Interball-1 and IMP 8 spacecraft demonstrated significant differences in existing magnetopause and bow shock models/theories, since estimates of the magnetosheath thickness were <10% of the magnetopause distance and both spacecraft measured the shock much closer to the Earth than model predicted.

The peculiar magnetopause/bow shock behavior is not understood currently and requires the development of new theories and observations describing how the Earth's

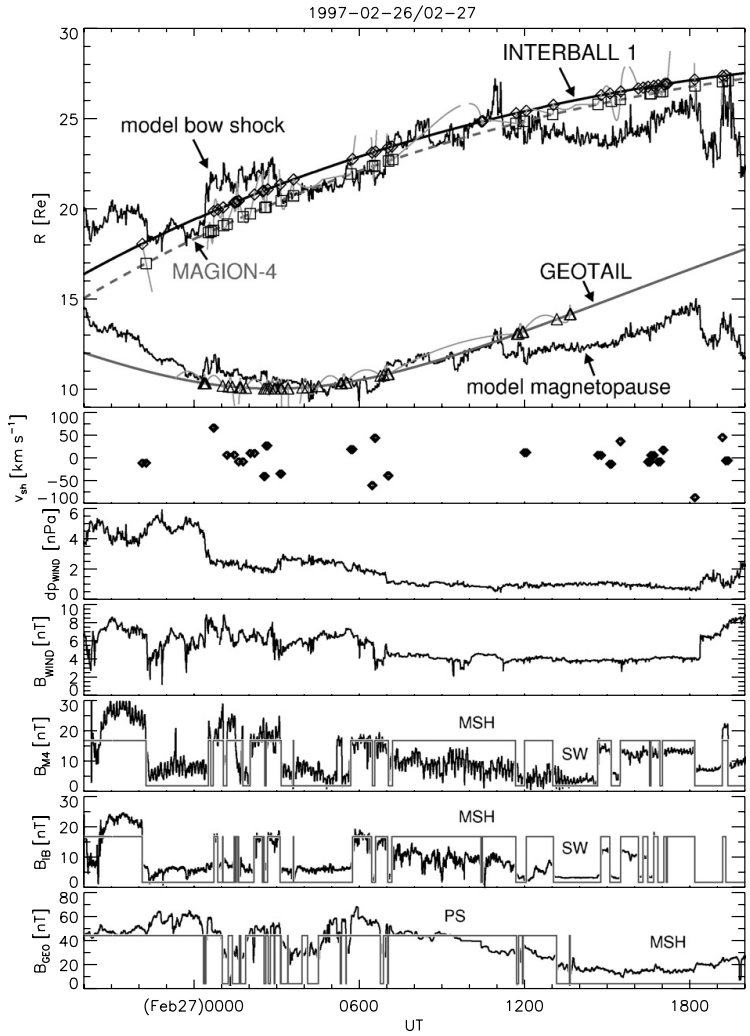

Fig. 2. An overview plot of the first event. Panels from top to bottom: first panel – radial positions of the Interball-1, Magion-4, and Geotail spacecraft and actual model locations of the bow shock and magnetopause and crossings of both boundaries (points); computed velocities (from two-point measurements of the Interball-1/Magion-4 satellite pair) of the bow shock motion, v_{sh}; wind solar wind dynamic pressure; wind IMF; and last three panels present magnetic fields from Magion-4, Interball-1, and Geotail together with identifications of particular regions. In the first panel, the Interball-1 orbit is denoted by the full line, the Magion-4 orbit by the dashed line.

magnetosphere reacts to different IMF orientations. Despite a progress in bow shock modeling, the differences between predictions and observations remain often as large as several R_E. The bow shock crossing is observed mostly due to the changes of its position (from one stationary state to another) which is affected by variations of solar wind conditions. Such crossings assigned to solar wind parameters do not correspond to an equilibrium position of the bow shock and vice versa.

To avoid this problem, we have performed study of two intervals during which the bow shock crossings were registered many times by the Interball-1/Magion-4 closely separated satellite pair or the bow shock spent a notable time between both satellites. Therefore, we deal with a small-scale motion of the bow shock location during a long time of stable upstream conditions. In order to determine the sources of this motion, two-point bow shock observations are complemented with simultaneous observations of the magnetopause displacement in one of intervals and by third point at the bow shock in the second interval. For a study of a small-scale motion of the bow shock, we have chosen relatively quiet solar wind conditions and observations when simultaneous bow shock and/or bow shock/magnetopause crossings on the different spacecraft were available. We tried to find such intervals of measurements when one quantity is changing far more than other to analyze an influence of a particular solar wind parameter.

In the study, we have concerned with changes of several parameters controlling the bow shock position

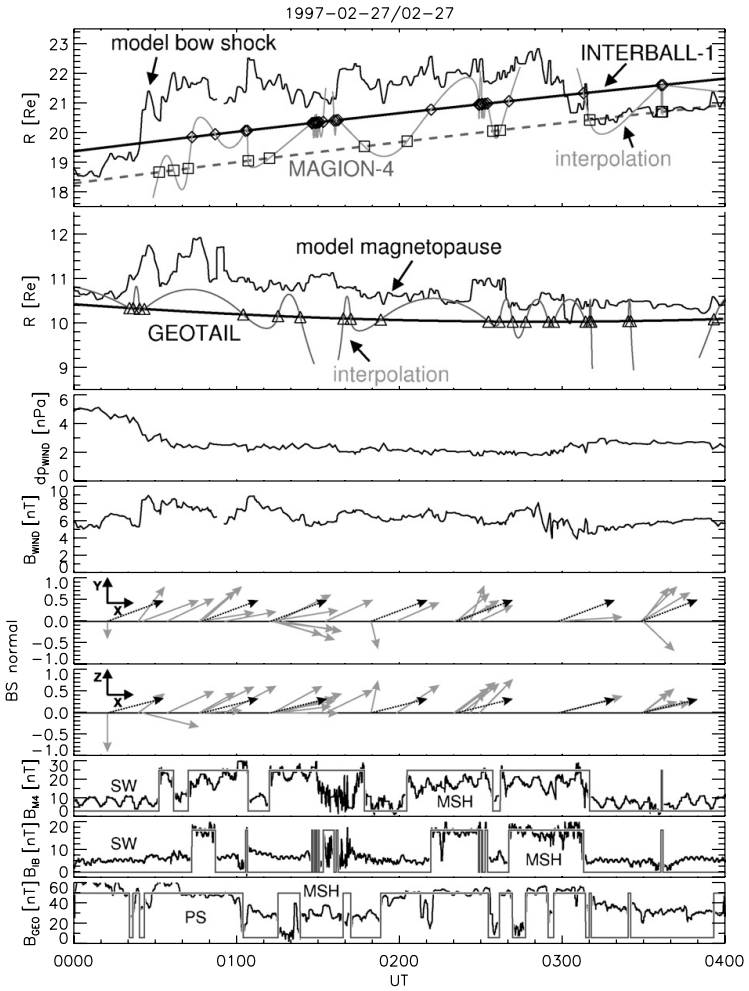

Fig. 3. A detail of the first event. Fifth and sixth panels show bow shock normals computed from the coplanarity theorem (grey arrows), and from the bow shock model (black arrows).

K. Jelínek et al. / Advances in Space Research 41 (2008) 1519–1527 1523

and dynamics. We discuss the plasma ram pressure, bow shock normals, the IMF magnitude, and a possible influence of the tilt angle.

2. Case 1 – the bow shock and magnetopause motions

We have performed a study of the interval from February 26, 1997; 20 UT till February 27, 1997; 20 UT where simultaneous observations of Interball-1/Magion-4 at the bow shock region and Geotail at the magnetopause were available. Projections of the spacecraft trajectories during a 24-h interval are shown in Fig. 1. Both Interball-1 and Magion-4 crossed the bow shock many times in high latitudes (their mutual separation was ~1.5 R_E in this region) and Geotail was located near the magnetopause in the equatorial plane. As a solar wind monitor, we have used the Wind (located upstream (216.6, 17.5, −10.7) R_E in the GSE coordinate system) plasma and magnetic field data shifted on a corresponding propagation time (~60 min) to the Interball-1 position.

In Fig. 2, an overview of this event is presented. The solar wind dynamic pressure (third panel in Fig. 2) was between ~4 and 6 nPa until to February 27, 0030 UT and then gradually decreased to values of 1–2 nPa. An average solar wind velocity was ~380 km/s at the beginning of the interval under study and from 0030 UT it gradually increased to ~450 km/s at the end of the interval. In Fig. 2, lower panels display the magnetic field strengths from all investigated spacecraft together with identification of different regions. The first panel shows geocentric distances of the spacecraft (Interball-1, Magion-4 and Geotail) together with current model locations of the bow shock and magnetopause (computed according to Jeřáb et al. (2005) bow shock and Petrinec and Russell (1996) magnetopause models, respectively). One can note a good global matching of predicted bow shock and magnetopause locations with observed crossings that are shown by points (Interball-1 – diamonds, Magion-4 – squares and Geotail – triangles) on the spacecraft trajectories. However, the figure suggests that the magnetosheath thickness is predicted with a higher accuracy than the position of its boundaries. This effect is clearly seen at second half of the interval (after 1200 UT) because both bow shock and magnetopause are predicted to be closer to the Earth than they are really observed.

An opposite situation occurs between 0000 and 0400 UT when both boundaries are predicted further from the Earth than observed. Since this time interval contains many crossings of both boundaries, we have plotted it in detail in Fig. 3. The organization of the plot is similar to that of Fig. 2 but we have added bow shock normals computed from coplanarity theorem (grey arrows), as well as from the bow shock model (black arrows). Since the bow shock speeds (v_{sh} in Fig. 2) determined from two-point Interball-1/Magion-4 observations do not exceed 50 km/s, we can assume that the bow shock is near the equilibrium state through the whole interval. This assumption is further confirmed by the fact that several bow shock crossings are observed by one spacecraft only (e.g., 0020, 0035, 0130 UT, etc.) and the bow shock is located between two shortly separated spacecraft for several minutes. Since the magnetopause is located closer to the Earth than predicted and the same is true for the bow shock location through a significant part of the interval, one would expect that the uncertainty of prediction of the bow shock position can be caused by an overestimation of the magnetopause distance from the Earth. However, a careful inspection of crossings of both boundaries reveals that there is no correlation between crossings of the magnetopause and the bow shock in this particular case (Jelínek et al., 2006).

This finding is rather surprising because the magnetopause and bow shock represent a coupled system. A solar wind disturbance modifies the magnetosheath parameters and causes the initial bow shock motion (e.g., Šafránková et al., 2007). Further, this disturbance affects the magnetopause location and waves launched from the magnetopause

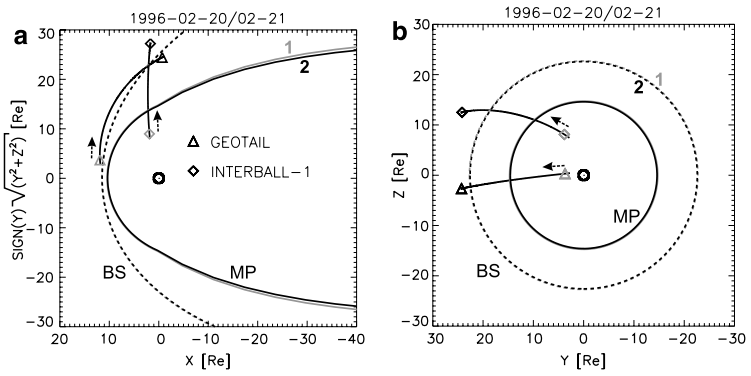

Fig. 4. (a) Positions of the Interball-1/Magion-4 and Geotail spacecraft during observations of multiple bow shock and magnetopause crossings (from 20 February 1996; 1200 UT to 21 February 1996; 1200 UT). For a sketch, the Petrinec and Russell (1996) model magnetopause and Jeřáb et al. (2005) bow shock models were used. (b) Projections of spacecraft trajectories onto the Y–Z plane.

change the bow shock location again. This change is accomplished with a generation of new waves and, consequently, a new equilibrium can be reached after several minutes. Nevertheless, Fig. 2 and blow-up of a part of the analyzed interval in Fig. 3 clearly show that the bow shock and magnetopause move independently in the analyzed case, thus the above discussion can be probably applied on distinct upstream disturbances. We are analyzing an interval with quiet upstream conditions and all fluctuations are generated at the bow shock (foreshock) or in the magnetosheath.

As a next step, we have analyzed the bow shock geometry during observed crossings in order to check if observed crossings can be attributed to surface waves. A possible shape of such waves is shown by the thin lines that an arbitrary way connects the observed crossings in Figs. 2 and 3. However, as can be seen from Fig. 3 presenting a blow-up of a part of analyzed interval, bow shock normals calculated from the magnetic coplanarity theorem are not consistent with surface wave assumption. It means that the crossings are connected with irregular variations of the magnetosheath thickness. Thus, we can conclude that the bow shock and magnetopause motions are affected by a turbulent behavior of the magnetosheath plasma. The studies of the magnetosheath fluctuations (e.g., Šafranková et al., 2002; Shevyrev et al., 2003) have shown that their amplitudes increase with a decreasing frequency and thus one would expect a correlation of the bow shock crossings over large distances.

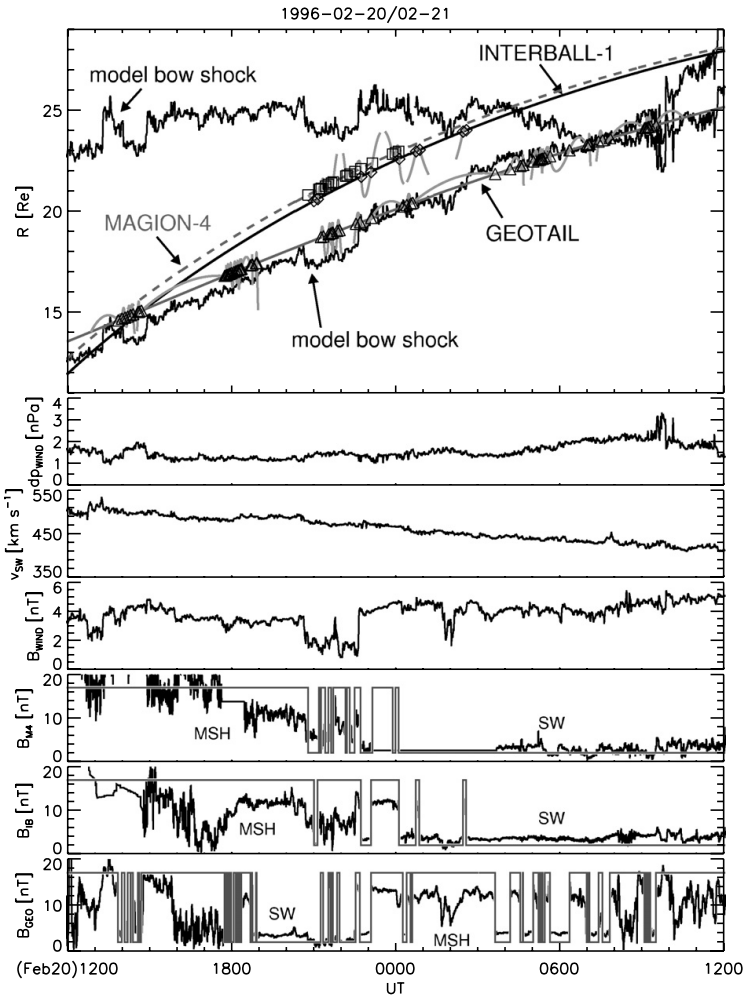

Fig. 5. An overview plot of the second event. Panels from top to bottom: first panel – radial positions of the Interball-1, Magion-4 and Geotail spacecraft and actual model locations of the bow shock and its crossings of all spacecraft; wind solar wind dynamic pressure; wind solar wind velocity; wind IMF; and last three panels present magnetic fields from Magion-4, Interball-1 and Geotail together with identifications of particular regions.

3. Case 2 – the motion of the bow shock

To check this idea, we have chosen the second event that was registered from February 20, 1996; 1200 UT to February 21, 1996; 1200 UT. The positions of Interball-1, Magion-4 and Geotail are depicted in Fig. 4. Similarly to the first case, Interball-1/Magion-4 moved in high latitudes, Geotail in the equator plane; all spacecraft located in the bow shock region. The separations of the spacecraft were ~1, 2 R_E for Interball-1 and Magion-4 and 10–15 R_E for Interball-1 and Geotail. A summary plot of the event is shown in Fig. 5. One can note exceptionally stable upstream conditions (middle panels) with a solar wind dynamic pressure being slightly below its average value. The solar wind speed decreases nearly linearly from 500 to 400 km/s in course of 24 h and this enables a precise propagation of solar wind features from Wind (located at (174, −13, 12) R_E in the GSE coordinate system) to the Earth. The lagged solar wind data were used for prediction of the bow shock distance in the direction from the Earth center to a particular spacecraft.

Model predictions of bow shock locations of all spacecraft are shown in the top panel in Fig. 5 together with orbits of the spacecraft. The observed crossings identified by a visual inspection of the plasma and magnetic field data are denoted with different points along the spacecraft orbits. The Jeřáb et al. (2005) model predicts a nearly constant bow shock distance at the Interball-1 location because the upstream conditions were stable and the spacecraft moves roughly along a radius vector from the Earth.

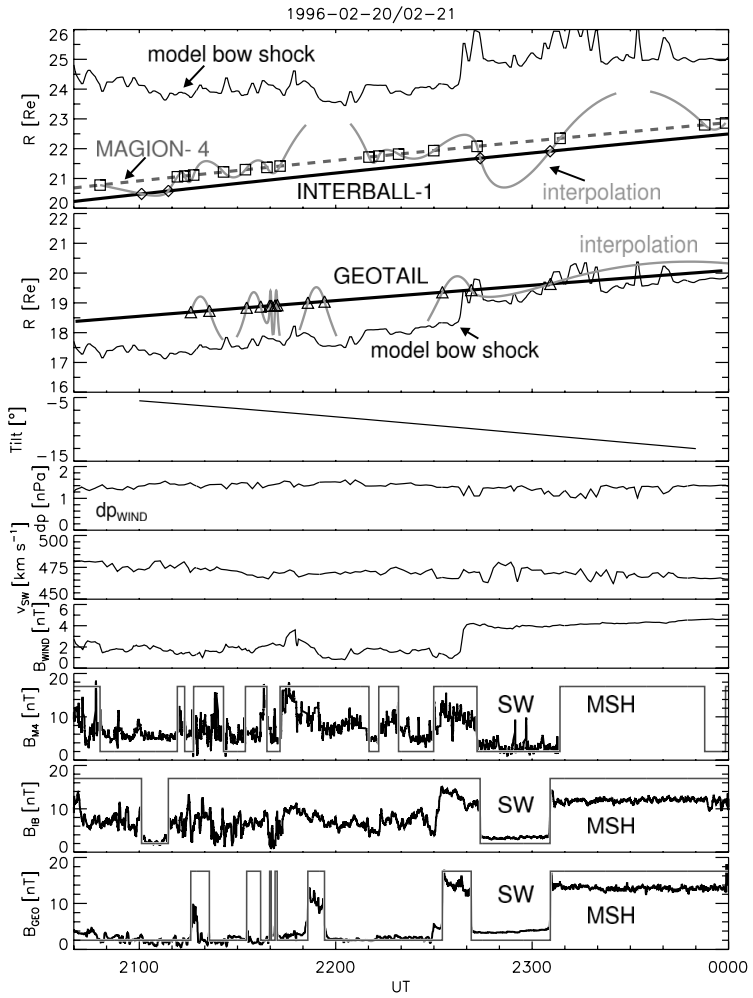

Fig. 6. A detail of the second event. The third panel shows the change of the tilt angle during the interval under study.

On the otherhand, the predicted distance of the bow shock increases with a time at the Geotail location because this spacecraft skims the bow shock from the subsolar region to the dawn flank. The most interesting feature that can be seen in the first panel of Fig. 5 is that, although the prediction of the bow shock location for Geotail is surprisingly good, a large error is seen at the Interball-1 location. We think that this error is caused by the latitude of Interball-1 and we will analyze this effect in detail.

Fig. 6 shows a blow-up of the interval 2040–2400 UT when Interball-1/Magion-4 observed a few bow shock crossings. Upstream conditions were again stable because a majority of crossings were observed by Magion-4 only, thus we could believe that the bow shock was a whole time very close to its location and its distance from the Earth increases gradually throughout the depicted interval. On the otherhand, the predicted bow shock distance was nearly constant and exhibited only one step-like increase at ~2240 UT due to the increase of the upstream magnetic field strength (note that the Jeřáb et al. (2005) model includes this strength as a parameter). Nevertheless, the difference between the bow shock predictions and Magion-4 observations was ~4 R_E at the beginning and only ~2 R_E at the end of the interval. We suggest that this effect is caused by the influence of the tilt angle and by the fact that Magion-4 was at the high latitude in the vicinity of the cusp. The tilt angle changed from $\sim -5°$ to $-14°$ during the interval as it can be seen from the corresponding panel in Fig. 6.

If we compare crossings observed by the different spacecraft, we can see a relatively good correspondence of the crossings observed by Magion-4 and Geotail. Magnetosheath intervals in the Magion-4 data are shorter but they are usually "nested" inside the Geotail magnetosheath intervals. This comparison supposes that the bow shock moves inward and outward simultaneously in both locations in spite of their large separation. We have suggested above that the magnetosheath fluctuations are responsible for a small-scale bow shock motion and an analysis of Fig. 6 leads to a conclusion that probably only those fluctuations with large amplitudes and long wavelengths have enough power to cause a notable bow shock displacement.

4. Conclusion

Our two-case study of simultaneous observations (1) of the bow shock and magnetopause, and (2) of the bow shock at low and high latitudes has shown:

- The bow shock is in a permanent motion due to local changes of upstream and downstream parameters.
- The bow shock location does not follow small magnetopause displacements.
- Although, the magnetopause location generally depends on IMF B_Z, no direct correlation between the bow shock motion and IMF B_Z changes has been found (not shown, see Jelínek et al., 2006).
- The bow shock motion during quiet solar wind intervals is not consistent with surface waves, rather "breathing" of the shock surface is observed. This fact is based on two-point observations of multiple crossings and further confirmed by an analysis of the local normals computed according to coplanarity theorem.
- The location of the high-latitude bow shock is probably a function of the tilt angle of the Earth dipole (Měrka and Szabo, 2004).

We should point out that these conclusions are based on two-case studies and thus a broader study including a statistics of the bow shock observations is needed for their further confirmation.

Acknowledgements

The present work was partly supported by the Czech Grant Agency under Contracts 205/05/0170 and 205/06/0875, by the Ministry of Education of the Czech Republic under the Research plan MSM 0021620860, and by the Charles University Grant Agency under project 147307.

References

Burgess, D. Collisionless shocks, in: Kivelson, M.G., Russell, C.T. (Eds.), Introduction to Space Physics. Cambridge University Press, Cambridge, pp. 129–163, 1995.

Cairns, I.H., Grabbe, C.L. Towards an MHD theory for the standoff distance of Earth's bow shock. Geophys. Res. Lett. 21, 2781–2784, 1994.

Cairns, I.H., Lyon, J.G. MHD simulations of Earth's bow shock at low Mach numbers: standoff distances. J. Geophys. Res. 100, 17173–17180, 1995.

Fairfield, D.H. Average and unusual location of the Earth's magnetopause and bow shock. J. Geophys. Res. 76, 6700, 1971.

Fairfield, D.H., A summary of observations of the Earth's bow shock, in: Physics of Solar Planetary Environments, pp. 514–527, 1976.

Farris, M.H., Russell, C.T. Determining the standoff distance of the bow shock: Mach number dependence and use of models. J. Geophys. Res. 99, 17681, 1994.

Formisano, V. Orientation and shape of the Earth's bow shock in three dimensions. Planet. Space Sci. 27, 1151, 1979.

Jelínek, K., Němeček, Z., Šafránková, J. Simultaneous observations of the bow shock and magnetopause motions, in: Safrankova, J., Pavlu, J. (Eds.), WDS'06 Proceedings of Contributed Papers: Part II-Physics of Plasmas and Ionized Media. Matfyzpress, Prague, pp. 14–20, 2006.

Jeřáb, M., Němeček, Z., Šafránková, J., Jelínek, K., Měrka, J. Improved bow shock model with dependence on the IMF strength. Planet. Space Sci. 53, 85–93, 2005.

Lepidi, S., Villante, U., Lazarus, A.J., Szabo, A., Paularena, K. Observation of the bow shock motion during time of variable solar wind conditions. J. Geophys. Res. 101, 11.107–11.123, 1996.

Maksimovic, M., Bale, S.D., Horbury, T.S., André, M. Bow shock motion observed with CLUSTER. Geophys. Res. Lett. 30, 1393, doi:10.1029/2002GL01676, 2003.

Měrka, J., Szabo, A. Bow shock's geometry at the magnetospheric flanks. J. Geophys. Res. 109, A12224, doi:10.1029/2004JA01056, 2004.

Měrka, J., Szabo, A., Šafránková, J., Němeček, Z. Earth's bow shock and magnetopause in the case of a field-aligned upstream flow: observation and model comparison. J. Geophys. Res. 108, 1269, doi:10.1029/2002JA00969, 2003a.

Měrka, J., Szabo, A., Narock, T.W., King, J.H., Paularena, K.I., Richardson, J.D. A comparison of IMP 8 observed bow shock position with model predictions. J. Geophys. Res. 108, 1269, doi:10.1029/2002JA00969, 2003b.

Němeček, Z., Šafránková, J. The Earth's bow shock and magnetopause position as a result of solar wind-magnetosphere interaction. J. Atmos. Terr. Phys. 53, 1049–1054, 1991.

Němeček, Z., Šafránková, J., Zastenker, G.N. Dynamics of the Earth's bow shock position. Adv. Space Res. (9), 167, 1988.

Newbury, J.A., Russell, C.T., Gedalin, M. The ramp widths of high-Mach-number, quasi-perpendicular collisionless shocks. J. Geophys. Res. 103, 29,581–29,593, 1998.

Peredo, M., Slavin, J.A., Mazur, E., Curtis, S.A. Three-dimensional position and shape of the bow shock and their variation with Alfvénic, sonic and magnetosonic Mach numbers and interplanetary magnetic field orientation. J. Geophys. Res. 100, 7907, 1995.

Petrinec, S.M., Russell, C.T. Near-Earth magnetotail shape and size as determined from the magnetopause flaring angle. J. Geophys. Res. 101, 137, 1996.

Šafranková, J., Přech, L., Němeček, Z., Sauvaud, J.-A. Density profile in the magnetosheath adjacent to the magnetopause. Adv. Space Res. 30, 1693–1703, 2002.

Šafranková, J., Němeček, Z., Jelínek, K. The bow shock velocity from two-point measurements in frame of Interball project. Adv. Space Res. 31, 1377–1382, 2003.

Šafránková, J., Němeček, Z., Přech, L., Samsonov, A., Koval, A., Andréeová, K. Interaction of interplanetary shocks with the bow shock, Planet. Space Sci., accepted, 2007.

Shevyrev, N.N., Zastenker, G.N., Nozdrachev, M.N., Němeček, Z., Šafranková, J., Richardson, J.D. High and low frequency large amplitude variations of plasma and magnetic field in the magnetosheath: Radial profile and some features. Adv. Space Res. 31, 1389–1394, 2003.

Sibeck, D.G., Lopez, R.E., Roelof, E.C. Solar wind control of the magnetopause shape, location, and motion. J. Geophys. Res. 96, 5489–5495, 1991.

Slavin, J.A., Holzer, R.E. Solar-wind flow about the terrestrial planets. 1. Modeling bow shock position and shape. J. Geophys. Res. 86, 1401–1418, 1981.

Slavin, J.A., Holzer, R.E., Spreiter, J.R., Stahara, S.S. Planetary Mach cones: theory and observation. J. Geophys. Res. 88, 19–35, 1984.

Slavin, J.A., Szabo, A., Peredo, M., Oven, C.J., Lepping, R.P., Fitzenreiter, R., Ogilvie, R.W., Stremberg, J.L., Lazarus, A.J. Near-simultaneous bow shock crossings by Wind and IMP 8 on December 1, 1994. Geophys. Res. Lett. 23, 207, 1996.

Spreiter, J.R., Summers, A.L., Alksne, A.Y. Hydromagnetic flow around the magnetosphere. Planet. Space Sci. 14, 223, 1966.

Volk, A.J., Auer, R.D. Motions of the bow shock induced by interplanetary disturbances. J. Geophys. Res. 79, 40–48, 1974.

Zastenker, G., Russell, C.T., Bridge, H., Lazarus, A., Smirnov, V., Němeček, Z., Šafránková, J. Bow shock motion with two-point observations: Prognoz 7, 8 and ISEE-1, 2; Prognoz 10 and IMP-8. Adv. Space Res. (9), 171, 1988.

Zhuang, H.C., Russell, C.T. An analytic treatment of the structure the bow shock and magnetosheath. J. Geophys. Res. 86, 2191, 1981.

C.10 The bow shock velocity from two-point measurements

Pergamon
www.elsevier.com/locate/asr
Available online at www.sciencedirect.com
SCIENCE DIRECT®
doi: 10.1016/S0273-1177(02)00951-1

THE BOW SHOCK VELOCITY FROM TWO-POINT MEASUREMENTS IN FRAME OF THE INTERBALL PROJECT

J. Šafránková[1], K. Jelínek[1], and Z. Němeček[1]

[1] *Charles University, Faculty of Mathematics and Physics, V Holešovičkách 2, 180 00 Prague 8, Czech Republic*

ABSTRACT

The bow shock is a highly dynamic boundary controlled by steady and transient variations in solar wind parameters. It has been found that both shape and position of this boundary are determined mainly by the dynamic pressure and by the upstream Mach number of the incoming solar wind. Intervals of multiple bow shock crossings, often lasting over intervals from minutes to hours, are currently interpreted in terms of bow shock motions with respect to the observing spacecraft.

In the present paper, we examine the bow shock velocity based on several series as well as several single bow shock crossings observed by two closely separated spacecraft (MAGION-4/INTERBALL-1). Our estimations of the bow shock velocity typically ranges from several tens of kilometers per second to approx. 120 km/s. These results correspond to those previously published for quasiperpendicular shocks but our set contains both quasiparallel and quasiperpendicular shocks. An analysis shows that about 80% of crossings can be explained by radial expansion/compression of the bow shock surface. The timing of the rest of events requires another mechanisms for explanation.

INTRODUCTION

The determination of the actual shape and position of the Earth's bow shock (BS) has been a subject of experimental and theoretical studies for many years. It has been found (*Formisano et al.*, 1973) that both shape and position are determined mainly by the dynamic pressure and by the upstream Mach number of the incoming solar wind. Multiple BS crossings, often lasting over intervals from minutes to hours, are currently interpreted in terms of BS motions with respect to the observing spacecraft (e.g., *Spreiter et al.*, 1966; *Formisano et al.*, 1973; *Němeček et al.*, 1988).

The estimation of the BS velocity typically ranges between several tens of kilometers per second to as much as 200 km/s. These results are corresponding to theoretical predictions by *Volk and Auer* (1974) who considered that BS velocities in the subsolar region of the order of 100 km/s can be induced by the BS interaction with solar wind discontinuities, while smaller velocities can be involved by smooth interplanetary perturbations such as Alfvén waves.

Recent observations of the bow shock motion confirm previous investigations. *Lepidi et al.* (1996) examined seven periods during which IMP 8 multiply crossed the Earth's bow shock. The authors found that the transition between the magnetosheath and solar wind consists of a series of multiple BS crossings. In most cases, outward and inward crossings find clear correspondence with temporal variations of the external solar wind parameters (*Němeček et al.*, 1988). They discussed an example in which the occurrence of multiple BS encounters might be interpreted as long-term oscillations of the BS profile following strong variations of the solar wind pressure. *Greenstadt et al.* (1990) found that the model of the BS proposed by *Fairfield* (1971) and normalized to solar wind conditions can explain the observed locations of the BS reasonably well. The solar wind pressure, flow direction, and Mach number give important contributions to explaining changing

Adv. Space Res. Vol. 31, No. 5, pp. 1377–1382, 2003

Printed in Great Britain
0273-1177/03 $30.00 + 0.00

BS positions over intervals of several hours.

Shock speed estimates obtained from Rankine-Hugoniot (R-H) conditions (*Lepidi et al.*, 1996) yield speeds that typically range between several tens and a few hundreds of kilometers per second (similar speeds were obtained by *Dobrowolny and Formisano* (1973)), and the directions of the velocities are consistent with those expected for the bow shock moving across the spacecraft. *Huterer et al.* (1997) analyzed IMP 8 and WIND BS crossings and concluded that the orientations of the shock normals are consistent with the nominal bow shock shape. The shocks were expected to move according to a simple "breathing model" in which the bow shock moves inward and outward to/from the Earth due to changes in external solar wind conditions. Moreover, the direction of the BS motion depends on the exact choice of the shock normal so that a slightly different shock normal can give a different sense of the BS motion. They conclude that the R-H equations that they used may be missing some terms which would provide an accurate description of the balance on both sides of the BS.

Newbury et al. (1998) examined the ramp widths of high-Mach-number ($M_A > 3$), quasiperpendicular shock ($\theta_{Bn} > 45^o$) and considered the bow shock velocities using the ISEE 1 and 2 spacecraft. Shock normals were calculated using the magnetic coplanarity assumption, where upstream and downstream states are defined by averaging over several minutes of steady, undisturbed field measurements. To avoid observations where two-dimensional fluctuations on the shock front may be an issue, coplanarity normals were compared with normals determined from an ellipsoidal bow shock model (with an eccentricity of 0.81 according to *Farris et al.* (1991)), and only those shocks where normals from both methods agreed within 10^o were selected. For these conditions, the shock velocities range from 2 km/s to 65 km/s. However, the authors estimated only those crossings with small spacecraft separation along the normal (20 - 500 km).

In this paper, we analyze ~ 130 BS crossings observed by the INTERBALL-1 and MAGION-4 spacecraft with motivation to determine the bow shock velocity for different solar wind conditions.

DATA SET AND PROCESSING

The basic data set includes a collection of the BS crossings observed simultaneously by INTERBALL-1 and MAGION-4, which were launched as part of the INTERBALL project. Both satellites moved along an elongated elliptical orbit with the inclination of 63^o, apogee of $\approx 195,000$ km, and perigee of ≈ 800 km. Due to orbital parameters and their temporal evolution, both satellites have scanned a broad range of local times throughout the magnetospheric tail toward the subsolar region.

Our data set involves ~ 130 crossings registered from February to April, 1996 and a few crossings from March to April, 1997. The crossings are spread from the subsolar region to the $X_{GSE} \approx -10\,R_E$ (as it is demonstrated in Figure 1a) and occurred under various upstream conditions: the solar wind velocity varied from 340 to 560 km/s, density from 1.5 to 20 cm^{-3}, and Mach number from 6 to 40. The set includes both outbound and inbound crossings, many of them being multiple. The effect of multiple crossings is most pronounced on the flanks where satellites encountered the bow shock region near the apogee and spent there many hours continuously.

BS crossings were identified manually on the basis of observations of ion and electron energy spectra (*Sauvaud et al.*, 1997; *Šafránková et al.*, 1997) and the magnetic field (*Klimov et al.*, 1997). The solar wind and IMF data were taken from the WIND observations. The time of propagation of the solar wind features from the WIND position to the BS registered on MAGION-4/INTERBALL-1 was computed as a two-step approximation from WIND solar velocity measurements. At first step, we calculate the time delay from the WIND coordinates assuming the solar wind velocity equal to 400 km/s. At second step, we use the velocity measured at this point and recalculate the delay. Values of the solar wind dynamic pressure and IMF were computed as five-minute averages centered around the time determined as given above.

Velocities (v_{sh}) are calculated by determining the time separation between shock observations and the spatial separation of both spacecraft in the direction along the shock normal. Providing that t_M is a time when MAGION-4 observes the BS crossing at a location described by the position vector R_M, and INTERBALL-1 observes the crossing at a location R_I in a time t_I, we can write

$$v_{sh} = \frac{(\vec{R}_M - \vec{R}_I)\vec{n}}{t_M - t_I} S$$

where $\vec{n}$ is a unit vector normal to the surface of the Formisano BS model (*Formisano*, 1979) at the point, where INTERBALL-1 crosses the bow shock. The geometry is schematically depicted in Figure 1b. The factor S describes the direction of the crossing ($S = +1$ for crossings from the solar wind to the magnetosheath and $S = -1$ for an opposite direction). Velocities calculated according to the equation are thus positive in all cases where the shock motion can be considered as a radial expansion/compression, i.e., when the spacecraft closer to the shock sees the crossing earlier.

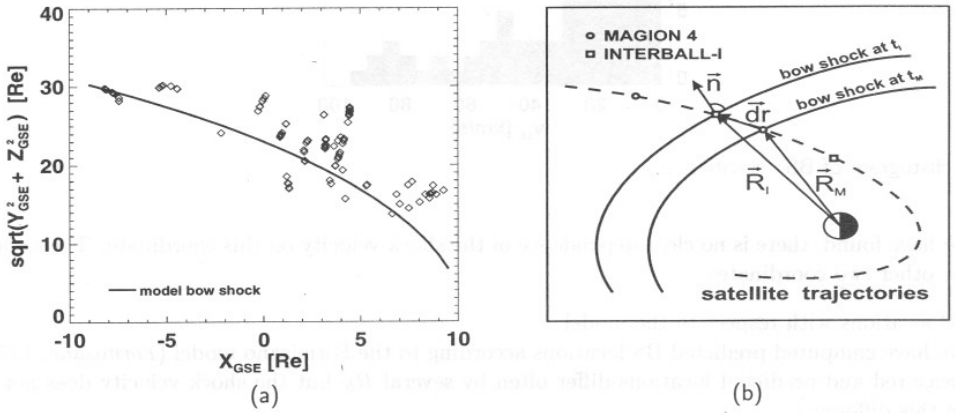

Fig. 1. The radial projection of analyzed BS crossings together with the mean model BS location (a); the method of the BS speed computation (b).

The negative velocities require another mechanism of a motion, e.g., a surface waves (*Zastenker et al.*, 1988). These crossings represent about 18% of our set and we have excluded them from the consideration for purposes of the present paper.

The spatial $(R_M - R_I)$ as well as the temporal $(t_M - t_I)$ separations varied in broad ranges. As a rule, these separations were small (of an order of hundreds km or units of second, respectively) in the subsolar region but they reached 2 R_E or several minutes on flanks. When the separation is small, the main source of the errors is the temporal resolution of measurements. However, in such a case, the profiles measured by two spacecraft are nearly identical and thus the time delay can be determined with an accuracy about 0.2 s and thus the overall error of the velocity determination is not worse than 10%.

EXPERIMENTAL RESULTS

The histogram of velocities determined for 112 crossings which remained for further investigation is plotted in Figure 2. The velocities range from 0 to 100 km/s but a majority of them (78%) is less than 40 km/s. This result is in agreement with previous studies (e.g., *Newbury et al.*, 1998) but it is more general because our set contains all crossings, regardless of upstream parameters, geometry, and θ_{Bn}.

The shock velocity can be a function of many factors. We have divided these factors into several groups and analyzed their influence on the velocity distribution separately.

1. Geometry of the crossings

- Spacecraft separations
  A portion of the crossings was observed near the apogee, where the angle between a shock normal and spacecraft separation vector was large. We think that this fact does not influence our statistics because the plot of v_{sh} versus this angle (not shown) does not exhibit any systematic ordering.

- Coordinates of BS crossings
  The variability of BS locations shown in Figure 1a seems to depend on the X_{GSE} coordinate but, as

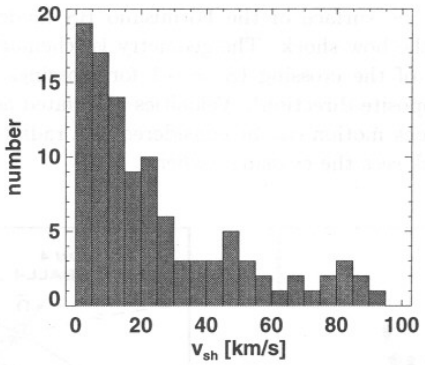

Fig. 2. Histogram of BS velocities, v_{sh}.

we have found, there is no clear dependence of the shock velocity on this coordinate. The same is true for other two coordinates.

- BS locations with respect to the model
  We have computed predicted BS locations according to the Formisano model (*Formisano*, 1979). The measured and predicted locations differ often by several R_E but the shock velocity does not depend on this difference.

2. Solar wind parameters

We have plotted the shock velocity as a function of following parameters: (1) solar wind density, (2) solar wind dynamic pressure, and (3) Alfvénic Mach number. Any of these plots do not exhibit an ordering of the data and we do not show them for this reason.

3. Solar wind and IMF variations

The bow shock motion is usually a result of a change of upstream conditions. Based on the study of several cases, *Němeček et al.* (1988) suggested that the shock velocity can be proportional to the jump of solar wind dynamic pressure responsible for a shock motion. To use a statistical approach, we have computed the jump magnitude, J as a difference between minimum and maximum of one minute averages on 20-minute intervals for a particular parameter. The intervals were centered around the time corresponding to the each bow shock crossing. Figure 3 shows the results in a form of histograms plotted for small and big jumps of the solar wind dynamic pressure (left) and Alfvénic Mach number (right). The break points between small and big jumps were chosen to have the same numbers of crossings in both groups. We can note that very small velocities ($v_{sh} < 5$ km/s) can be observed mostly during quiet upstream conditions. Probability of observations of high velocities does not depend on the magnitude of the pressure jump but it increases during disturbed IMF conditions resulting in big jumps of Mach numbers. This result can be influenced by the fact that all analyzed crossings were observed during almost quiet conditions because our "big jumps"(i.e., $J_p > 0.24$ nPa or $J_M > 2$ for Mach number) are rather standard solar wind or IMF fluctuations. Nevertheless, even such small fluctuations lead to a notable motion of the bow shock. For example, the pressure jump ~ 0.2 nPa would result in the bow shock displacement approx. $0.3\,R_E$. It is surprising that this displacement can sometimes proceed so fastly.

4. IMF direction

We have computed the θ_{Bn} angle as the angle between IMF determined from WIND measurements and the normal to the model BS. The histogram of shock velocities for quasiparallel and quasiperpendicular shocks in Figure 4a shows that the probability of observations of high velocities increases with decreasing θ_{Bn}. However, we should point out that all analyzed crossings were observed on the dusk flank of the BS and thus a majority of crossings are quasiperpendicular, in agreement with the prevailing IMF orientation.

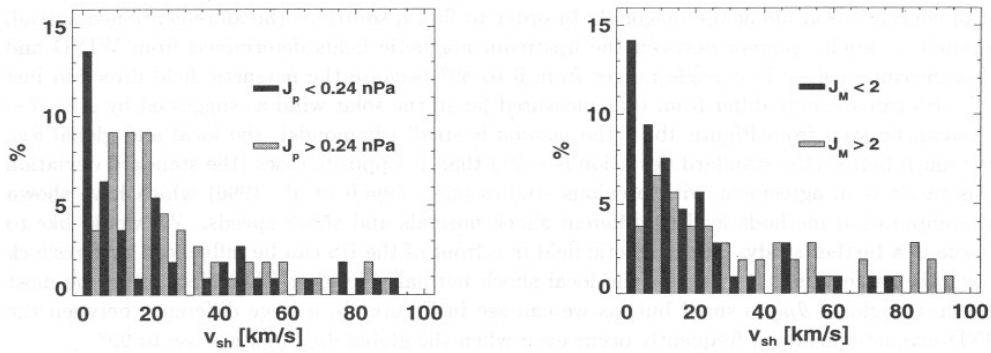

Fig. 3. A comparison of bow shock velocities recorded during quiet and disturbed intervals of the upstream dynamic pressure (a) and Alfvénic Mach number (b).

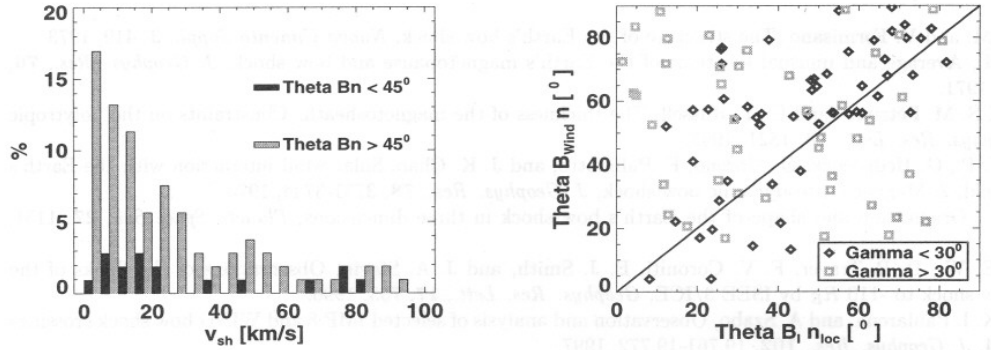

Fig. 4. Histograms of BS velocities for different θ_{Bn} angles (a) and the dependence of the "global" $\theta_{B_{WIND}n}$ angle on the "local" $\theta_{B_I n_{loc}}$ angle (b).

DISCUSSION AND CONCLUSION

Our extended analysis of the influence of different parameters on the speed of a BS motion determined from two-point observations has brought one important result. If we believe that the BS motion is not random, it would be determined by a combination of upstream and downstream parameters and their jumps. However, our (and many previous) study is based on upstream parameters, only. It means that we assume a proportionality between upstream and downstream values but, as the study of the magnetosheath flow (*Němeček et al.*, 2000) has shown, it is true only in a statistical sense. For this reason, we have computed the local shock normal, n_{loc} from the magnetic coplanarity assumption and the local θ_{Bn} as an angle between the coplanarity normal and upstream magnetic field measured by INTERBALL-1. Values of upstream and downstream magnetic fields were computed as averages on intervals from $t_I - 10$ minutes to $t_I - 5$ minutes and from $t_I + 5$ minutes to $t_I + 10$ minutes where t_I is the time of the INTERBALL-1 BS crossing. If a gap between two consecutive crossings was shorter than 12 minutes, these intervals were shortened proportionally.

Figure 4b shows the "global" $\theta_{B_{WIND}n}$ angle (computed from the WIND magnetic field and the model BS) as a function of the "local" $\theta_{B_I n_{loc}}$ angle. The points are spread in the whole plane of the plot with

a weak trend of concentration along the diagonal. In order to find a source of the aforementioned spread, we have computed an angle, *gamma* between the upstream magnetic fields determined from WIND and INTERBALL-1 measurements. This angle ranges from 0 to 80^o because the magnetic field direction just upstream of the BS can strongly differ from that measured far in the solar wind as suggested by *Kessel et al.* (1999). As can be seen from Figure 4b, if the *gamma* is small (diamonds), the local and global θ_{Bn} angles coincide much better (the standard deviation is ~ 21) than in opposite cases (the standard deviation is ~ 38). This result is in agreement with previous studies (e.g., *Lepidi et al.*, 1996) which have shown that different computation methods lead to different shock normals and shock speeds. We would like to address this issue in a further study. The magnetic field in a front of the BS can be influenced by foreshock fluctuations and the same would be true for the local shock normal. However, this effect would be most pronounced when the global θ_{Bn} is small but, as we can see in Figure 4b, a large difference between the IB-1 and WIND magnetic field can frequently occur even when the global $\theta_{B_{WIND}n}$ is close to 90^o.

ACKNOWLEDGEMENTS

The present work was supported by the Czech Grant Agency under Contract 205/00/1686 and by the Charles University Grant Agency under Contract 191/02.

REFERENCES

Dobrowolny, M. and V. Formisano, The structure of the Earth's bow shock, *Nuovo Cimento Suppl.*, **3**, 419, 1973.

Farfield, D. H., Average and unusual locations of the Earth's magnetopause and bow shock, *J. Geophys. Res.*, **76**, 6700-6716, 1971.

Farris, M. H., S. M. Petrinec, and C. T. Russell, The thickness of the magnetosheath: Constraints on the polytropic index, *Geophys. Res. Lett.*, **18**, 1821, 1991.

Formisano, V. P., G. Hedgecock, G. Moreno, F. Palmiotto, and J. K. Chao, Solar wind interaction with the Earth's magnetic field, 2, Magnetohydrodynamic bow shock, *J. Geophys. Res.*, **78**, 3731-3744, 1973.

Formisano, V., Orientation and shape of the Earth's bow shock in three dimensions, *Planet. Space Sci.*, **27**, 1151, 1979.

Greenstadt, E. W., D. P. Traver, F. V. Coroniti, E. J. Smith, and J. A. Slavin, Observations of the flanks of the Earth's bow shock to -110 R_E by ISEE 3/ICE, *Geophys. Res. Lett.*, **17**, 753, 1990.

Huterer, D., K. I. Paularena, and A. Szabo, Observation and analysis of selected IMP 8 and WIND bow shock crossings in late 1994, *J. Geophys. Res.*, **102**, 19,761-19,772, 1997.

Kessel, R. L., E. Quintana, and M. Peredo, Local variations of interplanetary magnetic field at Earth's bow shock, *J. Geophys. Res.*, **104**, 24,869-24878, 1999.

Klimov, S., et al., ASPI experiment: Measurements of fields and waves onboard the Interball-1 spacecraft, *Ann. Geophys.*, **15**, 514-527, 1997.

Lepidi, S., U. Villante, A. J. Lazarus, A. Szabo, and K. Paularena, Observations of bow shock motion during times of variable solar wind conditions, *J. Geophys. Res.*, **101**, 11,107-11,123, 1996.

Němeček, Z., J. Šafránková, and G. N. Zastenker, Dynamics of the Earth's bow shock position, *Adv. Space Res.*, **8**, (9)167, 1988.

Němeček, Z., J. Šafránková, G. N. Zastenker, P. Pišoft, K. I. I. Paularena, et al., Observations of the radial magnetosheath profile and a comparison with gasdynamic model predictions, *Geophys. Res. Lett.*, **27**, 2801, 2000.

Newbury, J. A., C. T. Russell, and M. Gedalin, The ramp widths of high-Mach-number, quasi-perpendicular collisionless shocks, *J. Geophys. Res.*, **103**, 29,581, 1998.

Šafránková, J., G. Zastenker, Z. Němeček, A. Fedorov, M. Simerský, et al., Small scale observation of magnetopause motion: Preliminary results of the Interball project, *Ann. Geophys.*, **15**, 562-569, 1997.

Sauvaud, J.-A., P. Koperski, T. Beutier, H. Barthe, C. Aoustin, et al., The INTERBALL- Tail ELECTRON experiment: Initial results on the low-latitude boundary layer of the dawn magnetosphere, *Ann. Geophys.*, **15**, 587-595, 1997.

Spreiter, J. R., A. L. Summers, and A. Y. Alksne, Hydromagnetic flow around the magnetosphere, *Planet. Space Sci.*, **14**, 223, 1966.

Volk, A. J. and R. D. Auer, Motions of the bow shock induced by interplanetary disturbances, *J. Geophys. Res.*, **79**, 40-48, 1974.

Zastenker, G. N., C. T. Russell, H. S. Bridge, A. J. Lazarus, V. N. Smirnov, et al., Bow shock motion with two-point observations: Prognoz 7, 8 and ISEE 1, 2; Prognoz 10 and IMP 8, *Adv. Space Res.*, **8**, (9)171-(9)174, 1988.

E-mail address of J. Šafránková: jana.safrankova@mff.cuni.cz

C.11 Simultaneous observations of the bow shock and magnetopause motions

Simultaneous observations of the bow shock and magnetopause motions

K. Jelínek, Z. Němeček and J. Šafránková

Charles University, Faculty of Mathematics and Physics, Prague, Czech Republic.

Abstract. The paper deals with several topics connected with a small-scale motion of the Earth's bow shock. We present (1) a short statistical study of bow shock speed as well as (2) search for the causes of its motion by a case study. For statistical study, we have identified a great number of bow shock (BS) crossings observed by two closely separated satellites and computed the speed of the bow shock motion. On the other hand, for a case study, we have chosen one event where INTERBALL-1 and MAGION-4 was moving near BS and GEOTAIL scanned the magnetopause region. We have analyzed a possible influence of upstream parameters derived from a distant solar wind monitor on many BS and magnetopause crossings. However, we did not find any correlations with observed bow shock or magnetopause crossings. From our preliminary study it follows that the small-scale bow shock motion connected with magnetosheath and/or foreshock fluctuations is a possible cause of observed crossings.

Introduction

The bow shock (BS), the most studied example of collisionless shock (e.g., *Farfield* [1971]; *Formisano et al.* [1973]; *Tsurutani and Stone* [1985]; *Burgess* [1995]; *Russell* [1995], and references therein), is formed in the solar wind where the supersonic plasma propagating from the Sun hits some obstacle. The Earth's magnetic field represents such an obstacle because charged particles cannot penetrate through the Earth's magnetic field and they have to, in a first aproach, flow around the Earth's magnetic dipole. Solar wind plasma is superconducting and its dynamic pressure causes a compresion of magnetic field lines as much as this pressure is balanced by a pressure of the magnetic field. We call magnetopause (MP) the boundary where it becomes. A position of such a structure is driven by solar wind dynamic pressure and by the B_Z-component of the interplanetary magnetic field (IMF) (*Petrinec and Russell* [1996], *Sibeck et al.* [1991]).

In a subsonic flow, a movement of particles is influenced far before the obstacle by sonic wave interactions. In a space, the solar wind plasma is supersonic and thus, information caried by waves that there is obstacle cannot travel upstream (i.e., a direction to the Sun). Therefore, in front of the magnetopause, it is formed the bow shock which slows down, heats up, and compress a solar wind plasma so as it can travel subsonicaly between these two boundaries (this region we call the magnetosheath (MSH)). The position and shape of the bow shock depend on a position of the magnetopause (*Farfield* [1971]; *Formisano et al.* [1979]) and the thickness of the magnetosheath is influenced by an upstream magnetosonic Mach number (*Formisano et al.* [1973]) but both regions are of course formed by upstream solar wind conditions.

In our study, we have concerned with changes of several parameters controlling the bow shock position and dynamics. We discuss: the plasma ram pressure, the θ_{Bn} angle (it is the angle between the direction of interplanetary magnetic field lines and the normal vector to the bow shock surface), the magnetosonic Mach number (M_{MS}), magnitude and the B_Z-component of IMF.

Many models of the bow shock location were developed. They are based on statistical set of BS crossings colected by one or more single spacecraft. Such a set of crossing locations was fitted by a quadratic form (i.e., elipsoid or paraboloid) with respect to the solar wind conditions in time of observations (e.g., *Formisano et al.* [1979]). Several models which predict locations

of the bow shock were compared in *Měrka et al.* [2003].

Despite a progess in bow shock modeling, the diferences between predictions and observations remain often as large as several Re. The bow shock crossing is observed mostly due to the changes of its position from one stationary state to another because of variations of solar wind conditions. Such crossings assigned to solar wind parameters do not correspond to an equillibrium position of the bow shock and vice versa. Therefore, we deal with a small-scale motion of the location of the bow shock and the velocity of its motion.

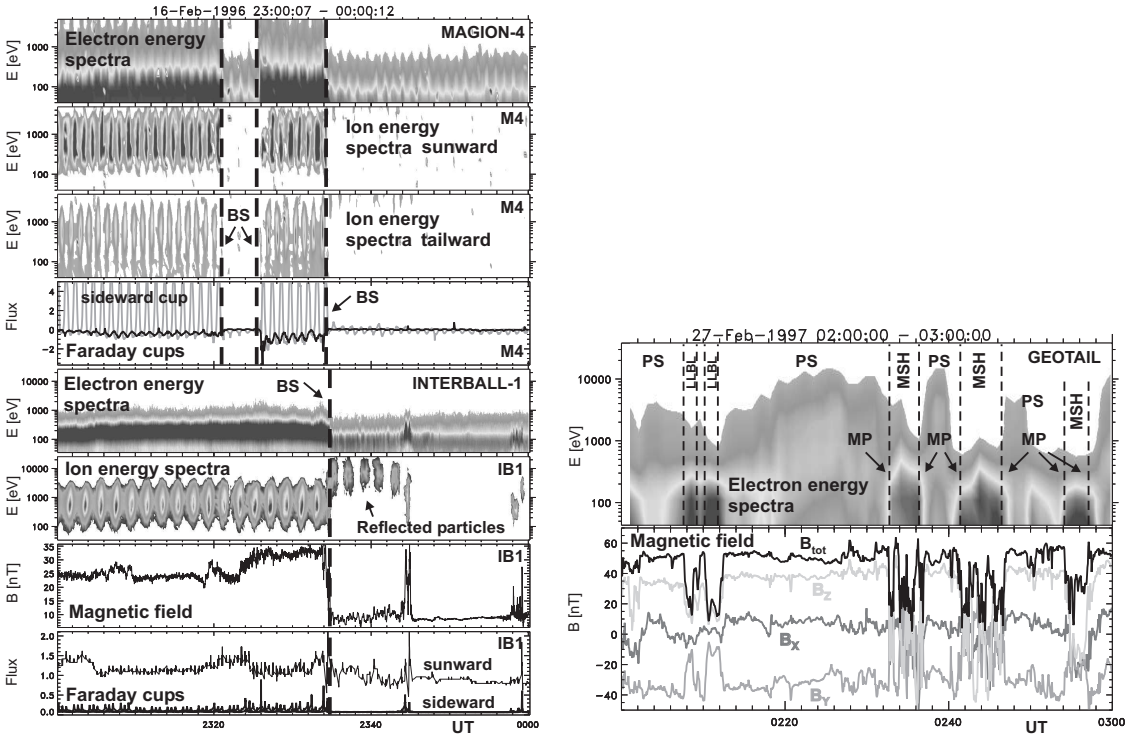

Figure 1. (left) An example of two-point observations of multiple shock crossings. Two first BS at 2321 and 2326 UT are observed only by MAGION-4, the second two at 2334 UT are registered by both MAGION-4 and INTERBALL-1. Panels in left from top to bottom: MAGION-4 measurements - sunward electrons, tailward and sunward ions, all spectra from the energy range of 50 eV - 5 keV, the ion flux; INTERBALL-1 measurements - electron and ion spectra, the magnetic field magnitude, and the ion flux. (right) This figure shows what way we used to identification of the magnetopause crossing by electron energetic spectra (top panel) and the magnetic field (bottom panel) in detail.

Speed of the bow shock motion

To investigation of the bow shock speed, we used a collection of the BS crossings observed by INTERBALL-1 and MAGION-4. Our data set involves approx. 200 BS crossings which were simultaneously registered by both spacecraft (these can be used for the bow shock speed calculation) and approx. 115 crossings registered by one of them, whereas the second one was moving in the solar wind or in the magnetosheath. BS crossings were identified by a visual inspection of observations of ion and electron energy spectra, ion fluxes, and magnetic fields. A way of a BS identification is shown in Figure 1 (left) when both types of studied crossings were observed simultaneously, first two crossings are observed only by the MAGION-4 (at $\approx$ 2321 and $\approx$ 2326 UT) spacecraft and following two crossings are observed by both spacecraft (at $\approx$ 2334 UT).

The solar wind and IMF data were taken from the WIND observations. The time of propagation of the solar wind features from the WIND position to BS registered on MAGION-4/INTERBALL-1 was computed as a two-step approximation from WIND solar velocity measurements. Observed crossings are spread from the subsolar region to the $X_{GSE} \approx -10\,Re$ and occurred under various upstream conditions: the solar wind velocity varied from 315 to 560 km/s, density from 1.5 to $20\,cm^{-3}$, and magnetosonic Mach number from 6 to 40. The set includes both outbound and inbound crossings.

We used the method of the bow shock speed calculation according to the equation

$$v_{sh} = \frac{\vec{R_2} - \vec{R_1}}{t_2 - t_1} \cdot \vec{n_{sh}} \tag{1}$$

where t_1 and t_2 are times of first and second bow shock, respectively observations, and R_1 and R_2 are first and second bow shock locations. The v_{sh} velocity is calculated in the direction along the shock normal $\vec{n_{sh}}$ that was determined from the BS model (*Formisano et al.* [1979]).

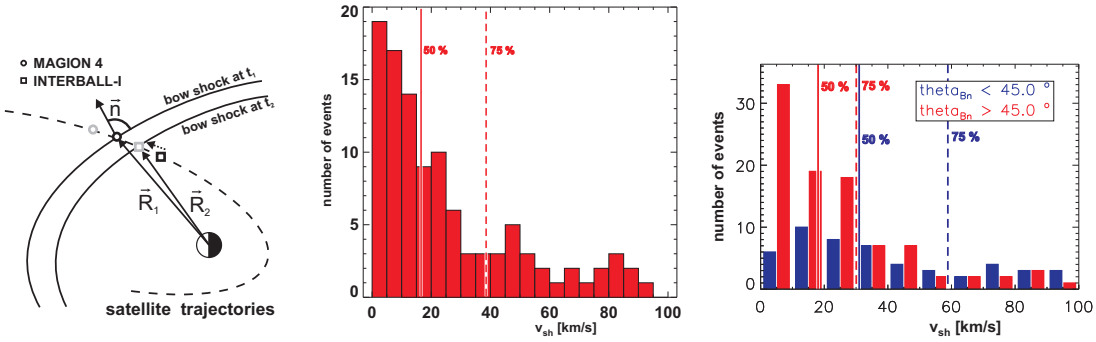

Figure 2. (left) Schematics of calculation of the bow shock velocity, v_{sh}, (middle) the resulting histogram of the bow shock velocity, (right) two histograms of the bow shock velocity v_{sh} for quasiperpendicular (grey columns) and quasiparallel shocks (black columns).

The ilustration of this calculation is presented in Figure 2 (left). The histogram in the middle of Figure 2 reveals that the estimated velocities of the bow shock range between several kilometers per second and ≈ 90 km/s but 75 % of them do not exceed 40 km/s. This result is in agreement with previous studies (e.g., *Němeček et al.* [1989]; *Lepidi et al.* [1996]; *Newbury et al.* [1998]; *Horbury et al.* [2002]; *Maksimovic et al.* [2003]; *Šafránková et al.* [2003]) that determined the speed in the range of units to hunderts of km/s, whereas a majority of observed velocities were under ≈ 40 km/s. However, our result is more general because our set contains all crossings regardless of upstream parameters, geometry and θ_{Bn}.

The histogram of velocities for quasiparallel and quasiperpendicular shocks in Figure 2 (right) shows that the probability of observations of high velocities increases with decreasing θ_{Bn}. However, we should note that a portion of analyzed BS crossings observed on the dusk flank was larger and thus, a majority of crossings are quasiperpendicular, in agreement with the prevailing IMF orientation.

Small-scale bow shock motion

In the second part of the paper, we are interested in a small-scale motion of the bow shock and thus, we have chosen relatively quiet solar wind conditions and observations when simultaneous BS and MP crossings on the different spacecraft were registered. We tried to find such intervals of measurements when one quantity is changing far more than other to analyze an influence of a particular solar wind parameter.

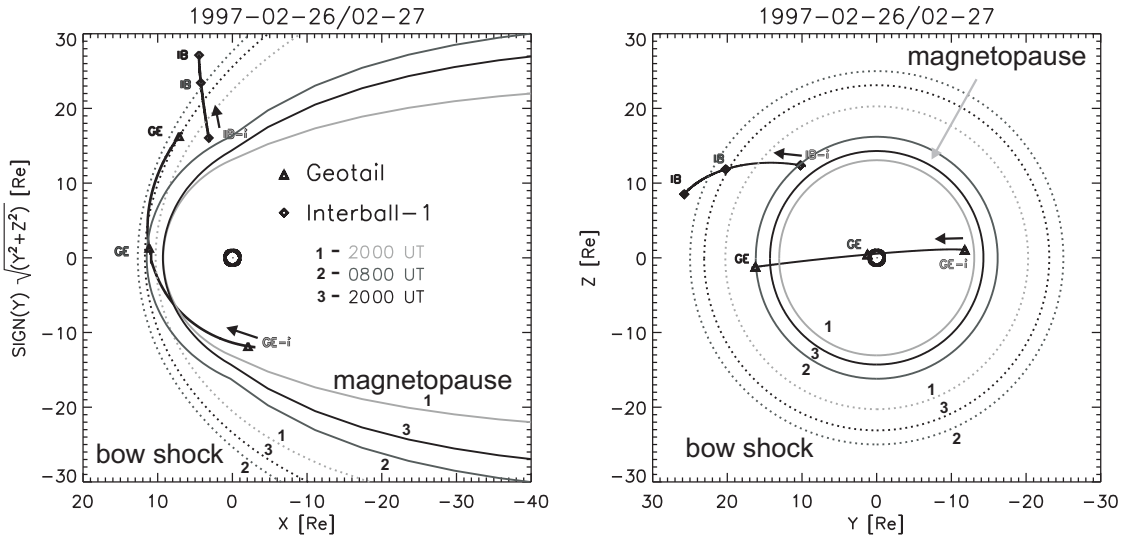

Figure 3. Positions of INTERBALL-1/MAGION-4 and GEOTAIL spacecraft during observations of BS and MP crossings (from February 26, 1997 2000 UT to February 27, 1997 2000 UT), together with the model bow shock and magnetopause locations in different times.

We performed a case study on February 27, 1997 where simultaneous observations of INTERBALL-1 and MAGION-4 in the bow shock region and GEOTAIL at the magnetopause were taken. Trajectories of all spacecraft during a 24-hour observation are documented in Figure 3. One can see that both INTERBALL-1 and MAGION-4 cross the bow shock many times in high latitudes and GEOTAIL is located near the magnetopause in the equatorial plane.

In the left part of Figure 4, an overview of this event is presented. The solar wind dynamic pressure is shown in the second panel; the first panel shows geocentric distances of three spacecraft (INTERBALL-1, MAGION-4 and GEOTAIL) and current model locations of bow shock and magnetopause (both computed from *Jeřáb et al.* [2003] and *Petrinec and Russell* [1996] models, respectively). The last three panels represent profiles of IMF B_Z, and B_Z components of the magnetic field from INTERBALL-1 and GEOTAIL. Through the analyzed event, the dynamic pressure gradualy decreases from $\approx$ 4 nPa to 1 nPa and IMF B_Z changes its value and sign from $\approx$ +5 nT to -7 nT. For this reason, we have chosen a subinterval from 0030 to 0400 UT when the pressure of the solar wind was nerly constant and only IMF B_Z was predominantly negative from -7 nT to near zero, as it is shown in Figure 4 (right) where details of this event are present. The speed of instantaneous bow shock motion calculated along the BS normal and the BS normal determined from a coplanarity theorem (4^{th} panel) are, with one exception around 0100 UT, very small $\approx$ 1-10 km/s. Both vector normals are shovn in 5^{th} and 6^{th} panels and one can see that their difference are small. However, the profile of the θ_{Bn} angle computed from WIND data (last panel) shows significant variations from quasiperpendicular to the close quasiparallel shock orientations.

As can be seen from Fig. 5a (heavy line), the IMF B_Z component was negative with two excurses to positive values. These changes would induce the magnetopause motion and one would expect that the magnetopause displacement would result in a corresponding motion of the bow shock. To analyze the degree of a IMF B_Z control of both boundaries, we have defined "indication functions". These functions are equal to 1 if the particular spacecraft is in the magnetosheath and to 0 when it is in the solar wind (INTERBALL-1, MAGION-4) or in the magnetosphere (GEOTAIL). These functions are shown in Fig. 5a for all spacecraft. Even a very brief visual inspection of this panel shows that the connection between magnetopause

and bow shock motions is rather weak and this conclusion is confirmed by the computed cross-correlation functions between particular indication functions and IMF B_Z that are plotted in Fig. 5c. To check our correlation method, we computed a cross-correlation coefficient between MAGION-4 and INTERBALL-1 indication functions (dashed line in Fig. 5c). Since these spacecraft are closely separated, one would expect a large correlation coefficient and indeed this coefficient peaks for a time lag near zero and its value is 0,53.

Since our statistical study revealed that the θ_{Bn} angle influences the speed of the bow shock motion, we are analyzing its possible influence on the bow shock location a similar way in Figs. 5b and 5d. Fig. 5b also shows the θ_{Bn} angle computed from the BS model and IMF B_Z and B_Z of INTERBALL-1 and MAGION-4 magnetic fields profile and the INTERBALL-1 indication function, whereas their cross-correlation coefficients as is shown in Fig. 5d. These coefficients do not exceed ± 0.3 for any reasonable time-lag and thus we can conclude that there is no direct connection between correlated quantities.

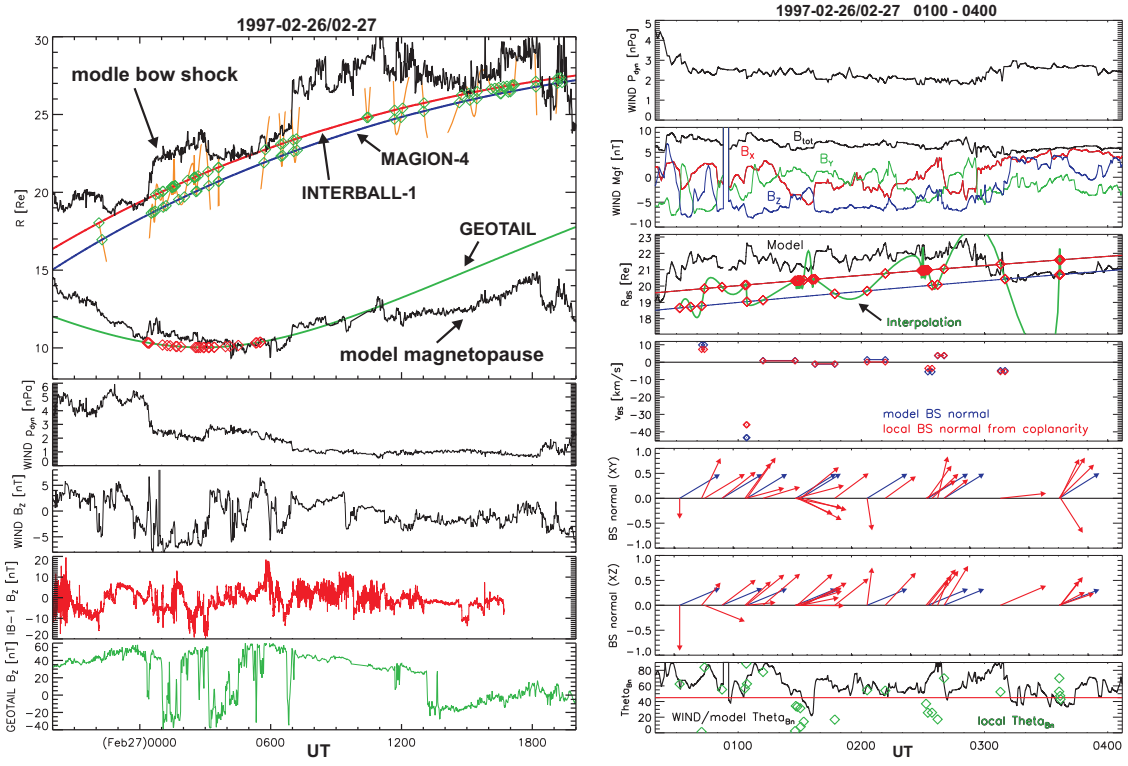

Figure 4. Time plots of simultaneous observations of BS and MP crossings from 27 February, 1997 (left) top panel - distances of particular spacecraft to the Earth and the model magnetopause (*Petrinec and Russell* [1996]) and bow shock (*Jeřáb et al.* [2003]); 2^{nd} panel - dynamic pressure of the solar wind measured by WIND; bottom panels - WIND, INTRBALL-1 and GEOTAIL B_Z components of the magnetic field; (right) top two panels are the dynamic pressure of the solar wind and IMF measured by WIND; 3^{th} panel - distances of spacecraft to the Earth and model bow shock; 4^{th} panel - represents the BS velocity; 5^{th} and 6^{th} panels show model and local normals to the bow shock and in the last panel are model and local θ_{Bn} angles.

Conclusion

We are presenting two topics: (A) an analysis of the speed of the bow shock motion in a statistical sense, and (B) a case study of small-scale changes of the bow shock and magnetopause locations. Our preliminery results suggest that the bow shock motion is much more complicated

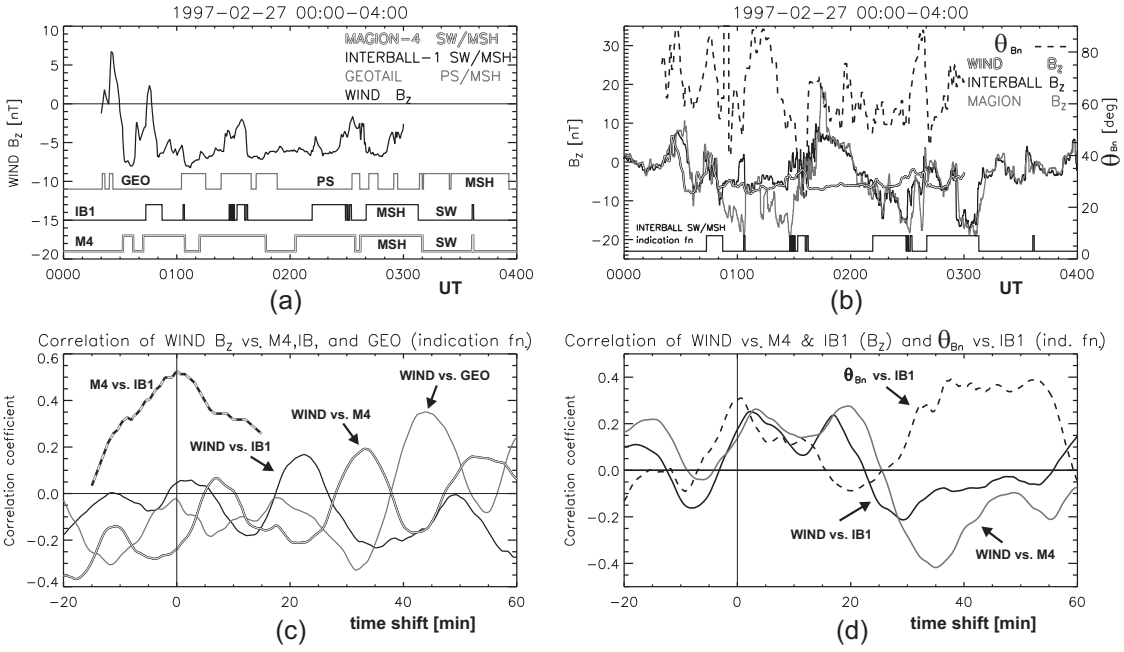

Figure 5. (a) IMF B_Z component and "indication functions" of WIND, INTERBALL-1 and GEOTAIL; (b) the θ_{Bn} angle and B_Z components from INTERBALL-1, MAGION-4 and GEOTAIL; (c) and (d) the correlation functions, in (c) between WIND B_Z and MAGION-4 (light gray), INTERBALL-1 (black) and GEOTAIL (gray) "indication functions" and between MAGION-4 and INTERBALL-1 (black-light gray) "indication function"; in (d) between WIND B_Z and MAGION-4 B_Z (gray) and INTERBALL-1 B_Z (black) and between model θ_{Bn} and INTERBALL-1 (black dashed line) "indication function".

than generally expected: The bow shock is in a permanent motion due to local changes of upstream and downstream parameters. The speed of this motion averaged over 0.5 - 1 Re is less than 100 km/s; in a majority of observed crossings it did not exceed 40 km/s. The probability of observations of large speeds decreases with θ_{Bn}. The bow shock location does not follow small magnetopause displacements. Although the magnetopause location generally depends on IMF B_Z, no direct correlation has been found. The bow shock motion during quiet solar wind intervals is not consistent with the presence of surface waves. The normal computed from the bow shock model and IMF from a distant monitor describes the bow shock properties better than local data.

Acknowledgments. The authors thank the WIND, GEOTAIL, and INTERBALL working teams for the magnetic field and plasma data. The present work was supported by the Czech Grant Agency under Contracts 202/03/H162, and 205/05/0170 and by the Charles University Grant Agency under Contract 247/20050.

References

Burges, D., Collisionless Shocks, In: *Introduction to Space Physics, M.G. Kivelson and C.T.Russell (eds)*, Cambridge: Cambridge University Press, Chapt. 5, pp. 129-163, 1995.

Farfield, D.H., Average and unusual location of the Earth's magnetopause and bow shock, *J. Geophys. Res.*, 76, 6700, 1971.

Farfield, D.H., A summary of observations of the Earth's bow shock, In: *Physics of Solar Planetary Environments*, pp. 514-527, 1976.

Formisano, V., G. Hedgecock, G. Moreno, F. Palmiotto, and J.K. Chao, Solar wind interaction with the Earth's magnetic field, 2, Magnetohydrodynamics bow shock, J. Geophys. Res., 87, 3731, 1973.

Formisano, V., V. Domingo, K.-P. Wenzel, The tree-dimensional shape of the magnetopause, *Planet. Space Sci.*, 27, 1137-1149, 1979.

Horbury T.S., et al., Four spacecraft measurements of the quasiperpendicular terrestrial bow shock: Orientation and motion, *J. Geophys. Res.*, 107, 10.1029/2001JA000273, 2002.

Jeřáb, M., Z. Němeček, J. Šafránková, K. Jelínek, J. Měrka Improved bow shock model with dependence on the IMF strength, *Planet. Space Sci.*, 53, 85-93, 2005.

Lepidi, S., U. Villante, A.J. Lazarus, A. Szabo, and K. Paularena, Observation of the bow shock motion during time of variable solar wind conditions, *J. Geophys. Res.*, 101, 11,107-11,123, 1996.

Maksimovic, M., S.D Bale, T.S. Horbury, and M. André, Bow shock motion observed with CLUSTER, *Geophys. Res. Lett.*, 30, No. 7, 1393, doi:10.1029/2002GL016761, 2003.

Měrka, J., A. Szabo, T.W. Narock, J.H. King, K.I. Paularena, J.D. Richardson, A comparison of IMP 8 observed bow shock position with model predictions, *J. Geophys. Res.*, 108, 1269 doi: 10.1029/2002JA009697, 2003.

Němeček, Z., J. Šafranková and G. Zastenker, Dynamics of the bow shock position *Adv. Space Res.*, 8, No. 9-10, (9)167-(9)170, 1989.

Newbury, J.A., C.T. Russell, and M. Gedalin, The ramp widths of high-Mach-number, quasi-perpendicular collisionless shocks *J. Geophys. Res.*, 103, No. A12, 29,581–29,593, 1998.

Petrinec, S.M., C.T. Russell, Near-Earth magnetotail shape and size as determined from the magnetopause flaring angle *J. Geophys. Res.*, 101, 137, 1996.

Russell, C.T. (ed.), Physics of collisionless shocks: Proceedings of the Symposium of COSRAR Scientific Commission D, Vol. D2.1, Pergamon Press, 1995.

Šafranková, J., Z. Němeček, K. Jelínek, The bow shock velocity from two-point measurements in frame of Interball project, *Adv. Space Res.*, 31, 1377-1382, 2003.

Sibeck, D.G., R.E. Lopez, E.C. Roelof, Solar wind control of the magnetopause shape, location, and motion, *J. Geophys. Res.*, 96, 5489-5495, 1991.

Spreiter, J.R., A.L. Summers, and A.Y. Alksne, Hydromagnetic flow around the magnetosphere, *Planet. Space Sci.*, 14, 223, 1966.

Tsurutani, B.T. and R.G. Stone, Collisionless shock in the heliosphere: Reviews of current research, *Washington DC, American Geophysical Union, Geophysical Monograph Series* **35**.

Wu D.J., J.K.Chao, and R.P. Lepping, Interaction between an interplanetary magnetic field cloud and the Earth's magnetosphere: Motions of the bow shock *J. Geophys. Res.*, 105, 12,627-12,638, 2000.